Conceptual Study of Moderately Coupled Plasmas and Experimental Comparison of Laboratory X-Ray Sources

by

CHIKANG LI

M.A., Physics, Brandeis University (1987)
M.S., Physics, Jilin University, Changchun, China (1985)
B.S., Physics, Sichuan University, Chengdu, China (1982)

Submitted to the Department of Nuclear Engineering
in partial fulfillment of the requirements for the degree of

Doctor of Philosophy

at the

MASSACHUSETTS INSTITUTE OF TECHNOLOGY

December 1993

Signature of Author .....
Department of Nuclear Engineering
December 6, 1993

Certified by .....
Richard D. Petrasso
Principal Research Scientist, Plasma Fusion Center
Thesis Supervisor

Certified by .....
Ian H. Hutchinson
Professor, Department of Nuclear Engineering
Thesis Reader

Accepted by .....
Allan F. Henry
Chairman, Departmental Graduate Committee

Conceptual Study of Moderately Coupled Plasmas and Experimental Comparison of Laboratory X-Ray Sources

by

CHIKANG LI

Submitted to the Department of Nuclear Engineering
on December 6, 1993, in partial fulfillment of the
requirements for the degree of
Doctor of Philosophy

ABSTRACT

In this thesis the fundamental concepts of moderately coupled plasmas, for which $2 \lesssim ln\Lambda_b \lesssim 10$, are, for the first time, presented. This investigation is motivated because neither the conventional Fokker-Planck approximation [for weakly coupled plasmas ($ln\Lambda_b \gtrsim 10$)] nor the theory of dielectric response with correlations for strongly coupled plasmas ($ln\Lambda_b \lesssim 1$) has satisfactorily addressed this regime. Specifically, herein the standard Fokker-Planck operator for Coulomb collisions has been modified to include hitherto neglected terms that are directly associated with large-angle scattering. From this consideration, a Rosenbluth-like vector potential is derived. This procedure allows us to effectively treat plasmas for which $ln\Lambda_b \gtrsim 2$, i.e. moderately coupled plasmas. In addition we have calculated a reduced electron-ion collision operator that, for the first time, manifests $1/ln\Lambda_b$ corrections. Precise calculations of some relaxation rates and crude calculations of electron transport coefficients have been made. In most cases they differ from Braginskii's and Trubnikov's results by terms of order $1/ln\Lambda_b$. However, in the limit of large $ln\Lambda_b$ ($\gtrsim 10$), these results reduce to the standard (Braginskii) form. As one of major applications of the modified Fokker-Planck equation, we have calculated the stopping powers and ρR of charged fusion products (α's, ^{3}H, ^{3}He) and hot electrons interacting with plasmas relevant to inertial confinement fusion. The effects of scattering, which limited all previous calculations to upper limits only, have been properly treated. In addition, the important effects of ion stopping, electron quantum properties, and collective plasma oscillations have been treated within a unified framework. Futhermore, issues of heavy ion stopping in a hohlraum plasma, which too have $\lesssim 10$, and are therefore moderately coupled, are also presented.

In the second major topic of this thesis, we present the advances made in the area of laboratory x-ray sources. First, and most importantly, through the use

a Cockcroft-Walton linear accelerator, a charged particle induced x-ray emission (PIXE) source has been developed. Intense line x radiation (including $K-$, $L-$, $M-$, and N-lines) with wavelengths from 0.5 Å to 111 Å have been successfully produced. The crucial feature of this source is that the background continuum is orders of magnitude lower than that from a conventional electron-beam x-ray source. Second, a new high intensity electron-beam x-ray generator has also been developed, and it has been used with advantage in the soft x-ray region ($\lesssim$ 3 keV). In particular, this generator has successfully calibrated novel new X-UV semiconductor diodes in both DC and AC modes. Finally, we have made direct comparisons of both sources (PIXE and electron-beam x-ray sources) to a commercially available radioactive α fluorescent x-ray source. The electron beam and α fluorescent sources are found to both have significantly higher continuum background than the PIXE source.

Thesis Supervisor: Richard D. Petrasso
Title: Principal Research Scientist, Plasma Fusion Center

Thesis Reader: Ian H. Hutchinson
Title: Professor, Department of Nuclear Engineering

Acknowledgments

Although being a graduate student is often an arduous task, my experience at MIT has been truly exciting and enjoyable. I would like to take this opportunity to express my gratitude to MIT, and to many people here at the Plasma Fusion Center who have assisted in this undertaking.

I would like, first, to thank my thesis advisor, Dr. Richard Petrasso, for his invaluable support, understanding, patience, and encouragement over the course of my whole graduate experience at MIT. He suggested many research interesting topics and helped me to develop physical insights into these issues. It has been a great pleasure working under his guidance on interesting research, both theoretically and experimentally.

I would like to thank Professor Ian Hutchinson, my thesis reader, for his critical suggestions on this thesis and for his time and advice during the course of my study. In addition, I learned a great deal by taking his graduate course *Principles of Plasma Diagnostics*.

I would like to thank Professors Jeffrey Freidberg, Dieter Sigmar, and Kevin Wenzel for serving as members of my thesis committee. Furthermore, I appreciate very much the help from Professor Freidberg and Professor Sigmar when I took the graduate courses *Fusion Energy* and *Plasma Transport Phenomena*.

Professor Wenzel deserves special thanks for his considerable help and support throughout my career at MIT. I have benefited greatly from the experience of working with him in the laboratory.

Several other people who have assisted me during the course of my thesis research program are gratefully acknowledged. This includes Dr. Peter Catto, Dr. Catherine Fiore, Mr. Bob Childs, Mr. Frank Silva, and many people in the Alcator C-Mod group and in Plasma Fusion Center. For their friendship and assistance, I want to express my great appreciation to fellow students here in the Plasma Fusion Center, especially Daniel Lo, Jim Lierzer, Cristina Borrás, Ling Wang, David Rhee, and Xing Chen.

I want to thank my parents, Professors Zhongyuan Li and Shufen Luo, my sister, and my brother for their lifetime of love and support. Their constant encouragement was crucial, especially in the darkest period of Chinese "Cultural Revolution", when I was forced to work in the countryside. Finally, I would like to thank my wife, Hong Zhuang, and my son, Larry, for their endless love, patience and support. Without the support from all these members of my family, it would have been impossible for me to finish my graduate study at MIT.

This work is supported in part by the U.S. Department of Energy and Lawrence Livermore National Laboratory.

Contents

List of Figures

List of Tables

Chapter 1

Thesis Organization

In this thesis we present the first conceptual and theoretical studies of moderately coupled plasmas. In particular, the Fokker-Planck equation is modified in order to analytically compute relaxation rates and transport coefficients. Of special importance is our determination of charged particle stopping powers and ranges in inertial confinement fusion (ICF) plasmas. In more detail, Chapter 2 reviews the traditional classification of weakly and strongly coupled plasmas and associated theories. In addition the motivation and justification for moderately coupled plasmas is therein presented. In Chapter 3 we discuss the modifications in the Fokker-Planck equation in order to treat moderately coupled plasmas. Chapter 4 contains simple illustrations of this equation. In Chapter 5 the issues of charged particle stopping and range in inertial confinement fusion plasmas are discussed within a comprehensive framework. Therein we include not only the modifications arising from the new Fokker-Planck equation but other essential concepts (such as electron quantum degeneracy, ion stopping, and collective plasma oscillations). And finally, in Chapter 6 a similar approach is applied to studying heavy ion stopping in inertial confinement hohlraum plasmas, which too is a moderately coupled plasma.

The second part of this thesis comprises an experimental study of novel laboratory x-ray sources that we have developed. We begin Chapter 7 with a brief review of x-ray generation and detection techniques. In Chapter 8, a newly-developed proton-induced x-ray emission (PIXE) source is described and characteristic operating parameters and experimental results are presented. Chapter 9 contains details of the design, construction, and applications of a new electron-beam x-ray generator. In Chapter 10 an experimental comparison among the two aforementioned x-ray source, and a radioactive x-ray source is made. Therein we show that the crucial feature of the PIXE source is that its continuum background is greatly reduced compared to either the electron-beam or α-induced radioactive x-ray sources. In Chapter 11 we conclude by summarizing the main results of this thesis and by recommending issues for future work.

Chapter 2

Introduction to Moderately Coupled Plasmas

In this chapter we present some fundamental concepts of the plasmas that pertain to this thesis. Emphasis will be placed on reviewing the different categories of plasmas in terms of their important physical characteristics. Furthermore, we introduce, to the best of our knowledge for the first time, the concepts and mathematical framework of moderately coupled plasmas. Such plasmas form a pivotal bridge between weakly coupled and strongly coupled plasmas.

2.1 Motivation

As it is well known, when the Coulomb logarithm ($ln\Lambda_b$) $\gtrsim 10$, a plasma is classified as a weakly coupled and, as a consequence, the test-field particle interactions are well approximated by binary interactions[1-10]. In the other extreme when $ln\Lambda_b \lesssim 1$, the plasma is strongly coupled and the interactions are modeled as many-body and collective in nature[10-14]. However, there is a large class of plasmas for which Coulomb logarithm is of order unity or greater ($ln\Lambda_b \simeq 2$ - 10), and for which the coupling parameter is $\Gamma \sim 10^{-1} - 10^{-4}$. Such plasmas, which form a

bridge between weakly coupled and strongly coupled plasmas, we term moderately coupled[15, 16]. It is worthwhile to point out that of the 99% plasma mass in the visible Universe, almost all is a moderately coupled, high-density plasma. This follows from the fact, as we will discuss latter, that most stars in the Universe are Sun-like, and the Sun is a moderately coupled plasma from core to photosphere.

2.2 Plasma Parameters and Classifications

Among several useful plasma parameters, two of the most fundamental are plasma density - - defined as the number of charged particles (electrons or ions) in unit volume, and plasma temperature - - defined as the average kinetic energy of particles in thermal equilibrium. Using these two parameters, several important concepts relevant to the classification of weakly, moderately, and strongly coupled plasmas are discussed.

A. Plasma Coupling Parameter (Γ) and the Coulomb Logarithm ($ln\Lambda_b$).

The plasma coupling parameter is usually defined as the ratio of the inter-particle potential to the particle kinetic energy. For example, for classical plasmas[17, 31],

$$\Gamma \;=\; \frac{e^2 n^{1/3}}{kT} \;. \tag{2.1}$$

[Note: Instead of using the inter-particle spacing ($n^{-1/3}$), the Wigner-Seitz radius associated with the particle, $a_1 = (3/4\pi n)^{1/3}$, is also often used[11, 60].] In contrast, for quantum degenerate plasmas[17], the Fermi energy E_F [$=\hbar^2(3\pi^2 n)^{2/3}/2m$] must replace the classical kinetic energy (kT). With the values of Γ at two opposite extremes ($<< 1$, and $\gtrsim 1$), plasmas have been historically defined as either weakly coupled or strongly coupled, respectively[10].

Another equivalent approach that is also widely used is the Coulomb logarithm, which originates as a consequence of the *ad hoc* cutoff procedure to eliminate the divergence in the cross section of Coulomb interaction[18, 19]. In plasma physics it is usually defined as

$$ln\Lambda_b \;=\; ln(\frac{\lambda_D}{p_{min}}) \sim ln(\frac{1}{\Gamma}) \;, \tag{2.2}$$

where λ_D is the Debye length and p_{min} is a characteristic impact parameter for closest collision in the binary interaction. The range of the Coulomb logarithm also delineates the various plasma regimes. One way to think about the Coulomb logarithm is, in the contex of weakly coupled plasmas, that it is a measure of the relative importance of small-angle collisions to the large-angle scattering. Thus for $ln\Lambda_b \gtrsim 10$, small-angle collisions totally dominate. Furthermore, Γ has other often-used relations,

$$\Gamma \;\sim\; \frac{1}{n\lambda_D^3} \;\sim\; \frac{\nu}{\omega_p} \;. \tag{2.3}$$

where $1/(n\lambda_D^3)$ is the inverse of the plasma parameter, and ν/ω_p is the ratio of the collision frequency to the plasma frequency.

B. The Degeneracy Parameter (Θ).

The degeneracy of a plasmas is defined as the ratio of the particle kinetic energy to the Fermi energy[72],

$$\Theta \;=\; \frac{kT}{E_F}, \tag{2.4}$$

This parameter determines the importance of quantum mechanical effects in plasmas. When $\Theta \ll 1$ ($\Theta \gg 1$), quantum (classical) effects are dominant.

Table 2.1:

Classification of plasmas

Plasmas	Γ	$\ln\Lambda_b$	Examples
Weakly Coupled	$<<< 1$	$\gtrsim 10$	magnetic confinement fusion plasmas (tokamak, mirror, pinches, etc.), solar corona, magnetosphere, ...
Moderately Coupled	10^{-4} - 10^{-1}	2 - 10	inertial confinement fusion plasmas, solar interior, x-ray laser plasmas, short-pulse laser plasmas, electrons in white dwarf, ...
Strongly Coupled	$\gtrsim 10^{-1}$	$\lesssim 1$	nonneutral plasmas, ions in white dwarf electrons in liquid helium, Fe crust in neutron star, wigner crystal, conducting metals . . .

In terms of above parameters, a nominal phase diagram for different categories of plasmas is shown in Fig.(2-1), in which the plasma density, $\mathrm{Log}_{10}\ (n_e)$ [$\mathrm{Log}_{10}\ (d_e)$, where d_e is inter-particle spacing], is plotted vs the plasma temperature, $\mathrm{Log}_{10}\ (T_e)$. The line that denoted $E_F = kT_e$ separates the quantum degenerate plasmas (region II) from the nondegenerate plasmas (region I). Furthermore, in classical region (region I), strongly and moderately coupled plasmas are separated by the straight line of $e^2 n_e^{1/3} = kT_e$. Similarly, in quantum degenerate region (region II), strongly and moderately coupled plasmas are separated by the straight line of $e^2 n_e^{1/3} = E_F$. With these delineation, consequently, one finds the domain of the moderately coupled plasmas in the transition region, i.e. below the lines of $E_F = kT_e$ and $e^2 n_e^{1/3} = kT_e$ for classical plasmas, and above the lines of $E_F = kT_e$ and $e^2 n_e^{1/3} = E_F$ for quantum degenerate plasmas. Table 2.1 gives some examples for these three regimes of plasmas.

It is worthwhile to point out that the condition $ln\Lambda_b \lesssim 1$ is only a necessary,

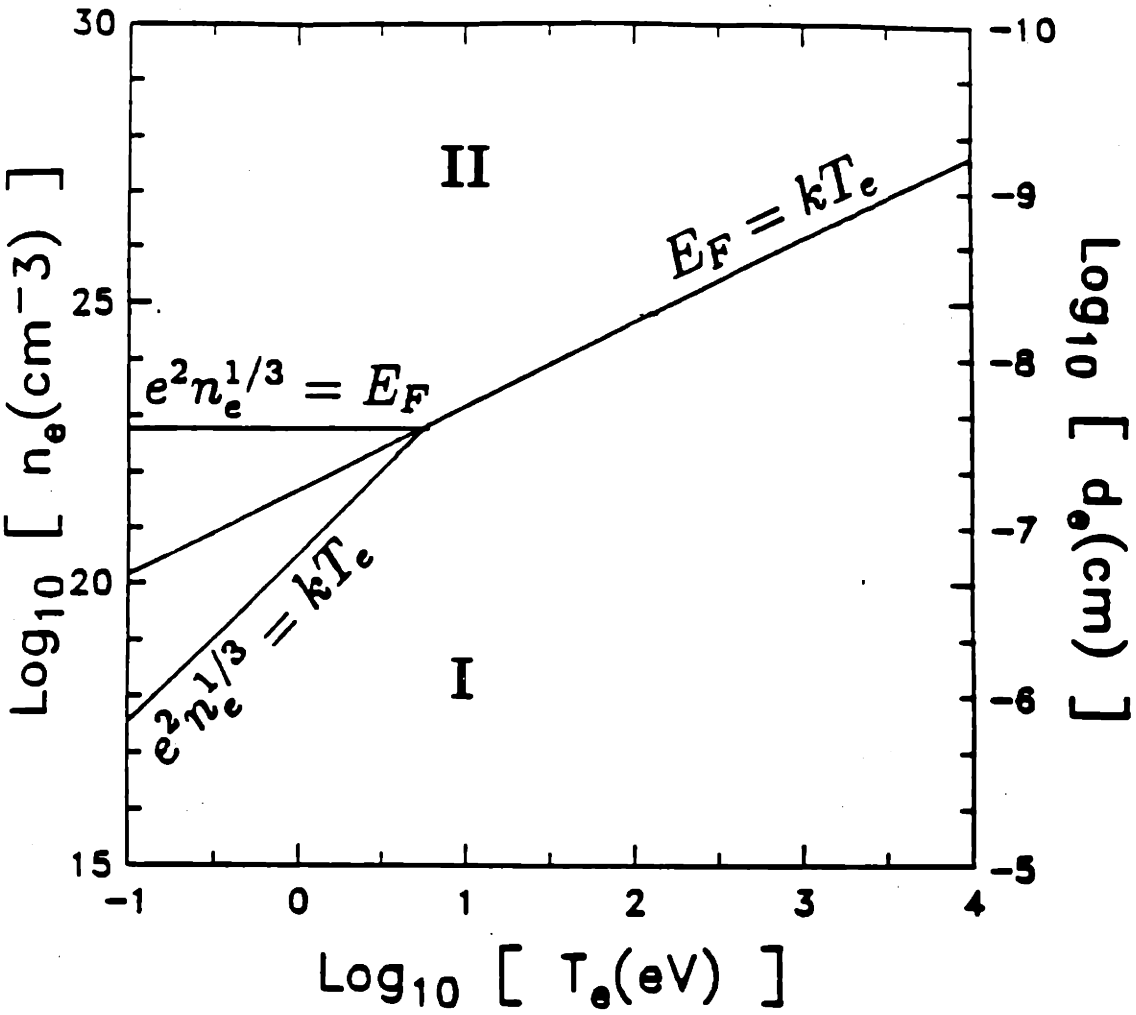

Figure 2-1: The nominal phase diagram of the plasmas density, Log_{10} (n_e) [Log_{10} (d_e)], versus the temperature, Log_{10} (T_e). The line that denoted $E_F = kT_e$ separates the quantum degenerate plasmas (region II) from the nondegenerate plasmas (region I). Furthermore, in classical region (region I), strongly and moderately coupled plasmas are separated by the straight line of $e^2 n_e^{1/3} = kT_e$. Similarly, in quantum degenerate region (region II), strongly and moderately coupled plasmas are separated by the straight line of $e^2 n_e^{1/3} = E_F$. With these delineation, consequently, one finds the domain of the moderately coupled plasmas in the transition regions, i.e. below the lines of $E_F = kT_e$ and $e^2 n_e^{1/3} = kT_e$ for classical plasmas, and above the lines of $E_F = kT_e$ and $e^2 n_e^{1/3} = E_F$ for quantum degenerate plasmas.

not sufficient for strongly coupled plasma. For example, some strongly magnetized non-neutral plasmas have $ln\Lambda_b \lesssim 1$ but are still weakly coupled. The reason is that in this case the Debye length is replaced by the gyro-radius of the particles (r_c, when $r_c < \lambda_D$) in calculating the Coulomb logarithm[20, 21].

A useful example of these plasma regimes is a star in different periods of its life. Take for instance the Sun whose Coulomb logarithm profile is illustrated in Fig.(2-2). While the solar corona consists of weakly coupled plasmas (typically, $T_e \sim 2$ million degree and $n_e \sim 10^6 - 10^8$ cm^{-3}), the solar interior is a moderately coupled plasma ($T_e \sim$ 0.001-1.3 keV and $n_e \sim 10^{16} - 10^{26}$ cm^{-3})[22]. Furthermore, when a Sun-like star burns off all its fuel and reaches the end of its life, it becomes a white dwarf and its ions are strongly coupled ($T_i \sim 10$ keV and $n_i \gtrsim 10^{30}$cm^{-3})[10].

2.3 Weakly Coupled Plasmas

Weakly coupled plasmas are well defined and most familar, with examples like magnetically confined fusion plasmas (tokamak, pinches, mirrors . .), the solar corona, the magnetosphere, lightning . . . Their typical low plasma density and relatively high temperature make the coupling parameters much less than unity ($\Gamma <<< 1$) and Coulomb logarithms are 10 or greater[10]. For example, space plasmas ($\Gamma \sim 10^{-13}$ and $ln\Lambda_b \sim 30$), tokamak plasmas ($\Gamma \sim 10^{-9}$ and $ln\Lambda_b \sim 20$), and the solar corona ($\Gamma \sim 10^{-9}$ and $ln\Lambda_b \sim 20$) are typical weakly-coupled plasmas[16].

Weakly coupled plasmas are equivalently characterized by the following scale-length ordering:

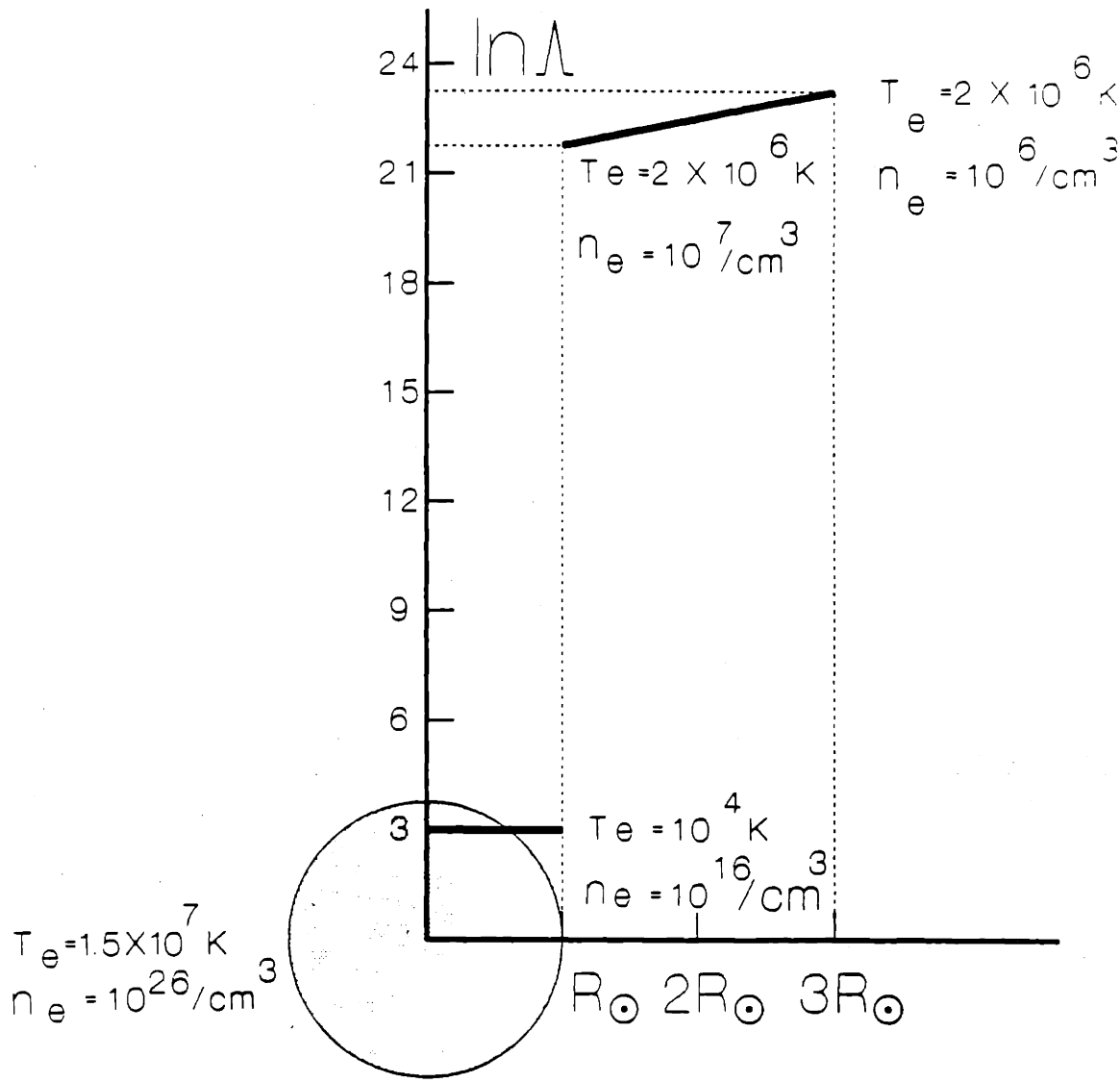

Figure 2-2: The Coulomb logarithm profile of the Sun. It is interesting that the profile is discontinuous at the surface of the Sun (photosphere). Two categories of plasmas, moderately coupled and weakly coupled, are then evident within the solar interior and in the solar corona, respectively.

Table 2.2:

Scale-length ordering for weakly coupled plasmas

	$p_\perp$(cm)	$n^{-1/3}$(cm)	λ_D(cm)	$\bar{\lambda}_{90^\circ}$(cm)
Solar corona	$\sim 10^{-9}$	$\sim 10^{-4}$	$\sim 10^{-1}$	$\sim 10^{6}$
$n_e \sim 10^{10}/cm^{-3}$, $T_e \sim 0.1$ keV				
Tokamak plasma	$\sim 10^{-11}$	$\sim 10^{-5}$	$\sim 10^{-2}$	$\sim 10^{6}$
$n_e \sim 10^{14}/cm^{-3}$, $T_e \sim 10$ keV				

$$p_\perp \ll n^{-1/3} \ll \lambda_D \ll \bar{\lambda}_{90^\circ} , \tag{2.5}$$

where $p_\perp$ is the impact parameter for 90° scattering, $n^{-1/3}$ is the inter-particle spacing, λ_D is the Debye length, and $\bar{\lambda}_{90^\circ}$ is the mean-free-path for 90° deflection. It is readily shown that this ordering is only valid when $ln\Lambda_b > 10$. Table 2.2 lists the typical examples.

In addition, because of the long-range nature of Coulomb interactions, a test particle suffers overwhelmingly small-angle collisions in weakly coupled plasmas. This point can be verified through the following estimate. For example, for an electron with energy of 1 keV colliding with an ion in a plasma ($n_i \sim 10^{15}$ cm^{-3}), the Coulomb logarithm is approximately 15, and the collision time is about 5×10^{-7} sec. Thus the 90° deflection time is estimated to be about 2.5×10^{-7} sec. Also the time for a single collision of an electron with a plasma ion can be roughly estimated in terms of the transit time of an electron through a Debye sphere of radius λ_D (about 5×10^{-4} cm under the present conditions), which is about 2.5×10^{-13} sec. Thus surprisingly, for an electron to be deflected by 90°, it takes of order 1 million collisions, as depicted in Fig.(2-3). Treating this as a random walk process,

$$\theta^2 \sim N(\Delta\theta)^2 , \tag{2.6}$$

where θ is the total deflected angle, N is the number of collisions, and $\Delta\theta$ is a characteristic angle of deflection for a single "step" (i.e. collision). Taking $\theta \simeq 90°$ and $N \simeq 10^6$, one finds that, on average, each collision causes a deflection of only $\sim 0.1°$. As a consequence, this implies that the motion of the particles is a diffusive process in configuration space (as well as velocity space).

Within the theoretical framework of the kinetic theory, weakly coupled plasmas are well addressed by the Fokker-Planck equation[3, 4, 6, 7, 8, 9].

$$(\frac{\partial f_t}{\partial \tau})_{coll.} = -\frac{\partial}{\partial v_i}(f_t < \Delta v_i >^{t/f}) + \frac{1}{2}\frac{\partial^2}{\partial v_i \partial v_j}(f_t < \Delta v_i \Delta v_j >^{t/f}) , \tag{2.7}$$

where the superscript and subscript t (f) represents the test (field) particle. The motion of the test particle is described as follows: in velocity space, the test particle undergoes numerous small deflections (small-angle binary interactions and therefore this represents a pure diffusive process). Because there is no memory or correlation before and after a collision, the process is Markovian. The grazing encounters, involving small fractional momentum and even smaller energy exchanges between the test and field particles, dominate the evolution of the particle distribution functions in velocity space. Furthermore, it is generally true that quantum degenerate effects are usually unimportant in weakly coupled plasmas because of the relatively low plasma density and high temperature. As a consequence the de Broglie matter wavelengths of the plasma particles are usually much smaller than the inter-particle spacing.

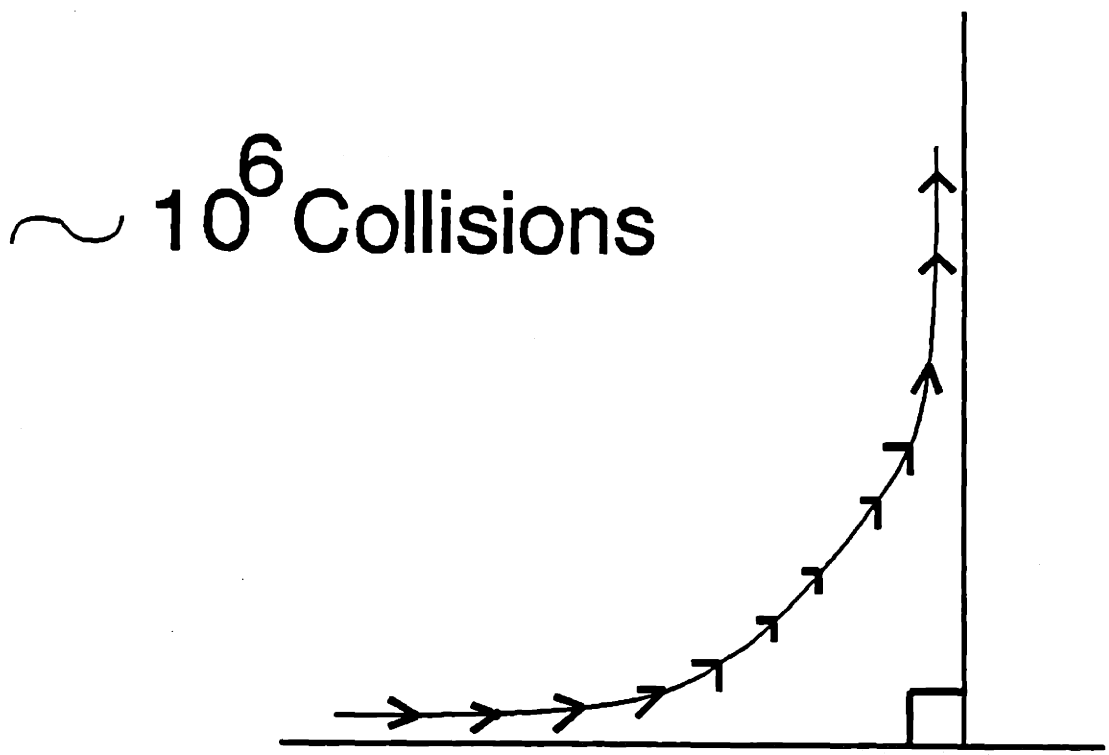

Figure 2-3: A schematic of 90° scattering for particles in a weakly coupled plasma. As shown, because the collisions are grazing ones (with only small fractional momentum and even less energy exchanges between the test and field particles), it takes of order 1 million collisions in order to obtain 90° deflection.

2.4 Strongly Coupled Plasmas

As pointed out in section 2.2, strongly coupled plasmas are often exemplified by solid and liquid metals, nonneutral one-component plasmas, etc. for which the common nature is that their coupling parameters, Γ, are of order or greater than unity and their Coulomb logarithms are equal to or less than 1. Considerations important to strongly coupled plasmas are:

- the inter-particle potential (E_P) is of the same order or even larger than the particle thermal kinetic energy (E_K). The interactions among the field particles must therefore be taken into account, and thus the Thomas-Fermi model should be used in calculating the particle energy ($E = E_P + E_K$);
- the collision frequency is of the same order or even larger than plasma frequency, and thus the plasma is very collisional;
- the particle motion in phase space is no longer a diffusive process and the model of binary interaction fails. The test particle actually suffers many body collective response;
- the interacting process is no longer a Markovian process but strongly Coulomb correlated, and thus the inter-particle correlation function must enter the framework of the kinetic theory;
- quantum mechanical effects may often be significant in strongly coupled plasmas, especially for those with fairly high densities and relatively low temperatures, such as solid and liquid metals ($n_e \sim 10^{22}$ and $T_e \sim 1$ eV).

It is obvious that the scale-length ordering [Eq.(2.5)] - - $p_\perp \ll n^{-1/3} \ll \lambda_D \ll \bar{\lambda}_{90^\circ}$ - - fails for the regime of strongly coupled plasmas. The Boltzmann equation with the traditional perturbative expansion techniques is also inadequate. The inter-particle correlation function plays a crucial role in kinetic theory[11]. For example,

in one approach the concept of inter-particle correlation is built into the dielectric response function.

2.5 Moderately Coupled Plasmas

In addition to the traditional two extremes, i.e. weakly and strongly coupled plasmas, there is a large class of plasmas for which the coupling parameter is of order $10^{-1} - 10^{-4}$ and the Coulomb logarithm is of order unity ($ln\Lambda_b \sim 2 - 10$). It is this category of plasmas that forms the bridge between the traditional two limits. This category of plasmas is exemplified by the solar interior, inertial confinement fusion plasmas, short-pulse laser produced plasmas, x-ray laser plasmas[15], etc. and consists of more than about 75% of the visible matters of the Universe. We would like to define this category of plasmas as moderately coupled plasmas. The location of moderately coupled plasmas in a phase diagram is shown in Fig.(2-1). They are basically positioned in the belted region below the lines of $E_F = kT_e$ and $e^2 n_e^{1/3} = kT_e$ for classical plasmas, and above the lines $E_F = kT_e$ and $e^2 n_e^{1/3} = E_F$ for quantum degenerated plasmas. Table 2.3 lists some parameters of interests for moderately coupled plasmas.

However, either of the present theories, i.e. for weakly coupled or strongly coupled plasmas, is not completely satisfactory to address this category of plasmas. This point can be verified in the following discussions.

- The conventional Fokker-Planck equation is only justified to be used to treat weakly coupled plasmas. This is because the terms that are of order $1/ln\Lambda_b$ in the Taylor-expansion of the operator in the Boltzmann equation have been truncated and therefore the effects of large-angle scattering are ignored. Directly applying the Fokker-Planck equation in treating moderately coupled plasmas is unjustified and results in unknown errors.

- The effects of large-angle scattering play a significant role in moderately coupled plasmas, which is usually addressed by Boltzmann-like collision operator. However, small-angle collisions, i.e. diffusion process in velocity space, still play an important or even a dominant role for Coulomb interactions in moderately coupled plasmas. Thus the Boltzmann-like collision operator may not be appropriate to describe the behavior of moderately coupled plasmas [see Fig.(2-4)].

- In contrast to the cases of weakly coupled plasmas, quantum degenerate effects may be significant at certain level and for certain cases in moderately coupled plasmas. This point can be seen from Table 2.3 where the values of the degenerate parameter Θ is of order 1 - 10. However, the degenerate effects are not as remarkable as in strongly coupled plasmas. In other words, moderately coupled plasmas are often times only weakly and partially degenerate, and the level of degeneracy could evolve with the variation of the plasma density and temperature.

- The assumption that the Coulomb collisions are statistically independent of each other can also be justified for moderately coupled plasmas by comparing the interaction time ($\sim 1/\omega_p$, where ω_p is the plasma frequency.) and the collision time. For example, for laser-fusion plasmas which have typical solid-like electron density $\sim 10^{23}/\text{cm}^3$ and electron temperature $\sim 10^2$ eV, since the collision time is always slightly larger than the interaction time, the test and field particles are still uncorrelated between the individual collisions. In another words, collision effects are significant but not overwhelming because the number of particles inside the Debye sphere is of order (and some times larger than) unity. This is consistent with the typical coupling parameters of moderately coupled plasmas since $\Gamma \sim 1/n_e\lambda_D^3$. The moderately coupled plasmas therefore fall into the regime between collisionless and collisional plasmas. In fact, as we know, only when $n_e\lambda_D^3$ is very large the collision

Table 2.3:

Typical velocity ratios in moderately coupled plasmas

	$n_e(cm^{-3})$	$T_e(keV)$	Γ	$ln\Lambda_b$	Θ	$v(cm/s)^*$	v/v_{the}	v/v_F
Solar core	$\simeq 5 \times 10^{25}$	$\simeq 1.3$	$\sim 10^{-2}$	~ 3	~ 3	$\sim 10^7$	$\sim$0.01	$\sim$0.01
ICF	$\sim 10^{26}$	~ 10	$\sim 10^{-3}$	~ 6	~ 13	$\sim 10^9$	~ 0.1	~ 0.5
Laser plasma (short pulse)	$\sim 10^{23}$	$\sim$0.1	$\sim 10^{-2}$	~ 3	~ 13	$\sim 6 \times 10^8$	~ 1	~ 2

* The test particle velocity: $v = v_D$ of the $\lesssim 1$ keV deuteron, the first step ${}^1H + {}^1H$ reaction product in the solar core; $v = v_\alpha$ of 3.5 MeV α's in ICF; and $v = v_e$ of 0.1 keV electron in the short-pulse laser produced plasmas.

effects can be neglected, this, of course, is the case for the weakly coupled plasmas. Therefore, the inter-particle correlation effects are weak and may be negligible for many cases in moderately coupled plasmas. For example, in a series of papers by Ichimaru *et al.*[12, 13], the correlation effects have been estimated to be only a few percent in calculating the charged particle stopping power in moderately coupled plasmas[12, 13], as shown in Fig.(2-5).

Based on these arguments, the perturbative expansion technique is shown to be still valid to treat the moderately coupled plasmas. However, it is clear that a new collision operator, which makes a compromise between the Boltzmann-like collision operator and conventional Fokker-Planck equation (i.e. including effects of both small-angle collisions and large-angle scattering), should be more appropriate for modeling and treating these moderately coupled plasmas. Consequently, this new operator desires the important properties: (1) it should be simple, and readily to be solved analytically; (2) it should involve more physics contents and phenomena; (3) it should reduce to the Boltzmann-like operator collision at one extreme, and to the Fokker-Planck equation at the another.

Because the collision operator in the Boltzmann equation can be written in

two parts[23]:

$$\left(\frac{\partial f_t}{\partial \tau}\right)_{coll.} = \overbrace{-\frac{\partial}{\partial v_i}(f_t < \Delta v_i >^{t/f}) + \frac{1}{2}\frac{\partial^2}{\partial v_i \partial v_j}(f_t < \Delta v_i \Delta v_j >^{t/f})}^{\textbf{Fokker-Planck equation}}$$

$$\underbrace{+ \quad \cdot \quad \cdot \quad \cdot \quad \cdot}_{\textbf{non-dominant Boltzmann-like collision operator}} \tag{2.8}$$

where the Fokker-Planck terms are dominant, and the Boltzmann-like collision operator, which summarized from all the higher order terms is of an order $1/\ln \Lambda_b$ smaller comparing to the formers, thus is non-dominant. A practical approach is to extend the traditional Fokker-Planck equation to include the effects of large-angle scattering, or in other words, to supplement large-angle scattering to the Fokker-Planck equation. Consequently, we would anticipate that a proper operator for moderately coupled plasmas should consist the above dominant Fokker-Planck terms (effects of small-angle collision, or diffusive process in velocity space) and some of terms in the non-dominant Boltzmann-like collision operator (effects of large-angle scattering).

2.6 Summary

In conclusion, in this chapter we have tried to classify plasmas into three basic categories: weakly, moderately and strongly coupled plasmas. Our classifications are not only based on the fundamental coupling parameter and the Coulomb logarithm, but also on the feasibility and validity of the associated kinetic theories. Specifically, we have found that the concepts of a moderately coupled plasma is necessary because neither the conventional Fokker-Planck approximation [for weakly coupled plasmas ($ln\Lambda_b \gtrsim 10$)] nor the theory of dielectric function with

correlations for strongly coupled plasmas ($ln\Lambda_b \lesssim 1$) has satisfactorily addressed this regime of plasmas. A new collision operator, a compromise between the Fokker-Planck equation and the Boltzmann-like collision operator, is suggested as appropriate for moderately plasmas. These issues are addressed in subsequent chapters.

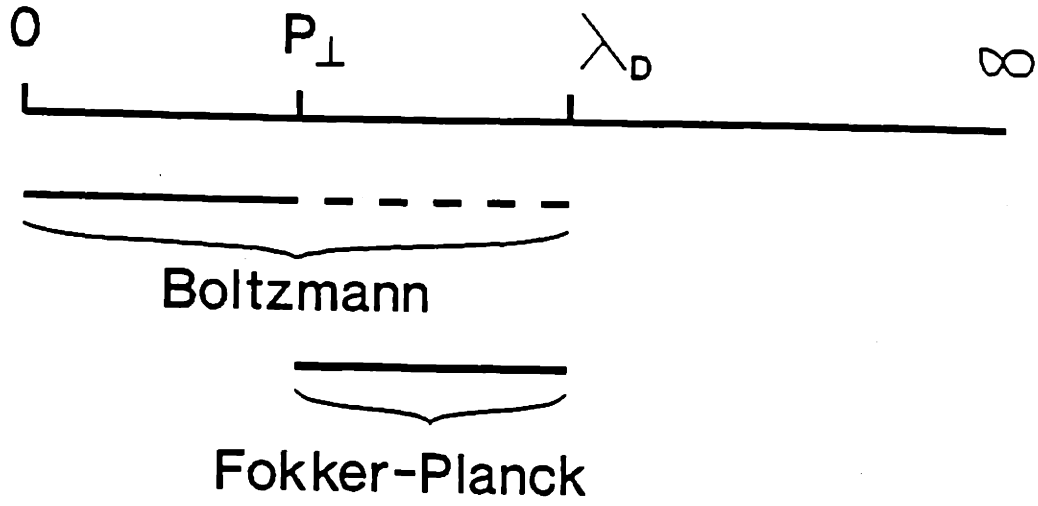

Figure 2-4: The coverage ranges of applicability in terms of impact parameter (p) for Boltzmann equation and Fokker-Planck equation[24].

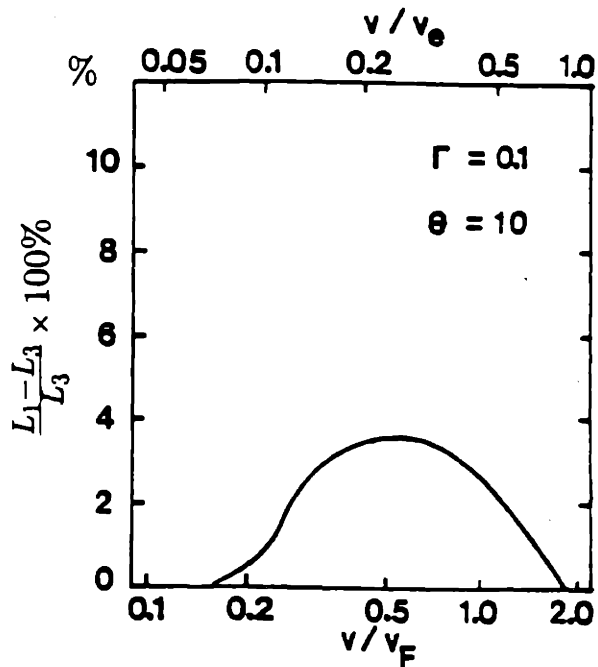

Figure 2-5: The comparison of the stopping number with or without correlations for a typical moderately coupled plasma (two components, $\Gamma = 0.1$ and $\Theta = 10$). Where L_1 is the stopping number calculated from the RPA theory (without correlation effects), and L_3 is from the DLFC theory (dynamical local-field correlation[13]). One finds that within regimes of density and temperature of our interests, the correlation effects are maximumed only a few percent[13].

Chapter 3

A Fokker-Planck Equation for Moderately Coupled Plasmas

In this chapter, the standard Fokker-Planck equation will be generalized to treat large-angle as well as small-angle binary collisions for moderately coupled plasmas [$2 \lesssim$ Coulomb logarithm $(ln\Lambda_b) \lesssim 10$]. Using this modified collision operator, a new vector potential that has a direct and practical connection to the Rosenbluth potentials is obtained. Some useful properties will be discussed.

3.1 Introduction

The Fokker-Planck equation, which was originally derived to treat the Brownian motion of molecules[25, 26], has been widely used to evaluate the collision term of the Boltzmann equation for describing small-angle binary collisions of the inverse-square type of force. In stellar dynamics[27], Chandrasekhar first discussed this theory for stochastic effects of gravity. The applications of this equation to classical plasma physics were first treated by Landau[1], Spitzer[2], as well as Cohen, Spitzer, and Routly[28], and an elegant mathematical treatment was completed by Rosenbluth, MacDonald, and Judd[3]. Their treatments, as

well as those of other workers[4, 5, 29], are based on the assumption that the Coulomb logarithm ($ln\Lambda_b$), which is a measure of the importance of small-angle binary collisions relative to large-angle scattering, is of order 10 or greater. Terms smaller by the factor of the Coulomb logarithm are neglected, i.e. large-angle scattering is ignored. The conventional Fokker-Planck equation, applicable to weakly coupled plasmas ($ln\Lambda_b \gtrsim 10$), is therefore only accurate to within an order of the Coulomb logarithm[4, 5, 29, 54, 55]. However, there is a large class of plasmas for which the approximation is invalid[13]: strongly coupled plasmas at one extreme ($ln\Lambda_b \lesssim 1$)[12, 30, 31, 32, 33], and moderately coupled ones in the intermediate regime ($2 \lesssim ln\Lambda_b \lesssim 10$)[34, 35, 36, 37, 38, 39]. It is to the moderately coupled plasmas, as exemplified by short-pulse laser plasmas[40, 41, 42, 43], inertial confinement fusion plasmas[56], x-ray laser plasmas[44, 45] and the solar core[46], to which our modifications of the Fokker-Planck equation are directed. As discussed in detail elsewhere[15], our modifications consist in retaining the third-order term and parts of the second-order term[23, 47], both of which are usually discarded[3, 4, 5, 6, 7, 29] in the Taylor expansion of the collision operator. (Fourth, fifth, sixth, and higher order terms in the expansion will be ignored since they are smaller than the third term at least by factors of 8, 80, 960 ...., respectively). After presenting some basic properties of the collision operator, we will use it, in next chapter, to calculate a reduced electron-ion collision operator, relaxation rates and first-order transport coefficients.

3.2 A Modified Fokker-Planck Equation

The Boltzmann equation for the rate-of-change of the test particle (sub or superscript t) distribution is

$$\frac{\partial f_t}{\partial \tau} + \mathbf{v} \cdot \frac{\partial f_t}{\partial \mathbf{x}} + \mathbf{a} \cdot \frac{\partial f_t}{\partial \mathbf{v}} = (\frac{\partial f_t}{\partial \tau})_{coll} \cdot \tag{3.1}$$

$(\partial f_t/\partial \tau)_{coll}$ is the collision operator and represents the time-rate-of-change of f_t due to collisions with the field particles (sub or superscript f). Its Taylor expansion[3, 4, 6] is written as

$$\begin{aligned}(\frac{\partial f_t}{\partial \tau})_{coll.} &= -\frac{\partial}{\partial v_i}(f_t < \Delta v_i >^{t/f}) + \frac{1}{2}\frac{\partial^2}{\partial v_i \partial v_j}(f_t < \Delta v_i \Delta v_j >^{t/f}) \\ &\quad -\frac{1}{6}\frac{\partial^3}{\partial v_i \partial v_j \partial v_k}(f_t < \Delta v_i \Delta v_j \Delta v_k >^{t/f}) \ , \end{aligned} \tag{3.2}$$

where the v_i, v_j, and v_k represent the components of the test-particle velocity in Cartesian coordinates. In our calculation (details in Appendix A), we follow the conventions of Rosenbluth *et al.*[3] and Trubnikov[4]:

$$\begin{cases} < \Delta v_i >^{t/f} &= -L^{t/f}(\frac{m_t+m_f}{m_f})\frac{\partial}{\partial v_i} H(\mathbf{v}) \\ < \Delta v_i \Delta v_j >^{t/f} &= -2L^{t/f}\frac{\partial^2}{\partial v_i \partial v_j} G(\mathbf{v}) + \frac{L^{t/f}}{ln\Lambda_b}[3\frac{\partial^2}{\partial v_i \partial v_j} G(\mathbf{v}) - \delta_{ij} H(\mathbf{v})] \\ < \Delta v_i \Delta v_j \Delta v_k >^{t/f} &= 4L^{t/f}\frac{1}{ln\Lambda_b}(\frac{m_f}{m_t+m_f})\frac{\partial^2}{\partial v_i \partial v_j}\Phi(\mathbf{v}) \end{cases} \tag{3.3}$$

where $L^{t/f} = (4\pi e_t e_f/m_t)^2 ln\Lambda_b$, where $ln\Lambda_b = ln(\lambda_D/p_\perp)$, λ_D is the Debye length of the field particles; $p_\perp = e_t e_f/m_r u^2$ is the impact parameter for 90° scattering, with m_r the reduced mass, e_t (e_f) the test (field) charges, $u = |\mathbf{v} - \mathbf{v}'|$ the relative velocity; m_t (m_f) is the test (field) particle mass. In addition,

$$H(\mathbf{v}) = -\frac{1}{4\pi}\int \frac{f_f(\mathbf{v}')}{|\mathbf{u}|} d\mathbf{v}' \ , \tag{3.4}$$

$$G(\mathbf{v}) = -\frac{1}{8\pi}\int |\mathbf{u}| f_f(\mathbf{v}')d\mathbf{v}' , \tag{3.5}$$

and

$$\mathbf{\Phi}(\mathbf{v}) = -\frac{1}{32\pi}\int \mathbf{u}|\mathbf{u}| f_f(\mathbf{v}')d\mathbf{v}' . \tag{3.6}$$

H and G, which appear in Eq.(3.3), are potentials defined by Rosenbluth *et al.*[3, 4]. $\mathbf{\Phi}$ is a new vector potential that derives from retaining the third term in Eq.(3.2). In Eq.(3.3), the factors multiplied by $1/ln\Lambda_b$ are a direct consequence of our third-order expansion. In contrast to $< \Delta v_i >^{t/f}$ and $< \Delta v_i \Delta v_j >_{\perp}^{t/f}$ which represent the effects of small-angle collisions[3, 4], $< \Delta v_i \Delta v_j >_{\parallel}^{t/f}$ and $< \Delta v_i \Delta v_j \Delta v_k >^{t/f}$ mainly represent the effects of large-angle scattering.

3.3 Discussion

In contradistinction to the conventional Fokker-Planck equation, the third-order moment and corrections of the second-order moment have been both included in our modified Fokker-Planck equation; each is of an order of Coulomb logarithm smaller than the first two order moments (the comparison, of course, is carried out in terms of dimensionless units because of the different dimensionality of the different order moments[4]) and this reflects the fact that for inverse-square type Coulomb force, there is no divergence for the third- and higher-order moments.

In addition, this modified collision operator satisfies the desired property that it is a compromise between Boltzmann-like and Fokker-Planck collision operator by extending it to the two opposite extremes: first, for the case of $ln\Lambda_b \lesssim 10$ (the effects of large-angle scattering dominant, dilute plasmas), by picking up all the

rest of higher order terms in Taylor expansion, we actually go back to Boltzmann-like collision operator; second, for the case of $ln\Lambda_b \gtrsim 10$ (the effects of small-angle collision dominant, weakly coupled plasmas) the above modified equation automatically return to the standard Fokker-Planck equation just by neglecting all the terms of a factor $1/ln\Lambda_b$.

Some of the useful properties of this new modified Fokker-Planck equation are listed. Properly making use of these properties for some practical cases would largely simplify the calculations.

3.3.1 Properties of the New Vector Potential Φ

The new vector potential Φ has the following useful properties:

$$\nabla_{\mathbf{v}}^2 \nabla_{\mathbf{v}}^2 \nabla_{\mathbf{v}} \cdot \Phi(\mathbf{v}) = f_f(\mathbf{v}) ; \tag{3.7}$$

$$\nabla_{\mathbf{v}}^2 \nabla_{\mathbf{v}}^2 \Phi(\mathbf{v}) = 0 ; \tag{3.8}$$

where $\nabla_{\mathbf{v}}^2$ is the Laplacian operator and $\nabla_{\mathbf{v}}$ is the first derivative, both of them are in velocity space (indicated by the subscript $\mathbf{v}$). The relations to the Rosenbluth potentials are also presented, which will be very useful in subsequent calculations,

$$\begin{aligned} \nabla_{\mathbf{v}}^2 \nabla_{\mathbf{v}} \cdot \Phi(\mathbf{v}) &= \nabla_{\mathbf{v}}^2 G(\mathbf{v}) \\ &= H(\mathbf{v}) . \end{aligned} \tag{3.9}$$

3.3.2 Relations of the First Three Moments

Making use of the relations of the potentials [Eq.(3.9)] one can also find the relations between these first three moments (details in Appendix B),

$$< \Delta v_i >^{t/f} = \frac{ln\Lambda_b}{2ln\Lambda_b - 2}(\frac{m_t + m_f}{m_f})\frac{\partial}{\partial v_j} < \Delta v_i \Delta v_j >^{t/f} \tag{3.10}$$

$$< \Delta v_i >^{t/f} = -\frac{ln\Lambda_b}{4}(\frac{m_t + m_f}{m_f})^2\frac{\partial^2}{\partial v_j \partial v_k} < \Delta v_i \Delta v_j \Delta v_k >^{t/f} \tag{3.11}$$

3.3.3 Fokker-Planck Equation in terms of Test-Particle Flux

The modified Fokker-Planck equation can be written in terms of the flux of the test particles produced by the collisions in velocity space,

$$(\frac{\partial f_t}{\partial t})_{coll.} = -\frac{\partial}{\partial v_i} J_i \tag{3.12}$$

where the test-particle flux is written as

$$J_i = a_i f_t + b_{ij}\frac{\partial}{\partial v_j} f_t + c_{ijk}\frac{\partial^2}{\partial v_j \partial v_k} f_t \tag{3.13}$$

with

$$\begin{cases} a_i = < \Delta v_i >^{t/f} - \frac{1}{2}\frac{\partial}{\partial v_j} < \Delta v_i \Delta v_j >^{t/f} + \frac{1}{6}\frac{\partial^2}{\partial v_j \partial v_k} < \Delta v_i \Delta v_j \Delta v_k >^{t/f} \\ b_{ij} = -\frac{1}{2} < \Delta v_i \Delta v_j >^{t/f} + \frac{1}{3}\frac{\partial}{\partial v_k} < \Delta v_i \Delta v_j \Delta v_k >^{t/f} \\ c_{ijk} = \frac{1}{6} < \Delta v_i \Delta v_j \Delta v_k >^{t/f} \end{cases} \tag{3.14}$$

3.3.4 Landau Form of Fokker-Planck Equation

Although the form of the Fokker-Planck equation most widely used essentially follows the convention of Rosenbluth, McDonald, and Judd, there is an equivalent but different form of the collision operator which was derived in the 1930's by Landau[1]. The form of the equation is therefore called the Landau form of the Fokker-Planck equation or the Landau equation. The equivalence of these two different forms is readily demonstrated by directly transforming the Fokker-Planck equation to the Landau equation. Similarly, for the modified Fokker-Planck equation, there is a corresponding Landau form which includes the same physical contents. The demonstration of equivalence is readily carried out by using the following relations,

$$\begin{cases} \frac{\partial}{\partial v_i} H(\mathbf{v}) &= -\frac{1}{8\pi} \int \mathbf{U}_{ij} \frac{\partial f'_f}{\partial v'_j} d\mathbf{v}' \ ; \\ \frac{\partial^2}{\partial v_i \partial v_j} G(\mathbf{v}) &= -\frac{1}{8\pi} \int \mathbf{U}_{ij} f'_f d\mathbf{v} \ ; \\ \frac{\partial^2}{\partial v_i \partial v_j} \Phi(\mathbf{v}) &= -\frac{1}{32\pi} \int \mathbf{U}_{ijk} f'_f d\mathbf{v}' \ , \end{cases} \tag{3.15}$$

where

$$\mathbf{U}_{ij} = \frac{u^2 \delta_{ij} - u_i v_j}{u^3} \ , \tag{3.16}$$

$$\mathbf{U}_{ijk} = \ = \ \frac{u_i}{u}\delta_{jk} + \frac{u_j}{u}\delta_{ki} + \frac{u_k}{u}\delta_{ij} - \frac{u_i u_j u_k}{u^3} \tag{3.17}$$

Substituting the above relations into the modified Fokker-Planck equation and after several steps of manipulations, the Landau form of Fokker-Planck equation is correspondly modified and can be expressed in terms of the the Landau-form-flux,

$$
\begin{aligned}
(\frac{\partial f_t}{\partial t})_{coll.} &= -\frac{L^{t/f}}{8\pi}\frac{\partial}{\partial v_i}\{m_t\int \mathbf{U}_{ij}(\frac{f_t}{m_f}\frac{\partial f'_f}{\partial v'_j}-\frac{f'_f}{m_t}\frac{\partial f_t}{\partial v_j})d\mathbf{v}' \\
&+\frac{3}{2ln\Lambda_b}(f_t\frac{\partial}{\partial v_j}+\frac{\partial f_t}{\partial v_j})\int \mathbf{U}_{ij}f'_f d\mathbf{v}' \\
&+\frac{1}{ln\Lambda_b}(f_t\frac{\partial}{\partial v_j}+\frac{\partial f_t}{\partial v_j})\int \frac{\delta_{ij}}{u}f'_f d\mathbf{v}' \\
&+\frac{1}{6ln\Lambda_b}\frac{\partial^2}{\partial v_j\partial v_k}(\frac{m_f}{m_t+m_f})\int \mathbf{U}_{ijk}f_t f'_f d\mathbf{v}'\} \qquad (3.18)
\end{aligned}
$$

where the first term is the conventional Landau-form operator, and the other terms all come from the modifications.

3.4 Summary

In summary, we have modified the standard Fokker-Planck operator for Coulomb collisions by including terms that are directly associated with large-angle scattering. This procedure allows us to effectively treat plasmas for which $ln\Lambda_b \gtrsim 2$, i.e. for moderately coupled plasmas. These modifications, in most cases, differ from Braginskii's and Trubnikov's results by terms of order $1/ln\Lambda_b$. However, in the limit of large $ln\Lambda_b$ ($\gtrsim 10$), these results reduce to the standard (Braginskii) form.

Chapter 4

Applications of the Modified Fokker-Planck Equation

For the purpose of illustrating the effects of the modifications made in chapter 3, we show in this chapter some applications. Our examples will concentrate on addressing two important issues in moderately coupled plasmas: first, the plasma relaxation rate; and second, the electron transport.

4.1 Introduction

When test and field particles in a plasma are not in thermal equilibrium with each other (the field particles themselves are assumed to be in thermal equilibrium), the effects of collisions (which results in both momentum and energy transfers) will tend to make their distribution functions relax toward thermal equilibrium. The relaxation rate therefore reflects the speed of these changes and transfers. The relaxation phenomenon of test particles due to the collisions with field particles, according to Spitzer[2], basically involves issues such as slowing down, energy exchange, removal of angular anisotropy, and energy loss because of the "dynamical friction", etc., and these are all fundamental concepts in plasma physics. Par-

ticularly in this chapter, three kinds of relaxation rates will be addressed: the momentum transfer rate, energy loss rate, and the 90° deflection collision rate. To obtain these relaxation rates, we basically calculate the collision rate of change of various distribution function moments.

The transport phenomena occuring in plasmas are generally due to the presence of spatial gradients, for example, the gradients of the density, electric or magnetic fields, and temperature. These spatial local transport processes that will be discussed in this chapter are still classical.

Conventional calculations utilize the Fokker-Planck equation[4, 5, 39]. However, we have found this treatment inadequate for moderately coupled plasmas since their Coulomb logarithm ($ln\Lambda_b$) is of order unity (typically, $ln\Lambda_b \simeq 2$ - 10). Because terms smaller by a factor of $1/ln\Lambda_b$ are truncated in the Taylor expansion, the application of the conventional Fokker-Planck equation can only be justified for weakly coupled plasmas, i.e. plasmas for which $ln\Lambda_b \gtrsim 10$[15, 16]. There are, however, two issues which are usually left unaddressed. First, since $ln\Lambda_b \lesssim 10$, there is no justification in using the standard formulas. Second, there has been, until now, no $ln\Lambda_b$ correction to these formulas. Specifically, these formulas are only justified when used in the "Spitzer regime" which is based upon the following length ordering:

$$p_\perp \ll n^{-1/3} \ll \lambda_D \ll \bar{\lambda}_{90^\circ} \ . \tag{4.1}$$

However, when $ln\Lambda_b < 10$, this ordering fails[16]. For these reasons, a proper treatment of these two issues is necessary in moderately coupled plasmas, for which $2 \lesssim ln\Lambda_b \lesssim 10$.

4.2 Relaxation Rates

In general, plasma relaxation rate is defined as

$$\frac{d\bar{F}}{dt} = -\nu\bar{F} , \tag{4.2}$$

where F is an arbitrary physical quantity which can represent the test particle's momentum, energy, or energy flow, etc. (i.e, F can be $\mathbf{v}$, v^2, $v^2\mathbf{v}$, etc.). And ν is the relaxation rate of the quantity F. In calculations, if the distribution function of the test particle (f_t) is known, the physical quantity is usually averaged over the velocity space, i.e.

$$\bar{F} = \frac{1}{n_t}\int F(\mathbf{v}')f_t d\mathbf{v}' . \tag{4.3}$$

By differentiating this equation over time, the rate of change of this quantity is then determined through the following equation

$$\frac{d}{dt}\bar{F} = \frac{1}{n_t}\int F(\mathbf{v}')(\frac{\partial f_t}{\partial t})d\mathbf{v}' , \tag{4.4}$$

$(\partial f_t/\partial t)$ is the collision operator where we use the modified Fokker-Planck equation. In our calculations, the test particle distribution function is assumed to be a delta-function,

$$f_t = n_t\delta(\mathbf{v}' - \mathbf{v}) . \tag{4.5}$$

The physical meaning for this distribution function is that a monoenergetic test particle beam is assumed. For the field particles, we assume a spherically symmetric equilibrium distribution, i.e. a Maxwellian distribution function

$$f_f(v) = \frac{n_f}{(2\pi T_f/m_f)^{3/2}} e^{-\frac{m_f v^2}{2T_f}} . \tag{4.6}$$

With these assumptions, a physical picture of a plane flux of test particles interacting with an equilibrium background plasma is formed. Through the modified Fokker-Planck equation, the relaxation rates for momentum transfer, energy loss, and 90° deflection are equivalently related to the rates of change of the moments $< \Delta v_i >$, $< \Delta v_i \Delta v_j >$, $< \Delta v_i \Delta v_j \Delta v_k >$, and this suffices for a reasonable statistical description of the behavior of the test particle. Based those assumptions and definitions the plasma relaxation rates are readily calculated. For example, the calculation of the momentum transfer rate (slowing down in the original direction of the test particle trajectory) is

$$\begin{aligned} \frac{d\bar{v}_i}{dt} &= -\nu_s^{t/f} \bar{v}_i \\ &= < \Delta v_i > ; \end{aligned} \tag{4.7}$$

and the energy loss rate is

$$\begin{aligned} \frac{d\bar{E}}{dt} &= -\nu_E^{t/f} \bar{E} \\ &= m_t (\frac{1}{2} < \Delta v_i \Delta v_i > + v_i < \Delta v_i >) , \end{aligned} \tag{4.8}$$

where $< \Delta v_i \Delta v_i >$ is the trace of the diffusion tensor. Substituting the rates of change of the of moments defined in chapter 3 and performing some manipulations, the relevant relaxation rates are readily calculated and the results are shown in the Table 4.1.

Table 4.1:
The modified (conventional) relaxation rates

Relaxation Rates	Conventional	$ln\Lambda_b \gtrsim 10$ Restriction[a]	Modified
Slowing Down $(\nu_s^{t/f})^*,\ddagger$	$(1+\frac{m_t}{m_f})\mu\nu_\circ$	No[d]	unchanged from Conventional
90° Deflection $(\nu_D^{t/f})^*,\ddagger$	$2(\mu+\mu'-\frac{\mu}{2x^{t/f}})\nu_\circ$	Yes	$2[1+\frac{1}{2ln\Lambda_b}(\frac{m_f-m_t}{m_f+m_t})](\mu+\mu'-\frac{\mu}{2x^{t/f}})\nu_\circ^{**}$
Energy Loss $(\nu_E^{t/f})^*,\ddagger$	$2(\frac{m_t}{m_f}\mu-\mu')\nu_\circ$	Yes	$2[\frac{m_t}{m_f}\mu-\mu'+\frac{1}{ln\Lambda_b}(\mu+\mu')]\nu_\circ$

[a] This condition applies to the Conventional results only.

* $\nu_\circ = \sqrt{2}\pi e_t^2 e_f^2 n_f ln\Lambda_b/\sqrt{m_t}E_t^{3/2}$ — the "basic relaxation rate."

** $\nu_D^{t/f} \simeq [<(\Delta \mathbf{v}_\perp)^2>/v^2] - [<(\Delta \mathbf{v}_\perp)^2 \Delta \mathbf{v}>/v^3]$

‡ $\mu = 2\int_0^{x^{t/f}} e^{-\xi}\sqrt{\xi}d\xi/\sqrt{\pi}$ — the Maxwell integral, and μ' is its first derivative. Their behaviors are shown in Fig.(4-1).

[d] As best we can tell, this was not known since it is stated[29] that $ln\Lambda_b \gtrsim 10$.

We find that even with the inclusion of all higher terms, the slowing down rate is unmodified from the conventional form. As best we can tell, this seems not to have been previously recognized since other workers indicated $ln\Lambda_b$ need be 10 or greater for its application[4, 29]. In contrast to this, the energy loss rate and 90° deflection rate both manifests $1/ln\Lambda_b$ corrections. To the best of our knowledge, this is the first time these corrections have been calculated. Because all the corrections come from the effects of large-angle scattering, the practical significance then depends on the mass ratio of test to field particle, which could be large, intermediate, and small due to m_e/m_i ($\sim 10^{-3}$), m_e/m_e or m_i/m_i (~ 1), and m_i/m_e ($\sim 10^3$), respectively. These corrections are important, for example, for the energy loss rate, it is, in part, utilized in estimating the energy loss for 3.5 MeV α's, 1.01 MeV Triton, 0.82 MeV ^{3}He, and fast electrons in inertial confinement fusion plasmas[49].

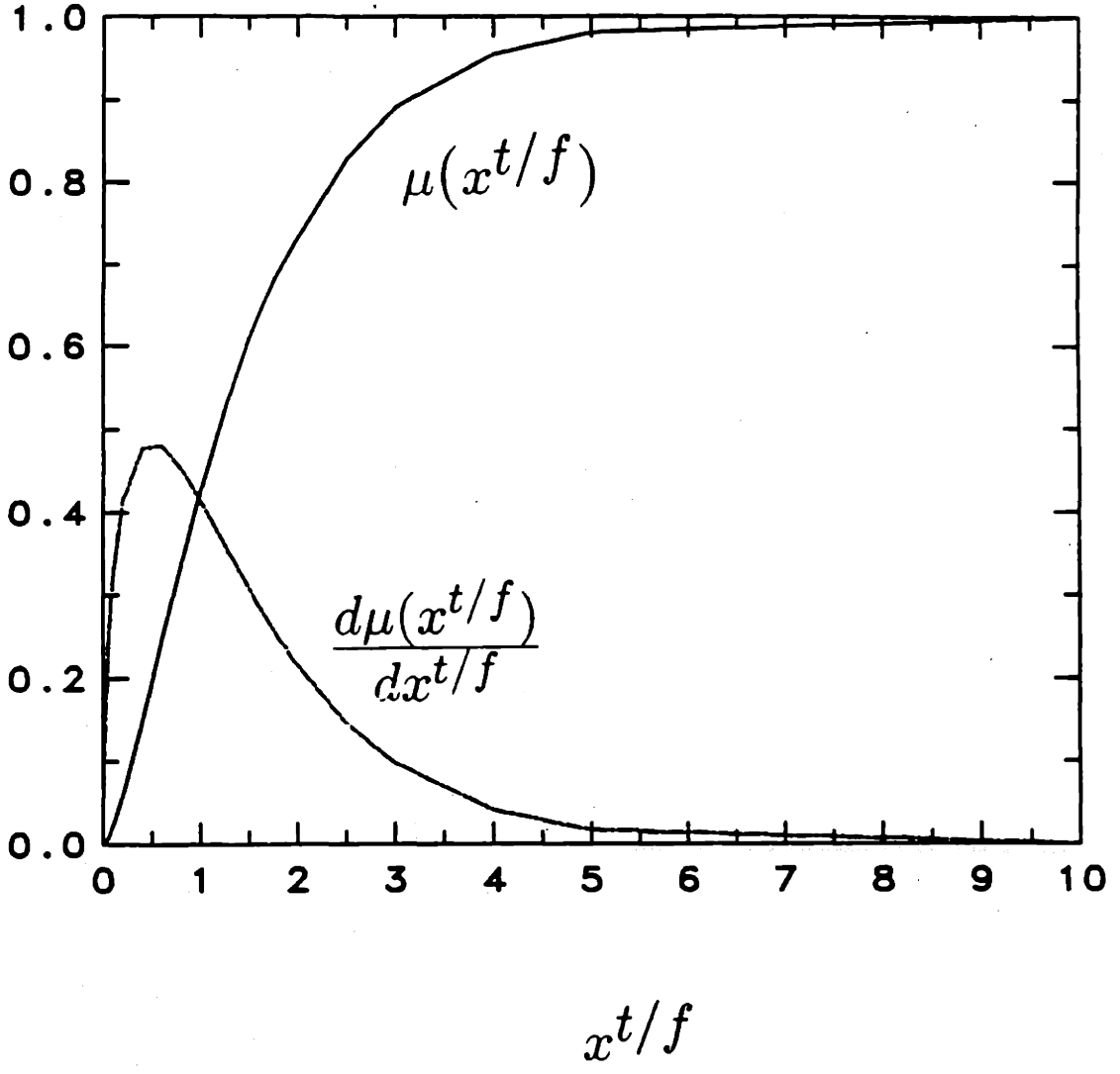

Figure 4-1: The Maxwell integral and its first derivative as a function of parameter $x^{t/f}(=v_t^2/v_f^2)$.

4.3 Electron Transport Coefficients

In our calculations, the Boltzmann equation is written as

$$\frac{\partial f_e}{\partial t} + \mathbf{v} \cdot \frac{\partial f_e}{\partial \mathbf{x}} + \mathbf{a} \cdot \frac{\partial f_e}{\partial \mathbf{v}} = C_e \ , \tag{4.9}$$

where $\mathbf{a} = e\mathbf{E}/m_e$, and the collision operator

$$C_e = C_{e-ion}(f_e, f_i) + C_{e-e}(f_e, f_e) \ . \tag{4.10}$$

Taking the high-Z approximation in our calculation (Lorentz-gas model), the electron-electron collision operator can be neglected. [The contribution from C_{e-e} to the electron conductivities is multiplying a factor of 1/(1+3.3/Z), for large Z, this contribution can neglected[39].] To calculate C_{e-ion}, we use the Landau form of the corresponding modified Fokker-Planck equation,

$$\begin{aligned}
(\frac{\partial f_e}{\partial t})_{coll.} = & -\frac{L^{e/ion}}{8\pi}\frac{\partial}{\partial v_i}\{m_e \int \mathbf{U}_{ij}(\frac{f_e}{m_{ion}}\frac{\partial f'_{ion}}{\partial v'_j} - \frac{f'_{ion}}{m_e}\frac{\partial f_e}{\partial v_j})d\mathbf{v}' \\
& + \frac{3}{2ln\Lambda_b}(f_e\frac{\partial}{\partial v_j} + \frac{\partial f_e}{\partial v_j}) \int \mathbf{U}_{ij} f'_{ion} d\mathbf{v}' \\
& + \frac{1}{ln\Lambda_b}(f_e\frac{\partial}{\partial v_j} + \frac{\partial f_e}{\partial v_j}) \int \frac{\delta_{ij}}{u} f'_{ion} d\mathbf{v}' \\
& + \frac{1}{6ln\Lambda_b}\frac{\partial^2}{\partial v_j \partial v_k}(\frac{m_{ion}}{m_e + m_{ion}}) \int \mathbf{U}_{ijk} f_e f'_{ion} d\mathbf{v}'\}
\end{aligned} \tag{4.11}$$

In the approximation where $m_e/m_{ion} \simeq 0$, i.e. the ions are assumed to be immovable and exhibit a delta function distribution

$$f_{ion} = n_{ion}\delta(\mathbf{v}') \ . \tag{4.12}$$

Substituting this distribution function into the Eq.(4.11) and performing some manipulations, one obtains the reduced electron-ion collision operator, which manifest $1/ln\Lambda_b$ corrections,

$$C_{e-ion}(f_e, f_{ion}) = A\frac{\partial}{\partial v_i}[(1-\frac{5}{6ln\Lambda_b})\mathbf{V}_{ij}\frac{\partial}{\partial v_j}f_e$$

$$+\frac{1}{ln\Lambda_b}(\frac{4}{3}\frac{v_i}{v^3}+\frac{\delta_{ij}}{v}\frac{\partial}{\partial v_j}+\frac{\mathbf{V}_{ijk}}{6}\frac{\partial^2}{\partial v_j\partial v_k})f_e] \ . \qquad (4.13)$$

Where $A = L^{e/ion}/8\pi = 2\pi n_e Z^2 e^4 ln\Lambda_b/m_e^2$, $\mathbf{V}_{ij}$ is the conventional diffusion tensor in velocity space,

$$\mathbf{V}_{ij} = \frac{\partial^2}{\partial v_i \partial v_j}\int |\mathbf{u}|\delta(\mathbf{v}')d\mathbf{v}'$$

$$= \frac{v^2\delta_{ij}-v_iv_j}{v^3} \ , \qquad (4.14)$$

and the new terms, including the third-rank tensor

$$\mathbf{V}_{ijk} = \frac{\partial^2}{\partial v_j \partial v_k}\int \mathbf{u}|\mathbf{u}|\delta(\mathbf{v}')d\mathbf{v}'$$

$$= \frac{v_i}{v}\delta_{jk}+\frac{v_j}{v}\delta_{ki}+\frac{v_k}{v}\delta_{ij}-\frac{v_iv_jv_k}{v^3} \ . \qquad (4.15)$$

The terms in Eq.(4.13) with coefficient $1/ln\Lambda_b$, are a consequence of this new expansion and are also mainly associated with large-angle scattering. In calculating the electron thermal or electrical conductivity, one finds that the complexity of the operator actually prohibits an analytical solution. In other words, one would not expect to obtain a linear relation between the heat flux and temperature, or between the current and electric field, as implied by the conductivities. For example, in the calculations of the electron conductivity, we assume a plasma with a fixed, neutralizing background of ions, and a uniform electron density. In order to carry thermal flux, the electron distribution function is warped in the direction

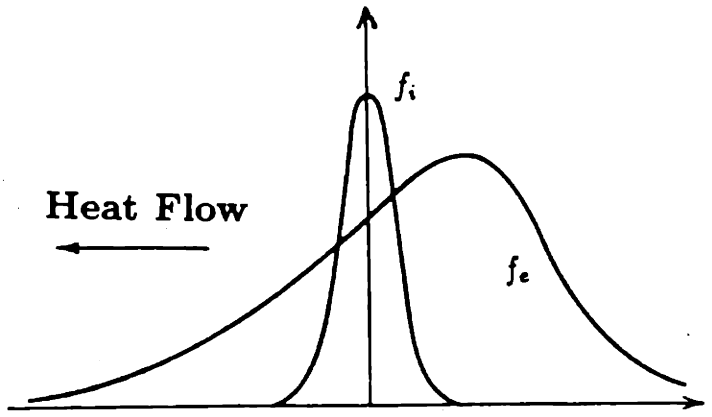

Figure 4-2: The electron and ion distribution functions for modeling the electron conductivity.

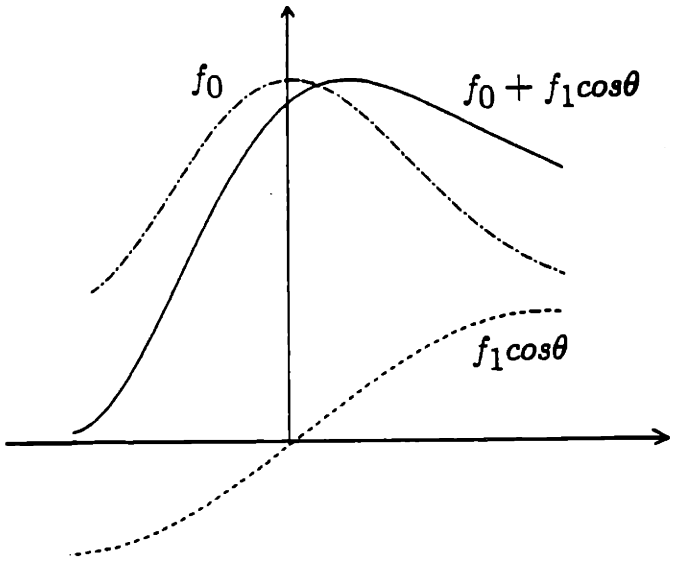

Figure 4-3: Electron distribution used in the calculation of the electron thermal conductivity.

of the heat flow, as shown in Fig.(4-2).

This warped electron distribution function can be expanded as a first-order Legendre polynomial in spherical coordinates,

$$f_e = f_0 + f_1 cos\theta \ , \tag{4.16}$$

where θ is the angle between v and the direction of the heat (also electric field). Fig.(4-3) shows this electron distribution.

Substituting f_e into the above Boltzmann equation with the reduced electron-ion collision operator and keeping only the first-order terms to the linearized equation (i.e. only keep terms which are proportional to $cos\theta$), the e-i collision operator is then given by

$$C^1_{e-ion}(f_1) = -2A(1 + \frac{1}{6ln\Lambda_b})\frac{f_1}{v^3} \ . \tag{4.17}$$

The steady-state solution to the Boltzmann equation with this reduced electron-ion collision operator is then determined to be

$$f_1 = -\frac{v^4}{2(1 + \frac{1}{6ln\Lambda_b})A}(\frac{\partial f_0}{\partial z} - \frac{eE}{m_e}\frac{\partial f_0}{\partial v}) \ . \tag{4.18}$$

The electron heat flux is

$$Q = \int v\frac{mv^2}{2}cos^2\theta f_1 d\mathbf{v} \ . \tag{4.19}$$

After performing the integration, the heat flux can be written as

$$Q = -\kappa\frac{\partial T_e}{\partial z} \ , \tag{4.20}$$

Table 4.2:
The modified (conventional) transport coefficients

Transport Coefficients	Conventional	$ln\Lambda_b \gtrsim 10$ Restriction[a]	Modified
Electron Electric Conductivity($\sigma_{\|\|}$)**	$\frac{32n_e e^2}{3\pi m_e \nu_{ei}}$	Yes	$\frac{32n_e e^2}{3\pi m_e(1+1/6ln\Lambda_b)\nu_{ei}}$
Electron Therm. Conductivity($\kappa_{\|\|}$)**	$\frac{16\sqrt{2\pi}n_e kT_e}{3m_e\nu_{ei}}$	Yes	$\frac{16\sqrt{2\pi}n_e kT_e}{3m_e(1+1/6ln\Lambda_b)\nu_{ei}}$
Light Collision Damping rate(ν)†	$\frac{\omega_{pe}^2}{\omega^2}\frac{8\pi}{3}A\bar{f}_0$	Yes	$\frac{\omega_{pe}^2}{\omega^2}\frac{8\pi}{3}(1+\frac{1}{6ln\Lambda_b})A\bar{f}_0$

[a] This condition applies to the Conventional results only.
** $\nu_{ei} = 4\sqrt{2\pi}Z^2e^4n_e ln\Lambda_b/3\sqrt{m_e}(kT_e)^{3/2}$ — the "basic electron-ion collision rate", and $v_e^2 = kT_e/m_e$ is assumed[5].

where

$$\kappa = \frac{16\sqrt{2\pi}n_e kT_e}{3m_e(1+1/6ln\Lambda_b)\nu_{ei}} . \tag{4.21}$$

A similar procedure can be carried out in order to calculate the electron electrical conductivity. The calculated results, with comparisons to results obtained without the modification, are presented in Table 4.2.

Another example is to calculate laser wave damping rate in plasmas, which arises because the fact that in laser-plasma interaction physics the issue that the target obtaining the highest absorption rate of incident laser energy can be understood by considering the balance of the energy dissipated, the damping of the laser-light wave into plasmas. Electron-ion collision provides a simple model of this damping[39]. To calculate the collisional damping of a laser light wave, which is defined as $\nu E^2/8\pi$ and ν is the damping rate, we can use the first-order approximation equation based on the assumptions discussed above

$$\frac{\partial f_1}{\partial t} - \frac{eE}{m_e}\frac{\partial f_0}{\partial v} = -2A(1+\frac{1}{6ln\Lambda_b})\frac{f_1}{v^3} . \quad (4.22)$$

Since $\mathbf{E} = \mathbf{E}_0 e^{-i\omega t}$, the equation is readily solved for f_1

$$f_1 = \frac{ieE_0}{m_e}\frac{\partial f_0}{\partial v}[\omega + \frac{i2A(1+\frac{1}{6ln\Lambda_b})}{v^3}]^{-1} . \quad (4.23)$$

Thus, the damping rate can be readily figured out from the following averaged absorption of energy

$$< \mathbf{J}_1 \cdot \mathbf{E} > = Re[-\frac{eE_0}{2}\int v f_1 cos^2\theta d\mathbf{v}] . \quad (4.24)$$

After some manipulations, the laser wave damping rate is determined as

$$\nu = \frac{\omega_{pe}^2}{\omega^2}\frac{8\pi}{3}(1+\frac{1}{6ln\Lambda_b})A\bar{f}_0 , \quad (4.25)$$

where $\bar{f}_0 = -\int_0^\infty dv g(v)(\partial f_0/\partial v)$, $g(v) = \{1+[2A/v^3\omega]^2\}^{-1} \simeq 1$ due to $\nu_{ei}/\omega \ll 1$[39], and ω is frequency of the laser light wave.

In these calculations, $1/6ln\Lambda_b$ corrections are, for the first time, evident. The fact that these corrections are much smaller than the $ln\Lambda_b$ corrections of the energy loss and deflection rate, is, we conjecture, due to the linearization of the Boltzmann equation and retention of only the first order correction in the electron distribution function. Here for the objective of illustration, we only calculate the "classical" electron energy transport as an example. Although still not completely correct, one sees that it has been modified in the correct direction. Therefore, in any future work, it will be important to include higher-order terms of the electron distribution function as well as retaining the non-linearities of the Boltzmann

equation. Such transport coefficients could be then applied to a variety of plasmas, such as short-pulse laser plasmas, x-ray laser plasmas, inertial confinement fusion plasmas, and the solar core.

4.4 Electron-Ion Mean-Free Path for Short-Pulse Laser Plasmas

The understanding of the electron transport in short-pulse laser plasmas ($ln\Lambda_b \sim$ 2-5), for example, the electron thermal and electric conductivities[39], is of fundamental importance. In these studies, $\bar{\lambda}_{90^\circ}$ (electron-ion 90° scattering mean-free-path) is usually compared to the temperature (L_T), density (L_n), and electric field (L_E) gradient scale lengths. The argument is usually made that if $\bar{\lambda}_{90^\circ} \gtrsim L_x$, the classical treatment of Spitzer and Härm[50] fails[15, 16, 39, 42, 51, 52]. Conventional calculations utilize the Fokker-Planck equation. However, we have found this treatment cannot be justified for moderately coupled plasmas.

To address these issues we have modified the Fokker-Planck equation by retaining the third-order term and parts of the second-order term, both of which are usually discarded in the Taylor expansion of the collision operator. This leads to a new electron-ion 90° scattering mean-free-path that manifests $1/ln\Lambda_b$ corrections. Originally defined by Spitzer[2], the 90° deflection rate ($\nu_D^{t/f}$) is a quantity that characterizes the perpendicular deflection of a test particle from its original direction of motion, as a consequence of collisions with field particles:

$$\nu_D^{t/f} = \frac{< (\Delta \mathbf{v}_\perp)^2 >}{v^2} , \tag{4.26}$$

where $< (\Delta \mathbf{v}_\perp)^2 >$ is the second-order moment for the change of the velocity in

the perpendicular direction. This definition assumes that the deflection is pure diffusive, or a small-angle interaction, process. In order to include the effects of large-angle scattering, we redefine this rate as

$$\nu_D^{t/f} = \frac{<(\Delta \mathbf{v}_\perp)^2>}{v^2} - \frac{<(\Delta \mathbf{v}_\perp)^2 \Delta \mathbf{v}>}{v^3} . \tag{4.27}$$

In addition to the new third-order moment, the second-order moment is also corrected to include the effects of large-angle scattering. These moments are[15, 16],

$$\begin{aligned} <\Delta v_i \Delta v_j>^{t/f} &= -2L^{t/f}\frac{\partial^2}{\partial v_i \partial v_j}G(\mathbf{v}) \\ &\quad + \frac{L^{t/f}}{ln\Lambda_b}[3\frac{\partial^2}{\partial v_i \partial v_j}G(\mathbf{v}) - \delta_{ij}H(\mathbf{v})] ; \end{aligned} \tag{4.28}$$

$$<\Delta v_i \Delta v_j \Delta v_k>^{t/f} = \frac{4L^{t/f}}{ln\Lambda_b}(\frac{m_f}{m_t+m_f})\frac{\partial^2}{\partial v_i \partial v_j}\Phi(\mathbf{v}) , \tag{4.29}$$

Substituting Eqs.(4.28) and (4.29) into Eq.(4.27), and assuming a Maxwellian field particle distribution, the 90° deflection rate is

$$\nu_D^{t/f} \simeq 2[1 + \frac{1}{2ln\Lambda_b}(\frac{m_f - m_t}{m_f + m_t})](\mu + \mu' - \frac{\mu}{2x^{t/f}})\nu_\circ , \tag{4.30}$$

This result differs from the standard formula (Spitzer and Trubnikov) by the $1/ln\Lambda_b$ corrections. In the approximation of $m_e/m_i \simeq 0$ (then $\mu \simeq 1$ and $\mu' \simeq 0$), an electron-ion 90° scattering mean-free-path ($\bar{\lambda}_{90^\circ}$) is obtained:

$$\bar{\lambda}_{90^\circ} \simeq \frac{T_e^2}{(1+1/2ln\Lambda_b)2\pi Z^2 e^4 n_e ln\Lambda_b} . \quad (4.31)$$

A decrease by a factor $(1 + 1/2ln\Lambda_b)$ is found over the standard calculation[15,18]. With the $1/ln\Lambda_b$ correction, this modified result has been justified for its application to short-pulse laser plasmas.

4.5 Comparison of Collision Frequencies to Fusion Reaction Rates

It is interesting to make a simple comparison of collision frequencies to fusion reaction rates. We consider three different cases: the solar core, inertial confinement fusion, and magnetic confinement fusion. Using our classifications, the first two are moderately coupled plasmas and the last one is a weakly coupled plasma. Two aspects of interests are: (1) by comparing collision frequencies to fusion reaction rates, one can obtain a clear quantitative picture of how many collisions would lead to a fusion reaction; (2) since the solar core and ICF plasmas are both moderately coupled plasmas, the modified 90° deflection rate must be used to calculate the collision frequencies. Assuming a Maxwellian field particle distribution, the 90° deflection rate is given,

$$\nu_D^{t/f} \simeq 2[1 + \frac{1}{2ln\Lambda_b}(\frac{m_f - m_t}{m_f + m_t})](\mu + \mu' - \frac{\mu}{2x^{t/f}})\nu_\circ . \quad (4.32)$$

As discussed before, this formula is also justified for $ln\Lambda_b \simeq$ 2-10; however, when $ln\Lambda_b \gtrsim$ 10, it reduces turns to the standard Trubnikov's formula. Consequently, we actually use this formula to treat both weakly and moderately coupled plasmas.

For controlled nuclear fusion, both inertially and magnetically confined, we primarily consider the deuteron-triton reaction,

$$D + T \rightarrow {}^4He + n + 17.6\ MeV\ . \tag{4.33}$$

The reaction rate is then determined as follows,

$$\nu_f = n_T < \sigma v > \ . \tag{4.34}$$

For the solar core, the most likely nuclear fusion reactions are described by the so-called proton-proton cycle because of the availability, that is two hydrogen nuclei that combine to form helium in the following series of steps[22],

$$\begin{cases} {}^1H + {}^1H \rightarrow {}^2D + e^+ + \nu + 1.44\ MeV \\ {}^2D + {}^1H \rightarrow {}^3He + \gamma + 5.49\ MeV \\ {}^3He + {}^3He \rightarrow {}^4He + {}^1H + {}^1H + 12.85\ MeV\ . \end{cases} \tag{4.35}$$

Because the first step is the slowest, it therefore determines the rate at which the whole chain reaction proceeds. In our calculations, it is this step that we chose for comparison, the fusion rate is given by,

$$\nu_f = \frac{1}{2} n_H < \sigma v > \ . \tag{4.36}$$

The calculated results are listed in Table 4.3. It is surprising to find that, in order to obtain a fusion reaction, it requires 10^{31} collisions in the solar core, but only about 10^4 collisions for other cases. Table 4.3 gives the ratios of collision frequencies to fusion rates for solar core, magnetic and inertial confinement fusions.

Table 4.3:

Ratios of collision to fusion rates

	$R = \nu_c/\nu_f$	τ_c (sec.)	τ_f (sec.)	λ (cm)
Solar Core	$\simeq \pi \times 10^{31}$	$\simeq 2 \times 10^{-15}$	$\simeq 6.4 \times 10^{16}$	$\simeq 1.0 \times 10^{-7}$
Magnetic Fusion	$\simeq 1.4 \times 10^{4}$	$\simeq 6.3 \times 10^{-3}$	$\simeq 9.1 \times 10^{1}$	$\simeq 6.1 \times 10^{5}$
Inertial Fusion	$\simeq 4.6 \times 10^{3}$	$\simeq 2 \times 10^{-14}$	$\simeq 9.1 \times 10^{-11}$	$\simeq 2.0 \times 10^{-6}$

This table also reveals how difficult it is for human to achieve controlled nuclear fusion on earth.

4.6 Summary

In summary, by using the modified Fokker-Planck operator, we, for the first time, could effectively treat plasmas for which $ln\Lambda_b \gtrsim 2$, i.e. moderately coupled plasmas with justification. Precise calculations of certain relaxation rates, and approximate calculations of electron transport coefficients, have been made, and, in most cases, the results differ from Braginskii's and Trubnikov's results by terms of order $1/ln\Lambda_b$. However, in the limit of large $ln\Lambda_b$ ($\gtrsim 10$), these results reduce to the standard (Braginskii) form. In addition, we have calculated a reduced electron-ion collision operator that, for the first time, manifests $1/ln\Lambda_b$ corrections.

Chapter 5

Charged Particle Stopping Powers in Inertial Confinement Fusion Pellet Plasmas

In this chapter, the effects of large-angle scattering, important for plasmas for which the Coulomb logarithm is of order 1, have been properly treated in calculating the range (R) and the fuel-areal density (ρR) of inertial confinement fusion (ICF) plasmas. This new calculation, which also includes the important effects of plasma ion stopping, collective plasma oscillations, and quantum effects, leads to an accurate estimate, not just an upper limit, of ρR. For example, 3.5 MeV α's from D-T fusion reactions are found to directly deposit $\simeq 47\%$ of their energy into a plasma of 20 keV deuterons and tritons. Consequently the α range (R) and ρR are reduced by about 60% from the case of pure electron stopping. In addition, the Fermi degenerate pressures are discussed for ICF pellet plasmas, and compared to the cases of the solar core and the white dwarf.

5.1 Introduction

The stopping of charged particles (α's, ^{3}H, ^{3}He, hot electrons . . .) in compressed pellet plasmas is a fundamental problem with close parallels to early work of Rutherford and Bohr who studied α stopping in solid materials[58]. In the context of inertially confined fusion plasmas (ICF), it involves the deposition of energy from charged particles, especially the α's, in the fuel material during the initial cold and compressed state and then during the evolution to full ignition and burn[53, 54, 55, 56, 59, 64, 65]. The tremendous range of pellet plasma conditions [$n_e \lesssim 10^{27}$ cm^{-3} and $0.1 \lesssim T_e$ (T_i) $\lesssim 40$ keV] is directly reflected in the range of the Coulomb logarithm - - $1 \lesssim ln\Lambda_b \lesssim 12$ - - a parameter fundamental to many plasma properties[1, 3, 4, 5, 28], including charged particle stopping. In particular, Fraley *et al.*[66] and later Mehlhorn[57] noted that when ion stopping is significant for α's, large-angle scattering is also likely to be important. Fraley *et al.* did calculate ion stopping, but because they were unable to estimate the effect of the large-angle scattering within the framework of the Fokker-Planck approximation, and because they neglected collective plasma effects, they concluded that their estimate of range (R) and fuel areal-density (ρR) was in fact only an upper limit. Mehlhorn attempted to treat large-angle scattering, but discarded his results in favor of the standard small-angle formulation when the large-angle results proved inconsistent. In addition, Fraley *et al.* and many others have applied stopping power formulas to $ln\Lambda_b \gtrsim 2$ plasmas in spite of the fact that these formulas were derived under the assumption that $ln\Lambda_b \gtrsim 10$. Therefore there was no rigorous justification in such applications. Furthermore, quantum mechanical corrections that are important during the initial portion of the evolution of the pellet are also added in this chapter. Specifically, it is found that the shifting of the effective quantum mechanical electron velocities strongly affects interactions between 3.5 MeV α's and the plasma electrons by dramatically enhancing the binary interactions over the collective effects. These changes of the early dynamics

could greatly affect the evolution of the pellet. However, their contributions have not hitherto been discussed.

5.2 Modeling the Stopping Power in ICF Pellet

As discussed in previous chapters that the ICF pellets are typical moderately coupled plasmas, which evolve with the plasma temperature from initial cold and compressed state (near complete Fermi degeneracy, $T_e \lesssim 1$ keV) to ignition ($T_e \sim$ 5-10 keV) and finally to the full burn state ($T_e \sim$ 10-40 keV). The tremendous dynamical ranges of the plasma temperature and density require that the issue of charged particle stopping should be treated dynamically within a comprehensive framework, which includes the different physics aspects: quantum mechanical effects; binary interactions (small-angle collisions and large-angle scattering); plasma collective effects; and plasma ion stopping. These relevant physical models are presented subsequently.

5.2.1 Quantum Mechanical Effects

Because of the high electron density in the pellet plasma ($n_e \gtrsim 10^{26} cm^{-3}$), the effect of electron degeneracy has to be considered in the earlier evolution. The condition for determining the degeneracy is[72]

$$\frac{h}{(2\pi m_e k T_e)^{1/2}} \gtrsim n_e^{-1/3} . \tag{5.1}$$

The physical explanation for this is that if the de Broglie wavelength of an electron is greater than or comparable to the inter-electron spacing, then quantum mechanical effects become important. Usually this effect appears in a system of

low temperature and high density, such as in metals and astrophysics. In magnetic confinement fusion, however, the electron density in tokamak plasma, for example, is too low ($n_e \sim 10^{14}cm^{-3}$) and the temperature far too high for degeneracy to be important. Applying this condition to ions, one finds also that even in the ICF pellet core, ion degeneracy is also negligible.

Thus let us consider electron degeneracy in the ICF pellet fuel. Suppose a D-T pellet is isentropically compressed and has a compression factor $\eta \sim 4$ (where the compression factor is defined as $\eta = n/n_{liquid}$), which corresponds to the electron density $n_e \simeq 5 \times 10^{26}$ cm^{-3}[53], we have

$$\frac{1.24 \times 10^{-9}}{\sqrt{T_e(keV)}} \gtrsim 1.26 \times 10^{-9} , \tag{5.2}$$

for ICF pellet fuel, where the electron temperature varies from $\sim$ 0.1 keV to 10 keV. The electron degeneracy determined by this formula is a function of the plasma electron temperature, and changes from being a strong degeneracy to finally being negligible. The degenerate electrons in the pellet fuel can be simply modeled as a Fermi free electron gas which obeys Fermi-Dirac statistics, $f_F(E)$,

$$f_F(E) = \frac{1}{e^{(E-E_F)/kT_e} + 1} , \tag{5.3}$$

where E_F $[=\hbar^2(n_e\pi^2)^{2/3}/2m_e]$ is the Fermi energy. The characteristic feature of this distribution is quite different from that of the Maxwellian distribution of a non-degenerate plasma. However, as the plasma temperature in the pellet fuel increases due to energy deposition of the fusion products, the distribution returns to Maxwellian.

Consequently, one finds a remarkable property in the pellet plasma due to this electron degenerate - - - the shifting of effective electron velocity. According to

Fermi-Dirac statistics, electrons (Fermions) near the Fermi energy are excited by the effects of finite temperature from inside the Fermi sphere up to the Fermi energy plus a few kT_e. This can be seen from the following discussion. By considering the density of the quantum state [$D(E) = 4\pi V(2m_e)^{3/2}h^{-3}E^{1/2}$] and Fermi statistics, one can determine the total number of electrons, N, and the total energy, E_{tot}, through

$$N = \int_0^\infty 4\pi V(\frac{2m_e}{h^2})^{3/2}\frac{E^{1/2}dE}{e^{(E-E_F)/kT_e}+1} , \tag{5.4}$$

and

$$E_{tot} = \int_0^\infty 4\pi V(\frac{2m_e}{h^2})^{3/2}\frac{E^{3/2}dE}{e^{(E-E_F)/kT_e}+1} . \tag{5.5}$$

The effective energy per electron is given: for the case of weak degeneracy ($kT_e/E_F \gtrsim 1$),

$$E_{eff} = \frac{E_{tot}}{N} \simeq \frac{3}{2}kT_e[1+\frac{1}{2^{5/2}}\frac{4}{3\sqrt{\pi}}(\frac{E_F}{kT_e})^{3/2} - \frac{1}{3^{5/2}}(\frac{4}{3\sqrt{\pi}})^2(\frac{E_F}{kT_e})^3 \ldots .] \tag{5.6}$$

and for the case of strong degeneracy ($kT_e/E_F \ll 1$),

$$E_{eff} \simeq \frac{3}{5}E_F[1+\frac{\pi^2}{12}(\frac{kT_e}{E_F})^2 - \frac{\pi^4}{80}(\frac{kT_e}{E_F})^4 \ldots .] . \tag{5.7}$$

Consequently a universal effective energy can be calculated by combining the cases of weak degeneracy [$E_{eff}(weak)$ from the Eq.(5.6)], and strong degeneracy [$E_{eff}(strong)$ from the Eq.(5.7)], i.e.

$$\frac{1}{E_{eff}} = \sqrt{\frac{1}{E_{eff}^2(weak)} + \frac{1}{E_{eff}^2(strong)}} \tag{5.8}$$

Fig.(5-1) gives a plot of the effective energy of a degenerate electron over the electron temperature for a typical ICF pellet plasma ($n_e = 5 \times 10^{26} cm^{-3}$). Because of the contribution from the quantum degenerate effects, it is shown that the electron effective energy is larger than the corresponding electron temperature, as predicted from Eq.(5.6). In particular, when plasma is strongly degenerate, the effective energy is almost completely independent of the electron temperature [expected from Eq.(5.7)]. Physically, it is interpreted that due to the effect of finite temperature, a fraction of the electrons has filled up higher energy levels (greater than the corresponding Fermi energy). This phenomenon significantly raises the effective velocity of electrons, which is defined as $v_{eff} = \sqrt{2E_{eff}/m_e}$. (On the other hand, the electron thermal velocity is defined as $v_{the} = \sqrt{2T_e/m_e}$.) Fig.(5-2) shows a comparison of the electron effective and thermal velocities. Consequently, it is the electron effective energy (effective velocity), not the electron temperature (thermal velocity), that should be used in the calculations for a degenerate system. However, as shown in Figs.(5-1) and (5-2) that with the increase of the plasma temperature, the effective energy (velocity) reduces to the thermal energy (velocity).

5.2.2 Binary Interactions

Binary interactions between test particle and field particle occur when the impact parameter is smaller than the Debye length of the plasma. This interaction results in the test particle losing its kinetic energy and depositing it to the field particles. Making use of the previous discussed energy loss relaxation rate, the general stopping power of a test particle for binary interaction is derived as

$$\frac{dE^{t/f}}{dx} = -\frac{(Z_t e)^2}{v_t^2}\,\omega_{pf}^2\,G(x^{t/f})\,ln\Lambda_b^{t/f}\,, \tag{5.9}$$

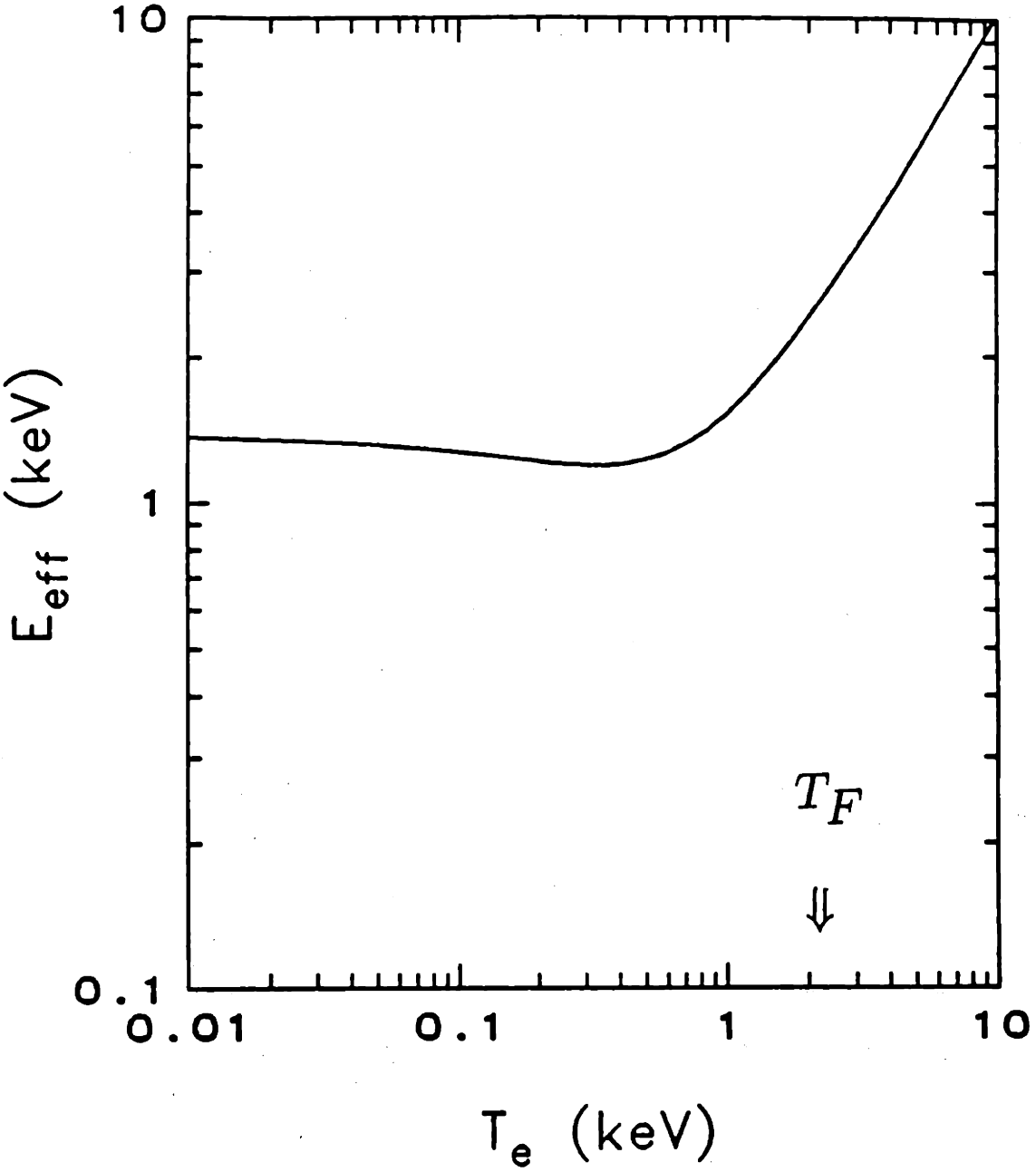

Figure 5-1: The effective quantum energy of a degenerate electron is plotted as a function of the plasma electron temperature in D-T pellet plasmas. Because of the Fermi-Dirac distribution, the average energy per degenerate electron is dramatically increased compared to the corresponding electron thermal energy. The Fermi temperature (T_F) is indicated by the arrow. One sees that the effect of electron degeneracy makes the E_{eff} independent of the temperature below the Fermi temperature. When $T_e \gtrsim 1$ keV, quantum degeneracy is negligible. Then the average energy of the electrons is equal to their thermal energy.

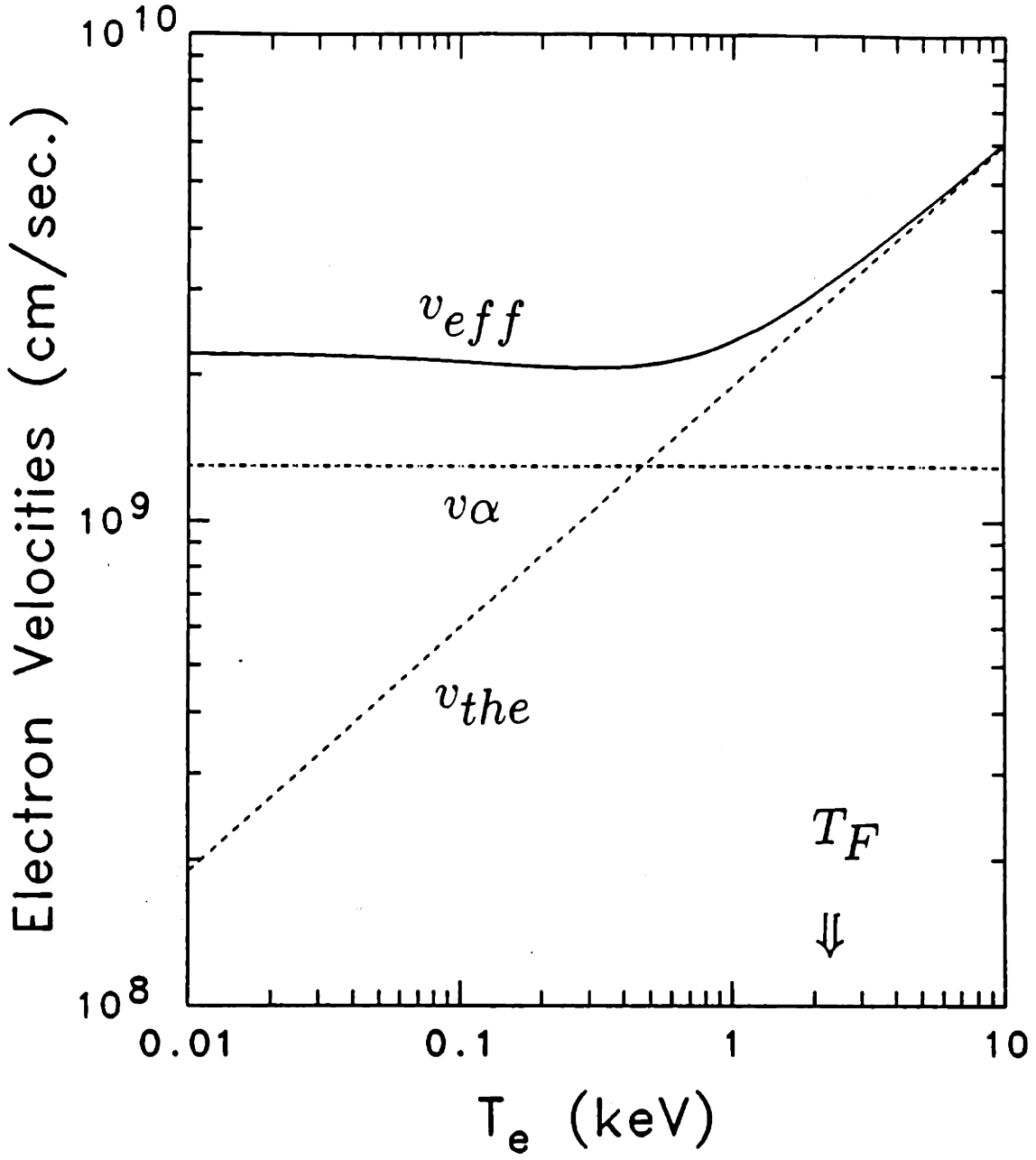

Figure 5-2: A comparison of $v_{eff} = \sqrt{2E_{eff}/m_e}$ and $v_{the} = \sqrt{2T_e/m_e}$ (v_α for 3.5 MeV fusion α particles is shown for reference). The Fermi temperature (T_F) is indicated by the arrow. One sees that the effect of electron degeneracy makes the E_{eff} independent of the temperature below the Fermi temperature. The divergence between v_{eff} and v_{the} for $T_e \leq 1$ keV illustrates the importance of electron quantum degeneracy effects in the calculation of the α stopping power.

where $Z_t e$ is the test charge, v_t (v_f) is the test (field) particle velocity with $x^{t/f} = v_t^2/v_f^2$, m_t (m_f) is test (field) particle mass, and $\omega_{pf} = (4\pi n_f e_f^2/m_f)^{1/2}$ is the field plasma frequency. The Coulomb logarithm, $ln\Lambda_b$, and the temperature coupling parameter, $G(x^{t/f})$, are carefully addressed as follows:

A. The Coulomb logarithm

The Coulomb logarithm is usually defined as

$$ln\Lambda_b^{t/f} = ln(\frac{\lambda_D}{p_{min}}) , \tag{5.10}$$

where, for the nondegenerate regime λ_D is the Debye length and p_{min} is the closest impact parameter for binary interaction. In the context of ICF, it is a measure of the relative importance of "dominant" terms (small-angle binary collisions) to the "non-dominant" terms (large-angle scattering, collective effects, etc.). For a dense plasma like ICF pellet, quantum mechanical effects must enter the calculation of Coulomb logarithm for electrons: (1) because of the effect of quantum degeneracy, the effective energy (velocity) has to be used for low temperature regime; and (2) the Heisenberg's uncertainty principle has to be used for high temperature regime. Including both effects, a universal formula is obtain as

$$p_{min} = \sqrt{p_\perp^2 + (\hbar/2m_r u)^2} , \tag{5.11}$$

where $p_\perp = e_t e_f/m_r u^2$ is the classical impact parameter for 90° scattering, with m_r the reduced mass and u the relative velocity. Using this universal formula, for example, Figs.(5-7a) shows the calculated Coulomb logarithms for fusion α's interacting with the electrons ($n_e = 1 \times 10^{26}$). Results for both binary interaction ($\ln\Lambda_b$) and collective effects ($\ln\Lambda_c$) from both quantum and classical approaches are compared. Quantum mechanical approach successively avoids the trouble of

providing a meaningless negative Coulomb logarithm in the region of low electron temperature. Fig.(5-3) gives a comparison of calculated Coulomb logarithm from our semi-quantum approach (solid line) with that from a random-phase-approximation (RPA) approach [solid circles [59]]. Both of them are thought to be reasonably equivalent.

B. The Effects of Small-Angle Collisions

Because of the nature of the long-range force of Coulomb interactions, the test particles suffer primarily small-angle collisions. It turns out that the test particles diffuse in velocity space. This diffusion process is well defined in terms of the conventional Fokker-Planck equation and the temperature coupling parameter $G(x^{t/f})$ defined as

$$G(x^{t/f}) = \mu(x^{t/f}) - \frac{m_f}{m_t}\frac{d\mu(x^{t/f})}{dx^{t/f}}. \tag{5.12}$$

C. The Effects of Large-Angle Scattering

The effects of large-angle scattering must be included to treat ICF pellet plasmas because their Coulomb logarithms are of order unity. This particular problem is overcome by our recent generalization of the Fokker-Planck equation, which properly treats the effects of large-angle scattering as well as small-angle collisions[15, 49] and is justified for application to $ln\Lambda_b \gtrsim 2$ plasmas. In subsequent discussions of charged particle stopping, we utilize one of the general results of that analysis:

$$G(x^{t/f}) = \mu(x^{t/f}) - \frac{m_f}{m_t}\{\frac{d\mu(x^{t/f})}{dx^{t/f}} - \frac{1}{ln\Lambda_b}[\mu(x^{t/f}) + \frac{d\mu(x^{t/f})}{dx^{t/f}}]\}\ . \tag{5.13}$$

The contribution of large-angle scattering is solely manifested by $1/ln\Lambda_b$ terms of

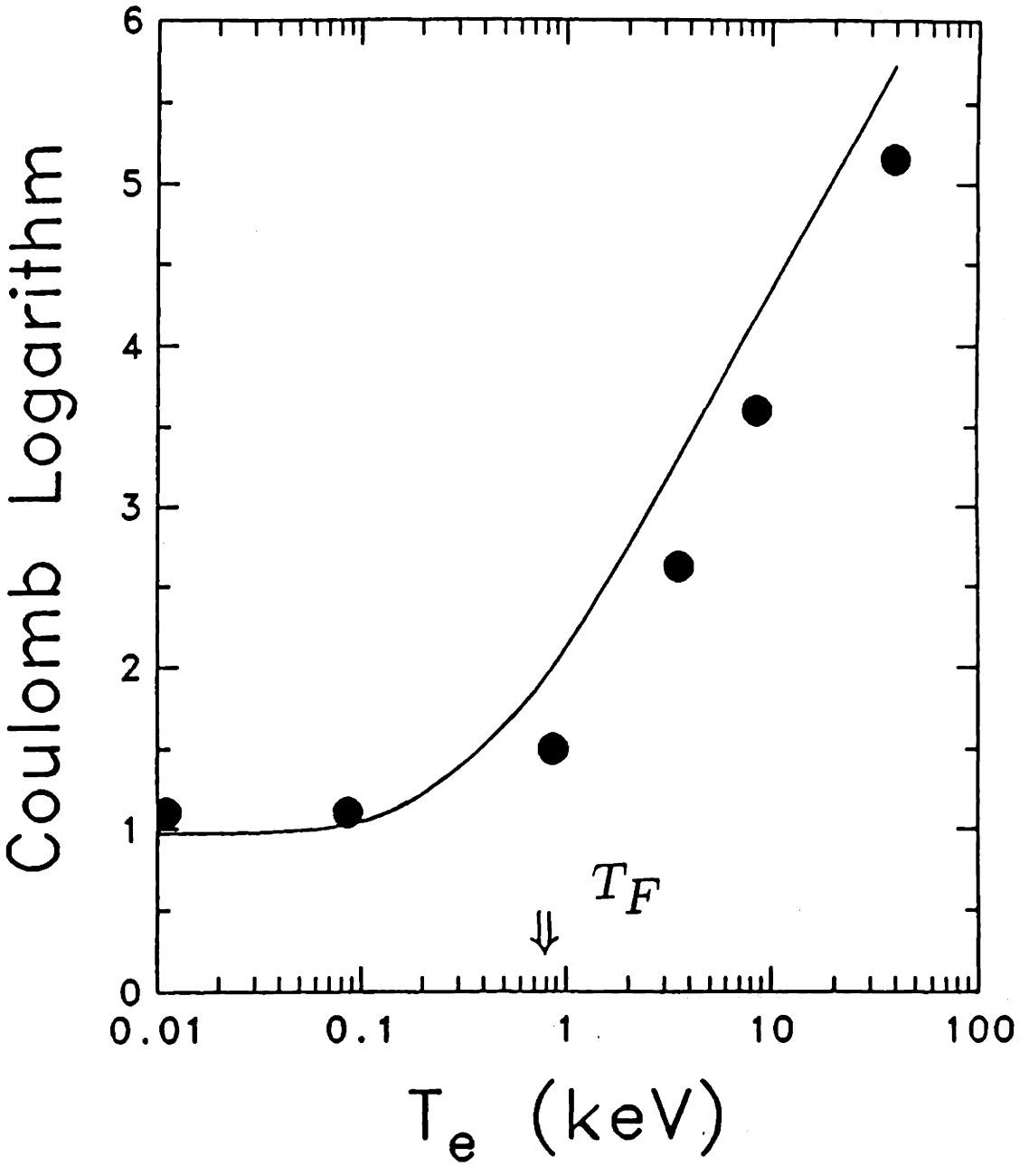

Figure 5-3: Coulomb logarithm for α-electron binary interaction (solid line, calculated from our semi-quantum approach.) in a D-T plasma ($n_e = 1 \times 10^{26}/cm^3$) compares to the result from a random-phase-approximation (RPA) calculation (solid dots[59]).

Eq.(5.4). In particular, if $ln\Lambda_b \gtrsim 10$ and we ignore this correction, then Eq.(5.13) reduces to Trubnikov's expression [Eq.(5.12)].

5.2.3 Collective Effects

When a test particle interacts with the plasma outside the Debye sphere, an electric field will be induced by the polarizing of the medium such that the plasma acts as a continuous medium with collective oscillations[67, 68, 69]. As a consequence, this induced electric field acts back and slows down the test paricle. The Lenard-Balescu equation, in principle, provides an adequate description of this phenomenon[24]. For the sake of simplicity and comparison with binary interaction, the stopping power due to field plasma oscillations is[68, 69, 70],

$$\frac{dE^{t/f}}{dx} = -\frac{2}{\pi}(\frac{Z_t e}{v_t})^2 Re \int_0^\infty \frac{i\omega}{\epsilon(\omega)}(\frac{\omega\lambda_D}{v_t})K_0(\frac{\omega\lambda_D}{v_t})K_1(\frac{\omega\lambda_D}{v_t})d\omega \ , \quad (5.14)$$

where $K_0(\omega\lambda_D/v_t)$ and $K_1(\omega\lambda_D/v_t)$ are the modified Bessel functions, and the dielectric constant with damping σ is $\epsilon(\omega) = 1 - \omega_{pf}^2/(\omega^2 + i\omega\sigma)$. Since the significant frequencies in the integral turn out to be $\omega \sim \omega_{pf}$, the calculation of the Coulomb logarithm in the equation above can be readily performed to provide (see Appendix C for details)

$$\frac{dE^{t/f}}{dx} \simeq -\frac{(Z_t e)^2}{v_t^2}\,\omega_{pf}^2\, ln\Lambda_c^{t/f} \ , \quad (5.15)$$

with

$$ln\Lambda_c^{t/f} \simeq \begin{cases} ln(1.123\sqrt{x^{t/f}}) & \sqrt{x^{t/f}} \gg 1 \\ \frac{K_1(1/\sqrt{x^{t/f}})K_0(1/\sqrt{x^{t/f}})}{\sqrt{x^{t/f}}} & \sqrt{x^{t/f}} \sim 1 \\ \frac{\pi}{2}e^{-\frac{2}{\sqrt{x^{t/f}}}} & \sqrt{x^{t/f}} \ll 1 \end{cases} \tag{5.16}$$

Because of different features of the logarithmic, Bessel and exponential functions, one finds that in the different regimes the stopping power has the distinguishing behaviors: $ln\Lambda_c$ is significant, moderate, and negligible in the cases of $x^{t/f} \gg 1$, ~ 1, and $\ll 1$, respectively. In other words, the contribution of collective plasma oscillations is only important for the cases of $x^{t/f} \gg 1$.

5.2.4 Plasma Ion Stopping

Plasma ion stopping is usually negligible compared to plasma electron stopping in plasmas of low temperature. This is because the charged particle velocities are more comparable to the thermal velocity of the plasma electrons. However, as the plasma temperature gets higher, contributions from plasma ion stopping become important. The relative importance of plasma ions to electrons for test charged particle stopping can be measured from their relative ratio[71]:

$$\frac{dE^{t/i}}{dx} / \frac{dE^{t/e}}{dx} \simeq \frac{v_{crit.}^3}{v_t^3} , \tag{5.17}$$

where a critical velocity is introduced, and it is defined as,

$$v_{crit.}^3 \simeq \frac{3\sqrt{\pi}}{4}\frac{n_i Z_i^2}{n_e}\frac{m_e}{m_i}\left(\frac{ln\Lambda_b^{t/i} + ln\Lambda_c + m_i/m_t}{ln\Lambda_b^{t/e}}\right)\left(\frac{2T_e}{m_e}\right)^{3/2}. \tag{5.18}$$

The physical interpretation of this critical velocity is that, as shown in Fig.(5-4), when $v_t < v_{crit}$, electron stopping is less important than ion stopping. Fig.(5-5) plots v_{crit} as a function of electron temperature. The quantum degeneracy is evident in this figure when electron temperature is less than its Fermi temperature (T_F).

5.3 Comprehensive Calculations

Comprehensive calculations are made within a unified framework of binary interactions (both small-angle collisions and large-angle scattering) for impact parameter smaller than the Debye length plus plasma collective oscillations for impact parameter outside the Debye sphere. Based on the model described previously, a generalized stopping formula is developed[49]

$$\frac{dE^{t/f}}{dx} \simeq -\frac{(Z_t e)^2}{v_t^2}\omega_{pf}^2[G(x^{t/f})ln\Lambda_b^{t/f} + \theta(x^{t/f})ln(1.123\sqrt{x^{t/f}})] \ . \quad (5.19)$$

In the above generalized equation, collective effects are represented by the second term $[ln\Lambda_c^{t/f} \equiv ln(1.123\sqrt{x^{t/f}})]$ where $\theta(x^{t/f})$ is a step function whose value is identically 0 (1) for $x^{t/f} \leq 1$ (>1). Degeneracy effects enter in both the calculation of $ln\Lambda$ and the parameter $x^{t/f}$. When fusion products (3.5 MeV α particles, for example) in the pellet fuel are generated, they are in the energy regime $x^{\alpha/e} \ll 1$ promptly, which justifies that binary interaction is the dominant mechanism for fusion products stopping. As the plasma electron temperature increases, quantum degenerate effects decrease. Table 5.1 gives the typical energy regimes in ICF pellet plasmas for 3.5 MeV α particles. For example, if v_{the} were mistakenly used instead of v_{eff} for $T_e \simeq 0.3$ keV, the stopping power would be undervalued by a factor ~ 3. Because of the non-linear evolution of pellet dynamics, such considerations could be important in the later evolution of the pellet.

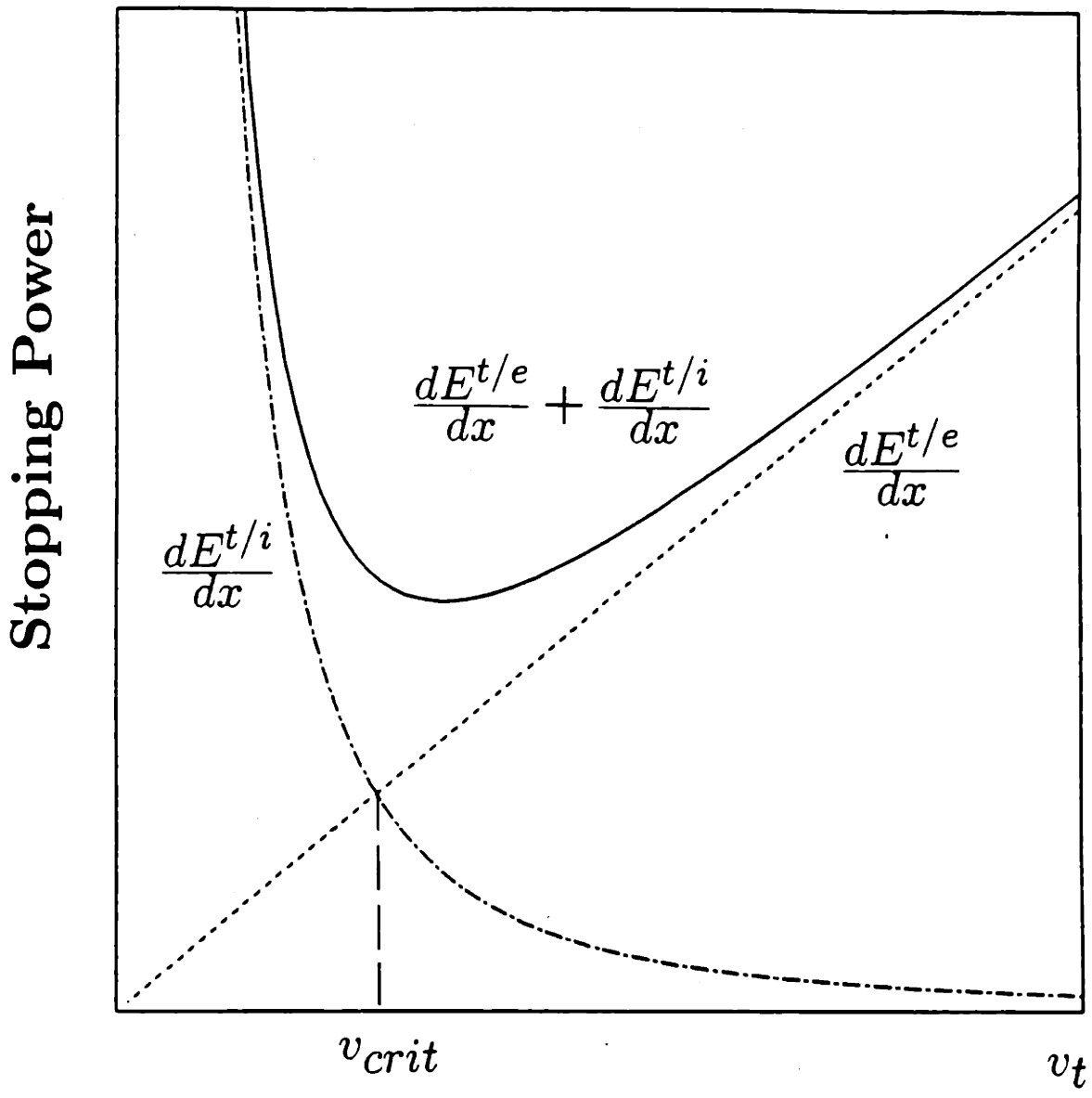

Figure 5-4: The physical explanation of the critical velocity is that when test particle velocity (v_t) > v_{crit}, electron stopping dominates. However, when v_t < v_{crit}, ion stopping is more important.

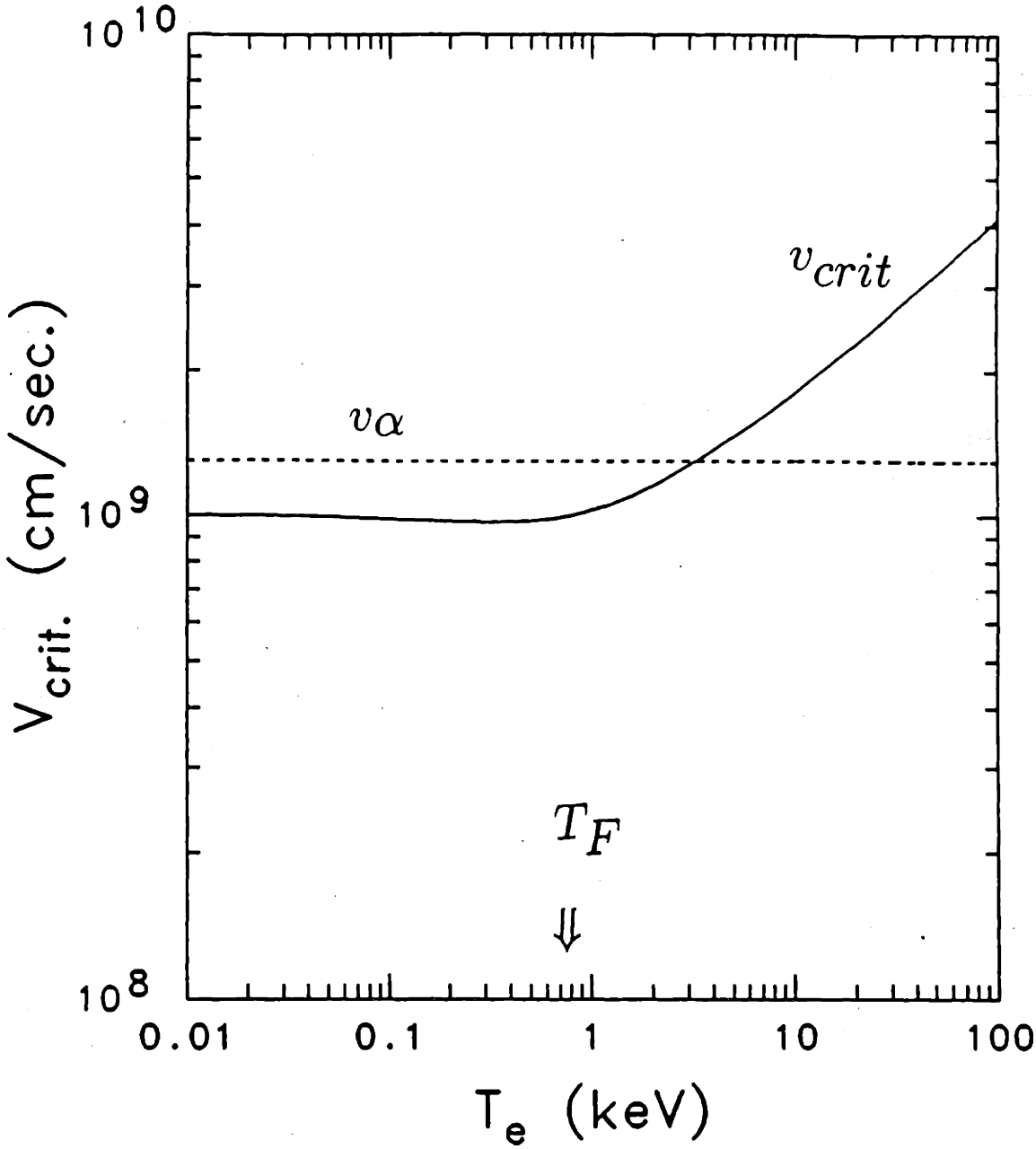

Figure 5-5: The critical velocity is plot as a function of the plasma electron temperature in a D-T plasma ($n_e = 1 \times 10^{26}/cm^3$). The Fermi temperature (T_F) is indicated by the arrow. It is the effects of quantum degeneracy that make v_{crit} independent of the temperature within the regime below the Fermi temperature. The v_α for 3.5 MeV fusion α particle is shown for reference (dashed line).

Table 5.1:
The energy regime for 3.5 MeV α particles in ICF pellet plasmas

T_e (T_i)	$x^{\alpha/e}$ ($v_e = v_{the}$)	$x^{\alpha/e}$ ($v_e = v_{eff}$)	$x^{\alpha/i}$
0.01 keV	~ 40	~ 0.25	$\sim 2.19\times10^4$
0.05 keV	~ 10	~ 0.25	$\sim 7.30\times10^3$
0.1 keV	~ 5	~ 0.25	$\sim 4.38\times10^3$
0.5 keV	~ 1	~ 0.25	$\sim 3.13\times10^3$
1.0 keV	~ 0.5	~ 0.25	$\sim 2.19\times10^3$
5.0 keV	~ 0.07	~ 0.07	$\sim 4.38\times10^2$
10.0 keV	~ 0.04	~ 0.04	$\sim 2.19\times10^2$

In order to illustrate the results of the generalized stopping power Eq.(5.19)], we consider the following four cases: α's, ^{3}H, ^{3}He, and hot electrons each interacting with field ions and field electrons.

5.3.1 3.5 MeV α's Stopping in D-T Pellet Plasmas

Fig. (5-6) shows the schematic of an α particle is that born at the "hot spot" of the pellet and stops in the fuel part of the pellet. One of the objectives in ICF research is to stop all the α's in the D-T fuel in order to achieve high burn efficiency and to sustain the fusion reaction. Fig.(5-7) shows the corresponding Coulomb logarithms for α - electron ($ln\Lambda^{\alpha/e}$) and α - ion ($ln\Lambda^{\alpha/i}$) interactions (3.5 MeV α's in a D-T plasma of $10^{26}/cm^3$). Note that for all charged fusion products (α's, ^{3}H, ^{3}He ...) interacting with *field electrons*, $x^{t/f}$ is usually much less than one, indicating that collective contributions can be ignored (see $ln\Lambda_c^{\alpha/e}$ in Fig. (5-7)). In contrast, for charged fusion products interacting with *field ions*, $x^{t/f}$ is usually much larger than one, and therefore collective effects are significant [dashed line, Fig. (5-7)].

In the case of α - electron interactions, Eqs.(5.13) and (5.19) nearly reduce

Table 5.2:
Fraction of 3.5 MeV α stopping by D-T plasma ions

T_e (keV)	D-T ion stopping (% of total)	electron stopping (% of total)
1.0	$\simeq 6$	$\simeq 94$
5.0	$\simeq 19$	$\simeq 81$
10.0	$\simeq 32$	$\simeq 68$
20.0	$\simeq 47$	$\simeq 53$
40.0	$\simeq 64$	$\simeq 36$

to Trubnikov's results[4] because the mass ratio of field-to-test particles, m_e/m_α, is of order 10^{-4}. However, when the field-to-test mass ratio (m_f/m_t) is of order 1 or 10^3 - - as it is for α's, ^{3}H and ^{3}He interacting with field ions, or for test electrons interacting with field ions - - Eqs.(5.13) and (5.19) must be used instead of Trubnikov's.

In more detail, the relative fraction of ion stopping (RF) is calculated as

$$RF(E_\alpha, T_e) = \frac{dE_\alpha^{\alpha/i}}{dx}/(\frac{dE_\alpha^{\alpha/i}}{dx} + \frac{dE_\alpha^{\alpha/e}}{dx})$$

$$\simeq \frac{v_c^3}{v_c^3 + v_\alpha^3} \,. \tag{5.20}$$

The total fraction of this D-T plasma ion stopping (TF) for a 3.5 MeV α particle is calculated by integrating the relative fraction (RF) at a given plasma electron temperature over the change in E_α,

$$TF = \int_{T_e}^{E_\alpha^0} [\frac{RF(E_\alpha, T_e)}{E_\alpha^0 - T_e}]|_{T_e=const.} dE_\alpha \,. \tag{5.21}$$

$E_\alpha^0 = 3.5$ MeV is the initial fusion α-particle energy. In more detail, Fig. (5-8) plots the ion stopping fraction, Eq.(5.20), for relevant α energies (≤ 3.5 MeV)

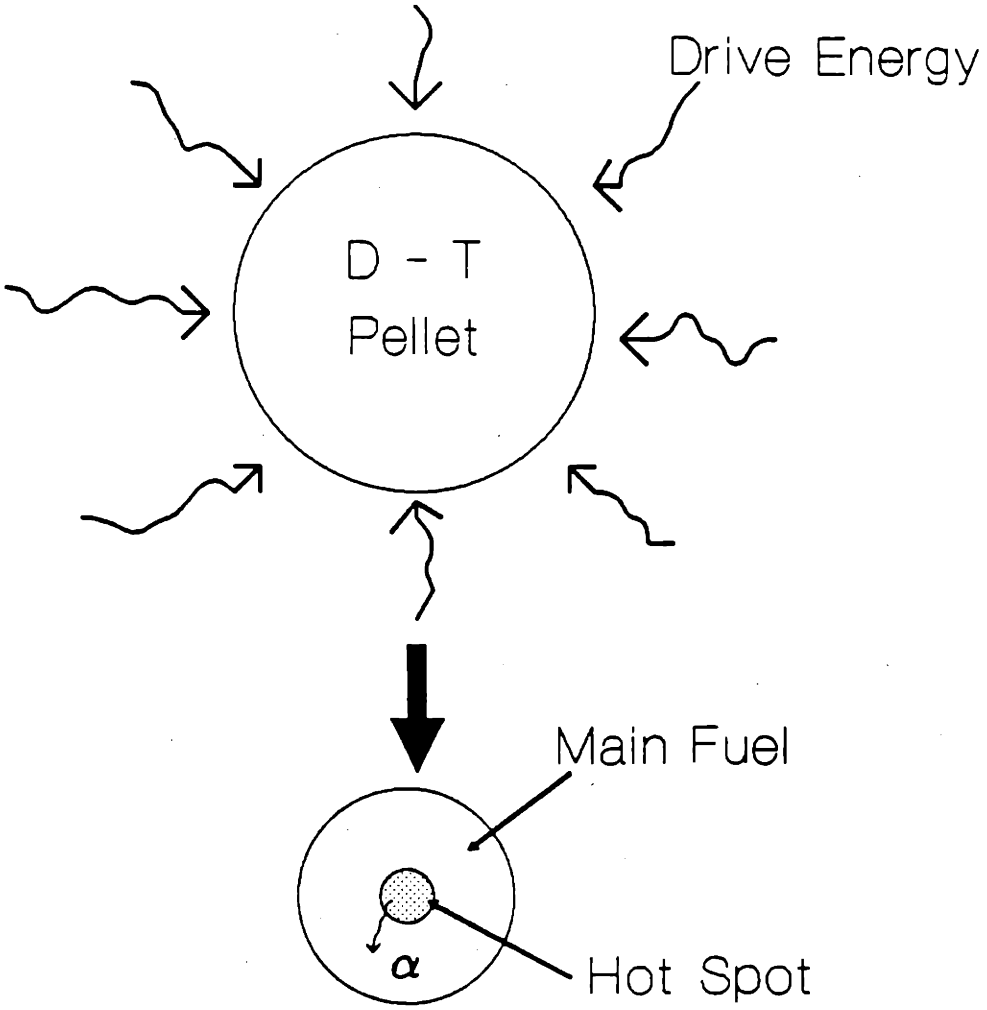

Figure 5-6: Schematic of α's stopping in an ICF pellet

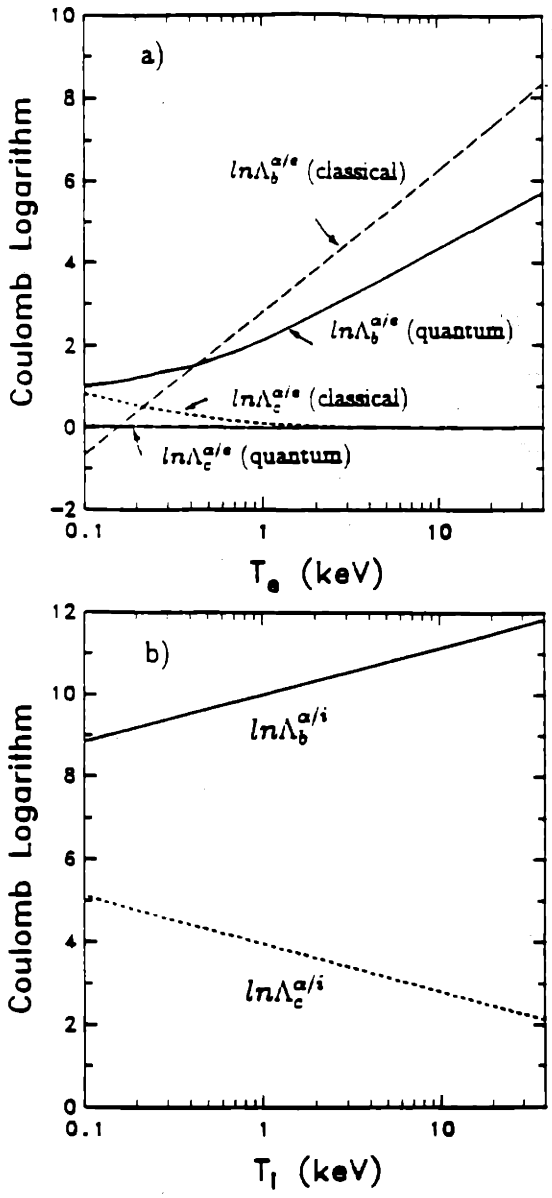

Figure 5-7: (a) Coulomb logarithms for α-electron binary interactions for 3.5-MeV α's originating from D-T reactions ($n_e = 10^{26}/cm^3$). The quantum calculation (solid line) is used in our text and subsequent figures. The classical (Spitzer) calculation (long-dashed straight line) is given for reference. The effect of collective plasma oscillations in this particular case is unimportant. Stopping power and ρR are calculated only for $T_e \gtrsim 1$ keV. (For $ln\Lambda_b^{\alpha/e} < 2$, strongly-coupled effects become an issue[15, 49, 73].). (b) The Coulomb logarithm for α-ion (deuteron and triton) interactions ($ln\Lambda_b^{\alpha/i}$) and α-ion collective interactions ($ln\Lambda_c^{\alpha/i}$). In contrast to the α-electron interaction [Fig. (a)], quantum effects are unimportant. However, collective effects are significant since $v_\alpha \gg v_i$ [v_i, the background ion (D or T) velocity].

and plasma temperatures. Table 5.2 shows the relative importances of ion and electron stopping for α's that thermalize from 3.5 MeV (n_e=10^{26}/cm^3, $T_e \simeq T_i$). Note that ion stopping becomes significant for $T_e \sim T_i \gtrsim 5$ keV. The range of α's is calculated as

$$R = \int_0^{E_\alpha} (\frac{dE}{dx})^{-1} dE \ . \tag{5.22}$$

Fig. (5-9) shows the corresponding ρR for α's (calculated from the 3.5 MeV birth energy to background thermal temperature). For example, at 20 keV inclusion of ion stopping (binary plus collective) reduces the ρR of pure electron stopping by about 60%. Also for the α's, Fig. (5-10) shows the density dependence of ρR. Effects of electron degeneracy can be clearly seen for density $\gtrsim 10^{27}$/cm^3 and temperature $\lesssim 5$ keV. (In the degenerate regime, our calculations are only semi-quantitative.) In the non-degenerate regime of Fig.(5-10), the results of Fraley *et al.*, which ignored (large-angle) scattering and collective effects, are about 20% larger. (They did not treat the degenerate regime.)

5.3.2 1.01 MeV ^{3}H and 0.82 MeV ^{3}He Stopping in D Plasmas

The development of novel ρR diagnostics are currently based upon the 1.01 MeV ^{3}H and 0.82 MeV ^{3}He[64, 74] that result from primary D-D fusion. As these ^{3}H (^{3}He) ions interact with background deuterons, secondary nuclear fusion reactions [D-T (D-^{3}He)] occur and secondary fusion products [14.1 MeV neutrons (14.7 MeV protons)] are generated. Because the neutron (proton) energy spectrum depends on the energy distribution of ^{3}H (^{3}He), it is by detecting these secondary neutrons (protons) that the information of charged particle stopping power and the fuel-areal density, ρR, is extracted. Because of the relevance of this diagnostic

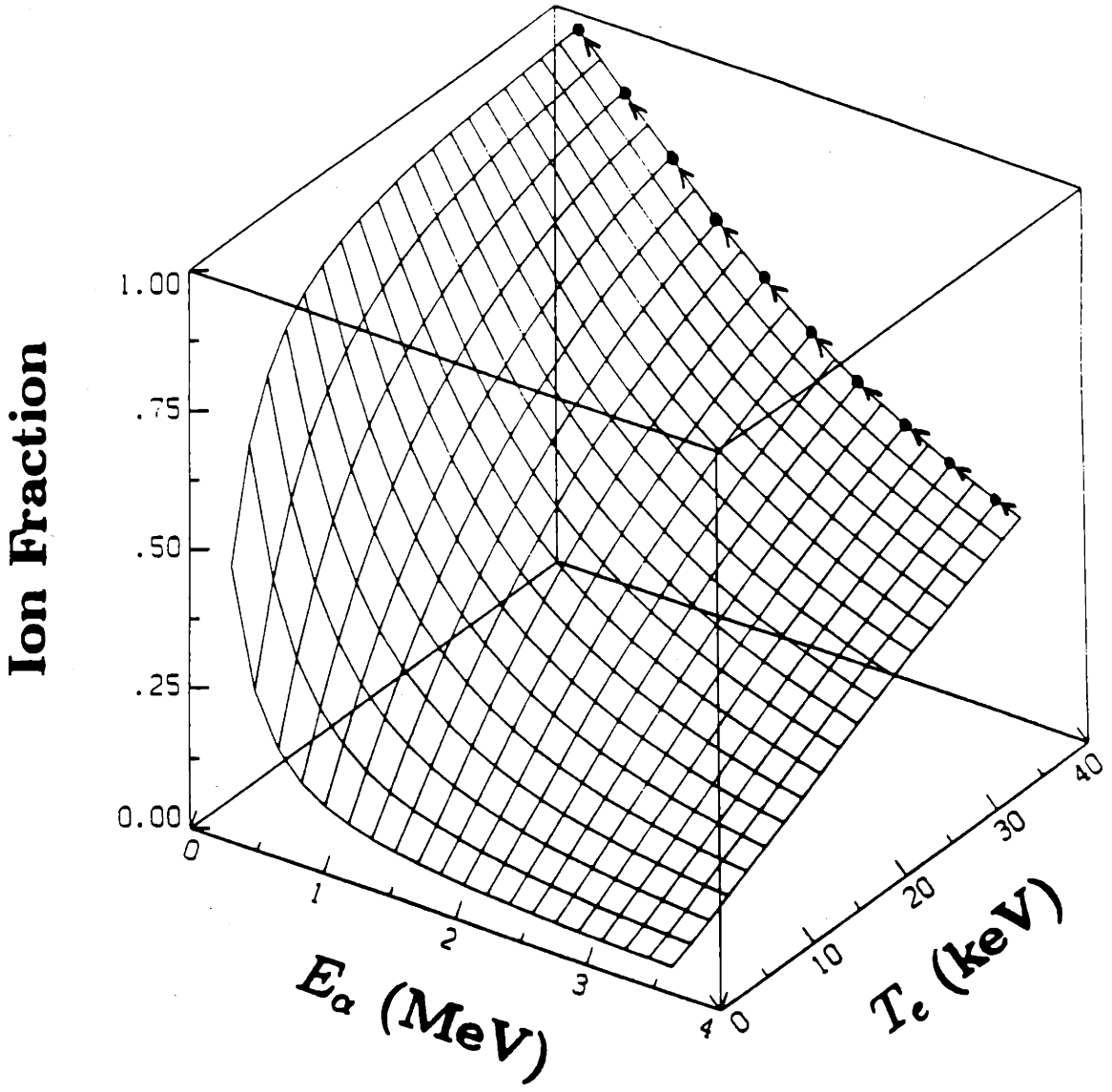

Figure 5-8: The relative fraction of α - field ion (D-T) stopping as a function of the α kinetic energy (E_α) and the plasma temperature ($T_e \sim T_i$). For $E_\alpha \lesssim 1.5$ MeV and $T_e \gtrsim 15$ keV, ion stopping is dominant. A 3.5 MeV α in a 40 keV plasma deposits its energy along the dotted trajectory. It initially deposits $\sim 35\%$ of its energy to ions, but, by the end of its range, $\gtrsim 95\%$ is going into the ions. By integrating over the trajectory, the total ion stopping is $\simeq 64\%$ (see Table 5.2). This effect significantly reduces the α range (R) and ρR by about 73% (see Fig. (5-9)).

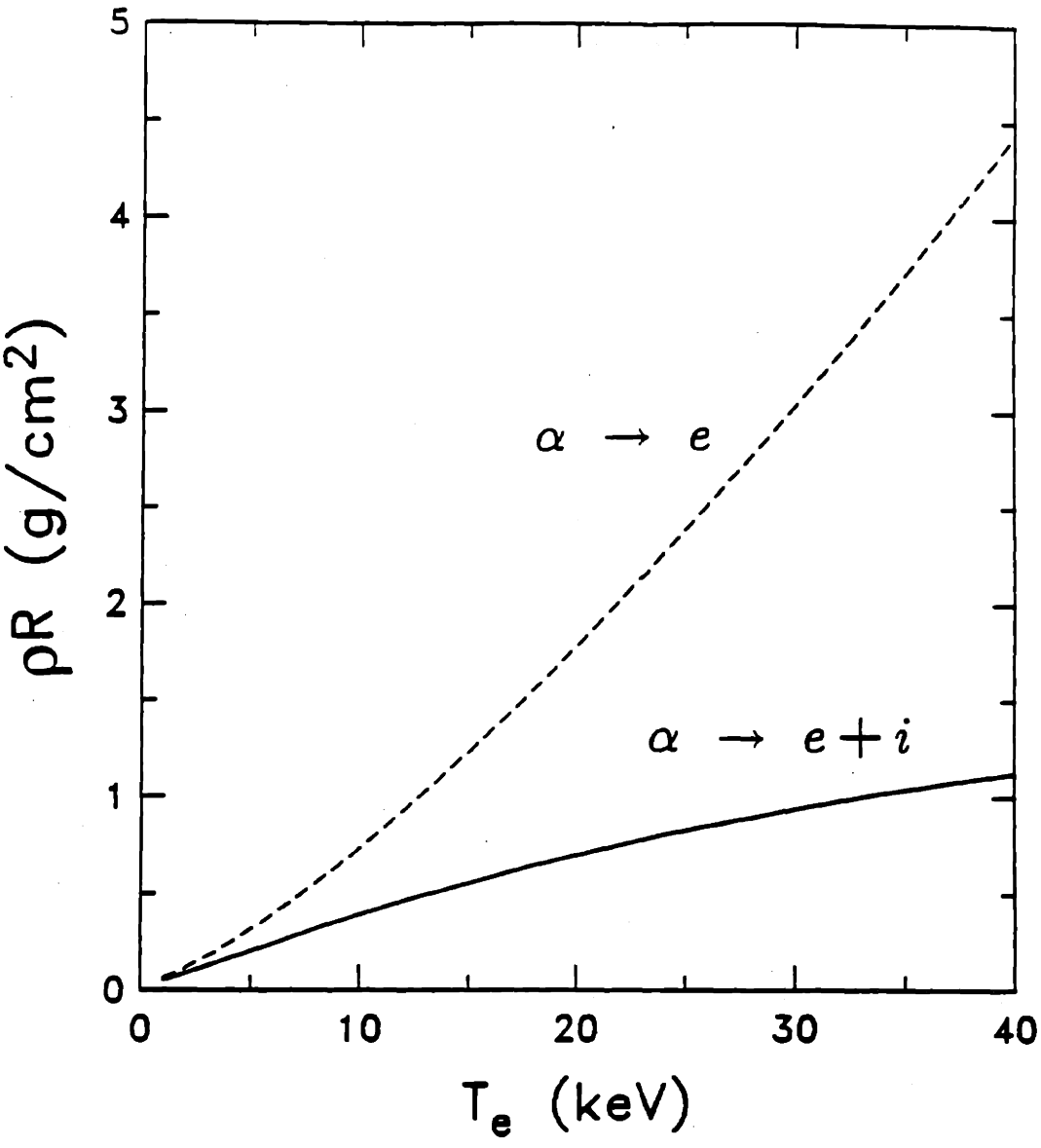

Figure 5-9: ρR for 3.5 MeV α interacting in a $10^{26}/\text{cm}^3$ D-T plasma. The dashed line represents pure electron stopping (scattering is negligible). The solid line results from the cumulative effects of electron binary interactions, ion binary interactions (small-angle plus scattering), and ion collective oscillations.

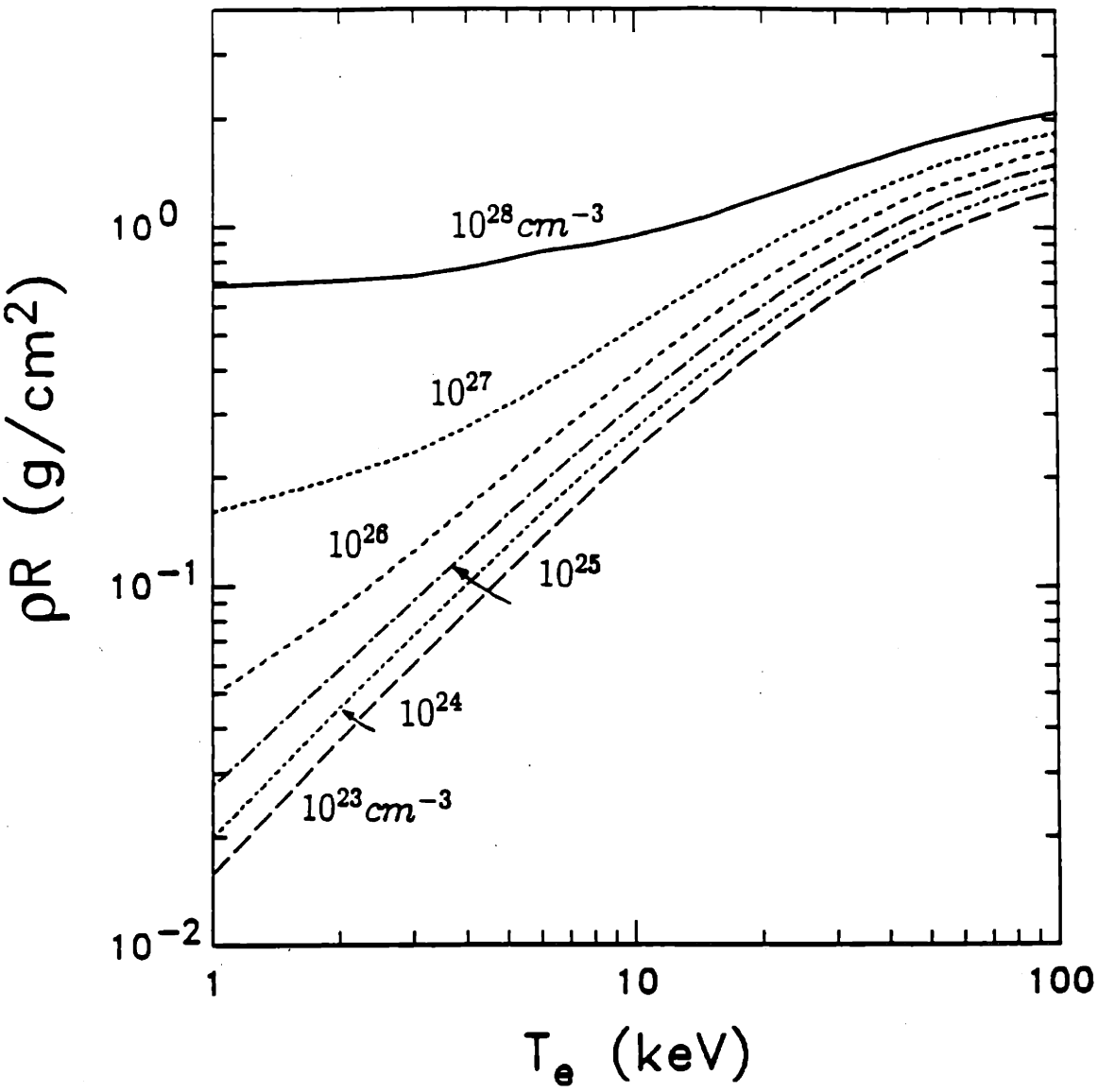

Figure 5-10: ρR curves for 3.5 MeV α interacting with D-T plasmas of various densities. Quantum degeneracy is important for $n_e \gtrsim 10^{27}/cm^3$ and $T_e \lesssim 5$ keV.

to present experiments, an accurate calculation of ρR is highly desirable. Upon the previous discussions, we apply the generalized stopping formula with comprehensive considerations to treat this issue. The ion contribution for 1.01 MeV triton stopping in a deuteron plasma is plotted as, in Fig.(5-11), a function of the plasma temperature ($T_e \sim T_i$) and the triton kinetic energy. As expected, this contribution is more significant than the case of 3.5 MeV α stopping in D-T plasma. The calculated ρR with and without the effect of ion stopping are shown in Fig.(5-12). As is evident, even for fairly low plasma temperatures the effects of ion stopping are extremely important.

5.3.3 Preheating by Suprathermal Electrons

To achieve ignition and high burn efficiency in ICF, the pellet is compressed to a density of $\gtrsim 10^4$ of the solid material. These compressions are performed isentropically, and the fuel part of the pellet is not heated before ignition so that ablation only occurs at the surface of the pellet. Consequently, the pellet can be compressed to pressures near Fermi degeneracy. However, this ideal condition could be severely perturbed because of the existence of suprathermal electrons, which are produced at the ablation surface due to a number of mechanisms. Because these suprathermal electrons, located at the tail of the electron distribution, are very energetic ($T_e \sim 1$ - 100 keV), they can penetrate the fuel and stream in the core of the pellet, far ahead of the ablation front, to preheat the D-T fuel. This phenomenon can largely reduce the pellet compression and ignition, especially for the direct drive scheme of ICF[75]. Consequently, the issues of the stopping power and range for those hot electrons are very important. Our calculation for this specific case is presented. Fig.(5-13) shows the schematic of the preheat problem.

In contrast to charged fusion products interacting with background electrons and ions, for which the scattering is small either because $m_e/m_\alpha \sim 10^{-4}$ or

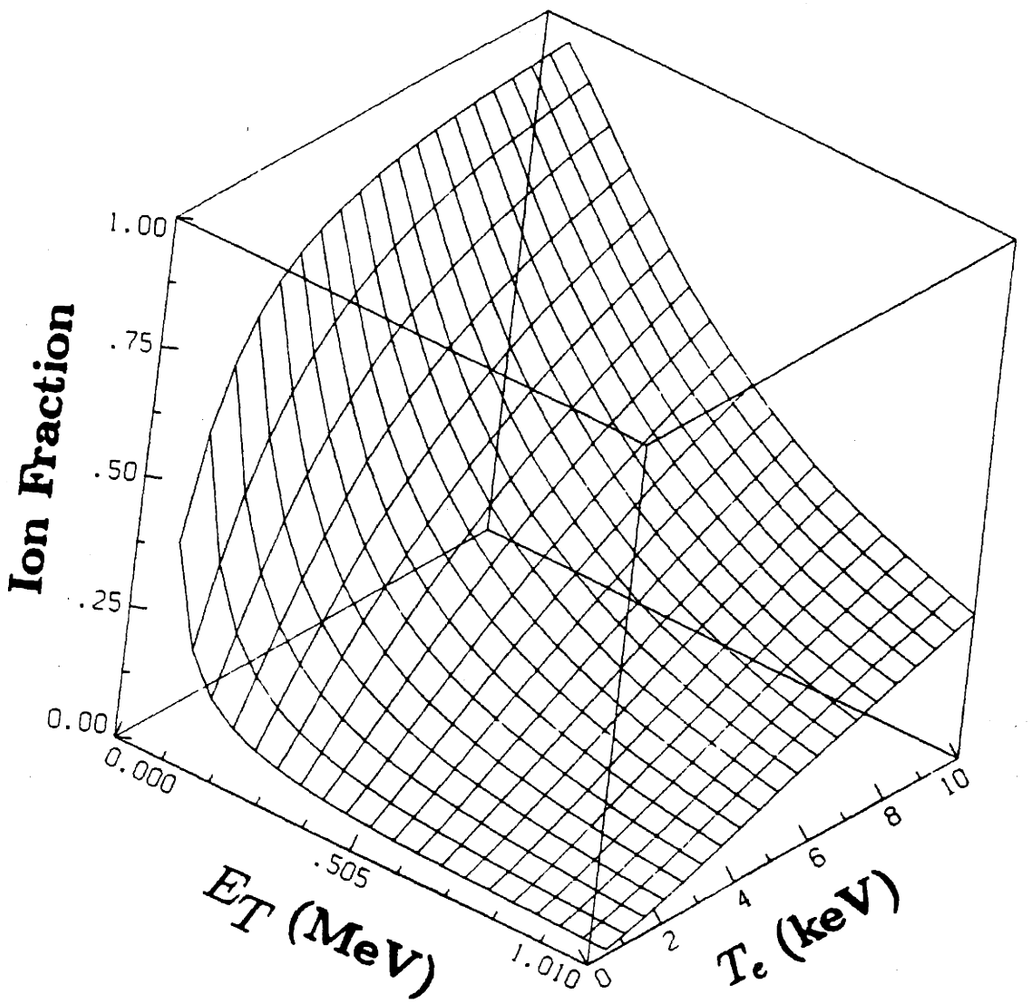

Figure 5-11: The relative fraction of 1.01 MeV triton - field ion (D) stopping as a function of the triton kinetic energy (E_T) and the plasma temperature ($T_e \sim T_i$). It can be seen that the ion contribution is more significant than the case of 3.5 MeV α stopping in D-T plasma.

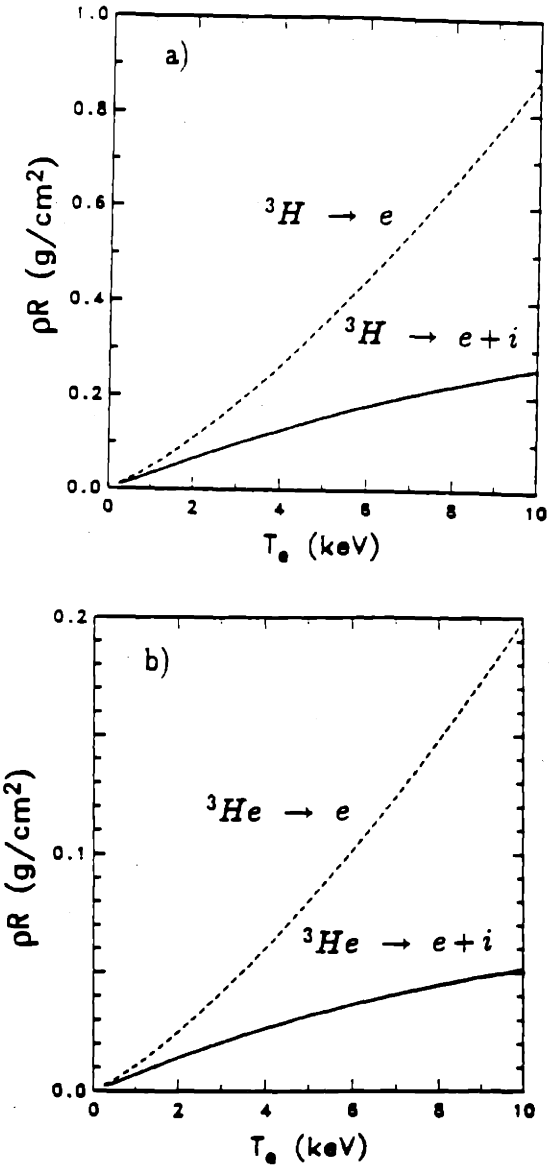

Figure 5-12: (a) ρR for 1.01 MeV ^{3}H interacting in a 6×10^{24}/cm^3 D plasma. The dashed line represents pure electron stopping (electron scattering is negligible). The solid line results from the cumulative effects of electron binary interactions, ion binary interactions (small-angle plus scattering), and ion collective oscillations. (b) ρR for 0.82 MeV ^{3}He interacting in a 6×10^{24}/cm^3 D plasma. The dashed line represents pure electron stopping (electron scattering is negligible). The solid line results from the cumulative effects of electron binary interactions, ion binary interactions (small-angle plus scattering), and ion collective oscillations.

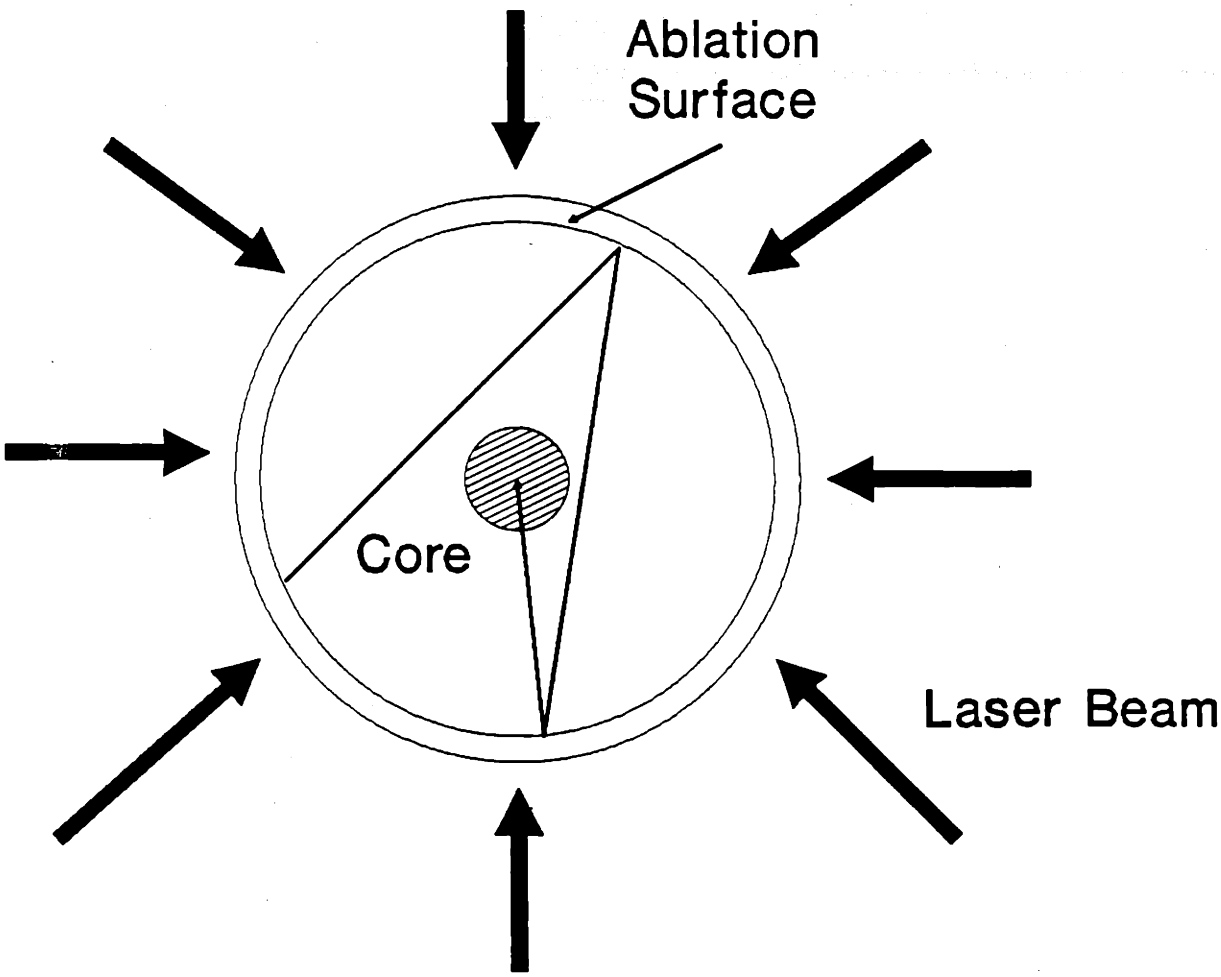

Figure 5-13: Schematic of preheating in ICF (direct drive scheme).

$ln\Lambda_b^{a/i} \sim 10$, scattering must be included in treating hot electrons interacting with cold electrons and ions. Such a situation arises just in the case of considering these hot corona electrons interacting with the cold core inside the pellet.

The dashed line in Fig.(5-14) shows ρR due only to small-angle binary collisions, which is the conventional calculation. The solid line includes as well large-angle scattering off electrons and ions plus the collective effects of the background electrons. As can be seen, these contributions are important.

5.4 The Fermi Degeneracy Pressure

As discussed before, the free electrons in a dense pellet plasma form a degenerate electron gas. The non-relativistic, degenerate equation of state can be derived from

$$PV = kT_e \int_0^\infty 4\pi V (\frac{2m_e}{h^2})^{3/2} E^{1/2} ln[e^{(E-E_F)/kT_e} + 1] dE \ . \qquad (5.23)$$

For the case of partial degeneracy (i.e. when $kT_e/E_F \gtrsim 1$), the total electron pressure can be expressed as

$$P \simeq n_e kT_e [1 + \frac{1}{2^{7/2}} \frac{n_e h^3}{(2\pi m_e kT_e)^{3/2}} - \bigcirc(\frac{1}{T_e^3}) \ldots .] \ . \qquad (5.24)$$

In the case of complete degeneracy ($kT/E_F \ll 1$), the total electron pressure can be expressed as

$$\begin{aligned} P &= \frac{2}{5}\frac{E_F^0}{V} + \frac{\pi^2}{6}\frac{k^2T_e^2}{E_F V} + ... \\ &= \frac{(3\pi^2)^{2/3}}{5m_e}(\frac{h}{2\pi})^2 n_e^{5/3} + (\frac{2\pi}{h})^2 \frac{m_e}{3}(\frac{\pi}{3})^{2/3} k^2 T_e^2 n_e^{1/3} + ... \end{aligned} \qquad (5.25)$$

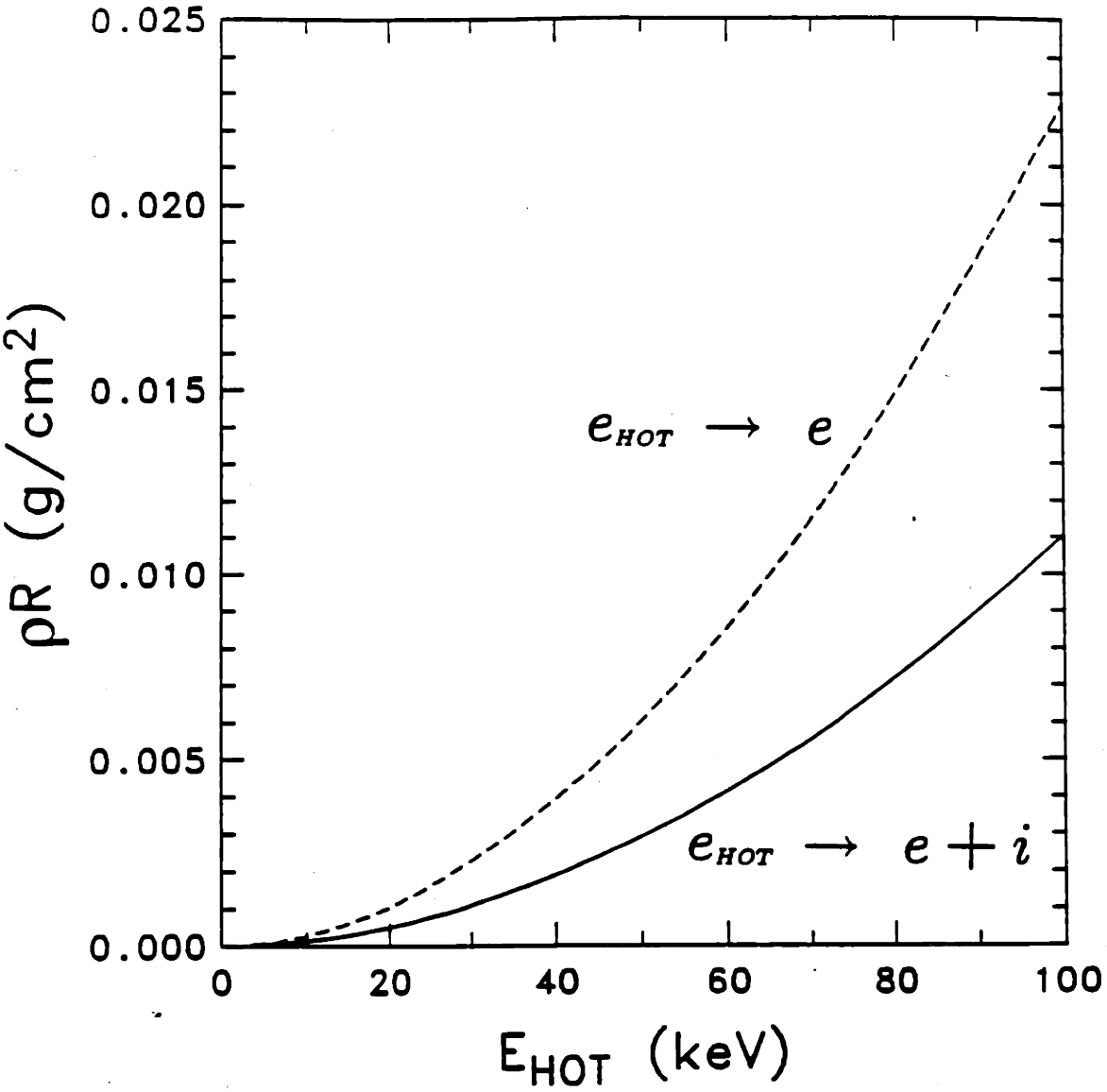

Figure 5-14: ρR for hot corona electrons interacting with a cold (core) D plasma ($n_e \sim 10^{23}/cm^3$ and $T_e \sim 50$ eV). The dashed curve shows the effects of pure small-angle binary collisions. The solid line results from the cumulative effects of electron small-angle collisions and large-angle scattering, electron collective oscillations, and large-angle ion scattering.

Table 5.3:
The electron pressure

	n_e (cm^{-3})	T_e (keV)	Total Pressure (atm.)	Fermi Degeneracy Contribution (%)
White Dwarf	$\simeq 10^{30}$	$\simeq 8.6$	$\simeq 2.3 \times 10^{17}$	$\gtrsim 99.9$
Solar Core	$\simeq 3.75 \times 10^{25}$	$\simeq 1.3$	$\simeq 7.90 \times 10^{10}$	$\lesssim 2$
ICF Pellet Fuel	5×10^{26}	0.1	$\simeq 6.7 \times 10^{11}$	$\gtrsim 90$
		0.5	$\simeq 7.0 \times 10^{11}$	$\simeq 56$
		1.0	$\simeq 9.5 \times 10^{11}$	$\simeq 31$
		5.0	$\simeq 4.1 \times 10^{12}$	$\simeq 3$
		10.0	$\simeq 8.0 \times 10^{12}$	$\lesssim 1$
		20.0	$\simeq 1.6 \times 10^{13}$	$\lesssim 0.5$

Note the strong dependence on the electron density in the first term of Eq.(5.25). This turns out to be the formula that has always been used to calculate the pressure of White Dwarf (almost completely degenerate; $n_e \simeq 10^{30} cm^{-3}$, $T_e \simeq 8.6$ keV).

Table 5.3 lists the calculated electron pressure for a few interesting cases using the above formulas. Note the relationship of the percentage contributions from Fermi degeneracy to the pressure as a function of electron density and temperature.

5.5 Summary

In summary, we have calculated the stopping powers and ρR of charged fusion products and hot electrons interacting with plasmas relevant to inertial confinement fusion. For the first time the effects of scattering, which limited previous calculations to upper limits[57, 66], have been properly treated. In addition, the important effects of ion stopping, electron quantum properties, and collective

plasma oscillations have also been included. We have seen that quantum effects are very important for the earlier dynamics of the pellet evolution, especially in the shifting of the effective degenerate electron velocity which greatly enhances the charged particle stopping powers and shortens the ranges. Ion stopping is found to be important for all charged fusion products. For hot electrons interacting with cold dense plasmas, the contributions of scattering and collective oscillations are significant.

Chapter 6

Heavy Ion Stopping Power in ICF Hohlraum Plasmas

Heavy ion stopping power is conceptually studied for hohlraum plasmas in inertial confinement fusion (ICF). We have found that classical kinetic theory can describe the ion energy loss in these high-electron-density plasmas if we include principal interaction mechanisms (i.e. both "dominant" and "non-dominant" contributions as discussed by Chandrasekhar[27]), and these contributions can be effectively included in the Coulomb logarithm of the stopping power. Also the restriction in the current theory for stopping power - - that the Coulomb logarithm must be comparable or greater than of order 10 - - is shown to be unduly restrictive. Furthermore the energy deposition of heavy ions is a sensitive function of the plasma electron temperature, even for high projectile energy, because the number density of free electrons in the hohlraum depends dynamically on the plasma temperature. This point is usually ignored because previous discussions are based on a constant free-electron-density model of plasma.

6.1 Introduction

In inertial confinement fusion (ICF) research, to achieve successful ignition and burn, the fuel pellet needs to be compressed and to implode spherically. The deviation that can be tolerated from the spherical symmetry is no larger than $1-2\%$[56, 76, 77, 78]. This stringent requirement, in fact, is extremely difficult to be achieved in pellet driven directly by heavy ions. Indirect drive heavy ion ICF, on the other hand, can easily satisfy this requirement because instead of directly illuminating the pellet, it makes use of uniform hohlraum thermal radiation to drive the pellet. Since the Stefan's law of black-body radiation is,

$$P = \sigma T_e^4 , \tag{6.1}$$

where P is the radiation power per unit area. For example, at the temperature $T_e \simeq 300$ eV, the thermal radiation flux is estimated to be $\sigma T_e^4 \sim 10^{15}$ W/cm^2, which has been determined to be sufficient for driving pellet implosion. In the past few years, heavy ion indirect drive inertial confinement fusion has been the most attractive scheme[56, 76]. Fig.(6-1) shows the schematic of heavy ion-hohlraum interactions. Consequently, the issue of heavy ion energy deposition in the hohlraum becomes an important issue, which basically relates to matters like stopping power, plasma heating efficiency, driver and target design etc. There are three media that heavy ions interact with - - solid, gas, and plasma - - as the target experiences a series of phase transitions during the course of energy deposition, i.e. solid $\rightarrow$ gas $\rightarrow$ partially ionized plasma.

Since it first appeared in the 1910's[58], the stopping power of charged particles in cold materials (solid and gas) has been extensively studied both theoretically and experimentally. Although there are four basic interactions between charged particles and matter, (i.e. the collisions, both inelastic and elastic, of particle with

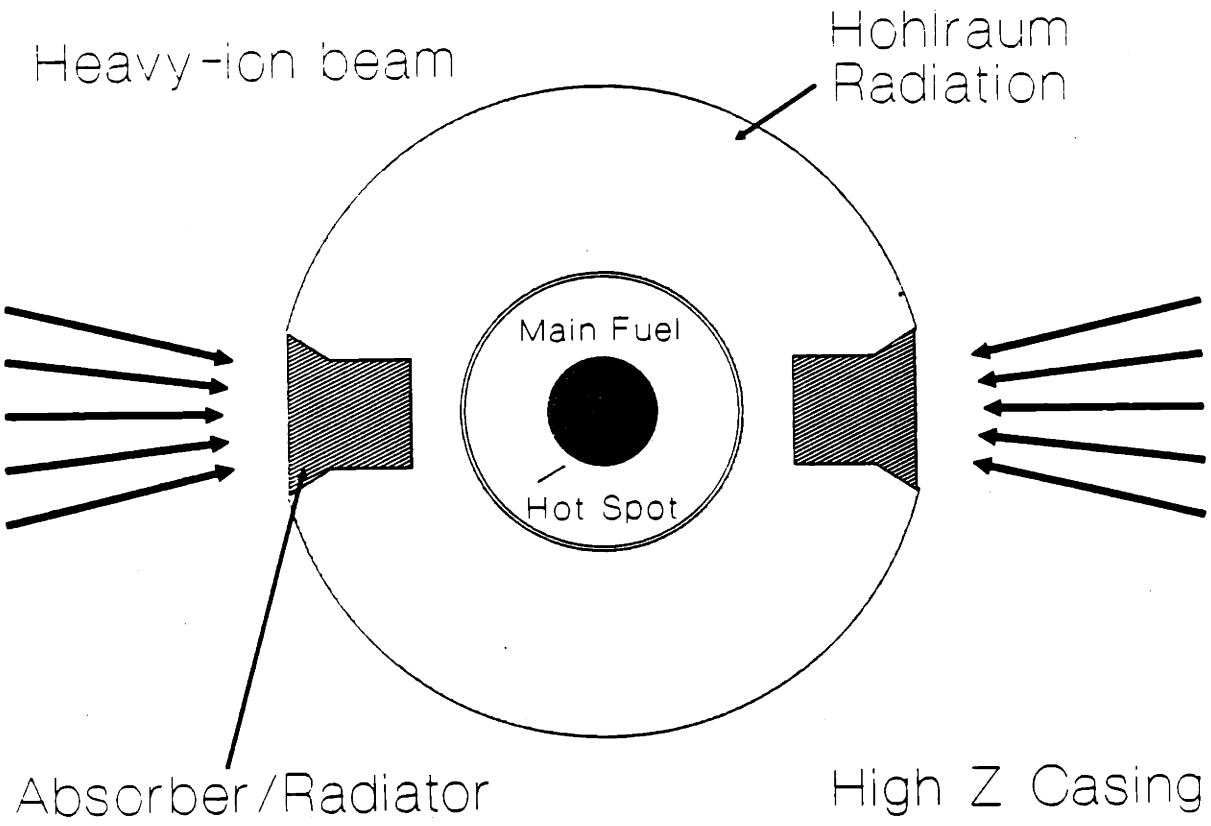

Figure 6-1: The Schematic of heavy-ion hohlraum interaction diagram.

atomic electrons and nuclei), the primary mechanisms of particle energy loss are the excitation and ionization of the atomic electrons. The Bethe theory, with some corrections such as relativistic effects, polarization, atomic shell effects,[57, 79] has been widely used for treating high-energy ion stopping. For low energy ions, the Lindhard-Scharff-Schiott model[80] provides a good descriptions. Additionly, Ziegler[81], Northecliffe and Schilling[82] have compiled extensive estimates of stopping power in various cold materials by interpolation and extrapolation from empirical data.

For a partially ionized plasma, both bound and free electrons as well as ions participate in the interactions with the charged particles. Their contributions can be calculated separately,

$$\frac{dE}{dx} = (\frac{dE}{dx})_{free} + (\frac{dE}{dx})_{bound} + (\frac{dE}{dx})_{ion} . \tag{6.2}$$

In the hohlraum plasmas, the contribution from the plasma ions is usually negligible because of the relative low plasma temperature. The heavy ion (i.e. the charged particle projectile) velocities are more comparable to the average thermal velocities of the free electrons at the typical hohlraum plasma temperature, and therefore most of the energy goes to the electrons.

In this chapter we will concentrate on discussing heavy ion stopping by free electrons. Some aspects of this issue, though often with simplifying assumptions, have been addressed through different approaches: 1) classical kinetic theory — by Nardi *et al.*[61], Mehlhorn[57], Brueckner *et al.*[83], and Karashima *et al.*[84] etc.; 2) quantum mechanical theory — by Dar *et al.*[85], Skupsky[59], Arista *et al.*[60], Maynard *et al.*[62], and Deutsch *et al.*[63] etc. This issue is quite subtle, however, due to a few unique features of the hohlraum plasma.

Table 6.1:
Typical parameters in ICF hohlraum plasmas

	ICF hohlraum plasmas
Electron temperature (T_e)	$\sim 1 - 1000$ eV
Electron density (n_e)	$\sim 10^{22} - 10^{24}$ cm^{-3}
Inter-electron distance (d_e)	$\sim 10^{-8} - 10^{-7}$ cm
Electron de Broglie length $(\bar{\lambda})$	$\sim 10^{-10} - 10^{-8}$ cm
Debye length (λ_D)	$\sim 10^{-7} - 10^{-8}$ cm
Coupling parameter (Γ)	$\sim 10^{-2} - 10^{-1}$
Plasma parameter $(n_e\lambda_D^3)$	$\sim 1 - 100$
Coulomb logarithm $(ln\Lambda_b)$†	$\sim 2 - 6$

† where the Coulomb logarithm refers to the binary interaction contributions only.

- hohlraum plasmas are typically solid-like plasmas with free electron densities similar to that of a highly conductive metals. However, because of the relative high temperature ($\sim$ 100 eV), hohlraum plasmas are typically moderately coupled plasmas and have Coulomb logarithm < 10.

- the evolution of hohlraum plasma parameters with respective to the variation of the plasma temperature requires a dynamic treatment. This point is ignored in previous treatments, i.e. a constant electron density has been assumed.

- most importantly, only a few related experiments have been carried out so far[86, 87, 88, 89], and the lack of experimental data makes precise theoretical prediction and simulation even more important.

6.2 Physical Modeling of ICF Hohlraum Plasma

In Table 6.1, some typical parameters of a practical high Z [in our calculations, gold (Z=79) is assumed] hohlraum plasma in heavy ion ICF are listed. Although they have solid-like densities, hohlraum plasmas are not identical to the free elec-

tron plasmas in metals because the electron temperature in hohlraum plasmas are usually much higher. The treatment is therefore not identical to that of Fermi's free electron gas model in metals. A phase diagram of the plasma condition based on the above criteria is shown in chapter 2 [Fig.(2-1)], which, together with the parameters in Table 6.1 can help us clarify the appropriate theory to describe hohlraum plasmas. The domain indicates that a hohlraum plasma is mostly in the regime of classical moderate coupled plasmas. Therefore, the classical gas approximation (Boltzmann statistics) based on kinetic theory, in principle, is appropriate to illustrate the physics of energy deposition in hohlraum plasmas.

In classical theory, there are basically two approaches: the dielectric response function theory; and the theory of binary interaction together with a simplified treatment of collective effects as a supplements. Physically, the former approach (dielectric response) depicts the plasma as a continuous medium. This medium responds to incident heavy ions by reacting through a medium-polarization-induced electric field. Brueckner *et al.*[83], as well as many others, have used this approach to treat plasmas that are partially ionized, which is similar to hohlraum plasmas. This approach provides a good description of plasmas with sufficiently low temperature such that the condition $v_i \gg v_e$ is always valid and the dielectric function, which is a function of the wave vector ($\mathbf{k}$) and frequency ($\omega = kv_e$), can be approximately treated as independent of k, i.e. $\epsilon(\mathbf{k},\omega) \simeq \epsilon(\omega)$[83, 84].

In contrast, the latter approach (binary + collective), however, gives a more transparent description of the stopping power and its evolution in a practical hohlraum plasma with a clear physical picture in each temperature regime, although some phenomenological constraints are involved. In this approach, the dominant mechanism by which charged particles interact with plasma electrons depends on the impact parameter, p. The physical picture is clearly defined by

dividing the impact parameter into 4 ranges in terms of the several characteristic lengths ($p_\perp$ – the impact parameter for 90° scattering, d_e – the mean interelectron spacing, and λ_D – Debye length),

$$\begin{cases} (1)\ \ 0 < p < \text{a few } \mathrm{p}_\perp \ \ - - - \text{large angle binary interaction;} \\ (2)\ \ \text{a few } \mathrm{p}_\perp < \mathrm{p} < \mathrm{d_e} \ \ - - - \text{small angle binary interaction;} \\ (3)\ \ d_e < p < \lambda_D \ \ - - - \text{many body interaction (multiple, unscreened);} \\ (4)\ \ \lambda_D < p < \infty \ \ - - - \text{collective plasma oscillations.} \end{cases} \tag{6.3}$$

Because the mean inter-electron spacing in hohlraum plasmas is of the same order or close to the Debye length, and the plasma parameter (number of electrons inside the Debye sphere) is not too big, we could actually neglect many body interactions.

We will address this heavy ion stopping based on binary interactions supplemented by collective effects. However, because hohlraum plasmas are typically moderately coupled plasmas and have Coulomb logarithm less than 10, the conventional classical kinetic theory (Fokker-Planck equation) is unjustified for treating these plasmas. Considering the unique features of hohlraum plasmas and the clarified physics, we will use the modified Fokker-Planck equation. The contributions from the so-called dominant term (small-angle binary interaction) and from all the nondominant terms, which are smaller than the dominant term by of order the Coulomb logarithm, will be included.

6.3 Heavy Ion Stopping in Hohlraum Plasmas

Suppose test particles having a distribution function f_t and density n_t are incident to the plasma in the hohlraum where the field particles have a distribution function f_f and density n_f. We also assume the condition that $n_t \ll n_f$ so that the interactions between the test particles can be neglected. Now we can apply the established model with the derived stopping power formulas to the hohlraum plasma. In the hohlraum, heavy ions stopping by plasma ions is always negligible. The heavy ion stopping power by free electrons for binary interactions is

$$(\frac{dE^{i/e}}{dx})_{\frac{p}{\lambda_D}\lesssim 1} = -\frac{(Z_{eff}e)^2}{v_i^2}\,\omega_{pe}^2\,G(x^{i/e})\,ln\Lambda_b\;; \tag{6.4}$$

and for collective oscillations is

$$(\frac{dE^{i/e}}{dx})_{\frac{p}{\lambda_D}\gtrsim 1} = -\frac{(Z_{eff}e)^2}{v_i^2}\,\omega_{pe}^2\,ln\Lambda_c\;. \tag{6.5}$$

Where $x^{i/e} = v_i^2/v_e^2$. The stopping power behaves differently for different values of $x^{i/e}$. Specifically, it is a measure of the importance of the contributions from binary and collective effects. Also these values correspond to the different charged particle energy regimes.

$$\begin{cases} x^{i/e} \gg 1 & \text{"}fast\text{" regime} \\ x^{i/e} \sim 1 & \text{"}intermediate\text{" regime} \\ x^{i/e} \ll 1 & \text{"}slow\text{" regime} \end{cases} \tag{6.6}$$

Therefore, the stopping power is an indirect function of the energy regime in terms of the temperature coupling parameter $[G(x^{i/e})]$ and Coulomb logarithm.

Table 6.2:
The energy regime ($x^{i/e}$) in ICF hohlraum plasma

T_e	$x^{i/e}$		
	1 MeV/amu	10 MeV/amu	100 MeV/amu
1 eV	5.45×10^2	5.45×10^3	5.45×10^4
10 eV	54.5	5.45×10^2	5.45×10^3
100 eV	5.45	54.5	5.45×10^2
1000 eV	5.45×10^{-1}	5.45	54.5

Table 6.2 gives the typical energy regimes ICF hohlraum conditions.

The typical values of the $x^{i/e}$ vary from much greater than 1 to of order 1 (only for the case of 1 MeV/amu and T_e=1000 eV), which corresponds to energy regimes that evolve from "fast" to "intermediate". We would discuss these significances in the following subsection.

6.3.1 Temperature Coupling Parameter $G(x^{i/e})$

Because of the mass ratio $m_e/m_i \sim 10^{-3}$, the second, third, and fourth terms in the coupling parameter $G(x^{i/e})$ are totally negligible. Physically, it means that the effects of large-angle scattering are not important. Therefore,

$$\begin{aligned} G(x^{i/e}) &= \mu(x^{i/e}) - \frac{m_e}{m_i}\{\frac{d\mu(x^{i/e})}{dx^{i/e}} - \frac{1}{ln\Lambda_b}[\mu(x^{i/e}) + \frac{d\mu(x^{i/e})}{dx^{i/e}}]\} \\ &\simeq \mu(x^{i/e}) \, . \end{aligned} \tag{6.7}$$

Furthermore, since $x^{i/e} \gg 1$,

$$G(x^{i/e}) \simeq 1 . \tag{6.8}$$

Due to this mass-ratio effect the contribution from the binary interactions and collective components can be effectively combined into a single Coulomb logarithm. It is generally true that for projectile-electron interaction[4, 29], the coupling parameter is $\simeq 1$ and the stopping power formula from the conventional kinetic theory is valid even though the Coulomb logarithm is less than 10 and any possible corrections is negligible (of course, this is not true for e-i, e-e, and i-i interactions). The widely-used restriction that the conventional stopping power is only valid for $ln\Lambda_b \gtrsim 10$ is therefore unduly restrictive for this specific case. Fig.(6-2) shows behaviors of this temperature coupling parameter, $G(x^{i/e})$, in ICF hohlraum plasmas.

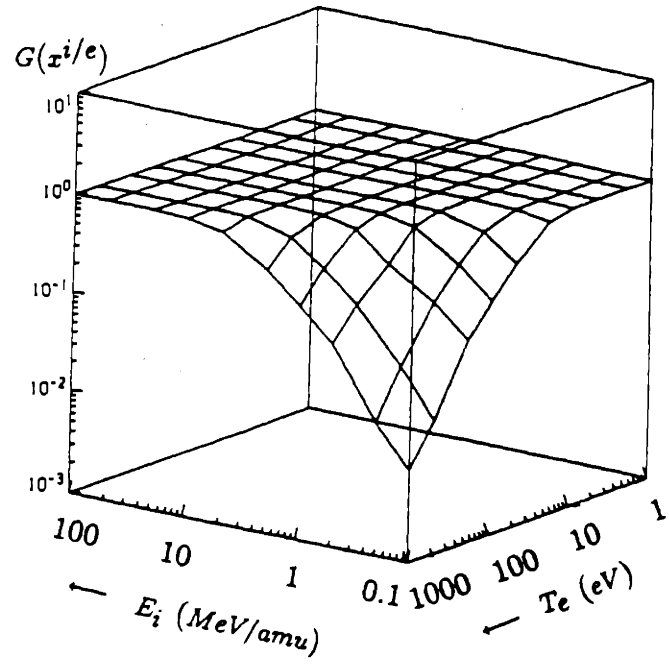

Figure 6-2: The behavior of the temperature coupling parameter, $G(x^{i/e})$, in a practical heavy ion (^{238}U) ICF hohlraum plasma (Au). While this parameter stay constant $[G(x^{i/e}) \simeq 1]$ within the "fast" regime, it significantly decreses in the "intermediate" regime. The physical interpretation is that in the "intermediate" regime, incident ions interact strongly with the plasma electrons due to ion projectile velocity being closer to the plasma electron thermal velocity.

By combining the stopping powers from contributions of binary interaction and collective effects, specifically for the case of heavy ion hohlraum plasma interactions, we obtain a unified formula

$$\begin{aligned} \frac{dE^{i/e}}{dx} &= \left(\frac{dE^{i/e}}{dx}\right)_{\frac{p}{\lambda_D} \lesssim 1} + \left(\frac{dE^{i/e}}{dx}\right)_{\frac{p}{\lambda_D} \gtrsim 1} \\ &= -\frac{(Z_{eff}e)^2}{v_i^2}\,\omega_{pe}^2\, ln\Lambda\ . \end{aligned} \tag{6.9}$$

Both binary interactions and collective effects are included into the Coulomb logarithm, which is defined in the next subsection. Within the "fast" regime, their relative contributions to the stopping power are distinguished by the magnitudes of the Coulomb logarithms.

6.3.2 Coulomb Logarithms

The variation of the Coulomb logarithm reflects the physics picture of the charged particle energy loss and the relative contributions from the two mechanisms - - binary interactions and collective effects. Within the "fast" regime the Coulomb logarithm is therefore the sum of the contributions from both binary interactions and excitation of collective plasma oscillations,

$$ln\Lambda \simeq ln\Lambda_b + ln\Lambda_c \ . \tag{6.10}$$

Figs.(6-3) and (6-4) show calculated values of $ln\Lambda_b$ and $ln\Lambda_c$ for different ion energies. One finds that in the "fast" regime, the contributions from both binary interactions and collective effects are significant; in the "intermediate" regime, however, the significance of collective effects largely reduced. Figs.(6-6) and (6-5) show the behaviors of the "total" Coulomb logarithm (binary + collective) as a function of the projectile kinetic energy for different plasma electron temperatures, and a function of the plasma electron temperature for different ion kinetic energies, respectively in a practical hohlraum plasma. Note that in the "fast" regime, the stopping is independent of the plasma electron temperature which can be seen by adding the two Coulomb logarithms together (assuming n_e is a constant).

$$\begin{aligned} ln\Lambda_b + ln\Lambda_c &\simeq ln\frac{\lambda_D}{p_\perp} + ln(1.123\sqrt{x^{i/e}}) \\ &\simeq ln(\frac{\Xi v_i}{\omega_{pe} p_\perp}) \end{aligned} \tag{6.11}$$

where Ξ is a number of order 1.

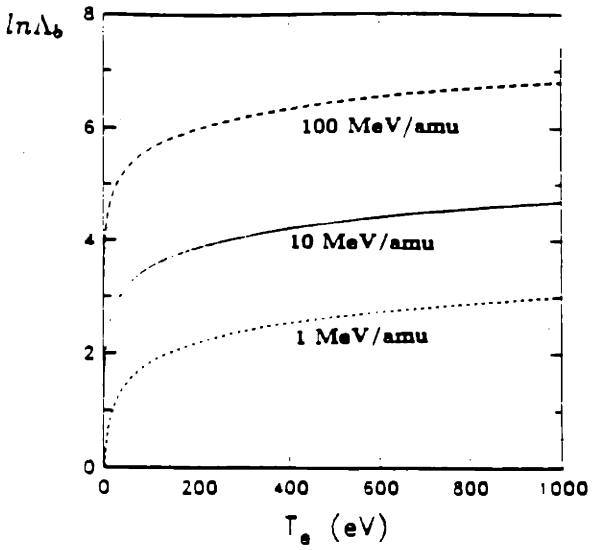

Figure 6-3: Contribution to the Coulomb logarithms from binary interactions (i.e. $ln\Lambda_b$) as a function of the plasma electron temperature for ion energy of 1, 10, 100 MeV/amu. In our calculations, we assumed ^{238}U projectile ions and a Au plasma.

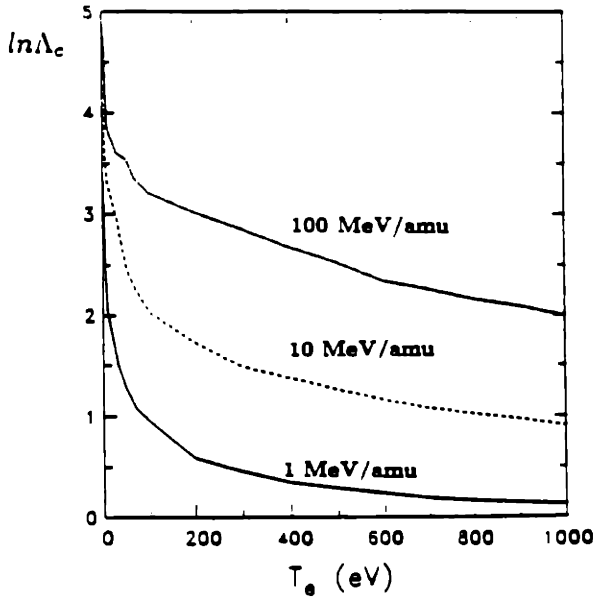

Figure 6-4: Contribution to the Coulomb logarithm from collective plasma oscillations (i.e. $ln\Lambda_c$) as a function of the plasma electron temperature in a practical hohlraum plasma ($T_e \lesssim 1$ keV). One finds that: for the case of E_i (projectile ion energy) =100 MeV/amu, the system always stays within the "fast" regime; for the cases of E_i=1 MeV/amu and 10 MeV/amu, the system varies from "fast" to "intermediate" regimes as T_e increases.

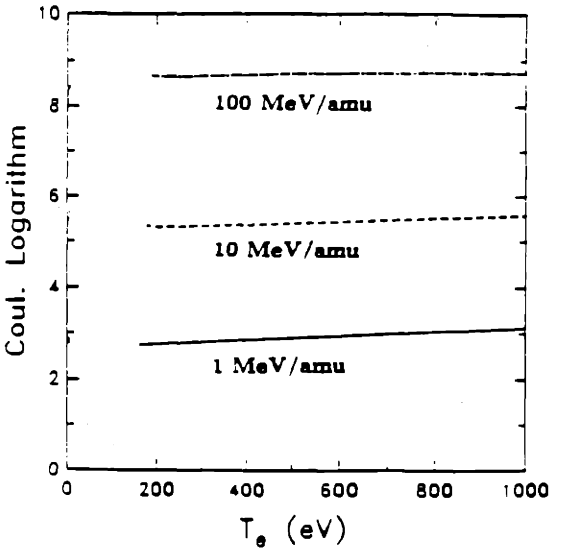

Figure 6-5: The behavior of the "total" Coulomb logarithms as a function of the hohlraum plasma electron temperature for three different projectile ion energies.

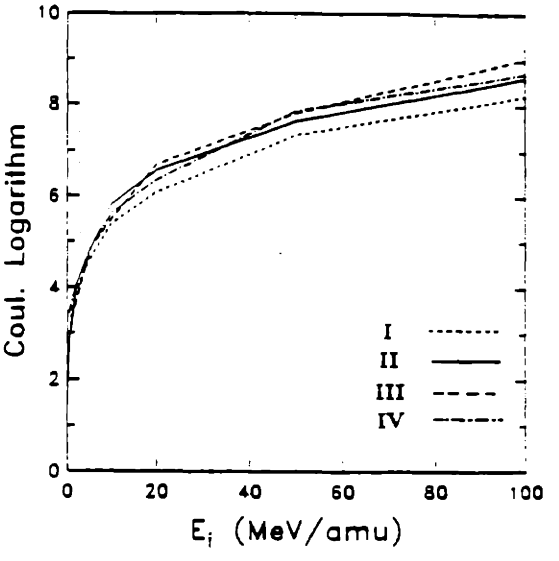

Figure 6-6: The behavior of the "total" Coulomb logarithm as a function of the projectile ion energy for different hohlraum plasma electron temperatures. The curves I, II, III, and IV corresponding to the cases where the plasma electron temperature T_e= 1, 10, 100, and 1000 eV, respectively. One finds that the Coulomb logarithm is insensitive to any finite temperature effect.

6.3.3 Effective Charge State of Heavy Ions

As appeared in the stopping power formula, the effective charge state of the projectile ion plays an important role in the stopping power ($\propto Z_{eff}^2$). Similar to the cases of stopping in solid and gas, when a projectile ion passes through a plasma the charge state of the ion fluctuates frequently because of the variation in the competition between the loss and capture of electrons. It is more difficult for a projectile ion to capture a free electron than a bound one because of the existence of an excess binding energy in the former case. Nardi *et al.*.[93] theoretically addressed this issue in detail by considering all possible ionization and recombination processes. An effective equilibrium charge state of the projectile ion is dynamically determined by solving a set of coupled equations. However, some semi-empirical scaling formulas are also available for this issue. In Fig.(6-7), the effective charge state is plotted as a function of the projectile energy for ^{238}U ion in gold target based on three scaling laws. Curve I is from Th. Peter's formula[94], which assumes that the target is a fully ionized plasma. Curve III follows Brown's and Moak's formula[95], which is for a cold solid target. Curve II, is a compromise between a fully ionized plasma and cold solid targets (i.e for a partially ionized plasma) and is based on Nikolaev's and Dmitriev's formula[96]

$$Z_{eff} = Z[1 + (\frac{Z^{0.45}v_0}{v_i})^{1/k_1})]^{-k_1} \tag{6.12}$$

where $v_0 = 3.6 \times 10^8$ cm/sec and $k_1 = 0.6$. Since the hohlraum plasmas are typically partially ionized, we chose this scaling formula to determine the effective equilibrium charge state in our calculations. From Fig.(6-7) it is found that the differences for these three curves are $\sim \pm 10\%$ when $E_i \simeq 10$ MeV/amu, but are negligible when $E_i \sim 100$ MeV/amu or higher.

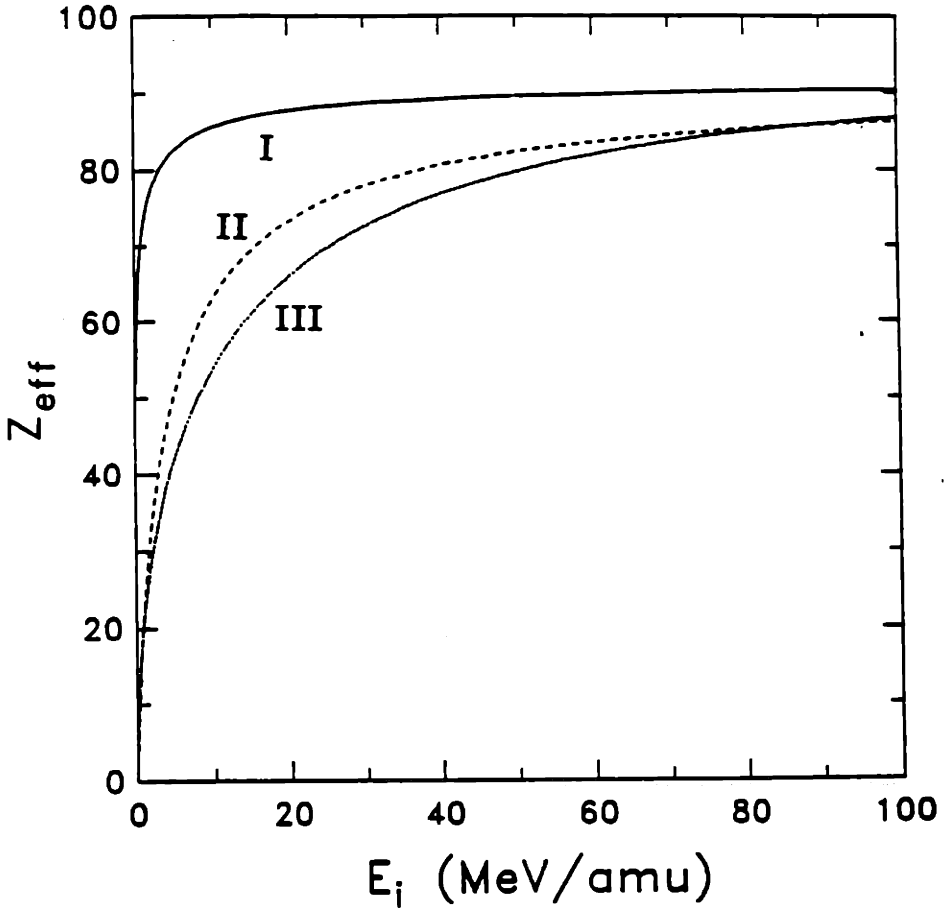

Figure 6-7: Variations of equilibrium effective charge states of a projectile ion (uranium Z=92) passing though into a target (gold, Z=79) as a function of the ion energy. Curves I, II, and III are calculated based on the scaling formulas from Th. Peter[94], Nikolaev and Dmitriev[96], Brown and Moak[95], respectively.

6.3.4 Finite Temperature Effects of the Stopping Power

Hitherto most of the workers assumed that the electron density is constant during the period of energy deposition and the effect of plasma temperature evolution is only included in the Coulomb logarithm. Because of the insensitivity of the Coulomb logarithm, this temperature effect only appears at relatively low projectile energies and becomes totally negligible at higher projectile energies in the stopping power of the heavy ions in ICF[63]. This assumption is incorrect and should not be applied in calculating the stopping power in a practical hohlraum plasma because the free electron density in the hohlraum is a function of the plasma electron temperature, which can be determined in terms of the Saha equation. Consequently, in addition to the weak temperature effects in the Coulomb logarithm and in the temperature coupling factor $G(x^{i/e})$, one finds the following direct relation between the stopping power and the plasma electron temperature which is more sensitive,

$$\frac{dE^{i/e}}{dx} \propto \omega_{pe}^2 \propto n_e \propto T_e^{3/2} e^{-U/T_e} \tag{6.13}$$

where U is the ionization energy of the atom.

6.4 Comparison with Dielectric Response Approach

In the dielectric response approach, following Lindhard[97], the stopping power formula evaluated based on the physical phenomenon that a charged particle moving through a plasma polarizes the medium around trajectory, thus introducing a local induced electric field. It is this induced field that reacts with the charged particle and causes slowing down and energy loss. In other words, the dielectric

response approach describes the linear response of the electrons in a plasma. The stopping power is then defined[59]

$$\frac{dE}{dx} = \frac{Z_t e}{v_t}\mathbf{v}\cdot\mathbf{E}_{ind} \,. \tag{6.14}$$

This induced electric field is related to the dielectric response function of the plasma through a Fourier transform, and therefore the stopping power is given by[11, 12]

$$\frac{dE}{dx} = \frac{Z_t^2 e^2}{2\pi^2 v_t}\int d\mathbf{k}\frac{\mathbf{k}\cdot\mathbf{v}}{k^2} Im\frac{1}{\epsilon(k,\mathbf{k}\cdot\mathbf{v})} \,, \tag{6.15}$$

where $\epsilon(k,\mathbf{k}\cdot\mathbf{v})$ is the longitudinal dielectric response function which depends on both frequency and wave number. It is usually convenient to introduce a dimensionless quantity called the stopping number, L, and the above formula can be written as

$$\begin{aligned}\frac{dE}{dx} &= -\frac{4\pi Z_t^2 Z_f^2 e^4}{m_f v_t^2} n_f L \\ &= -\frac{(Z_t e)^2}{v_t^2}\omega_{pf}^2 L \,,\end{aligned} \tag{6.16}$$

where the stopping number is defined as

$$L = -\frac{m_f v_t}{n_f Z_f^2 e^2}\int \frac{d\mathbf{k}}{(2\pi)^3}\frac{\mathbf{k}\cdot\mathbf{v}}{k^2} Im\frac{1}{\epsilon(k,\mathbf{k}\cdot\mathbf{v})} \,. \tag{6.17}$$

Using the method of random-phase-approximation (RPA), which originates from treating totally degenerate plasmas, the dielectric function for nondegenerate classical case is determined to be

$$\epsilon(k,\mathbf{k}\cdot\mathbf{v}) = 1 + \sum\frac{4\pi Z_f^2 e^2}{m_f k^2}\int d\mathbf{v}\frac{\mathbf{k}\cdot\frac{\partial f}{\partial \mathbf{v}}}{\omega - \mathbf{k}\cdot\mathbf{v} + i\delta} \,, \tag{6.18}$$

where $i\delta$ is an infinitesimal quantity which indicates how to treat the pole of the integral.

Considerable work have been carried out to calculate this integral the dielectric function and the stopping number. Specifically, for heavy charged particle stopping in hohlraum plasmas, since $x^{i/e} \gg 1$, the stopping number is asymptotically estimated at some limits to generate

$$L = ln(\frac{1.123 m_e v_t^2}{\hbar\omega_{pe}}) , \tag{6.19}$$

thus giving an expression for the stopping power equivalent to Eq.(6.9) that we obtained from considering the binary interactions supplemented by collective effects. It is also called the Bethe stopping number. Compared to the standard Bethe formula for the cold target, the mean ionization potential ($\bar{I}$) of the cold target has been replaced by the excitation energy of the plasma wave ($\hbar\omega_{pe}$). Typically, $\hbar\omega_{pe}$ is much smaller than $\bar{I}$. [For example, for a Au plasma of density 0.193 g/cm^3, one finds $\hbar\omega_{pe} \simeq 7.4$ eV, however, for a cold Au target, $\bar{I} \simeq 800$ eV (here the effective Z for the Au plasma has been assumed to be about 68.7, $\bar{I} = kZ$ and k is the empirical constant of about 11.5 eV)].

Fig.(6-8) compares the stopping power of a proton beam in a gold plasma based on both binary interaction plus collective effects and that calculated from the dielectric response function approach. A plasma density of 0.193 g/cm^3, electron temperature of T_e=1 keV, and the average ionization degree Z=68.7 are assumed. One finds that when the proton energy is relative large (i.e. $v_p \gg v_{the}$), the two approaches give essentially the same results.

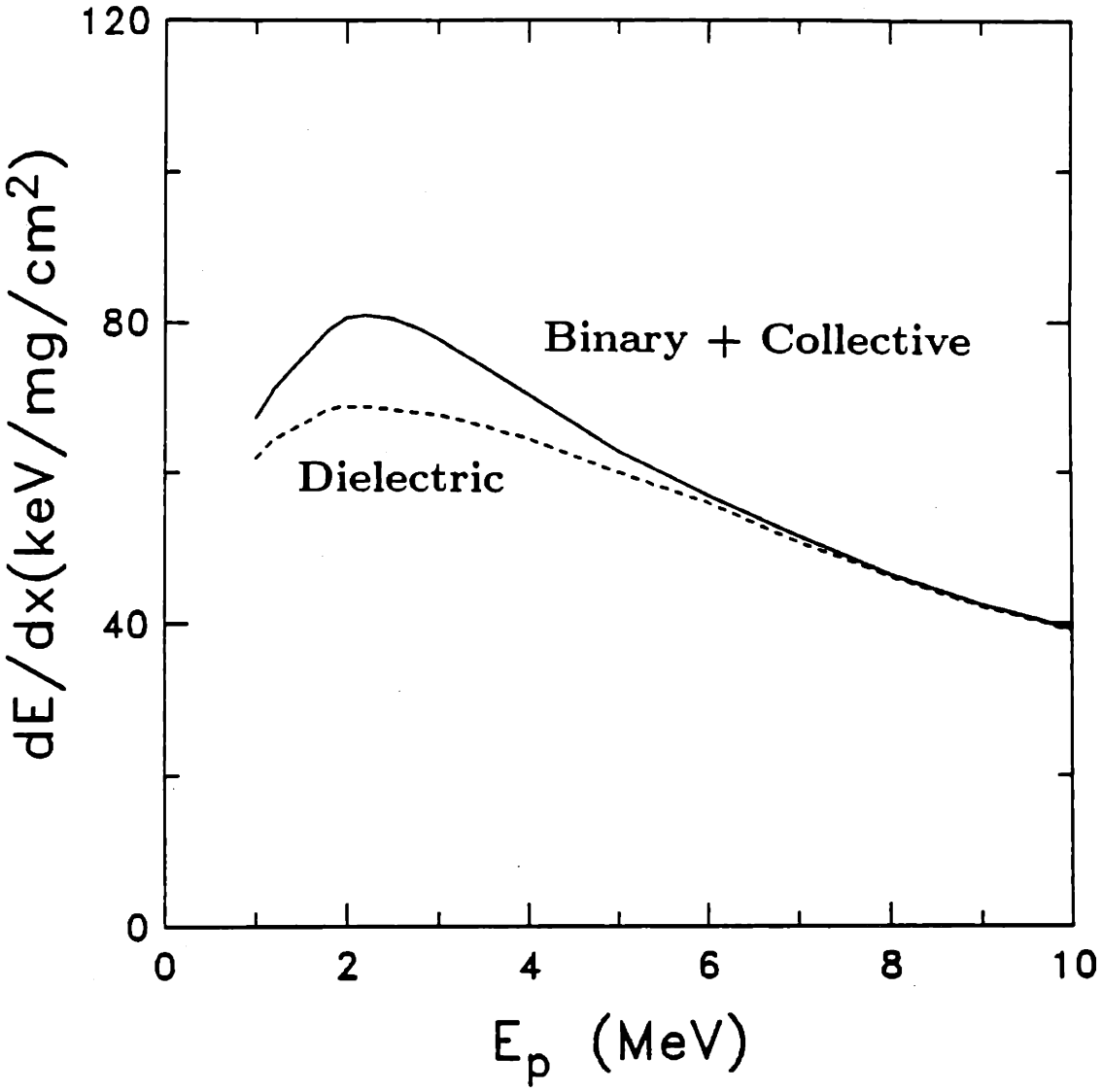

Figure 6-8: Comparison of proton stopping power (dE/dx) from dielectric response approach to that from binary interaction plus collective effects. When proton energy is relative large (i.e. $v_p \gg v_{the}$), the two are essentially the same.

6.5 Summary

As a result of the above discussion, we conclude that stopping power based on classical binary interactions and excitations due to collective plasma oscillations is adequate for heavy-ion ICF hohlraum plasmas. Most important, it is justified that the restriction that requires the Coulomb logarithm to be much greater than 10 is not necessary for using the conventional stopping power formula to treat heavy ion stopping in hohlraum plasmas and any correction is negligible. In addition, the evolution of the stopping power must be considered as a function of the plasma density. The finite temperature effect is significant for heavy-ion stopping in a piratical hohlraum plasma even for very high energy ions. Finally, we have compared the binary and dielectric response approaches for treating heavy ion interacting with hohlraum plasmas and found that they are essentially the same in this regime. However the binary interaction approach is much simpler and physical transparent.

Chapter 7

Introduction to Laboratory X-Ray Generation and Detection

7.1 Motivation

To perform x-ray diagnostics in plasma physics, various basic laboratory techniques of x-ray generation and detection are essential. For characterizing x-ray detectors and optics, and measuring x-ray filter transmissions, a high-intensity, selectable-wavelength source is often desirable. A conventional electron-beam x-ray source often emits significant thick-target bremsstrahlung because of the $1/m_e$ dependence in the differential radiative cross section. Such sources typically exhibit characteristic lines superimposed on a continuum. One method of avoiding this problem is to utilize filters, often of the same Z as the target, to selectively reduce the continuum [99, 141]. Unfortunately, this technique will significantly reduce the intensity of the desired line radiations. Futhermore, most commercially available x-ray tubes only provide slightly harder x rays [$\gtrsim$ 4 keV (Ti K line, for example)], because the tube window (usually made by mica) doesn't let lower energy x rays penetrate. This problem prevents the applications of these x-ray sources from the fields of ultra soft x ray ($\lesssim$ 3 keV). To eliminate these problems, and

for other reasons, we recently comparatively investigated the issues of x-ray generation and detection. Specifically, we have developed two charged-particle beam x-ray sources, which, as will be presented in the subsequent charpters, contribute to both further advancing the laboratory x-ray techniques and understandings. In this chapter, we will briefly review the fundamental knowledges of x-ray generation and detection.

7.2 Physical Model of the X-Ray Generation

One of the major consequences resulting from a charged particle depositing its kinetic energy into a target is the emission of x rays. This phenomenon is observed through the x-ray spectrum where characteristic x-ray lines are superimposed on a background continuum. It is well known there are two kinds of x rays: discrete line radiation and continuous bremsstrahlung.

Discrete line radiation results from the relaxation of orbital electrons. No matter what ionization or excitation process causes a vacancy in the inner-shell of an atom, it will be reoccupied within an order of magnitude of 10^{-16} seconds by an outer-shell electron with the resulted emission of either Auger electrons or characteristic x rays, or both[105, 125]. The bremsstrahlung comes from the acceleration or deceleration of charged particles because of the Coulomb interactions, or in other words, from the deflection of the bombarding particle in the Coulomb field of a nucleus (bremsstrahlung caused by target electron is negligible in the non-relativistic regime).

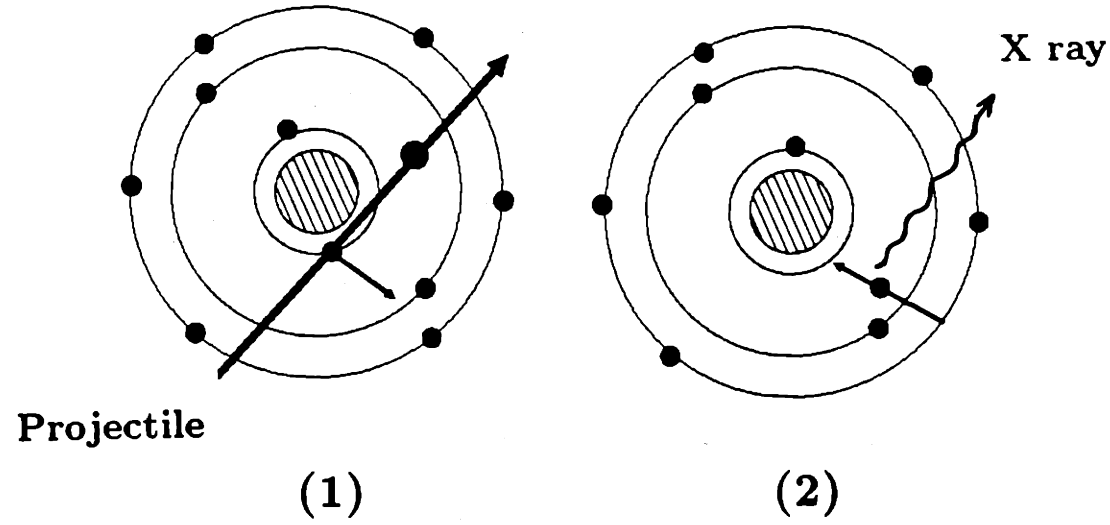

Figure 7-1: Schematic of discrete x-ray generation process. (1) An inner shell vacancy is created by a projectile. (2) An x ray is emitted due to the relaxation of outer shell electron.

7.2.1 Discrete Line Emission.

As indicated in Fig.(7-1), after an inner-shell electron of the atom in the target is ejected by a charged particle, an outer-shell electron reoccupies the resulting vacancy.

The energy of the characteristic x ray emitted is equal to the energy difference between the inner and outer shells. In accordance with quantum mechanics, the transition between different shells and subshells is characterized by the principal quantum number, n, and the orbital angular quantum number, l. Of the two shells involved, for example, Fig.(7-2) denotes x rays of different n (K, L, M, N, . . .) and, l, (α, β ,γ . . .). The energy distribution of some main K, L,and M x rays are displayed in Fig.(7-3).

Consider a rough model (degenerate) in which only the principal quantum numbers are involved in the transitions (i.e. shell-shell transitions). The x-ray energy produced between n_2 and n_1 transition is calculated as[102],

$$\Delta E_{n_1,n_2} = R_Y Z^2 [\frac{1}{n_2^2} - \frac{1}{n_1^2}] , \tag{7.1}$$

where R_Y is the Rydberg constant in energy unit. It is shown that the x-ray energy is approximately proportional to the square of the target atomic number, Z^2. The typical x-ray spectra of K , L , and M x rays for some elements are given in Fig.(7-4)

7.2.2 Continuous X-Ray Emission

As implied by the classical Larmor's formula, a charged projectile will emit electromagnetic radiation when its speed or direction changes due to Coulomb interaction with the target electric field. This electromagnetic radiation is called bremsstrahlung[70, 79]. Because the initial and the final states of the projectile are free states, as shown in Fig.(7-5), the bremsstrahlung energy distribution is continuous from zero right up to the projectile kinetic energy, i.e.

$$(h\nu)_{max} = \frac{1}{2} M v^2 . \tag{7.2}$$

In addition, since the acceleration of the projectile is overwhelmingly produced by the target nucleus, the intensity of the bremsstrahlung is proportional to the square of the target atomic number and inversely proportional to the square of the mass of the projectile.

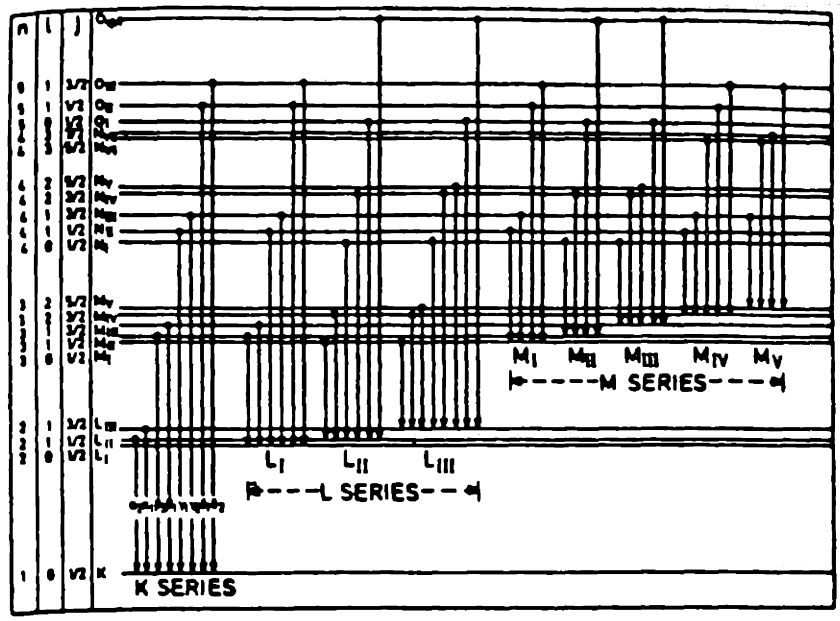

Figure 7-2: Atomic energy-level diagram for $K-$, $L-$, and M-shell transitions[103].

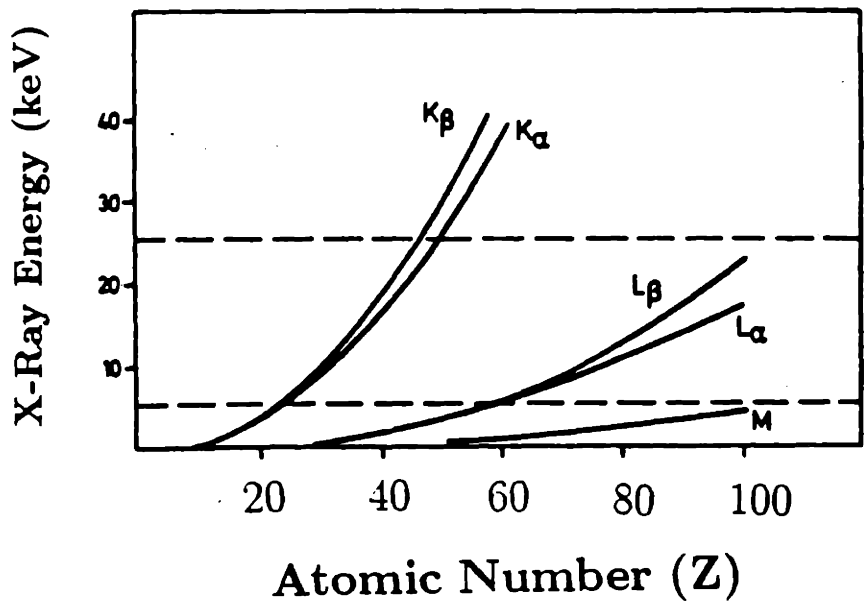

Figure 7-3: The plot of x-ray energies for some of main K, L, and M x rays as a function of the target atomic number Z[103]. One sees that the K x-ray energies roughly proportional to the Z^2. However, because of the effects of inner-shell shielding, as shown in this diagram, energies of L, especially M x rays are depicted far off from the Z^2 scaling.

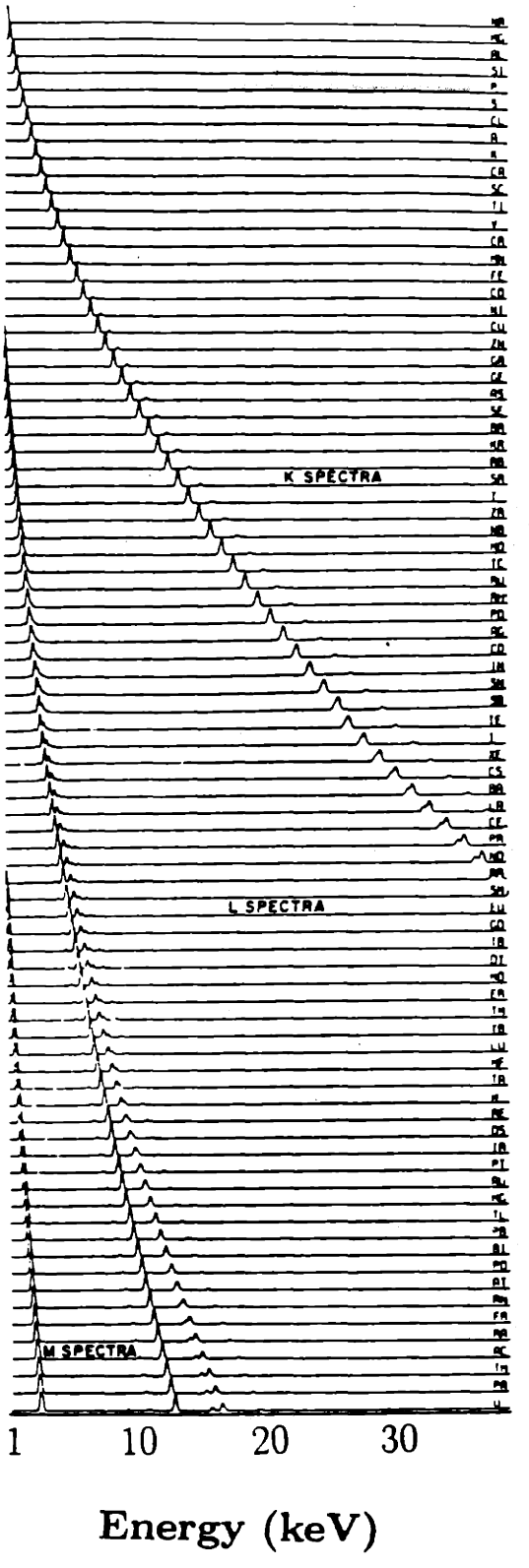

Figure 7-4: The plot of measured Si(Li) characteristic x-ray energy spectra of various elements[104].

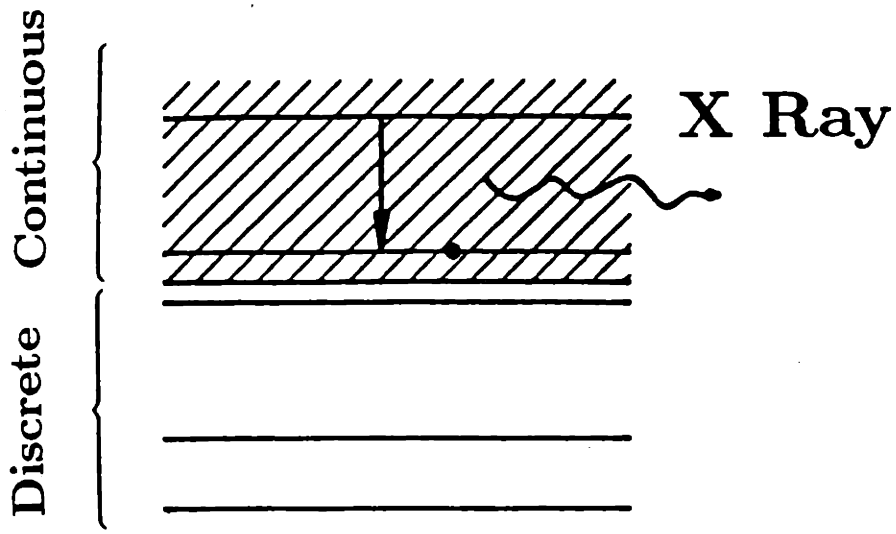

Figure 7-5: The energy diagram of the atomic process for bremsstrahlung.

$$\text{Intensity} \quad \propto \quad a^2 \sim \frac{z^2 Z^2}{M^2} e^4 \,, \tag{7.3}$$

where a is the acceleration of the projectile, z (M) is the charge state (mass) of the projectile. Therefore, the bremsstrahlung radiation produced by a heavy charged particle (proton, α's . . .) is only of order a part in 1 million of that produced by an electron at the same velocity. It is important to note that only the classical case is considered here; however, when the condition $\alpha Z/\beta \ll 1$ is met ($\beta = v^2/c^2$ and $\alpha = 1/137$ is the fine structure factor), quantum mechanical theory of bremsstrahlung must be used. In addition, when the projectile is so energetic that relativistic effects need to be taken into account, bremsstrahlung produced by target electrons will become significant.

Table 7.1:
Coefficients for K- and L-shell fluorescence yields[107]

	K-line	L-line
B_0	$(3.70 \pm 0.52) \times 10^{-2}$	0.17765
B_1	$(3.112 \pm 0.044) \times 10^{-2}$	2.98937×10^{-3}
B_2	$(5.44 \pm 0.11) \times 10^{-5}$	8.91297×10^{-5}
B_3	$-(1.25 \pm 0.07) \times 10^{-6}$	-2.67184×10^{-7}

7.2.3 Fluorescence Yield

The probability of x-ray production in the de-excitation process is called the fluorescence yield[106, 125] (specifically, for example, the K-shell fluorescence yield refers to the probability of K-shell x-ray production). Another alternative for de-excitation is the emission of Auger electrons whose energy is dissipated in lattice oscillations. For K- and L-shell fluorescence yields, a rigorous solution is provided by the Dirac-Hartree-Slater treatment of the bound electron wavefunction[125]. However, there exists a simple semi-empirical formula for the fluorescence yield, ω_f $(0 \leq \omega_f \leq 1)$, as a function of the target atomic number Z[107],

$$(\frac{\omega_f}{1-\omega_f})^{1/4} = \sum_{i=0}^{3} B_i Z^i \ , \tag{7.4}$$

where the coefficients, B_i, are given in Table 7.1.

7.3 Charged Particle Stopping Power in Solid Material Targets

As discussed in the preceding section, x rays (both discrete and continuum) are generated from Coulomb interactions between an incident charged particle and

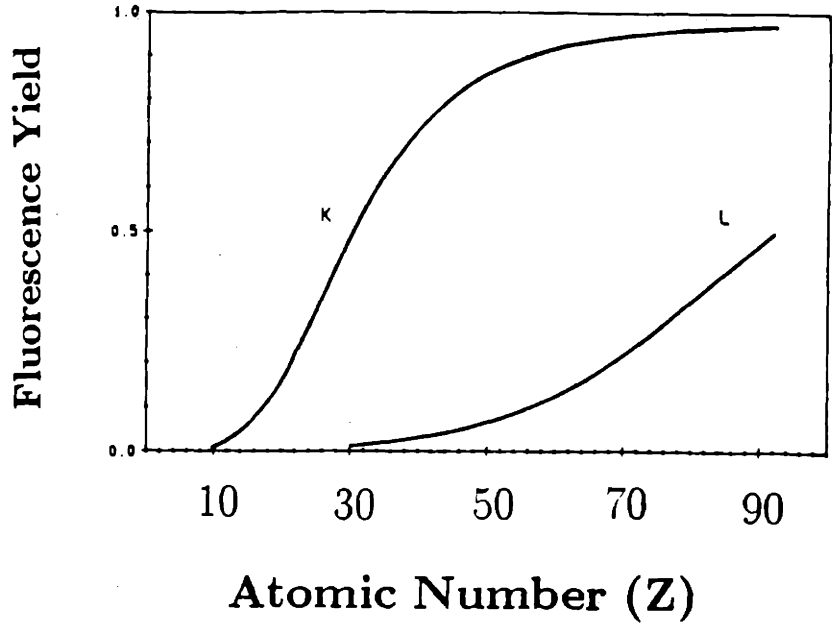

Figure 7-6: The fluorescence yields of K- and L-shell as a function of the target atomic number, Z[125].

the atomic electrons (discrete) and primarily the nucleus (continuum). In general, four fundamental interacting mechanisms are involved in the interaction between the projectile and the target[79]: (1) inelastic collisions with the atomic electrons; (2) inelastic collisions with the nucleus; (3) elastic collisions with the atomic electrons; and (4) elastic collisions with the nucleus. However, as a charged projectile travels through a solid material, the dominant interaction will be with the atomic electrons. This can be justified from the following arguments:

- The velocity of the projectile is more matched with the orbit velocities of the atomic electrons. The atomic nuclei, on the other hand, are relatively stationary.

Discrete line emissions result from inelastic collisions between the charged particle and the atomic electrons, and the continuous bremsstrahlung comes primarily from inelastic collisions between the charged particle and atomic nuclei. Similar to its interaction with plasmas, the charged particle interacts with solid material with two basic consequences - - kinetic energy loss and angular deflection.

The charged projectile finally stops after traveling a finite distance. The stopping power and the range depend on the type and energy of the projectile charged particle, and on the target material.

7.3.1 Heavy Particle Projectile Stopping

(1) Bethe Formula for High Energy Projectile.

For treating heavy particle stopping in solid material, the Bethe formula[79] provides a precise description for the cases of high energy projectile (i.e the ratio of the projectile velocity to the orbital velocity of the atomic electron is much greater than unity). It is also assumed in this model that the projectile has nearly a straight trajectory. Specifically, the Bethe formula, with some corrections accounting for relativistic effects, polarization, and atomic shell shielding, is given as follows[79, 57]

$$\frac{dE}{dx} = -\frac{4\pi z^2 e^4}{m_e v^2} NZ[ln(\frac{2m_e v^2}{I}) - ln(1-\beta^2) - \beta^2 - \sum_i \frac{C_i}{Z} - \frac{\delta}{2}] \quad (7.5)$$

where, I is the average ionization energy, $\sum_i C_i/Z$ is the sum of the effects of shell corrections, and δ is the correction term for polarization effect, and the relativistic effect is reflected by the terms of the parameter β $(=v/c)$. However, the Bethe formula is not appropriate for treating the case of low energy projectile interacting with a cold target, even if some further corrections are added. In fact, it can be seen that if we ignore these corrections which are small, therefore, when $2m_e v^2 \leq I$, the Coulomb logarithm becomes zero or negative that the stopping power formula turns out to be singular.

(2) Linhard-Scharff-Schiott (LSS) Model for Low Energy Projectile.

The LSS model is based on the Thomas-Fermi quantum mechanical description of electron clouds of projectile and target nucleus. In addition to the effects of ionization and excitation, the effects of elastic Coulomb collisions between the projectile and the target nucleus have also been taken into account (i.e. nuclear stopping). The stopping power formula is given by[80, 57]

$$\frac{dE}{dx} = \frac{0.0793 z^{2/3} Z^{1/2} (1+A)^{3/2}}{(z^{2/3}+Z^{2/3})^{3/4} A_2} \sqrt{\frac{(1+A) z Z e^2}{1.6 \times 10^{-9} A a}} \frac{4\pi A N a^2}{(1+A)^2 \times 10^4} \sqrt{E} \quad (7.6)$$

where $A = A_2/A_1$, and A_1 (A_2) is the atomic weight of the projectile (target atom); N is the target number density; $a = 0.4683(z^{2/3} + Z^{2/3})^{-1/2} \times 10^{-8}$. This model has been proven to provide an appropriate description of stopping power in the low projectile energy regime[57].

(3) Ziegler's Empirical Formula.

Ziegler's stopping power formula is derived by making use of the methods of interpolation and extrapolation, and is based on an extensive pool of experimental data. It has the form[81]

$$\frac{dE}{dx} = \rho \frac{S_L S_H}{S_L + S_H} \frac{602.22}{A_Z} , \quad (7.7)$$

where

$$S_L = aE^b + cE^d ; \quad (7.8)$$

and

$$S_H = \frac{e}{E^f} ln(\frac{g}{E} + hE) . \quad (7.9)$$

The constants a, b, c, d, e, f, g, and h for various elements are all derived from the empirical data; A_Z is the atomic weight of the target; and ρ is the target density. Ziegler claimed[81, 125] that this formula is quite accurate for describing the stopping power of projectile proton with energies between 25 keV and 10 MeV.

7.3.2 Electron Projectile Stopping

In contrast with the case of heavy charged particle stopping, an electron projectile obviously, having the same mass as an target atomic electron, suffers tremendous scattering with large angular deflection. As a result, its track becomes so convoluted that the penetration depth becomes significantly smaller than the actual traveled path length. The energy lose of an electron per unit path length is then written[108],

$$\frac{dE}{dx} = -\frac{4\pi e^4}{m_e v^2} NZ\{ln(\frac{\beta\gamma\sqrt{\gamma-1}m_e c^2}{I}) + \frac{1}{\gamma^2}[\frac{(\gamma-1)^2}{8} + 1 - (2\gamma^2+2\gamma-1)ln2]\}\ , \tag{7.10}$$

where $\gamma = 1/\sqrt{1-\beta^2}$.

7.4 Ionization of Inner-Shell Electrons due to Heavy-Ion Projectile-Target Interaction.

Historically, three theoretical approaches based on the definitive projectile-target interaction physics have been developed to model the inner-shell electron ionization process. They are[125], chronologically, the plane-wave Born approximation, (PWBA), the impulse model (also called Binary Encounter Approximation, BEA), and the most advanced of all, the ECPSSR theory (the meaning of this acronym

are discussed latter). Roughly, the PWBA and BEA are only high-energy approximations and are, therefore, only appropriate for treating the case where the projectile energy is greater than the binding energies of the inner-shell target electrons. The ECPSSR model, however, is more generalized and precise. In addition, it is generally true that the corresponding classical forms of these models are also justified in treating the cases when the de Broglie wavelength of the projectile is smaller than the characteristic scale length, $d = zZe^2/Mv^2$.

7.4.1 Plane-Wave Born Approximation (PWBA).

The plane-wave Born approximation is a semi-classical model which employs perturbation theory in treating, for a Coulomb interaction, the transition from an initial state (plane-wave projectile and bound atomic electron) to a final state (plane-wave projectile and free electron). In this approximation, the distortion to the projectile wave function, due to the atomic electron which is removed from the ground state, may be neglected. Based on these physical arguments, the differential cross section in the Born approximation in CM system is given by[109]

$$d\sigma_{n',n} = 8\pi Z^2 (\frac{e^2}{\hbar v})^2 \frac{dq}{q} \mid \int \psi^*_{n'}(\mathbf{r}) e^{i\mathbf{q}\cdot\mathbf{r}} \psi_n(\mathbf{r}) d\mathbf{r} \mid^2 , \tag{7.11}$$

where $\mathbf{q} = (\mathbf{p} - \mathbf{p}')/\hbar$ is the change of the momentum of the projectile. The electrons are represented by non-relativistic wave functions which are determined through the Schrödinger equation. For example, for the n^{th}-shell (n=1, 2, 3, ... means $K-$, $L-$, $M-$, ... shell), the wave function, ψ_n, is determined in

$$-\frac{\hbar^2}{2m}\nabla^2\psi_n - [\frac{Z_{eff}e^2}{r} - V_n(r)]\psi_n = E_n\psi_n , \tag{7.12}$$

where $V_n(r)$ describes the reduction in the binding energy due to outer electrons,

and Z_{eff} is the effective nuclear charge for the n-shell. After performing the integration, the cross section is given by

$$\sigma_I^{PWBA}(E) = \frac{8\pi z^2}{Z_{eff}^4 \eta_n} f_n a_0^2 , \tag{7.13}$$

where a_0 is the Bohr-radius of hydrogen, and with

$$\eta_n = \frac{1}{Z_{eff}^2}(\frac{\hbar v}{e^2})^2 , \tag{7.14}$$

and

$$f_n = \int\int dW \frac{dQ}{Q^2} |F(Q)|^2 , \tag{7.15}$$

where $Q = (a_0 q/Z_n)^2$, and $F(Q)$ is the so-called "form factor" which is determined by

$$F_{n,n'} = \int \psi_{n'}^*(\mathbf{r}) e^{i\mathbf{q}\cdot\mathbf{r}} \psi_n(\mathbf{r}) d\mathbf{r} . \tag{7.16}$$

7.4.2 Impulse Approximation Model [Binary Encounter Approximation, (BEA)]

The impulse approximation model treats the interaction between the projectile and the target atomic electron as a binary interaction by summing over the momentum exchanges in the calculation of the ionization cross section. In addition, this model also includes the modifications to account for the nuclear repulsion of the projectile. The only role played by the target atomic nucleus is in establishing the initial momentum distribution of the struck electron. Since the classical and quantum mechanical CM differential cross sections are essentially identical, the

classical analysis is usually used to transform the differential cross section to the laboratory system. Thus the final cross section is given by[110, 111]

$$\sigma_I(\mathbf{v}) = N_i \int_0^\infty \underbrace{\int_{E_b}^{E} (\frac{d\sigma}{d\Delta E})\ d\Delta E}_{\sigma_1} f(\mathbf{v}')d\mathbf{v}' , \tag{7.17}$$

where σ_1 is the cross section for the ionized electrons which have binding energy E_b. After considering two effects, namely the modification of the impact parameter due to the repulsion of the projectile, and the reduction of the projectile kinetic energy because of its motion in the repulsive field, the cross section for the impulse approximation is given by

$$\sigma_I^{BEA}(E) \simeq \sigma_I(E')[\frac{1}{2} + \frac{1}{2}(1 - \frac{2}{\pi}\frac{z/Z}{E/E_0})^{1/2}]^2 , \quad . \tag{7.18}$$

where $E' = E - 2zE_b/Z$.

7.4.3 ECPSSR Model

A more advanced model, the ECPSSR model, has been developed since the 1980's. This approach has a series of modifications to the PWBA, which basically treats angular deflection and velocity change due to the nuclear Coulomb field (C). The electron orbit of the target atom is affected by the projectile as perturbed stationary states (PSS). The model also includes relativistic effects (R) and energy loss due to the collisions (E). All this physics have been included in the formalism in terms of the modifications of the effective projectile energy and the effective atomic electron binding energy[112, 113, 114]. Thus

$$\sigma_I^{ECPSSR}(E) = C_n^E f_n(z_n)\sigma_I^{PWBA}(E) , \tag{7.19}$$

where C_n^E accounts the effects of the Coulomb deflection, perturbed stationary-state effects, relativistic effects, and energy loss effects. f_n is the straight-line

Table 7.2:

Coefficients for universal ionization σ_K and σ_L for a projectile proton

	K-line	L-line
b_0	2.0471	3.6082
b_1	-0.65906×10^{-2}	0.37123
b_2	-0.47448	-0.36971
b_3	0.9919×10^{-1}	-0.78593×10^{-4}
b_4	0.46063×10^{-1}	0.25063×10^{-2}
b_5	0.60853×10^{-2}	0.12613×10^{-2}

energy-loss function. The details of these parameters have been given in Ref. [112].

7.4.4 Universal Ionization Cross Section

In addition to the theoretical approaches, in the latter part of the 1970's a universal ionization cross section formalism was also developed which is a compromise between the existing experiment data and the non-relativistic BEA concept. Specifically, for a projectile proton[124, 125],

$$\sigma_I(E) = \frac{1}{U_I^2} exp\{\sum_{n=0}^{5} b_{Z,n}[ln(\frac{E}{\lambda U_I})]^n\} , \tag{7.20}$$

where U_I is the K- or L-shell ionization energy (for L-shell it has been averaged over three subshells), E is the proton energy, λ is the ratio of proton to electron mass (i.e. λ=1836.1514), and the b is determined by fitting this fifth-order polynomial to the experimental data. This universal cross section is widely used because of its simplicity and relative accuracy. Table 7.2 gives these coefficients[124].

7.5 Principles of X-Ray Detection

In the detection of x rays, there are two basic issues of interest: first, the flux of the measured x ray (the number of photons per unit area per unit time); and second, the energy spectrum of the measured x ray. These two pieces of information can be usually obtained by operating the x-ray detector in different modes, i.e. the current mode and the pulse mode. In order to achieve these objectives, a large variety of x-ray detectors have been developed and used in laboratory. These detectors, according to their operating modes, are generally divided into two categories: the spectrometer (for pulse mode) and the diode (for current mode). The former one (spectrometer) records each individual quantum of radiation which interacts with the detector. The latter one (diode), on the other hand, measures the average current over a myriad of interactions and through which the information of x-ray flux can be obtained.

7.5.1 The Pulse Mode of Operation

The pulse mode of operation is a response of a detector to each individual photon. This photon generates charges within the detector active region that are proportional to the photon energy. Therefore, the totality of all pulses reflects the energy distribution of the x rays. Practically, one actually measures the so-called differential pulse height distribution in which the differential number of events (ΔN) within a small increment in pulse in height (ΔH) is recorded. These pulses are first converted into corresponding voltage pulses by preamplifier, and then are further amplified by the main amplifier. Finally, the amplified voltage pulses are distributed and placed into the different channels in terms of their pulse heights (this final step was done by the multichannel analyzer, MCA). The flow diagram of pulse mode operation is displayed in Fig.(7-7). In addition, the response to

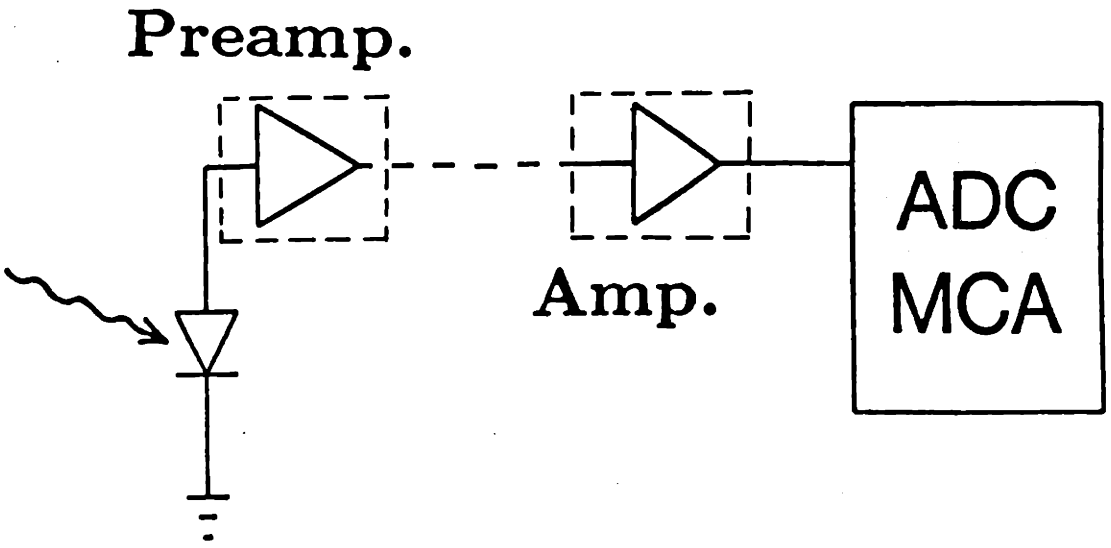

Figure 7-7: The schematic of pulse mode of operation for x-ray detector

monoenergetic radiation of a detector operated in pulse mode is a single peak of near Gaussian shape, the experimentally measured spectral width basically reflects noise broadening and statistics in the charge creation process in the detector.

7.5.2 The Current Mode of Operation

The current mode of operation gives an average current response of the detector to the radiation, which can be illustrated by Fig.(7-9) and the following integrating,

$$I(t) = \frac{1}{T}\int_{t-T}^{t} i(\tau)d\tau \ , \tag{7.21}$$

where $i(\tau)$ is a current response to an individual quantum of radiation and $I(t)$ is the average current output over the time period T. Because of this averaging

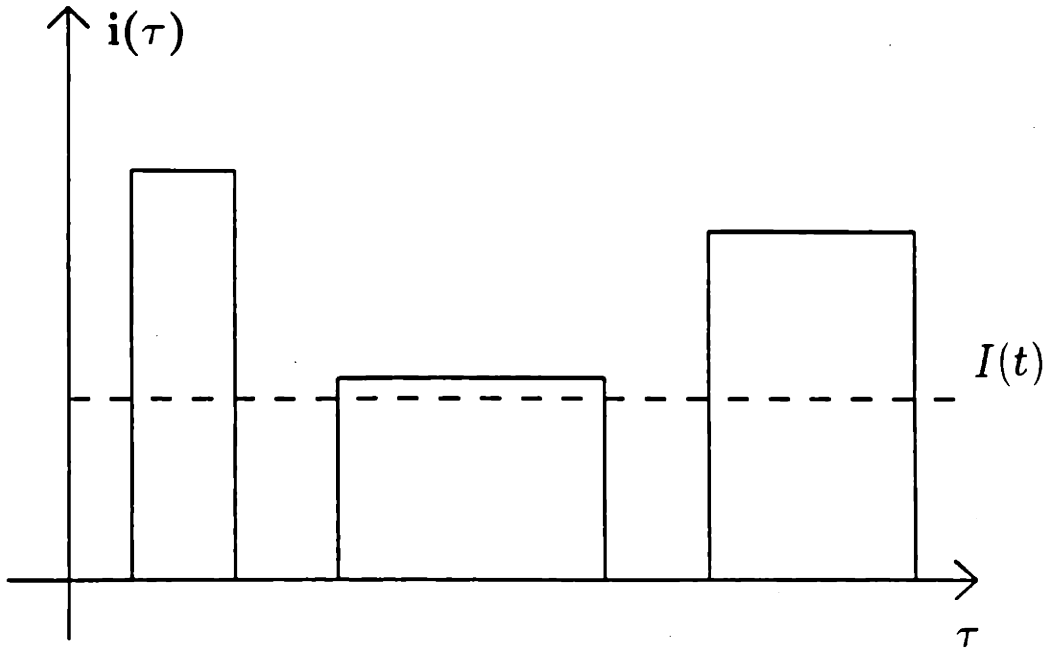

Figure 7-8: A illustration of current mode operation for an x-ray detector. Where each individual burst of current may have different amplitudes, the output, however, is the averaged $I(t)$.

process, the energy information of each quantum of radiation is lost and what is measured is just the information of the flux.

Practically, it is straightforward to operate a detector in current mode. Basically there are two ways, in terms of a current and voltage measurement:

(1) Using a electrometer to measure the output current.

(2) Using a oscilloscope to measure the output voltage from a current-voltage convertor.

It is generally true that the detector is not an ideal constant current source.

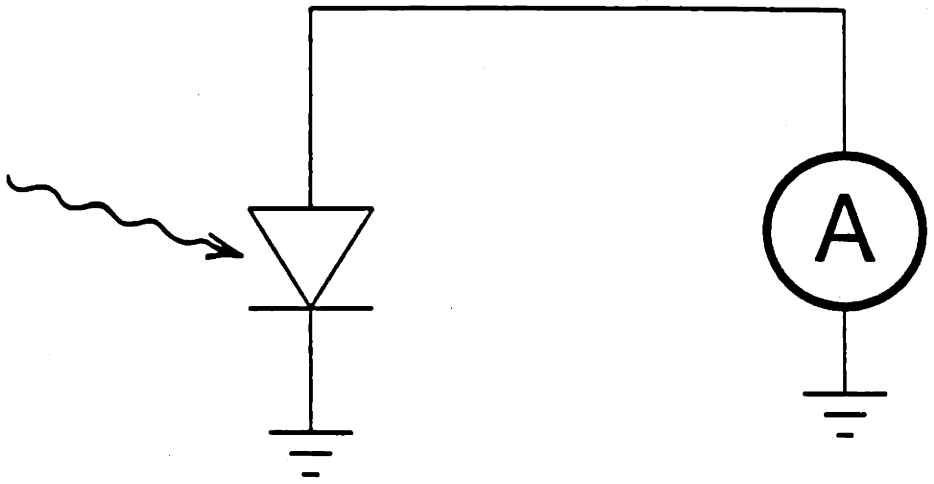

Figure 7-9: The schematic of the measurement of the output current.

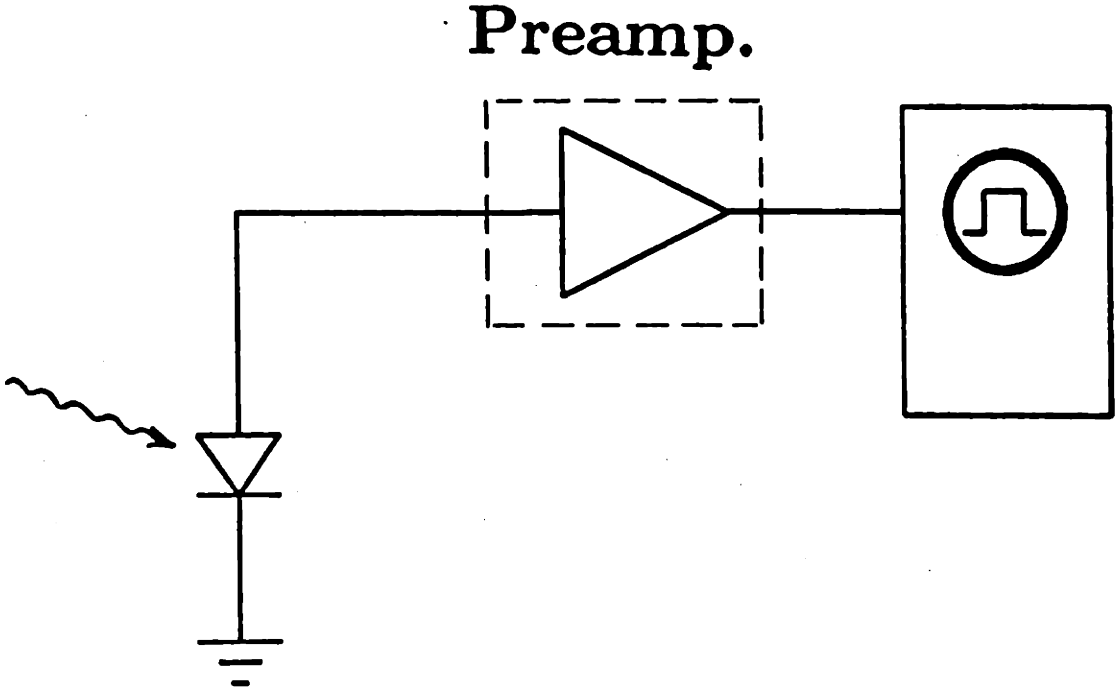

Figure 7-10: The schematic of the measurement of the output voltage.

Thus the dynamic range of the linear response of the detector to the radiation flux depends on its output impedance (should be as small as possible).

7.6 X-Ray Spectrometers (Pulse Mode Detector)

7.6.1 Si(Li) Spectrometer

The lithium-drifted silicon detector [Si(Li)] is one of the most widely used x-ray spectrometers. As shown in Fig.(7-11), through the use of lithium drifting, the Si(Li) detector can be formed with a much greater active thickness, or depletion depth (usually a few millimeter), compared to that of the common junction or surface barrier semiconductor detector (usually a few hundred micrometers). This issue is important in order to attenuate soft x rays [for example, the e-folding distances for copper K-lines (8.05 keV for K_α and 8.9 keV for K_β) are about 65 μm and 90 μm, respectively; and for molybdenum the e-folding lengths of K-lines (17.5 keV for K_α and 19.6 keV for K_β) are about 670 μm and 920 μm, respectively] The empirical quantum efficiency for a Si(Li) detector with 3 mm thick crystal and a 8 mil thick beryllium window is displayed in Fig.(7-12). This Si(Li) detector is suitable for measuring x rays with energy between 1 keV and 40 keV. Also, in spite of the thick active volume, the volume-related bulk leakage current of the Si(Li) detector is very small because of its operating at the boiling point of nitrogen (77 K). Therefore, the Si(Li) detector has very high rejection of thermal noise. Furthermore, this Si(Li) detector has very good energy resolution, which is usually defined as the full-width-at-half-maximum of a spectral peak divided by the peak energy. For example, for our EG&G ORTEC Si(Li) spectrometer[116], the full width at the half width of ^{55}Fe MnK_α x rays (5.9 keV) is about 160 eV, which means the K_α x rays of neighboring elements can be fully resolved by using

this spectrometer.

7.6.2 Flow Proportional Counter

A flow proportional counter is a special type of gas detector with the following characteristics, first, the counting gas continuously flows through the detector with an adjustable flow rate and pressure; and second, the counter is always operated in the proportional regime where the signal (current electron-ion pairs) is amplified linearly due to gas multiplication. The configuration of our flow proportional counter is displayed by Fig.(7-13). Basically, it consists of an anode (1 mil tungsten wire), a cathode (the detector body itself), a sideview replaceable window, a high-voltage connector, and connector for gas flow[119].

The proportional counter is always operated in pulse mode. Thus, it is called a quantum detector. When an individual quantum of radiation interacts with the molecules (or atom) of the counting gas, charged pairs are created and will be accelerated by the applied electric field[115],

$$\varepsilon(r) = \frac{V}{rln(b/a)} \tag{7.22}$$

where a is the anode wire radius, b is the cathode inner radius, and V is applied bias voltage. During the migration of these charges, many collisions with the neutral gas will occur. If the electric field is large enough and the kinetic energies of the migrating charges are greater than the threshold of the ionization potential of the counting gas, secondary ionization process will continuously occur which forms avalanches in the detector. This is illustrated in the Fig.(7-14),

We chose a flow proportional counter based on the following properties: first, the pressure of the counting gas is ideally adjusted so that a sufficiently large

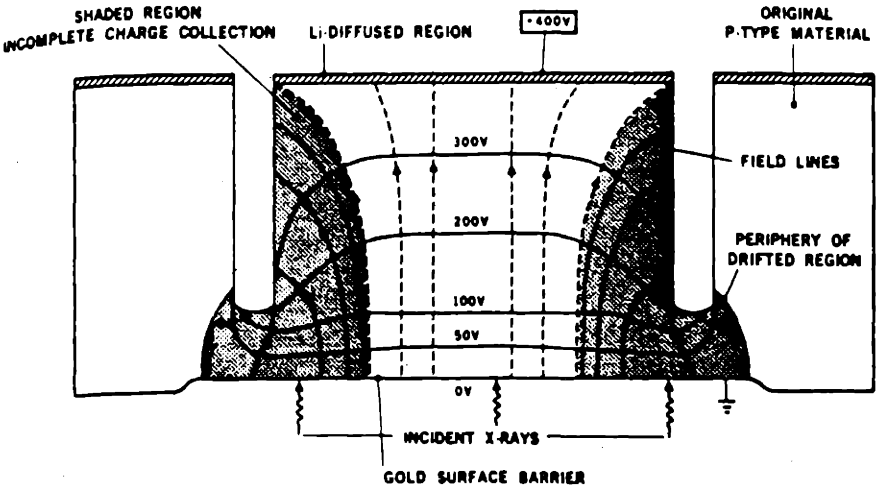

Figure 7-11: The schematic of a Si(Li) spectrometer[117]

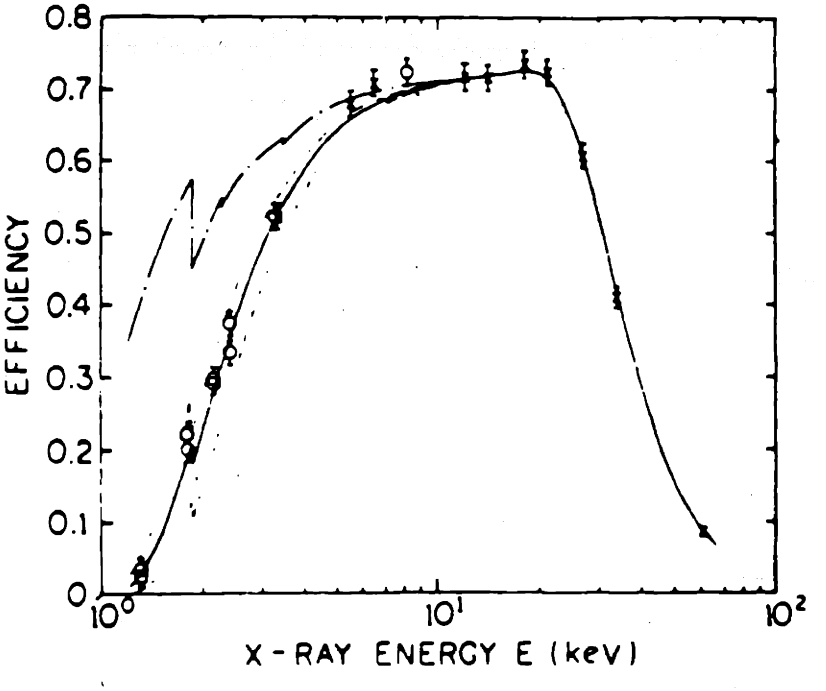

Figure 7-12: The efficiency of the typical Si(Li) spectrometer[118]

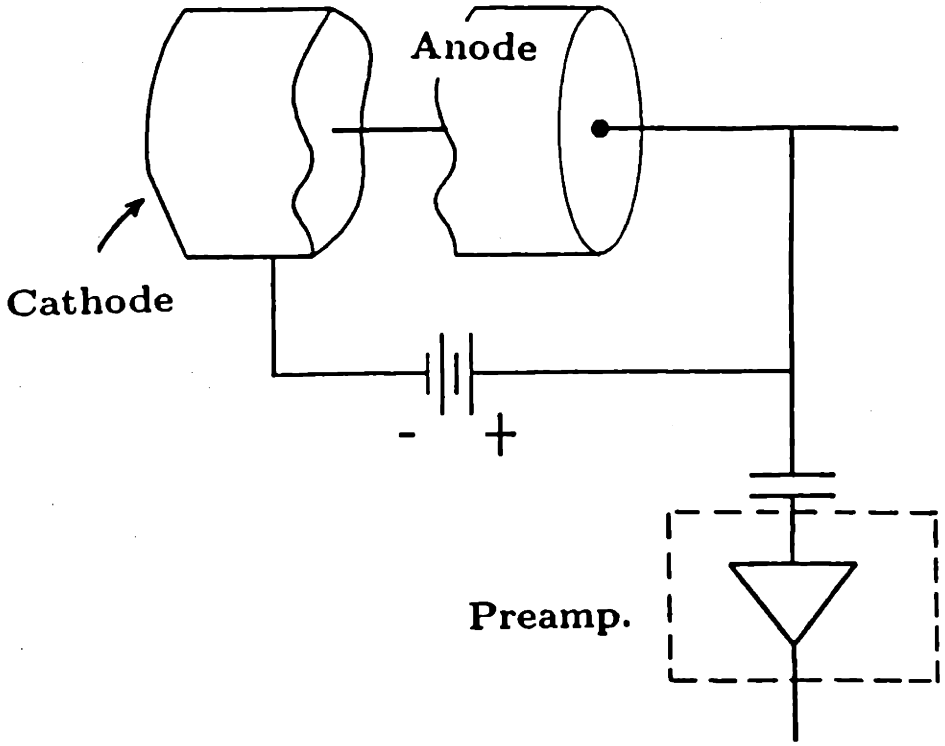

Figure 7-13: The schematic of the flow proportional counter

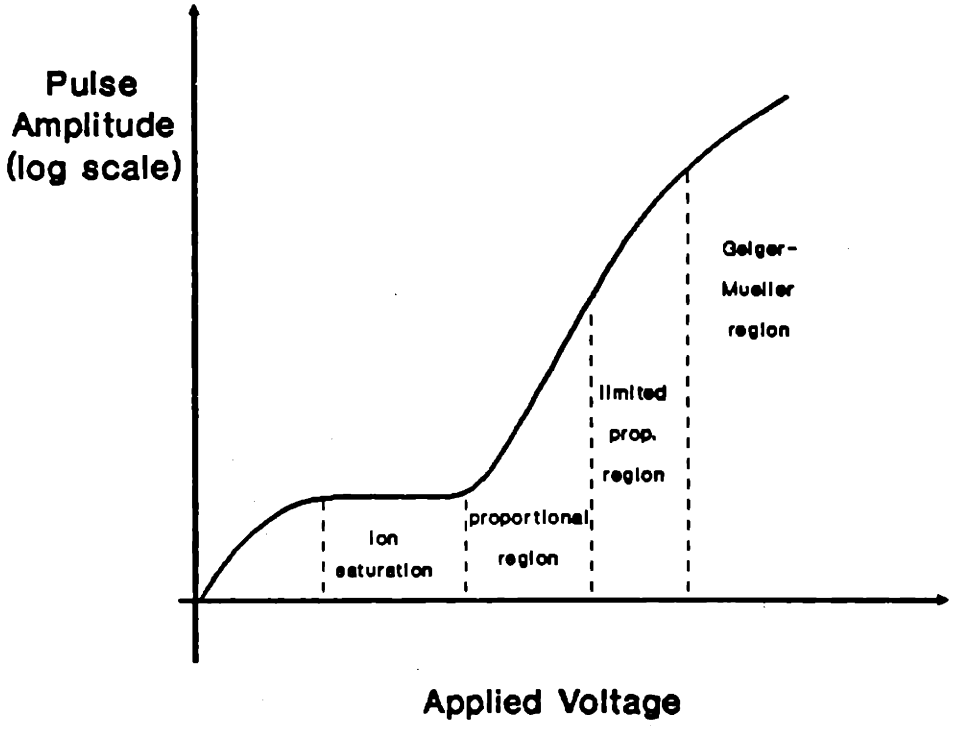

Figure 7-14: The proportional region of the gas detector

fraction the x rays are absorbed within the counter gas by the time they reach the anode wire; second, the window is made sufficient transparent to the x rays of interest.

7.7 X-Ray Diodes (Current Mode Detector)

7.7.1 Surface Barrier Diode (SBD)

A silicon surface barrier diode is a reverse-biased planar diode with metal coating (usually Al and Au) on both sides of the wafer. The junction of an SBD is formed by either the Al or Au coating evaporated on the silicon wafer. Usually the coated thickness is $\sim 100 - 1000$ Å. The reverse-bias voltage creates a depleted region in the wafer. The depletion depth in a uniformly doped wafer is determined as[115]

$$d = \sqrt{\frac{2\epsilon}{n_A e}(V + V_0)}\,, \tag{7.23}$$

where ϵ is the dielectric constant of the wafer material, n_A is the doping density, V is the applied bias voltage, and V_0 is the intrinsic junction potential (barrier height). X-ray photons striking the detector knock out bound electrons. The created charge carriers (free electrons and the holes) are subsequently accelerated by the reverse-biased voltage across the junction and are collected as the detector current. SBDs have several merits including: compact dimension, insensitivity to magnetic field, stable and simple to operate, etc. It has been demonstrated as a good detector for x-ray flux monitoring, for magnetic fusion plasma imaging, and for other physics experiments. Unlike the Si(Li) detector, the bulk leakage current is not the important noise source for SBDs. Instead, leakage current created on the surfaces of the junction is the primary source of thermal noise, which, as a consequence, limits SBDs to be operation only in current mode. Of course, SBDs are good spectrometers for charged particles, for example, for charged fusion

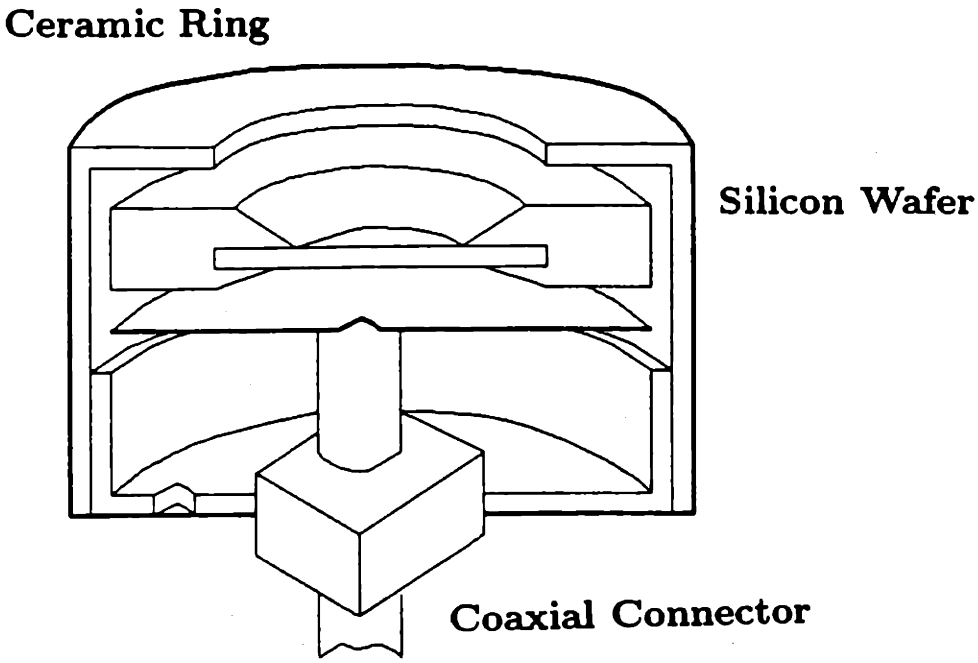

Figure 7-15: The schematic of a surface barrier detector (SBD)

products. Consequently, SBDs are usually used for measuring x-ray flux, rather than individual photons.

7.7.2 X-UV Photodiode

Silicon photodiodes with stable, high quantum efficiency in the soft x-ray and ultraviolet wavelength regions have recently become available[120, 121]. These detectors are referred to as X-UV photodiodes because of the spectral region over which they are sensitive. In addition to their high efficiency and stability, X-UV detectors have the added advantages of having a large dynamic range, low noise, low cost, requiring little or no bias voltage, and having large sensitive areas. These advantages make the X-UV detector quite attractive for measuring radiation emitted from space and laboratory plasmas. Fig.(7-16) shows a schematic of a 1 cm^2 active area X-UV absolute diode, which was fabricated on a three inch diameter

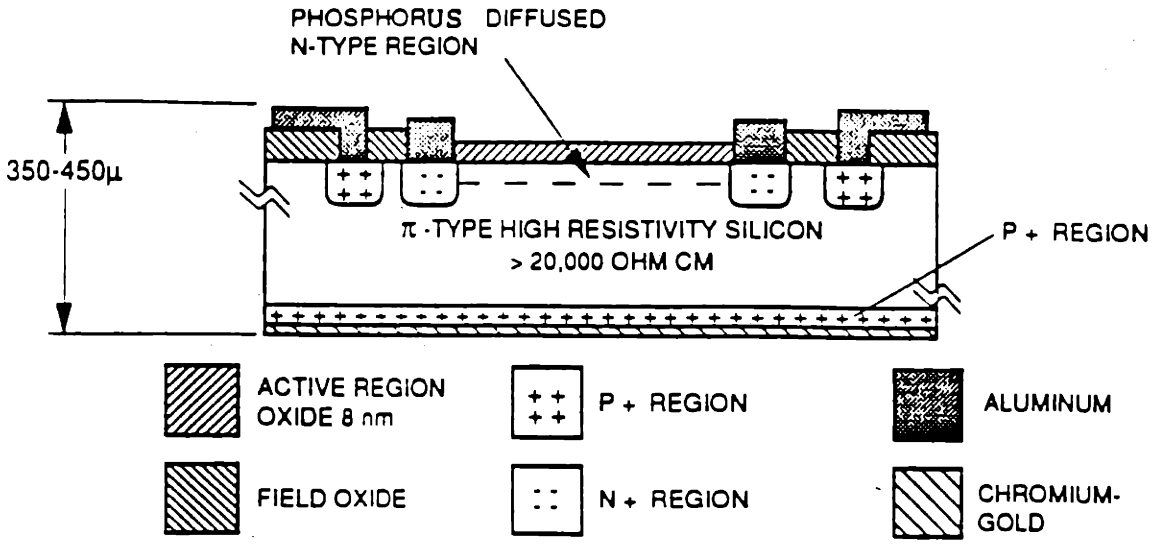

Figure 7-16: The schematic of an XUV detector

high resistivity (> 20000 Ω-cm), 450 μm thick p-type silicon wafer. Because there is no recombination of photon-generated carriers in the doped n^+ region and at the Si-SiO_2 interface, the X-UV diode has a 100% internal quantum efficiency for soft x rays with energy of up to 6 keV. This quantum efficiency decreases with increasing x-ray energy above 6 keV because of the limited thickness of the silicon.

Chapter 8

A Proton-Induced X-Ray Emission (PIXE) Source

8.1 Introduction

Ion induced x rays were first observed by Chadwick in the 1910's[123], who used a radioactive α-particle source. Since then, especially in the past three decades, the fundamental characteristics of PIXE - - ionization cross sections, stopping power, and fluorescence yields, etc. - - have been carefully studied [124, 125]. X-ray emission induced by heavy charged particles is a well established technique with many applications. To the best of our knowledge, however, the applications have concentrated on analyzing the elemental composition of materials. Thus, little effort, if any, has been expended on exploiting the high intensities of PIXE as a tool for characterizing x-ray instrumentation.

A high-intensity PIXE source has been developed for the purpose of characterizing x-ray detectors and optics, and measuring filter transmission. With energetic proton beams of up to 165 keV, intense x-ray line radiations (0.5Å $\leq \lambda \leq$ 111 Å) have been generated from the $K-$, $L-$, M-, and N-shells of elements with $4 \leq$ Z

≤ 92. The PIXE spectrum has orders-of-magnitude lower background continuum than a conventional electron-beam or radioactive α-fluorescence source[122]. Section 8.2 describes the experimental arrangement and technical details of our PIXE source. In section 8.3, we show typical PIXE $K-$, $L-$, M-, and N-line spectra as well as measured $K-$, $L-$, M-, and N-shell x-ray production efficiencies for various elements.

8.2 Experimental Arrangement

The experimental arrangement is depicted in Fig.(8-1). Fluorescent x rays generated by energetic ions are detected by diagnostics in two "arms" offset by 116° with respect to the forward direction of incident beam. In order to adjust the x-ray flux and to expedite the identification of characteristic x rays, an aperture/filter chamber is placed between the detector(s) and the PIXE source. Each chamber has a 24-position aperture wheel and a 24-position filter wheel, both independently rotatable through 360°.

8.2.1 The Cockcroft-Walton Linear Accelerator

The ion beam is provided by a Cockcroft-Walton linear accelerator which was originally designed for neutron generation. Large sections of the accelerator have been recently rebuilt [126]. Its principal components are: an RF (radio frequency) ion source; a solenoid beam focusing lens, and an electrostatic ion extraction system; an accelerating column; a beam collimation system; a water-cooled target(s); and a Faraday cup. Fig.(8-2) depicts a detailed cross section of this generator. It is found for PIXE experiments that the positively-biased collimator system plays an important role in eliminating background continuum radiation. This is be-

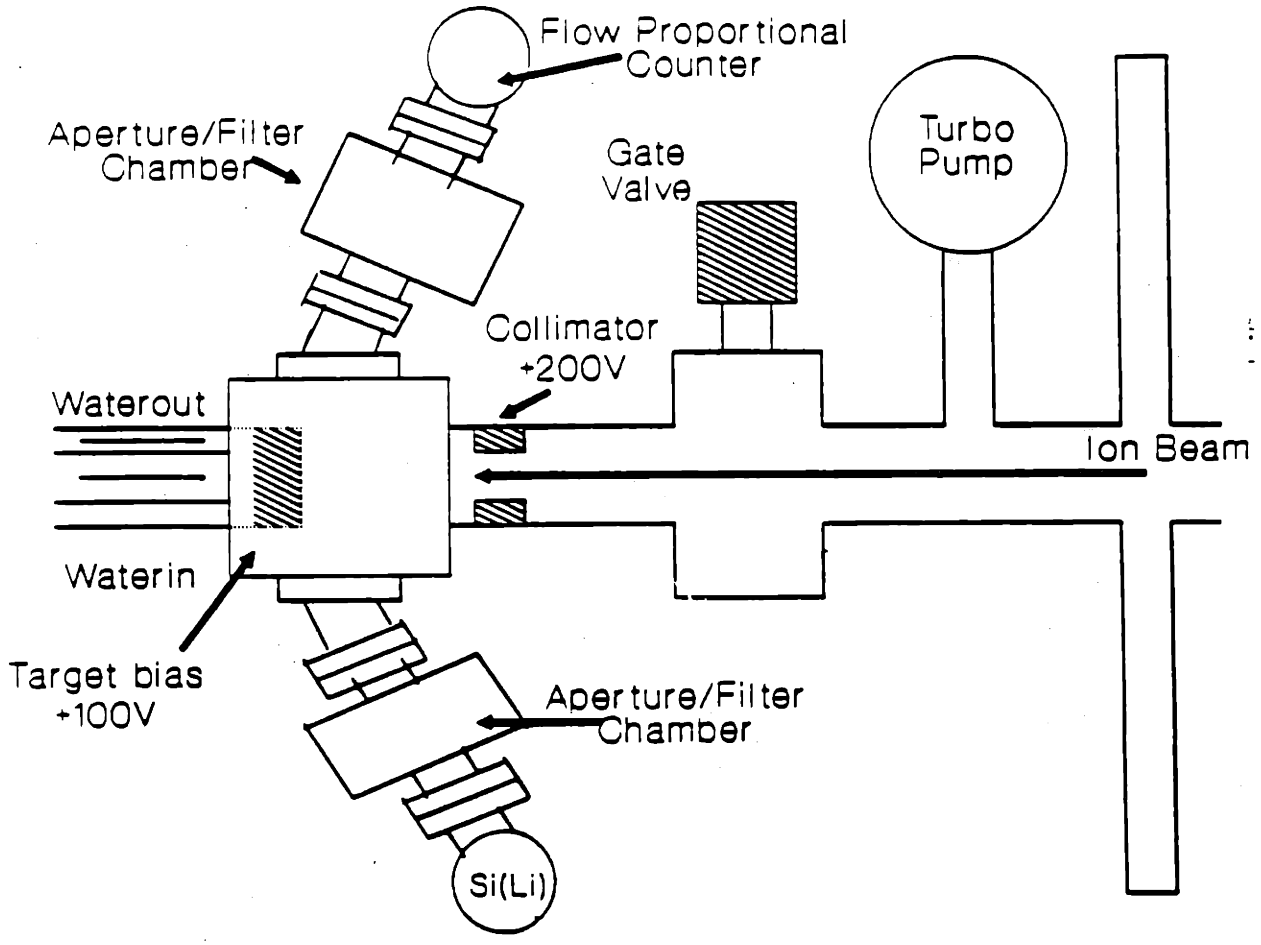

Figure 8-1: Schematic diagram of the PIXE experimental arrangement.

cause when protons are accelerated, a number of secondary electrons are created inside the chamber which will produce secondary-electron bremsstrahlung x rays. Similarly, the positively-biased target prevents secondary electrons emitting from being emitted from the target. The uncertainty in the ion-beam energy is determined to be $\lesssim 5\%$, and the ion current for conducting (non-conducting) targets is known to within $\lesssim 10\%$ (15%). The accelerator can be operated with voltages up to 165 kV and ion currents up to 300 μA. Although several charged species – such as H^+, D^+, $^3He^+$, and $^4He^+$ – have been used as projectile ions, here we concentrate only on x rays that are induced by H^+.

8.2.2 The Targets

Target preparation is one of the central issues for PIXE experiments. The targets are "thick" and are made using one of six methods: (1) direct machining of materials such as Al, Cu, and Mo; (2) vacuum deposition of materials such as Cr and Ti; (3) epoxy-bonding of pure metal foils such as Be, Zn, and Ta; (4) electric discharge machining (EDM) for difficult-to-machine materials like W, and Ta; (5) pressed powders on a metal substrate using a man-powered press or a locomotive crusher (for Li, B, and Si); and (6) special vacuum depositions process done at LLNL (for elements such as B, U, and Ti). The method chosen depends on such factors as the mechanical, thermal, and electric properties of the specific material, as well as the cost.

8.2.3 Diagnostics

Three energy-dispersive detectors [two Si(Li) spectrometers and a flow proportional counter] have been used to characterize the PIXE source: (1) an ORTEC Si(Li) spectrometer with an 8-μm beryllium window and energy resolution R $\simeq$ 160 eV (for ^{55}Fe), which can measure photons of energy between $\simeq$0.6 keV to $\sim$30 keV (the crystal is 2.71 mm thick and the efficiency for 30 keV x rays is about

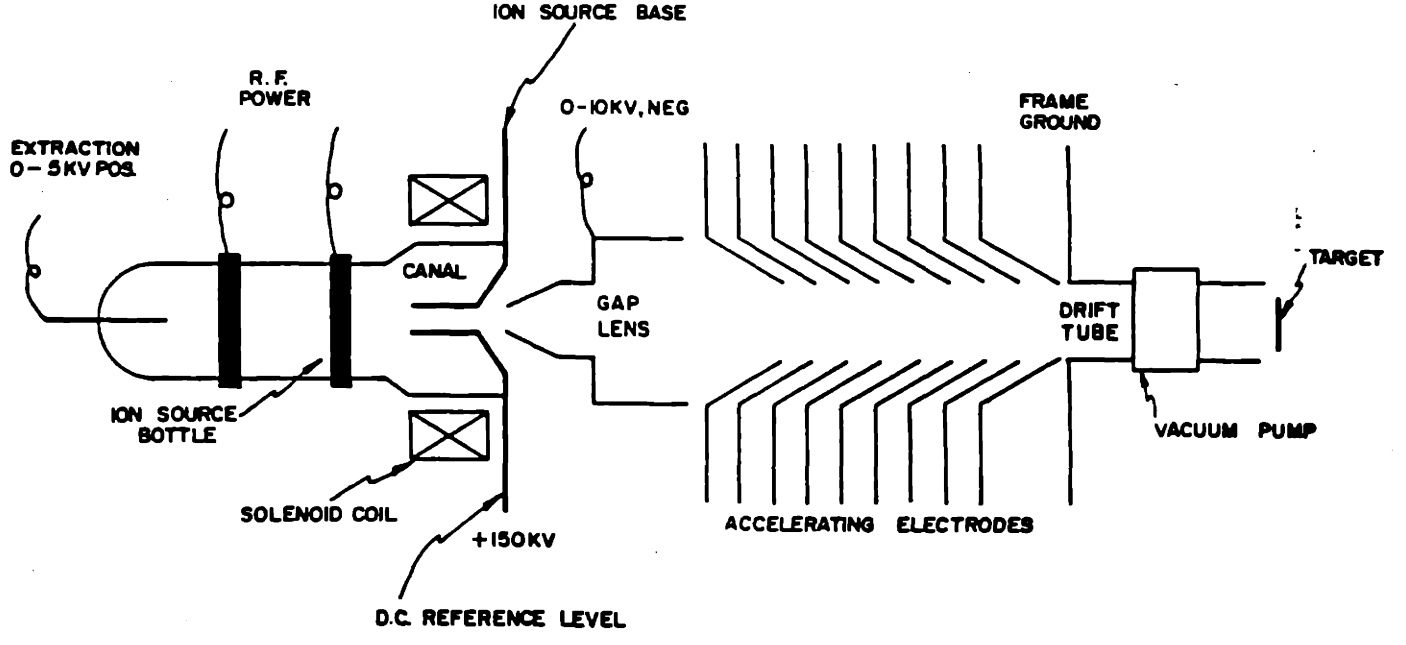

Figure 8-2: The schematic diagram of a Cockcroft-Walton linear accelerator.

40%); (2) a Kevex Si(Li) spectrometer with a 25-μm beryllium window; and (3) a flow proportional counter with a thin window (for example, we have used a 0.5-μm mylar film coated with $\simeq$ 100 Å aluminum). Using this proportional counter, we have measured very low-energy x rays (such as the Be K-line, E = 0.111 keV; B K-line, E = 0.183 keV; and the C K-line, E = 0.277 keV; see Fig.(8-3). A leak valve and a manometer have been used to control and measure the flow gas pressure, which is either atmospheric or sub-atmospheric. A microcomputer based ADC (Analog-Digital-Convertor) and MCA (Multi-Channel-Analyzer) have been utilized for data acquisition.

8.3 Experimental Results.

Characteristic x rays have been generated from the $K-$, $L-$, $M-$, and N- shells of elements with $4 \leq Z \leq 92$, with wavelengths from 0.5 Å to 111 Å. Typical PIXE spectra are shown in Figs.(8-3), (8-4), (8-5), and (8-6). Fig. (8-3) shows the measured K-line PIXE spectra of Be (Z=4), B (Z=5), C (Z=6), and F (Z=9). These spectra were obtained with a flow proportional counter. Fig. (8-4) shows the Si(Li) PIXE spectra of K-lines from Al (Z=13), V (Z=23), Co (Z=27), and Cu (Z=29). Fig. (8-5) shows the Si(Li) PIXE spectra of L-lines from Zn (Z=30), Mo (Z=42), Ag (Z=47), and Sn (Z=50). Fig. (8-6) shows Si(Li) PIXE spectra of M-lines from Ta (Z=73), W (Z=74), Pb (Z=82), and U (Z=92). From Fig.(8-6) one can also see that the N-lines of Uranium are more intense than the M-lines. (In fact the N-lines consist of wavelengths at 8.60 Å, 8.76 Å, 8.81 Å, 10.09 Å, and 10.40 Å.) From all these spectra, it is clear that the background continuum is negligible compared to the lines.

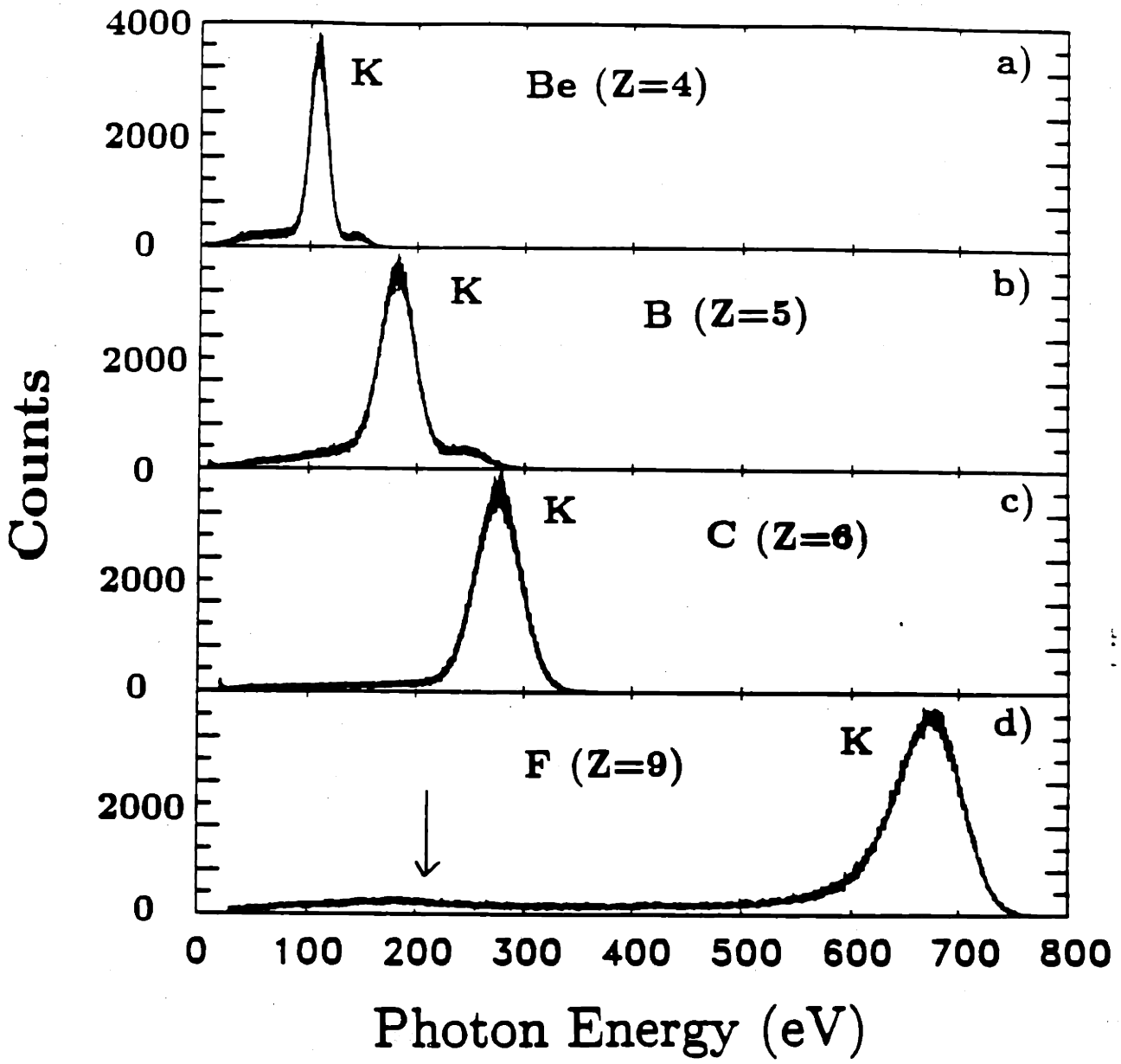

Figure 8-3: The PIXE spectra of, a) Beryllium, b) Boron, c) Carbon, and d) Fluorine. The K lines are at 0.108 keV, 0.183 keV, 0.277 keV, and 0.68 keV, respectively. The spectra are measured by a flow proportional counter with a 0.5-μm mylar window. The flow gas is either 99.05% He + 0.95% isobutane, or 90% Ar + 10% methane (P10). The proton beam energy was 150 keV, for which the maximum secondary-electron generated bremsstrahlung energy is 0.3 keV. [This bremsstrahlung component is indicated by the arrow in d)]

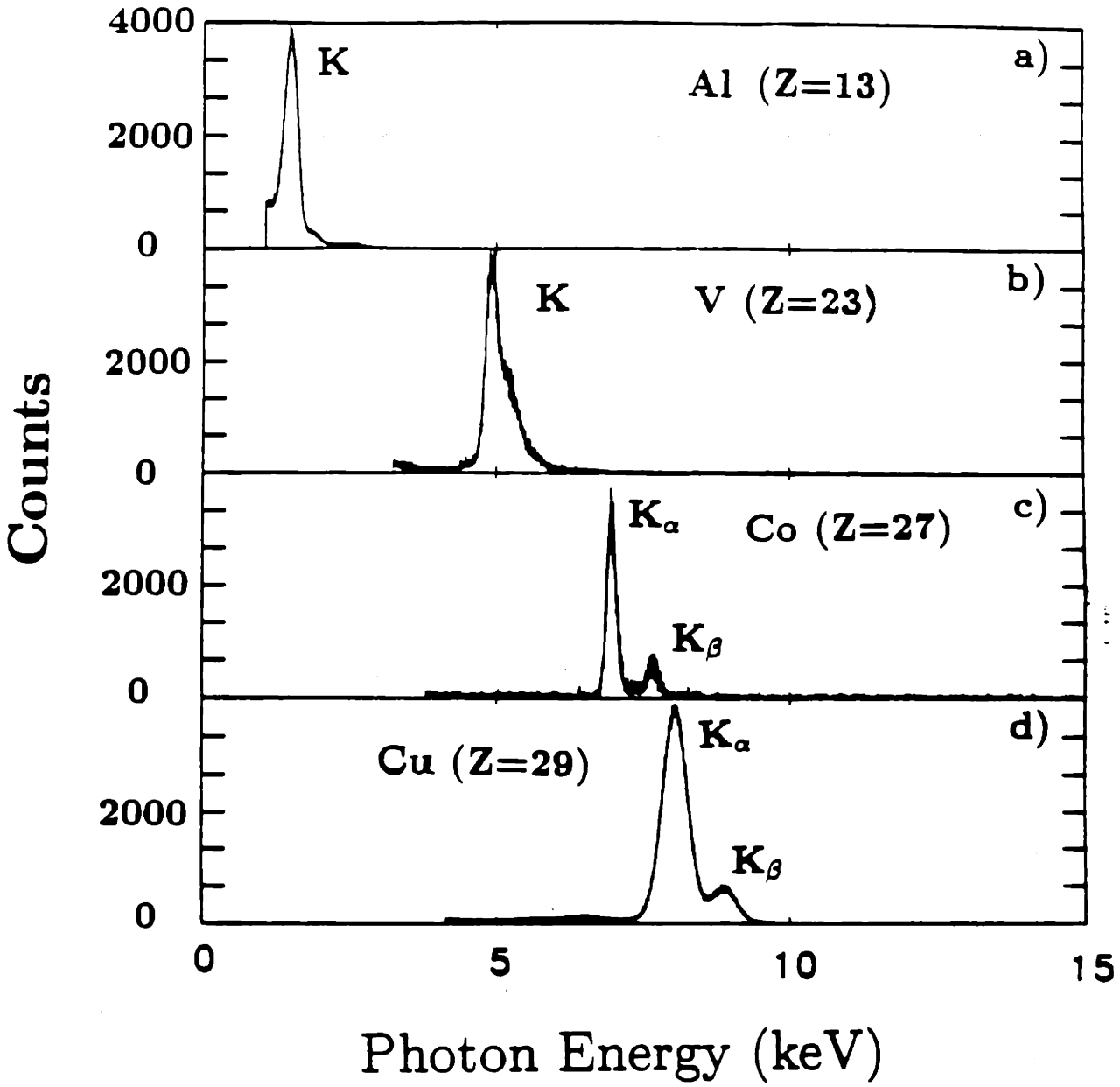

Figure 8-4: The PIXE spectra of, a) Aluminum (K_α line at 1.485 keV), b) Vanadium (K_α line at 4.95 keV), c) Cobalt (K_α line at 6.95 keV and K_β line at 7.65 keV), and d) Copper (K_α line at 8.05 keV and K_α line at 8.9 keV). The incident beam consisted of protons accelerated to 150 keV. Two different Si(Li) detectors were used for these measurements.

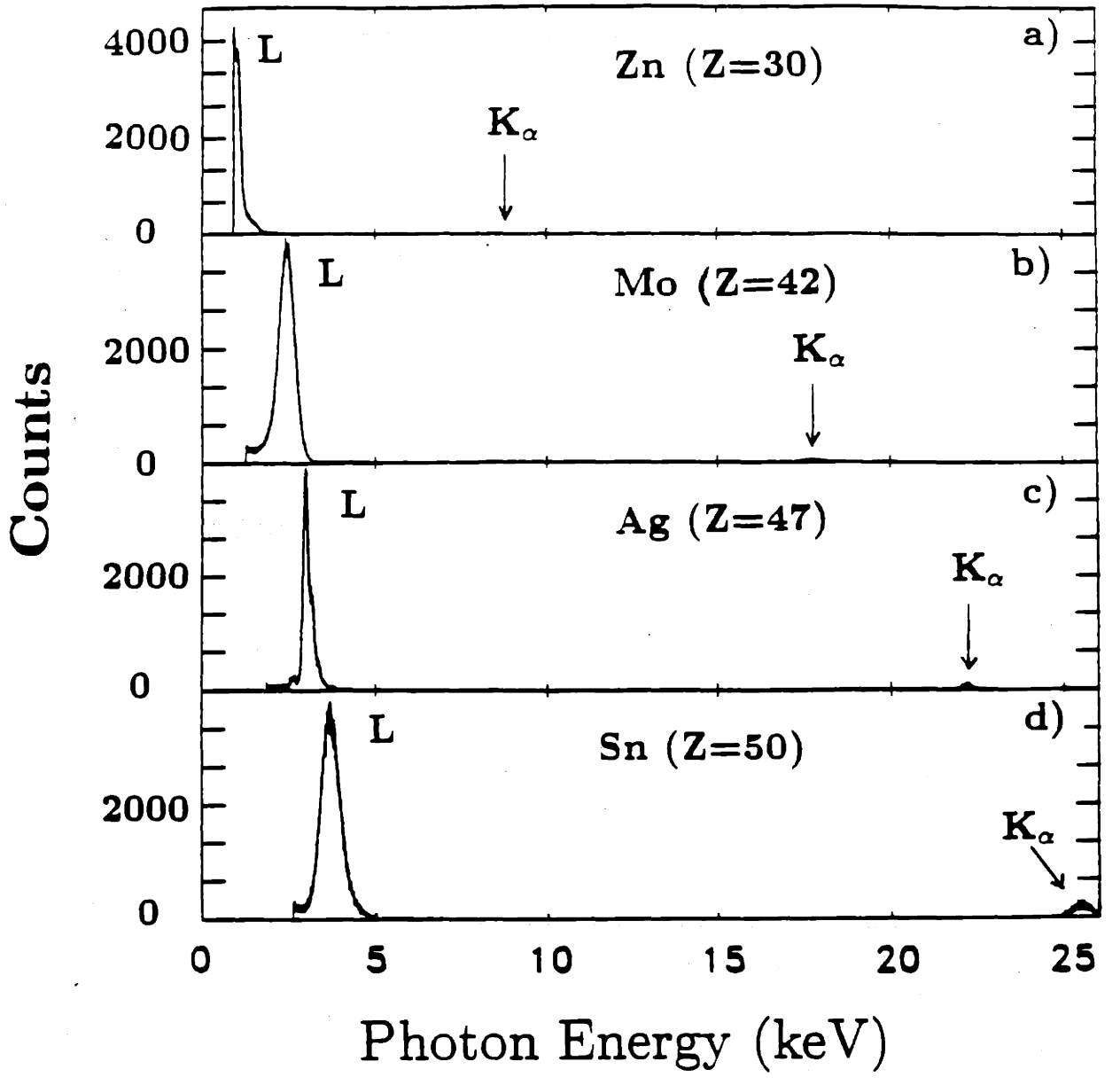

Figure 8-5: The PIXE spectra of, a) Zinc [the L lines are around 1.01 keV and the K lines are around 8.6 keV (see arrow)]; b) Molybdenum [the L lines are around 2.29 keV and the K_α line is at 17.5 keV (see arrow)]; c) Silver [the L lines are around 2.98 keV and the K_α line is at 22.16 keV (see arrow)]; d) Tin (the L lines are around 3.44 keV and the K_α line is at 25.27 keV). Two different Si(Li) detectors were used for these measurements. For these spectra, protons were accelerated to 150 keV.

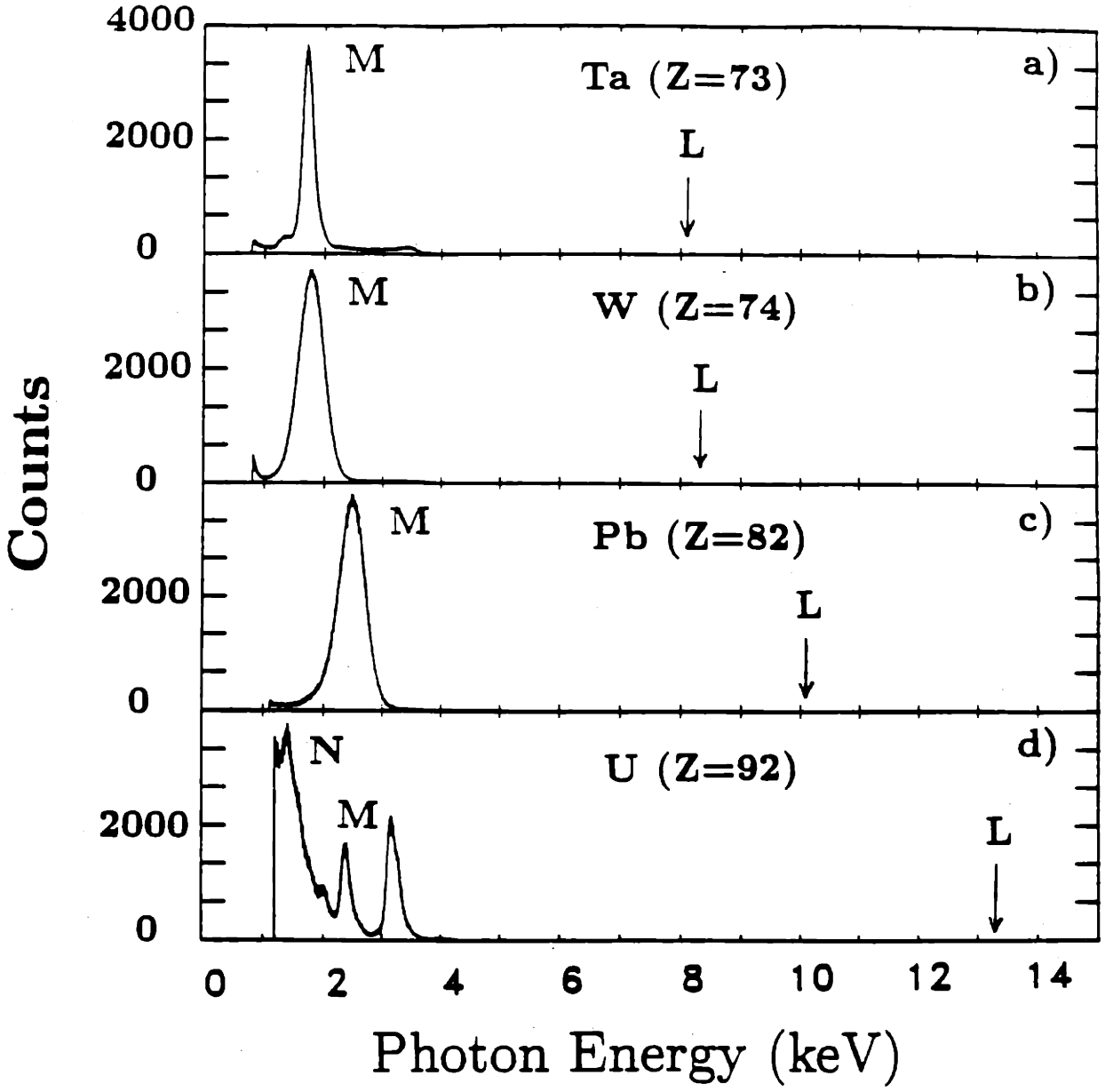

Figure 8-6: The PIXE spectra of, a) Tantalum [the M lines are around 1.71 keV and the L lines are around 8.14 keV (see arrow)]; b) Tungsten [the M lines are around 1.77 keV and the L lines are around 8.39 keV (see arrow)]; c) Lead [the M lines are around 2.4 keV and the L lines are around 10.5 keV (see arrow)]; d) Uranium [the N lines are around 1.4 keV, the M_α line is at $\sim$ 2.5 keV and M_ζ line is at $\sim$ 3.16 keV, and the lines are around 13.6 keV (see arrow)]. Two different Si(Li) detectors were used for these measurements. For these spectra, protons were accelerated to 150 keV.

8.4 Discussion

In general, the PIXE background continuum is mainly bremsstrahlung from secondary electrons [124, 125, 127, 128]; the endpoint energy is $4m_e E_p/m_p \simeq 300$ eV, since the proton energy E_p is 150 keV. Note in Fig.(8-3), especially in figure (d) that this continuum is detectable, but at a very low level. Other possible mechanisms for background continuum include the projectile ion bremsstrahlung, and γ-ray induced Compton electron bremsstrahlung. The probability of projectile ion bremsstrahlung is usually determined by

$$\sigma = \int \frac{C_0 A_p Z_p^2 Z^2}{E_p E_x} \left(\frac{Z_p}{A_p} - \frac{Z}{A}\right)^2 d\Omega \,, \tag{8.1}$$

where C_0 is an empirical constant; Z_p (Z), A_p (A), are the atomic number and atomic weight of the projectile (target), respectively; Ω is the solid angle; E_p is the projectile kinetic energy and E_x is the x-ray energy. As shown in all the previous spectra in the region for $E_x \geq 0.3$ keV, this projectile ion bremsstrahlung are totally negligible. For the case of bremsstrahlung induced by Compton scattered electrons, we have found this too to be negligible. This is because our Cockcroft-Walton linear accelerator can only provide protons with energy up to about 165 keV at which the probabilities of γ ray being generated through nuclear reactions are relative low (except for proton-boron interaction).

To a good approximation, the characteristic x-radiation pattern is isotropic. Experimentally, therefore, one can measure the fraction of emitted photons per unit ion charge striking the target. This yield is defined by

$$Y_{exp}(E) = \frac{4\pi}{\Omega} \frac{1.6 \times 10^{-13} N(E)}{T_Z(E)\varepsilon(E)} \,, \tag{8.2}$$

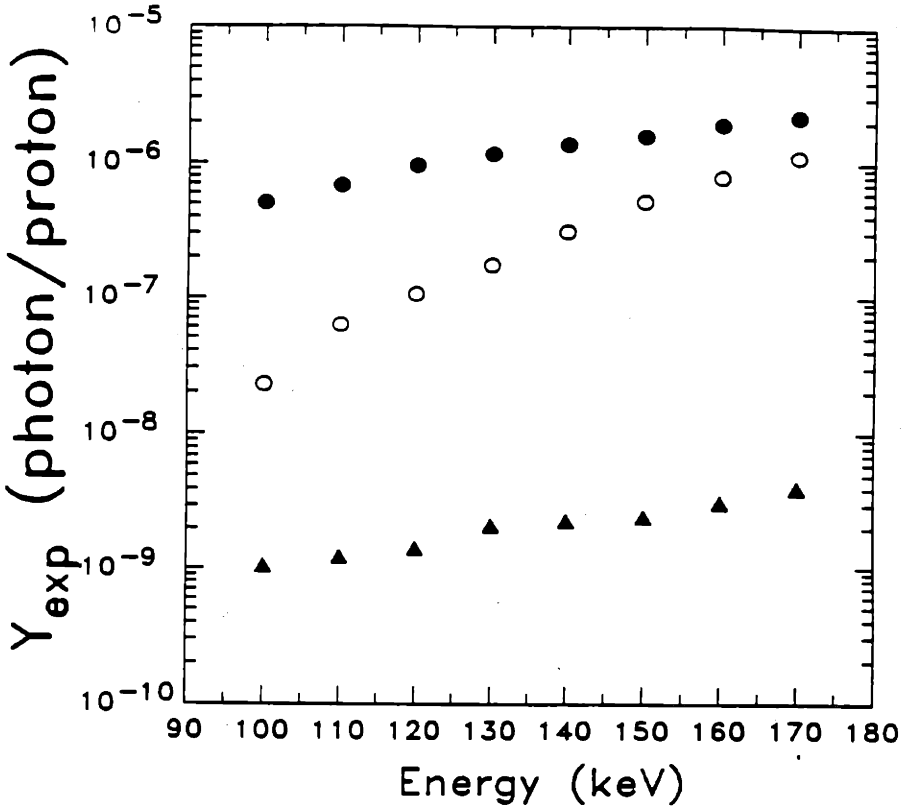

Figure 8-7: The PIXE x-ray production efficiencies of uranium $L-$, $M-$, and N-line radiation are plotted as a function of incident photon energy. The L lines (solid triangle), M lines (open circle), and N lines (solid circle).

where $N(E)$ is the experimentally measured number of photons (of energy E) per micro-coulomb of ions, $T_Z(E)$ is the transmission of the windows and filters associated with the x-ray detector, Ω is the solid angle subtended by the detector (assuming a point source at the target, which is a good assumption for our guessing), and $\varepsilon(E)$ is the intrinsic detector efficiency. The PIXE x-ray production efficiencies of uranium $L-$, $M-$, and N-line x rays are plotted as a function of incident proton energy, in Fig.(8-7).

Fig. (8-8) shows a log-log plot of the measured x-ray yields as a function of the x-ray wavelength, and Fig. (8-9) shows a log-log plot of the measured x-ray yields as a function of the target atomic number. These efficiencies, which roughly agree with the results of other researchers [130], generally increase with the x-ray wavelength and the principal quantum number of the target, but decrease with

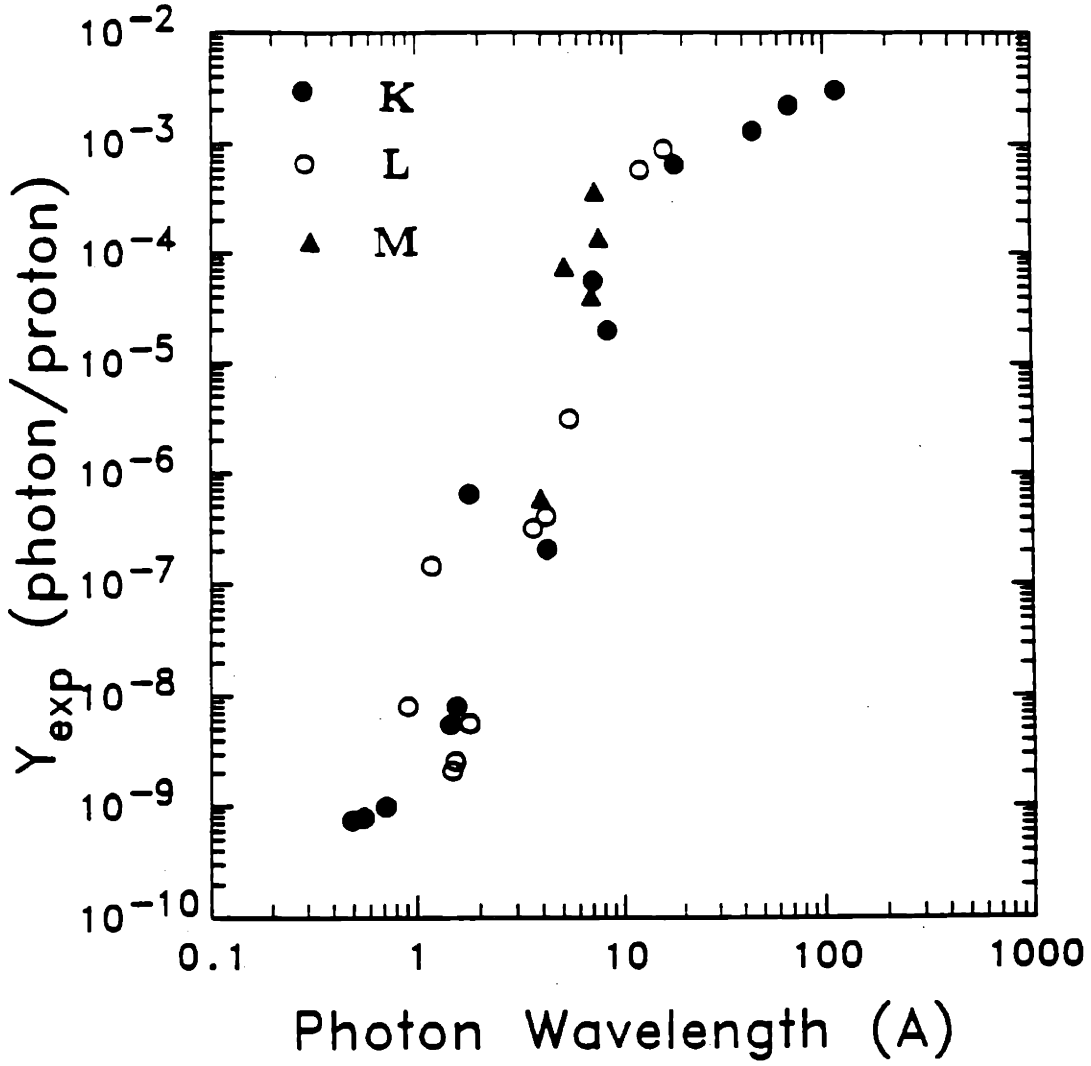

Figure 8-8: The PIXE x-ray yields are plotted as a function of the photon wavelength for K lines (solid circle), L lines (open circle), and M lines (solid triangle). For these data, protons were accelerated to 150 keV.

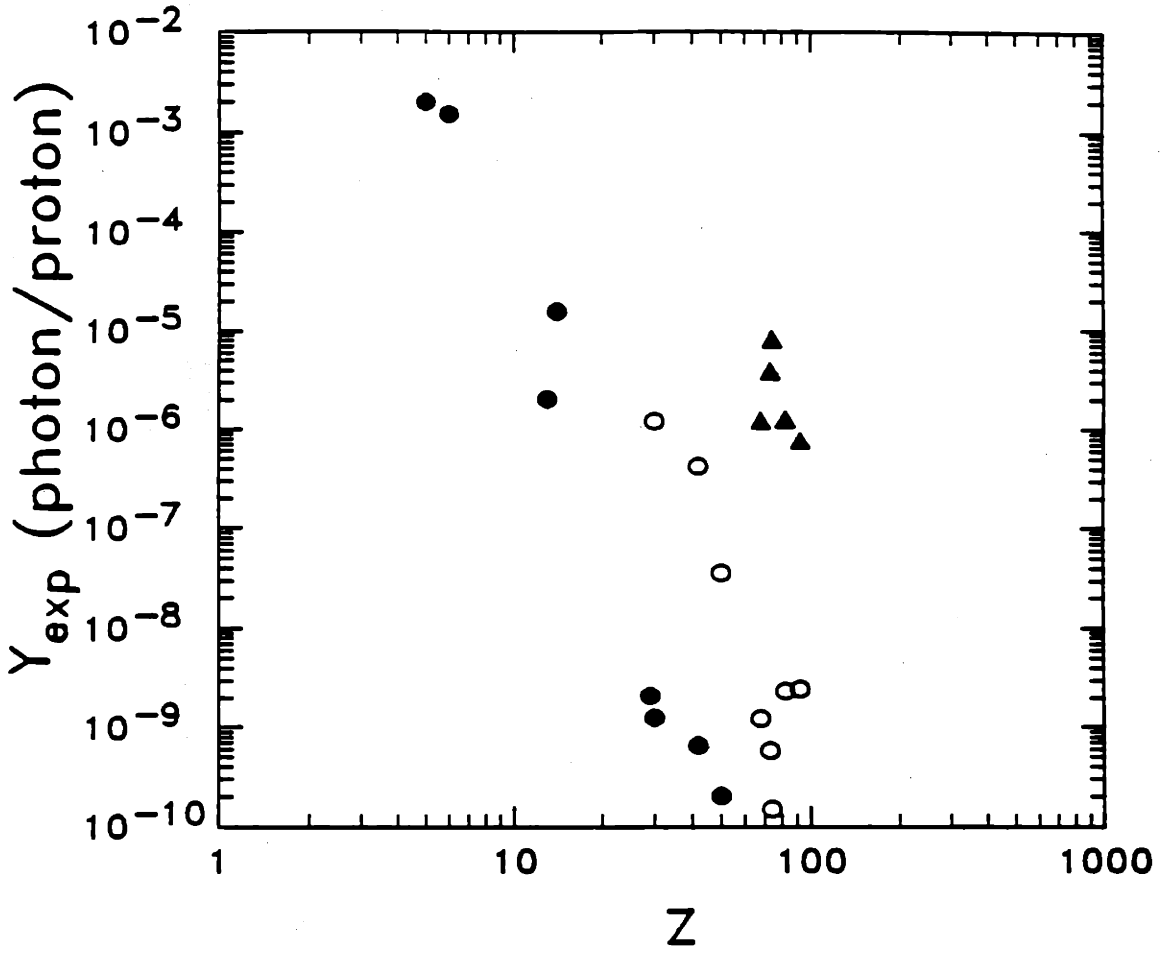

Figure 8-9: The PIXE x-ray yields are plotted as a function of the target atomic number for K lines (solid circle), L lines (open circle), and M lines (solid triangle). For these data, protons were accelerated to 150 keV.

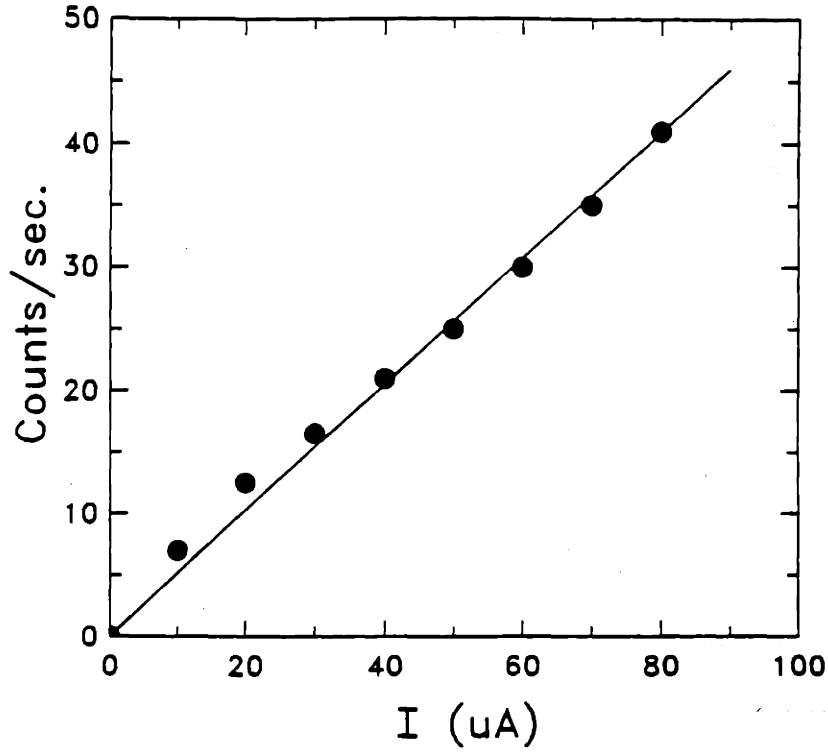

Figure 8-10: The copper PIXE x-ray count rate is plotted as a function of incident proton current. The flux is quite linear over a large dynamic range. For these measurements, the accelerator was operated at 150 kV.

the target atomic number. In addition, the PIXE flux produced in our Cockcroft-Walton linear accelerator is quite linear within a large dynamic range of incident proton currents, as shown in Fig.(8-10).

8.5 Comparison of Experimental Measurements and Theoretical Predictions.

In this section, we make a semi-quantitative comparison of the PIXE x-ray yields from our experimental measurements with theoretical estimations. Theoretical

calculations of the PIXE x-ray yields are complicated and strongly depend on many different physical parameters. Typically, these include ion stopping powers $[S(E)]$, ionization cross sections (σ_Z), x-ray fluorescence yields and radiative widths; the fraction of specific transitions, transmissions of x rays in the target, etc. Although the errors associated with these data bases have been improving, some parameters are still not well established. For example, the ionization cross section is only relatively accurate for certain materials, and from specific energy regimes. Therefore, our comparison is only semi-quantitative and is just used as a reference for our experiments. In addition, we will only present the K x-ray yields here since this theory is most reliable.

Theoretically, the PIXE x-ray yields $[Y(E)]$ are estimated from the following[125]

$$Y(Z) = \frac{N_{av}\omega_Z b_Z \epsilon_Z C_Z}{A_Z} \int_{E_0}^{0} \frac{\sigma_Z(E) T_Z(E) dE}{S(E)} \tag{8.3}$$

where N_{av} is the Avogadro's number, ω_Z is the x-ray fluorescence yield, b_Z is the fraction of the specific transition, ϵ_Z is the detection efficiency, C_Z is the concentration of the element Z (target), E_0 is the incident projectile energy, and A_Z is the atomic number of the target.

In addition, the matrix stopping power[81, 125] $[S(E)]$ is given by

$$S(E) = \frac{S_L S_H}{S_L + S_H} \frac{602.22}{A_Z} , \tag{8.4}$$

where

$$S_L = aE^b + cE^d , \tag{8.5}$$

and

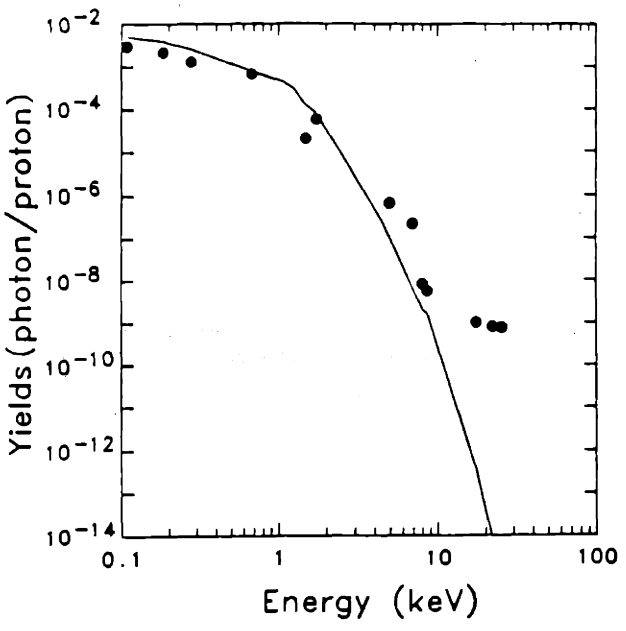

Figure 8-11: The comparison of experimental measurements K x-ray yields to theoretical estimations

$$S_H = \frac{e}{E^f} ln(\frac{g}{E} + hE) . \tag{8.6}$$

The ionization cross section[124, 125] is defined as

$$\sigma_Z(E) = \frac{1}{U_Z^2} exp\{\sum_{n=0}^{5} b_{Z,n}[ln(\frac{E}{\lambda U_Z})]^n\} , \tag{8.7}$$

and the x-ray transmission in target $[T_Z(E)]$ is defined as

$$T_Z(E) = exp\{-(\frac{\mu}{\rho})_Z \frac{cos\alpha_0}{cos\theta_{T_0}} \int_{E_0}^{E} \frac{dE}{S(E)}\} , \tag{8.8}$$

where μ is x-ray target mass absorption coefficients, ρ is target density, θ_{T_0} is the take-off angle of the x rays from the target plane, α_0 is the angle for ion beam off the target axis (for our case it is fixed to 0°). For simplicity, we used a semi-empirical formula for the ionization cross section which fails in the high x-ray energy regime[131], above 10 keV. This is illustrated in Fig. (8-11), where

the experimental measurements roughly agree in the low x-ray energy regime, but fail in the high x-ray energy regime.

8.6 Summary

A charged particle induced x-ray emission source (PIXE) has been developed for the purpose of characterizing x-ray detectors and optics, and measuring filter transmissions. It produces intense line x radiations from 0.5 Å to 111 Å. The background bremsstrahlung continuum is orders of magnitude lower than that from a conventional electron-beam x-ray source. For these reasons, we conclude that PIXE has important features as a tool for characterizing x-ray instrumentation.

Chapter 9

A High Intensity Electron-Beam X-Ray Generator

9.1 Introduction

To prevent target contamination and to avoid electron-beam slowing down in air, as well as some other secondary reasons, most commercially available x-ray tubes are permanently sealed within high vacuum ($\lesssim 10^{-8}$ Torr). Therefore, they can only provide $\gtrsim$ 4 keV (Ti K line) x rays because the vacuum seal produced by the tube window (typically mica) are opaque to low energy x rays. This problem limits the applications of these x-ray generators in many fields, especially in those requiring the absolute calibration of x-ray detectors and optics, or the relative calibration of x-ray imaging arrays in the ultra-soft x ray regime ($\sim$ 0.1 - a few keV). Because of this problem, an x-ray source which can generate uniform, intense soft x rays is highly desirable. However, to construct this kind of x-ray generator, several issues need to be addressed[141, 145].

1. The detector system must be placed inside the vacuum chamber.

2. The generator must be operated in high vacuum in order to keep the target clean. (Otherwise, the low energy electrons used for generating soft x rays would be rapidly attenuated within the contaminant layer of the target surface.)

3. Because of the very low fluorescence yields for low Z elements, the efficiency of generating ultra soft x ray lines is very low. To compensate for this, it is required that the source must be able to handle high power.

4. In order to obtain relatively uniform x rays in a large planar area, the distance and the spacing between the target and the detector system must be sufficient large.

9.2 Design and Construction of A High Intensity Electron Beam X-Ray Source

9.2.1 Design Philosophy

(1) Electron gun

The design of the electron-gun is a complicated issue which involves considerable physics such as electron emission, space-charge effects, etc. For our immediate objective, however, we don't need that complexity. Our design requirement is that the electron gun can generate high power and can provide an emission current up to $\simeq$ 300 mA. This being the case, the Richardson-Dushman equation[132] is used to estimate the emission current density,

$$J = A_0\, exp[-\frac{\alpha}{kT}]\, T^2\, exp[-\frac{\phi}{kT}]\ \ (A/cm^2)\ , \tag{9.1}$$

where A_0 is the Richardson constant, α is the extracting electric field correction, and ϕ is work function of the filament material. The exponential term

$exp[-(\alpha + \phi)/kT]$ is actually the dominant factor because it varies much more rapidly with temperature than the T^2.

(2) Target

The common disadvantage of the electron-beam x-ray source is that the production efficiency of the characteristic line radiation is quite low ($\lesssim 10^{-3}$)[79, 135], and most of the power generate heat and thereby increase the target temperature. The target itself may melt if too much power has been applied. The cooling of the target is therefore an important issue.

(3) Vacuum system

In order to obtain x-ray flux that is uniform on a detector plane, sufficient spacing is required between the target and the detectors (if this is case we can assume the x-ray source is nearly point like). This requires that the vacuum chamber be sufficient large. In addition, there must be enough space in the vacuum chamber to provide room for the filters and electronic equipment.

(4) Detector system

In order to detect ultra-soft x rays [$\lesssim$ 1 keV, such as Al K-line (1.5 keV), C K-line (0.28 keV), Be K-line (0.11 keV)], the detectors must be installed inside the vacuum chamber to avoid attenuation by any window materials and air. However, it is important that the detector system can be readily installed or manipulated within the chamber[141, 145].

9.2.2 Construction

According to the aforementioned design requirements, an existing vacuum chamber was selected. As depicted in Fig.(9-1), roughing pump II is used for preliminary vacuum evacuation while the turbo-molecular pump, which has a large

pumping rate (250 litres/min), is used for achieving high vacuum. A bare tungsten wire (10 mil in diameter) is twisted into a coil to form the filament. The power of the electron gun is either supplied by an isolated high-voltage transformer (for the case of the filament operating with a negative high-voltage bias. ie. the target is grounded), or directly supplied by a DC power supply (for the case of the target operating with a positive high-voltage bias). To obtain 300 mA of emission current, about 50 Watts of power is needed.

We have found using the configuration of grounding the filament and biasing the target positively eliminates spurious signals, that often plagued the alternative configuration (i.e negative biasing the filament while grounding the target). However, the second configuration does have the advantage that the target can be easily water cooled. Two DC high voltage power supplies were used alternatively for providing high voltage power. Fig.(9-2) shows the output voltage from one of them. It is found that when the DC voltage output is about 15 kV, the AC ripples are about 1 kV (peak-peak). In order to eliminate such undesirable ripples, we designed and built an RC power filter [the circuit is shown in Fig.(9-3)] which can provide satisfactory DC output. The distance between the filament and the target is about one inch. This power supply can provide a maximum voltage of up to 40 kV and a maximum emission current of up to 300 mA. An SBD is installed inside the chamber to monitoring the x-ray signal. In addition, a variety of filters are placed in front of the detectors to either check the attenuation or eliminate the bremsstrahlung background. For our current interests, the available targets are pure elements of C, Al, Ti, Cu, and Mo.

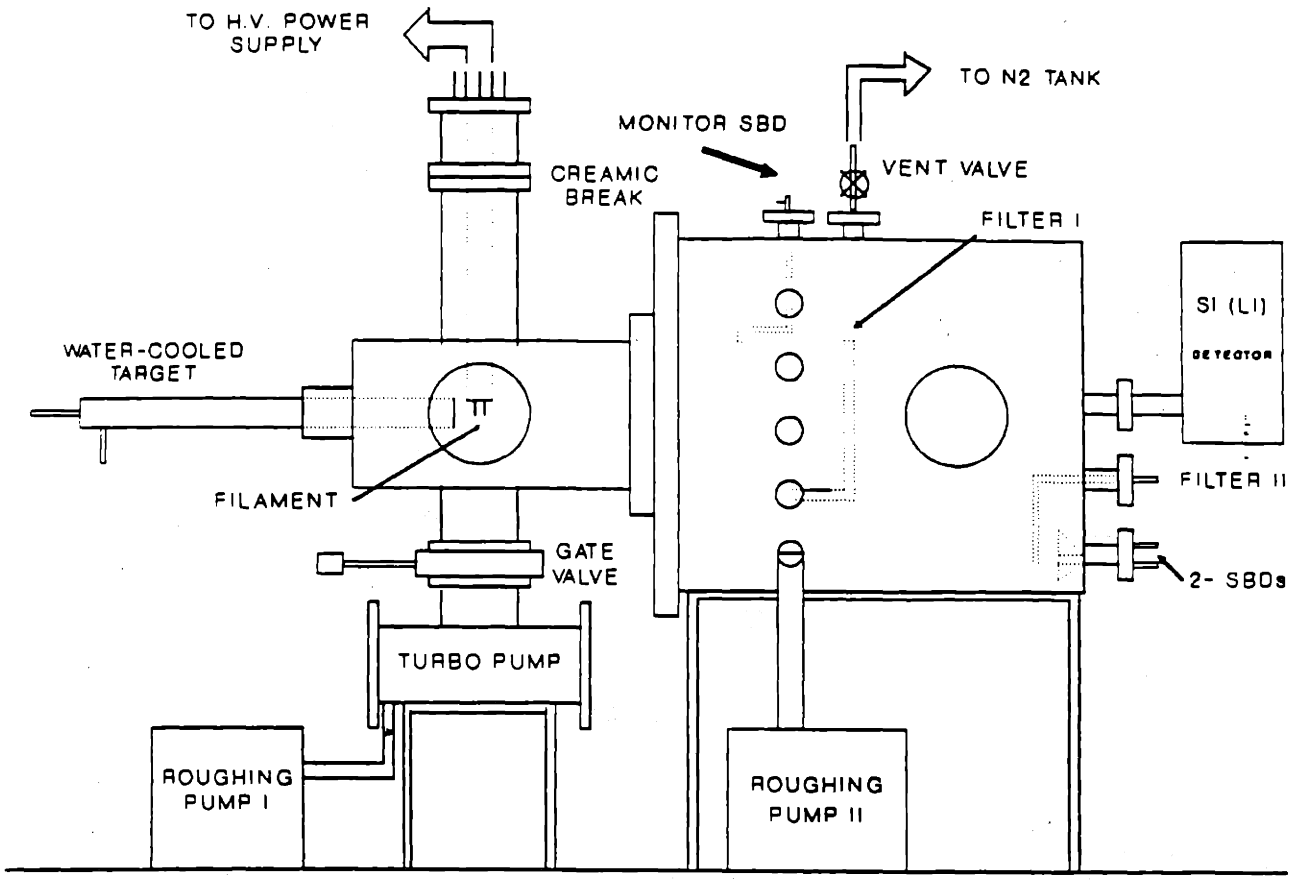

X-RAY SOURCE SCHEMATIC

Figure 9-1: The schematic of the high intensity electron-beam x-ray generator. The distance between the target and the detector system (on the back of the vacuum chamber) is $\gtrsim$ 1 m, and the detector chamber has a diameter $\simeq$ 0.6 m. Two pump systems, one for preliminary vacuum evacuation and the other for high vacuum pumping, are located underneath the chamber.

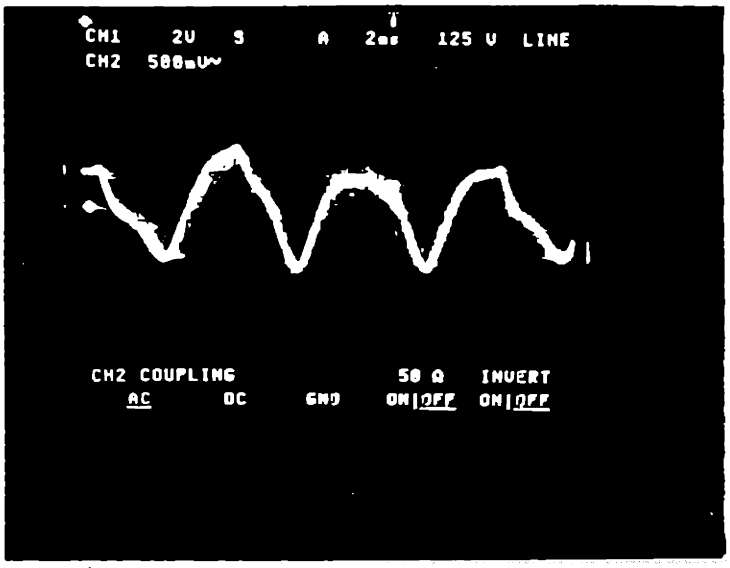

Figure 9-2: The high voltage output from a DC power supply shown in channel 2 measured by using a high-voltage probe. The AC ripples are about 1 kV (peak-peak) when the total DC output is 15 kV.

9.3 X-Ray Generator Characteristics

Three different classes of x-ray detectors have been utilized to characterize this x-ray generator: (1) two Si(Li) spectrometers; (2) a proportional gas-flow counter; (3) and several surface barrier silicon diodes. The first two class of detectors are operated in pulse mode, and the last one is operated in current mode.

9.3.1 Source X-Ray Spectra

The source x-ray spectra are shown in Figs.(9-4), (9-5), (9-6), (9-7), which were all measured using a Kevex Si(Li) spectrometer. In Fig.(9-4), the unfiltered aluminum K lines with some bremsstrahlung continuum are shown in figure (a). [The K_α and K_β lines cannot be separated due to the limit of energy resolution of this Si(Li) detector.] In figure (b) the filtered aluminum spectrum is given. For this measurement an aluminum filter of $\simeq 4$ mg/cm^2 was used and it was found that the pure aluminum K line x rays make up $\simeq$ 97% of the total x ray counts. Both

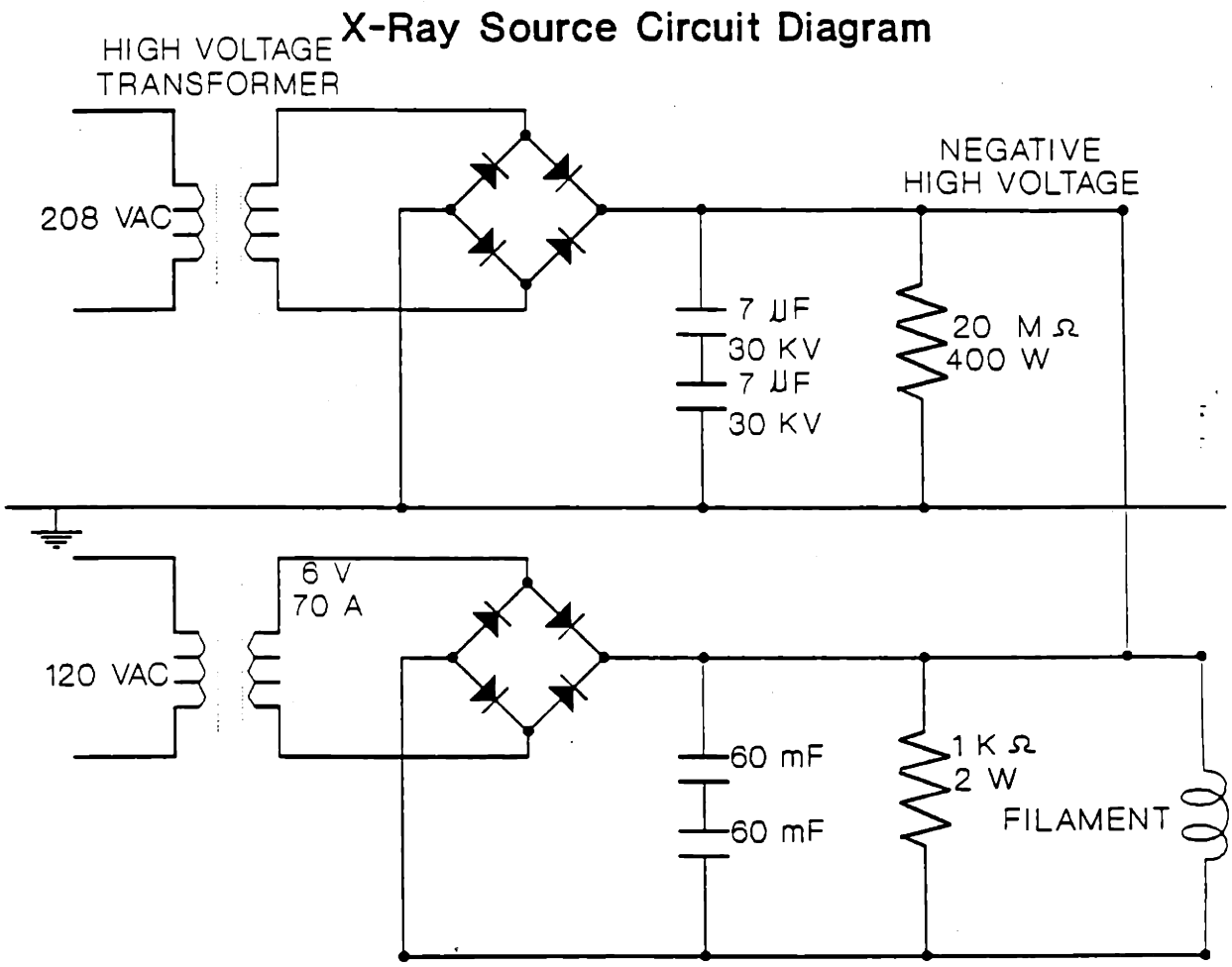

Figure 9-3: The circuit of the power-filter for high voltage power supply (upper circuit) and the filament (lower circuit).

spectra were taken by running the x-ray generator at 5 kV and emission current $\simeq$ 1 mA.

In Fig.(9-5a), the unfiltered Cu spectrum is shown. Fig.(9-5b) shows the filtered copper spectrum. For this measurement a copper filter of $\simeq$ 33 mg/cm^2 was used. for this configuration, $\simeq$ 94% of the total x ray counts are K emission. Both Cu spectra were taken by running the x-ray generator at 15 kV and emission current $\simeq$ 1 mA.

In Fig.(9-6), the unfiltered spectrum of molybdenum K lines superimposed on a strong bremsstrahlung continuum is given in figure (a). Compared to the unfiltered spectra of aluminum and copper, one finds that the bremsstrahlung from the molybdenum target is much stronger because molybdenum has a higher atomic number, Z=42 (for copper, Z=29; for aluminum, Z=13, and because the bremsstrahlung production efficiency is proportional to the target atomic number Z). In figure (b) the filtered molybdenum spectrum is given. For this measurement a molybdenum filter of $\simeq$ 64 mg/cm^2 was used and it was found that molybdenum K line x rays now make up $\simeq$ 70% of the total x ray counts. All spectra shown in Fig.(9-6) and (9-7) were taken by running x-ray generator at 30 kV and emission current $\simeq$ 1 mA. Note that in Fig.(9-7), an unfiltered molybdenum spectrum shows a very strong Mo L line around 2.5 keV. [Actually, it consists of several lines such as L_{α_1} (2.293 keV), L_{α_2} (2.289 keV), L_{β_1} (2.395 keV), L_{β_2} (2.516 keV), and L_{γ_1} (2.624 keV), etc.]

9.3.2 Source X-Ray Flux

The linearity of the x-ray flux is checked using an SBD, and the results were displayed in Fig.(9-8). The x-ray flux is linear at somewhat low levels and devi-

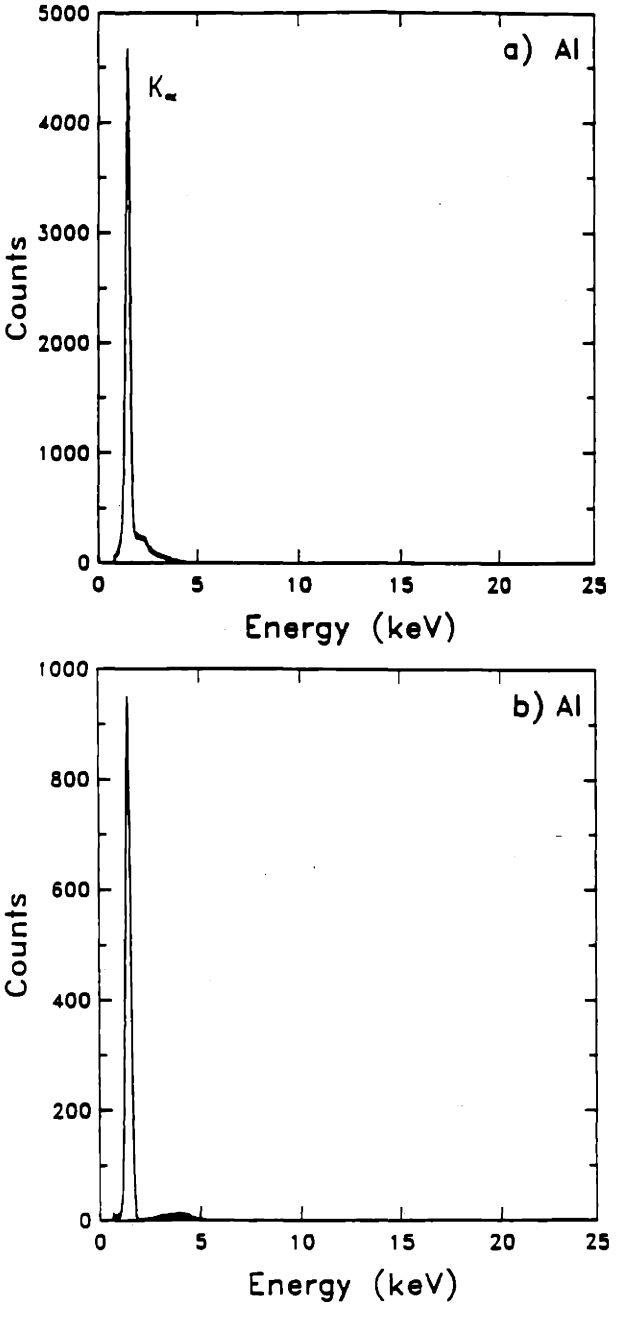

Figure 9-4: (a). An unfiltered aluminum spectrum. (b) A filtered aluminum spectrum. Both spectra were measured using a Kevex Si(Li) spectrometer.

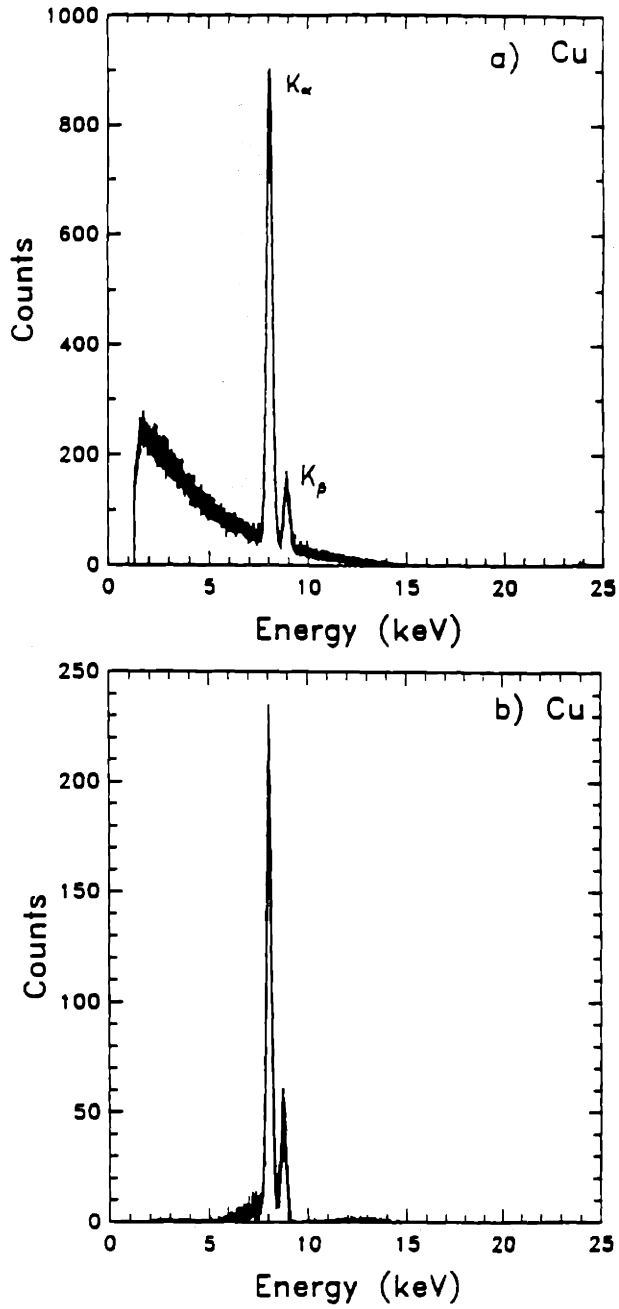

Figure 9-5: (a). An unfiltered copper spectrum. (b) A filtered copper spectrum. Both spectra were measured using a Kevex Si(Li) spectrometer.

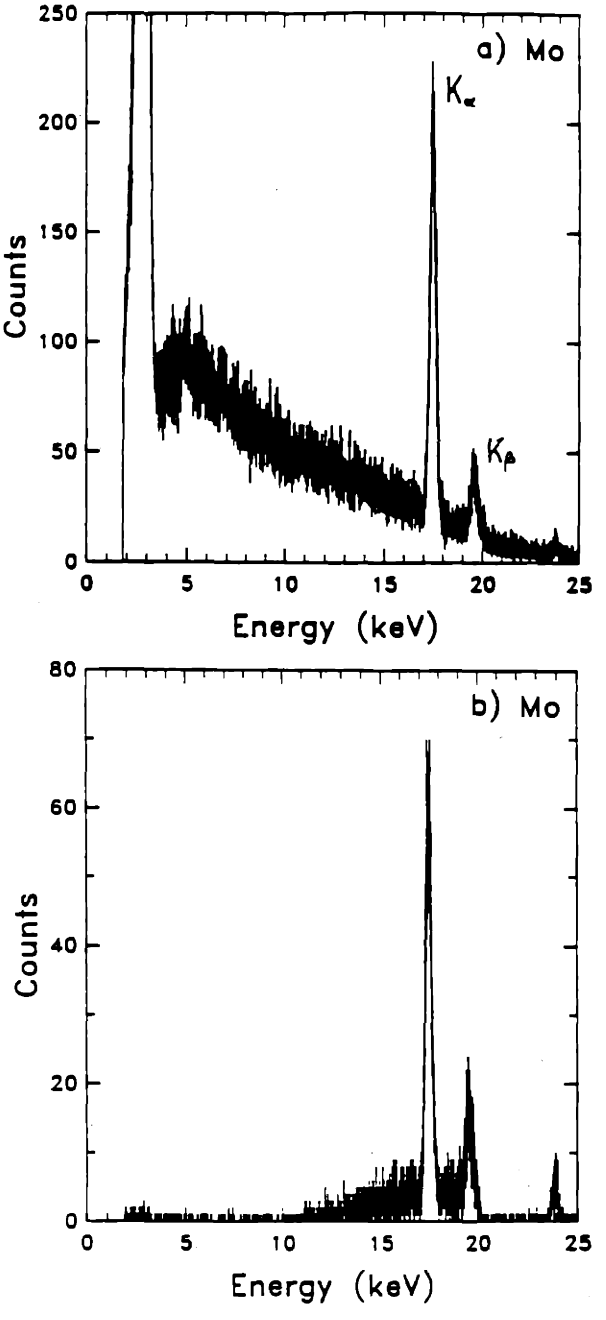

Figure 9-6: (a). An unfiltered molybdenum spectrum. (b) A filtered molybdenum spectrum. One finds that compared to the case in (a), the L-line has been significantly reduced. Both spectra were measured using a Kevex Si(Li) spectrometer.

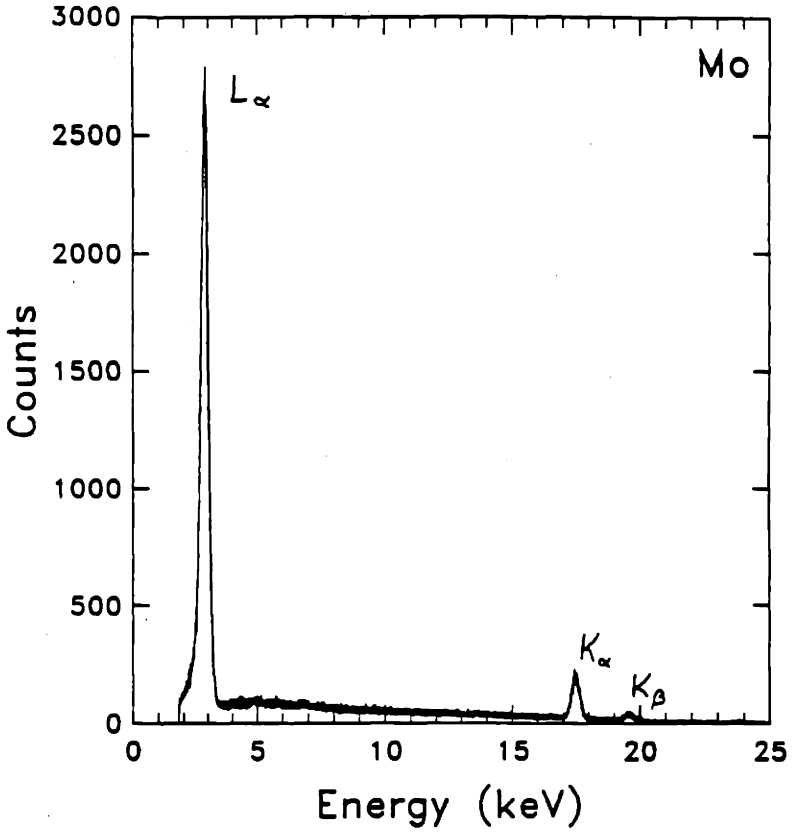

Figure 9-7: An unfiltered molybdenum spectrum shows a very strong Mo L line around 2.5 keV. (Same as Fig.(9-6a), but on different scale.)

ation above $\sim$ 20 mA are believed caused by the visible light leakages to which the detectors are sensitive. (The higher the emission currents the brighter is the filament.)

The uniformity of the x-ray flux is measured by an array of 4 SBDs aligned vertically. As shown in Fig.(9-9), the x-ray flux is relative uniform on an area of 40×12 cm^2. The maximum difference from center to the edge is about 40%. The difference between the top and bottom detectors is probably due to the filament holder obscuring certain detectors. The measurement was carried out in the configuration of negatively biasing the filament (grounding the Cu target). The time dependent fluctuating x-ray signal was also measured by placing a chopper in front

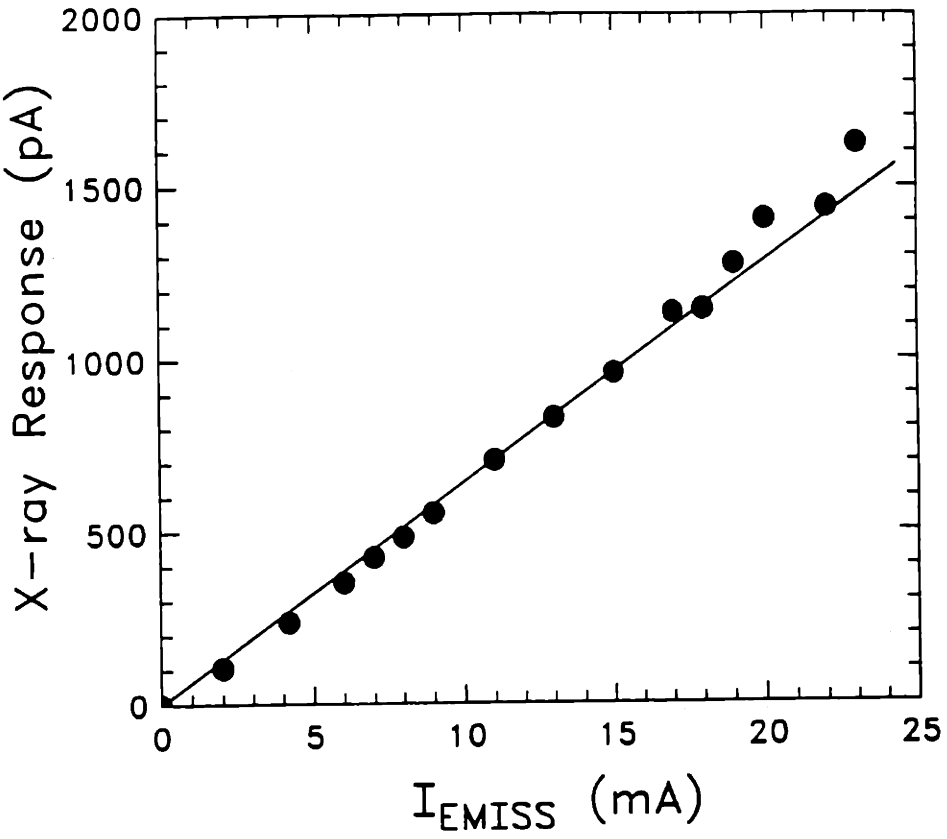

Figure 9-8: The linearity of the x-ray radiation.

of an SBD. As shown in Fig.(9-10), the chopper was operated at the frequency of $\simeq$ 660 Hz.

9.4 Calibration of X-Ray Detectors

As a first application[141], we used this self-built high intensity x-ray generator to absolutely calibrate X-UV silicon diodes. X-UV diodes, as introduced in Chapter 7, can be used as radiation monitors in many fields, especially in fusion plasma and astrophysics research, if their absolute response is known as a function of the photon energy. For these detectors, the measurements of the absolute response in the ultraviolet region ($\sim$ 10 - 150 eV) have been previously done[120, 143, 144]. Our calibration will cover the region between 1.5 keV and 17.5 keV. The experiments were performed by simultaneously measuring the signal outputs from the

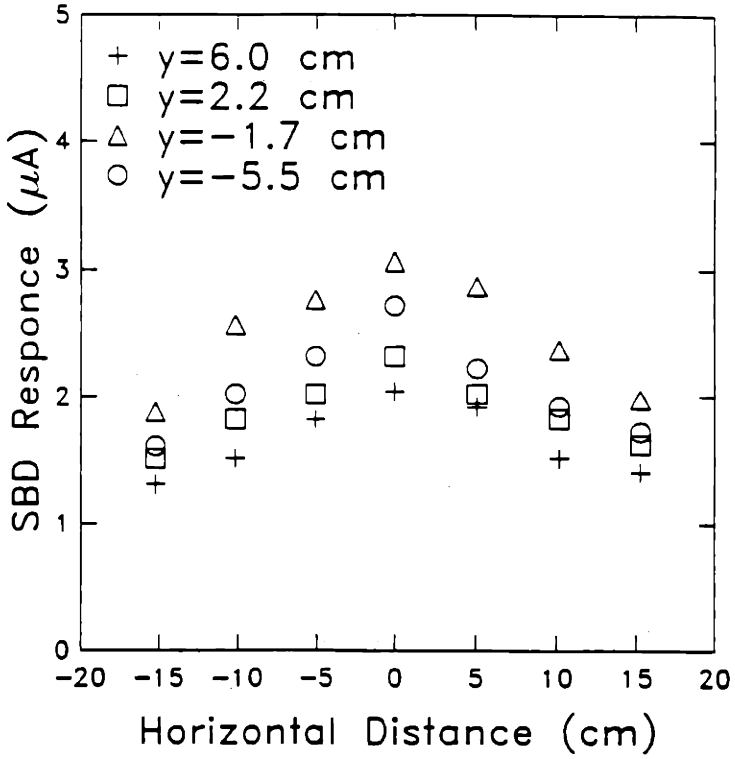

Figure 9-9: The uniformity of the x-ray radiation measured using 4 SBDs aligned vertically (y=0.0 cm corresponds to the center of target plane).

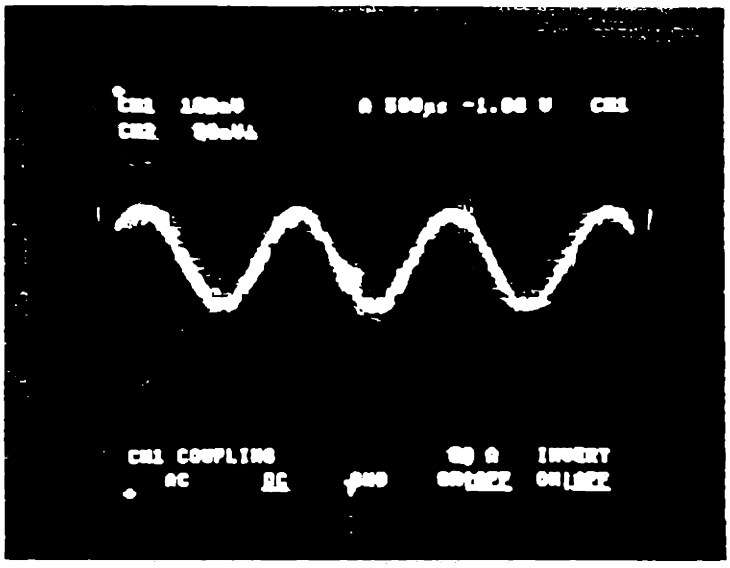

Figure 9-10: The $\simeq$ 660 Hz chopped SBD signal current provides a fluctuating x-ray signal.

X-UV diodes and an SBD. Both diodes were subject to the same conditions: faced the same target and had the same brass collimator with an aperture 0.32 cm in diameter. The SBD we used was a partially depleted SBD from EG&G ORTEC, serial number 16-675B, whose absolute x-ray response from 0.3 keV to 17.5 keV have been previously measured[100, 99]. In addition, the uniformity of the x-ray flux striking on both diodes was also checked by rotating them about an axis between the two detectors and repeating the measurements at rotation angles of 0°, 90°, 180°, and 270°[141].

(1) The monoenergetic x rays.

To measure the absolute response of X-UV diodes as a function of the photon energy, we need monoenergetic line radiations. However, like all other electron-beam x-ray sources, our generator also emits significant bremsstrahlung continuum. For this reason, we again used so-called absorption edge filter technique (typical filters we used for obtaining different quasi x ray lines are listed in Table 9.1). In addition the test filters are used to check the effectiveness of the line filters. Figs.(9-11), (9-12), (9-13), (9-14), and (9-15) display the filtered x-ray spectra of K line radiation from aluminum (1.5 keV), titanium (4.5 keV), manganese (5.9 keV), copper (8.05 and 9.8 keV), and molybdenum (17.5 and 19.8 keV). These spectra indicate that the characteristic x rays we used were satisfactorily clean for the calibration measurements.

Table 9.1:
The list of the material and thickness of filters

Target material	K_α-line (keV)	Test Filter	Line Filter
Al	1.5 keV	17 μm Al	17 μm Al
Ti	4.5 keV	17 μm Al	25 μm Ti
Cu	8.0 keV	86 μm Al	50 μm Cu
Mo	17.5 keV	86 μm Al	124 μm Mo

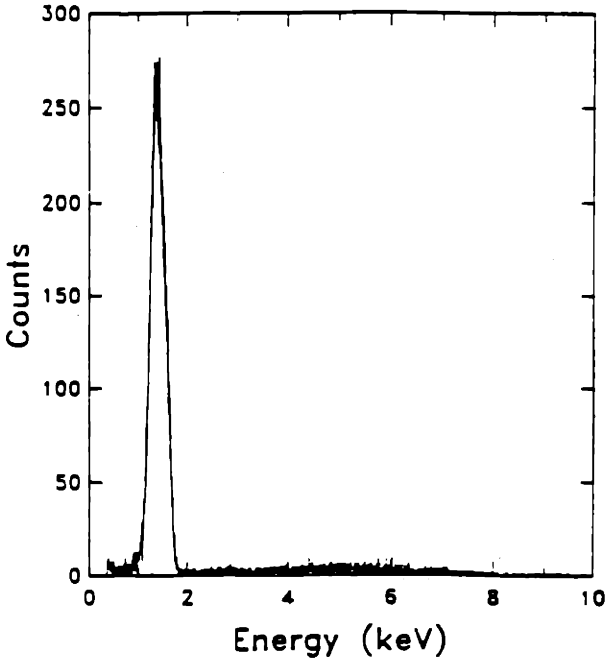

Figure 9-11: A filtered spectrum of Al K line from an aluminum anode (8 kV, 1 mA emission current). An EG&G ORTEC Si(Li) spectrometer was used for this measurement.

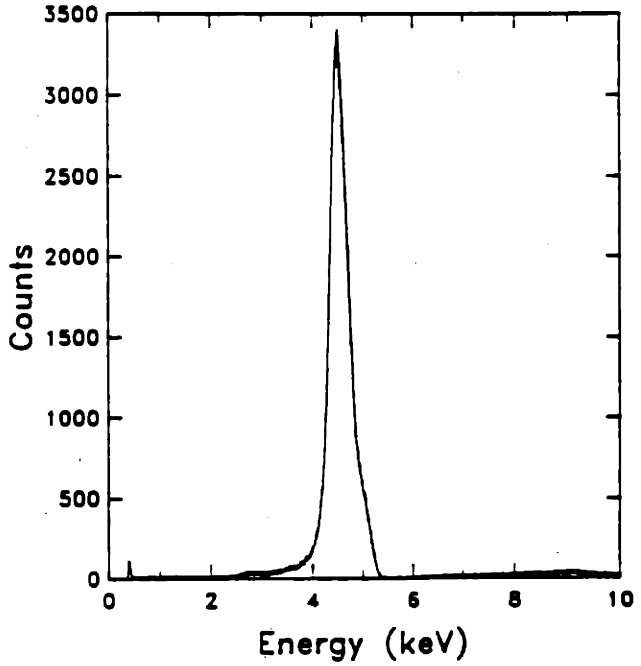

Figure 9-12: A filtered spectrum of Ti K line from a titanium anode (16 kV, 1 mA emission current). An EG&G ORTEC Si(Li) spectrometer was used for this measurement.

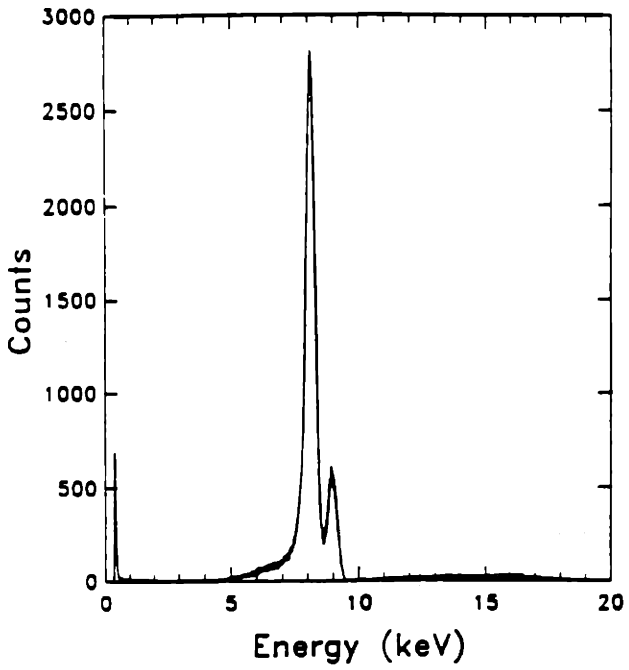

Figure 9-13: A filtered spectrum Mn K line from a manganese anode (^{55}Fe). An EG&G ORTEC Si(Li) spectrometer was used for this measurement.

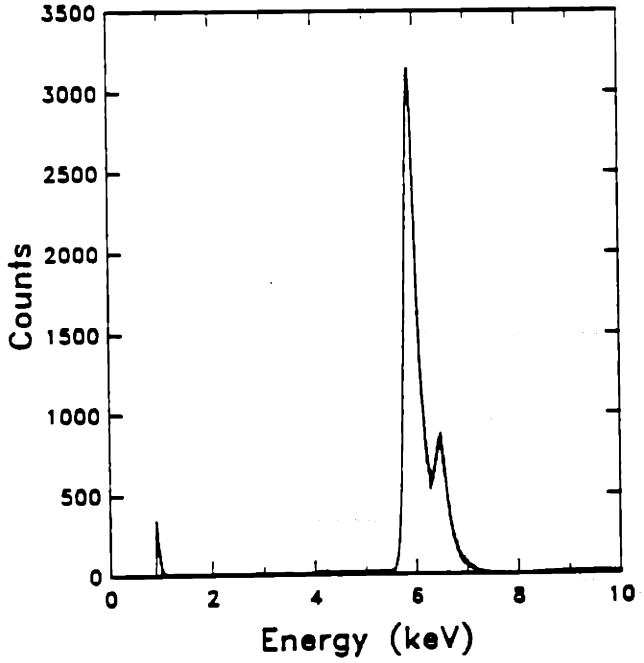

Figure 9-14: A filtered spectrum of Cu K line from a copper anode (20 kV, 1 mA emission current). An EG&G ORTEC Si(Li) spectrometer was used for this measurement.

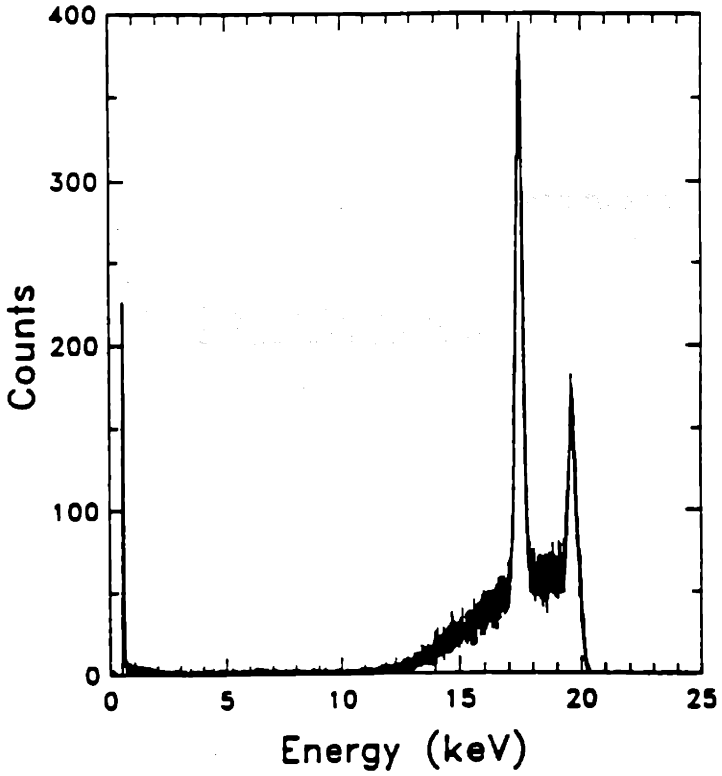

Figure 9-15: A filtered spectrum Mo K line from a molybdenum anode (25 keV, 1 mA emission current). An EG&G ORTEC Si(Li) spectrometer was used for this measurement.

(2) The measurements of DC response.

The measurements of DC response were performed when both diodes were operated in current mode. The positive signal currents from both detectors were simultaneously measured with two identical Keithley 617 digital electrometers. The background dark current, due to leakage current and a slight amount of visible light response, were monitored and subtracted from the total signal current to obtain the net x-ray signal current. Table 9.2 lists the ratio of measured DC response of $X-UV$ #1 to that of an SBD.

(3) The measurements of AC response.

In order to determine the effects of different bias voltages, we utilize AC x-ray

Table 9.2:
The measured DC responses of $X-UV$ #1 diode

X rays	Energy	I_{X-UV}/I_{SBD}
Al (K)	1.5 keV	$\simeq 1.06$
Cu (K)	8.0 keV	$\simeq 0.83$
Mo (K)	17.5 keV	$\simeq 0.63$

measurements. This method is effective because the leakage current increases dramatically when an external bias voltage is applied and the background current usually drifts. Therefore it is difficult to establish a stable DC background current (which is then subtracted from the total measured x-ray current). Utilizing the AC response, however, eliminates this undesired DC background current. For this reason, as well as many others, we built a preamplifier with a capacitor isolating the biased detector from the current-to-voltage amplifier. As displayed in Fig.(9-16), it is a 2 μF capacitor that filters the DC background current.

In order to generate an AC x-ray flux, we used a mechanical chopper placed Immediately in front of the diodes. This chopper has a chopper-wheel with 8 rectangular apertures. The chopping speed can be adjusted outside the vacuum chamber. The typical AC responses for different energy x rays of one of the X-UV diodes are shown in Fig.(9-17)[141]. It is found that the signal-to-noise ratio for molybdenum is worse than for the other targets. This is because at the maximum source high voltage (25 kV) for molybdenum, the efficiency for K line generation (17.5 keV) is low, relative to the other low Z targets [Fig.(9-17)].

(4) Summary the DC and AC Measurements

The DC and AC responses for three X-UV diodes and an SBD are summarized in Fig.(9-18)[141] where the measured result for each diode is plotted as a function of the photon energy. The solid lines are calculated responses for which silicon total

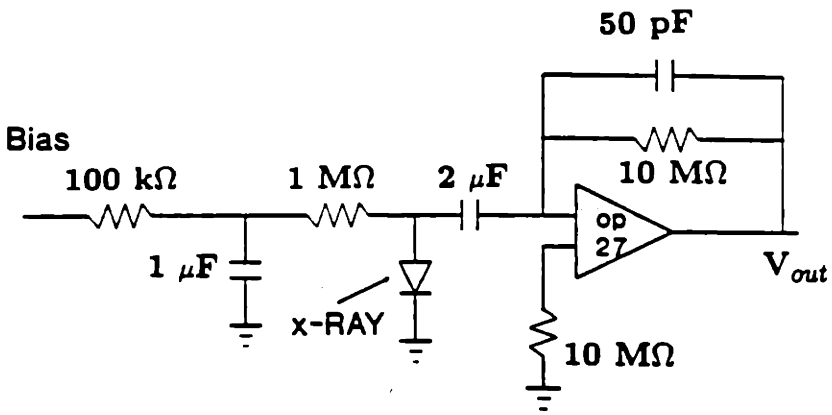

Figure 9-16: The circuit of an AC-coupled preamplifier. The 10 MΩ feedback resistor provides a gain of 10 mV/nA, and the 50 pF capacitor filtered out noise with frequency above 2 kHz.

thickness of 347 μm for the SBD and 375 μm for the X-UV diodes are assumed. It is found in these figures that the response of the X-UV diode decreases with the photon energy faster than the calculations predicted.

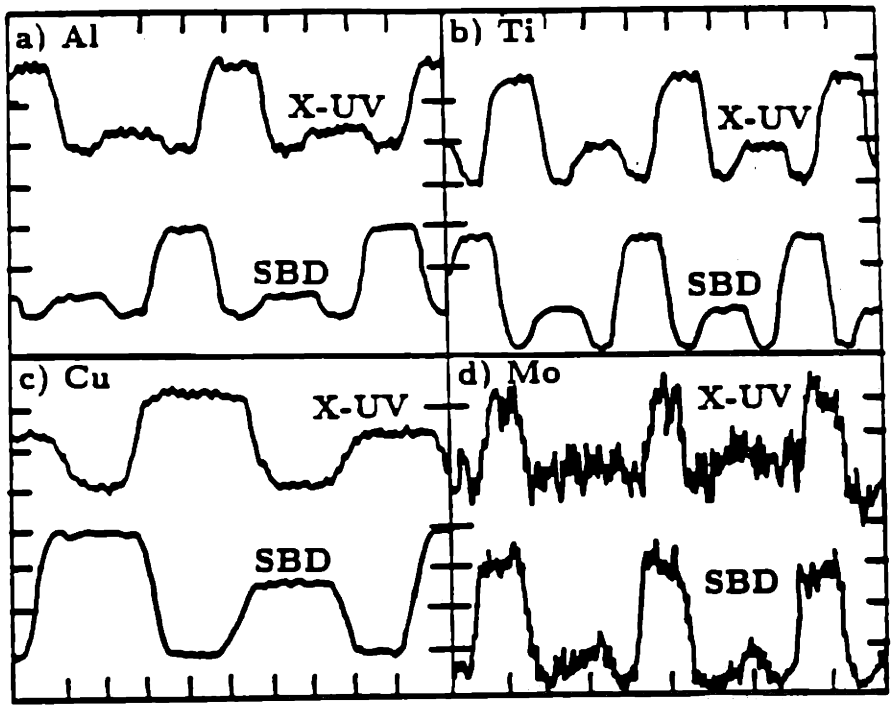

Figure 9-17: The typical measured AC response signals of an X-UV diode to K-line x rays of aluminum, titanium, copper, and molybdenum[141].

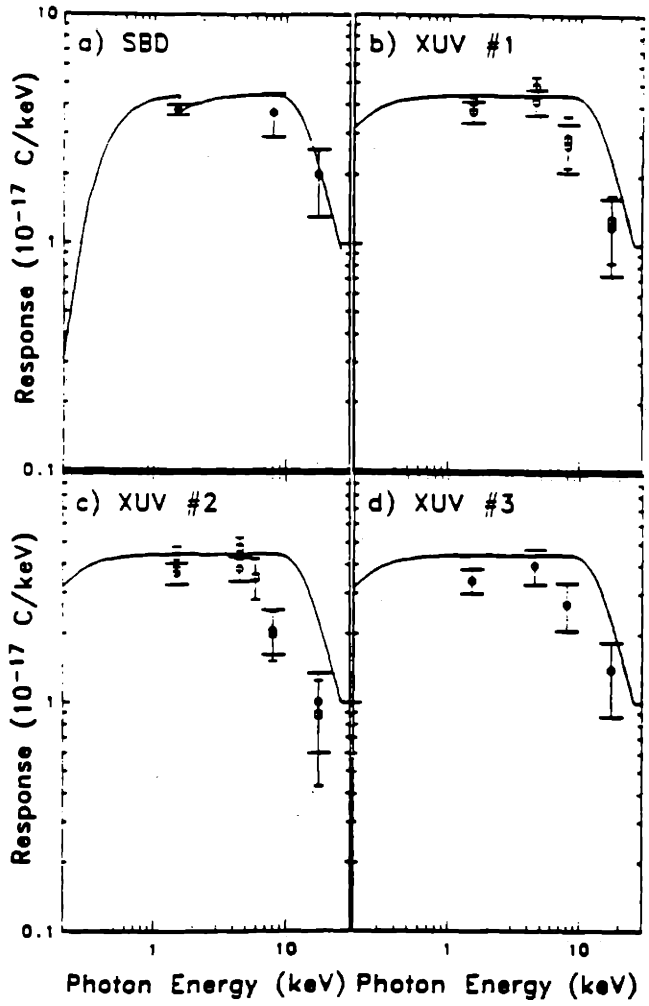

Figure 9-18: A summary of the DC and the AC responses as a function of photon energy. The DC responses are displayed by squares with narrower error bars and the AC responses are displayed by circles with wider error bars. The solid lines are calculated responses by assuming that the sensitive thickness is 347 μm for the SBD and 375 μm for the X-UV diodes[141].

Chapter 10

Comparative Study of the X-Ray Sources

10.1 Introduction

For the purpose of absolutely calibrating x-ray detectors and optics and measuring x-ray filter transmission, we comparatively investigated three kinds of x-ray sources: (1) a conventional electron-beam x-ray source; (2) a radioactive α fluorescence x-ray source (X-Ray KIT); and (3) a newly developed proton-induced x-ray emission (PIXE) source. Our studies are based on experimental and calculated results for both x-ray detection modes[145] (pulse and current). First, in the pulse mode of operation, x-ray spectra from these three sources are measured and compared with emphasis on line radiation and its relative intensity over the background continuum. In addition, the conventional absorption filter technique with the associated advantages and disadvantages will be discussed in this chapter. Second, in the current mode of operation, the x-ray flux from these three sources, from the point of view of absolutely calibrating silicon x-ray detectors, are semi-quantitatively estimated and compared.

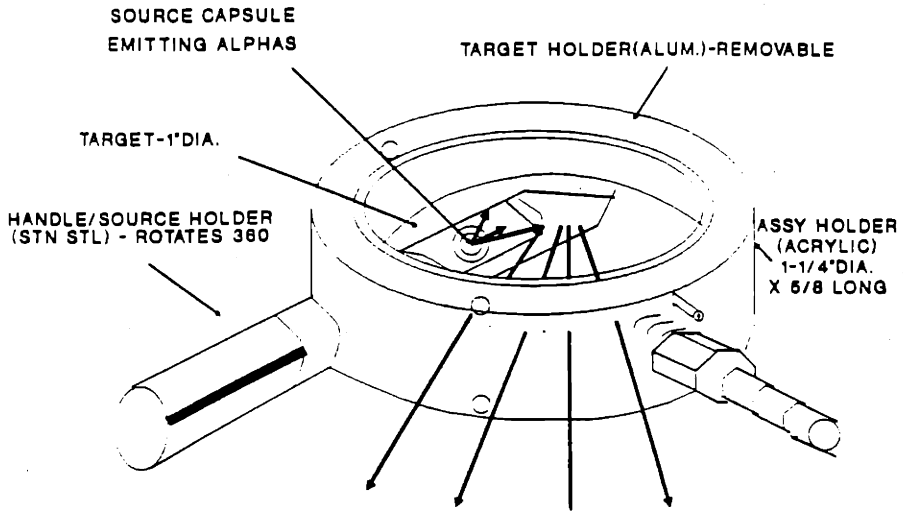

Figure 10-1: Schematic diagram of ^{244}Cm "X-Ray Kit" x-ray source.

10.2 X-Ray Sources

In addition to the electron-beam x-ray generator and the PIXE source described in previous chapters, the most common conventional x-ray source used in the laboratory with selectable wavelength is a spontaneous radioactively-decayed particle fluorescence source. This kind of x-ray source makes use of the energetic α's from radioactive isotope(s) (for example, ^{244}Cm, ^{241}Am, or ^{210}Po) to bombard various targets. Fig. (10-1) shows a commercially available, compact "X-Ray KIT"[146] with a ^{244}Cm radioactive source. The x rays are induced at the target by 5.9 MeV α's from the sealed ^{244}Cm source of 1 mCi (half life $T_{1/2} \simeq 17$ years). The replaceable target series includes C, Al, Ti, Cu, and Mo, etc. In order to detect very soft x rays, this X-Ray Kit source and the detector are all placed in vacuum. The schematic of the experimental arrangement for soft x-ray measurement using a flow proportional counter is depicted in Fig.(10-2).

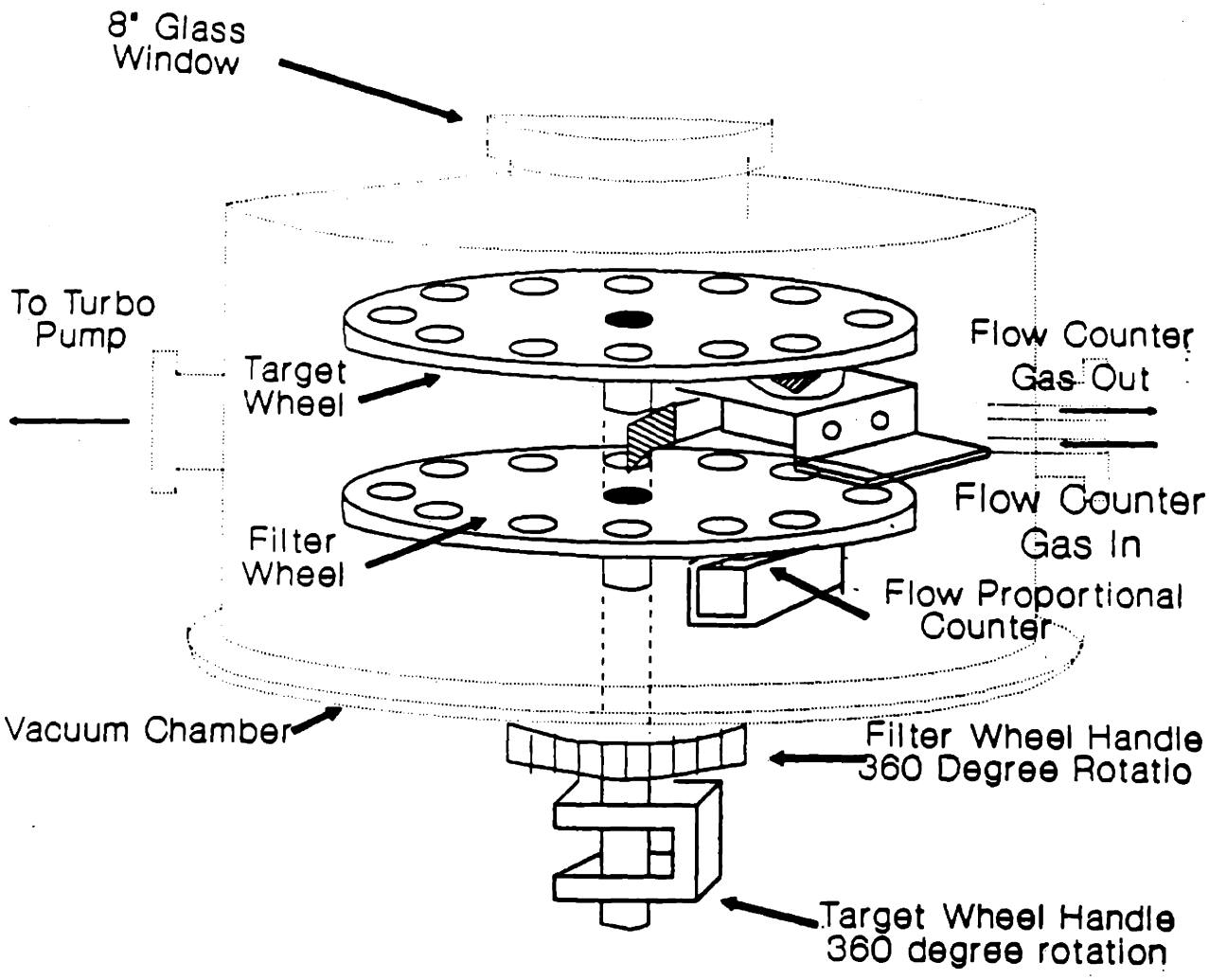

Figure 10-2: Schematic diagram of the X-Ray Kit experimental arrangement.

10.3 Comparison of the X-Ray Spectra

In Fig.(10-3), a comparison of the x-ray spectra of molybdenum from the PIXE, the X-Ray KIT, and the electron-beam source are made. For these measurements, a Si(Li) spectrometer was used. As expected and shown earlier, the PIXE spectrum has a remarkably low background continuum; in fact, the small background between K and L lines is actually caused only by Compton down-scattering from higher energy K lines. This argument can be justified from the fact that, for example, as shown in Fig.[10-3(a)], there are no counts of energy higher than Mo K lines even though the accelerator was operated at 150 kV. Bremsstrahlung from secondary electrons, which has an endpoint energy (head-on collision) of $4E_p(m_e/m_p)$ ($\simeq$ 300 eV for our case, where the proton energy E_p is 150 keV), are detectable only at a very low level (as discussed before). On the other hand, background continuum x-ray spectra from the electron-beam generator is orders of magnitude higher. For the x-ray spectra from the X-Ray KIT, the background continuum, on which the line radiation is superimposed, is also quite severe. Besides bremsstrahlung caused by secondary electrons (up to 3 keV) for this case, two other contributions are: (1) bremsstrahlung induced by Compton scattering in the target by the γ rays. These γ rays come from both α induced nuclear reaction in the target and from γ decay from the ^{244}Cm source, which have of energies 0.043 MeV, 0.1 MeV, 0.15 MeV, 0.262 MeV, 0.59 MeV, and 0.82 MeV etc. (2) Compton-down scattering of x rays and low energy γ rays directly from the ^{244}Cm source. A spectrum of these radiations directly measured from the ^{244}Cm are shown in Fig.(10-4). The individual lines have been identified and labeled in the figure, most of which are L and M lines from plutonium and uranium (the radioactive daughter and granddaughter of ^{244}Cm).

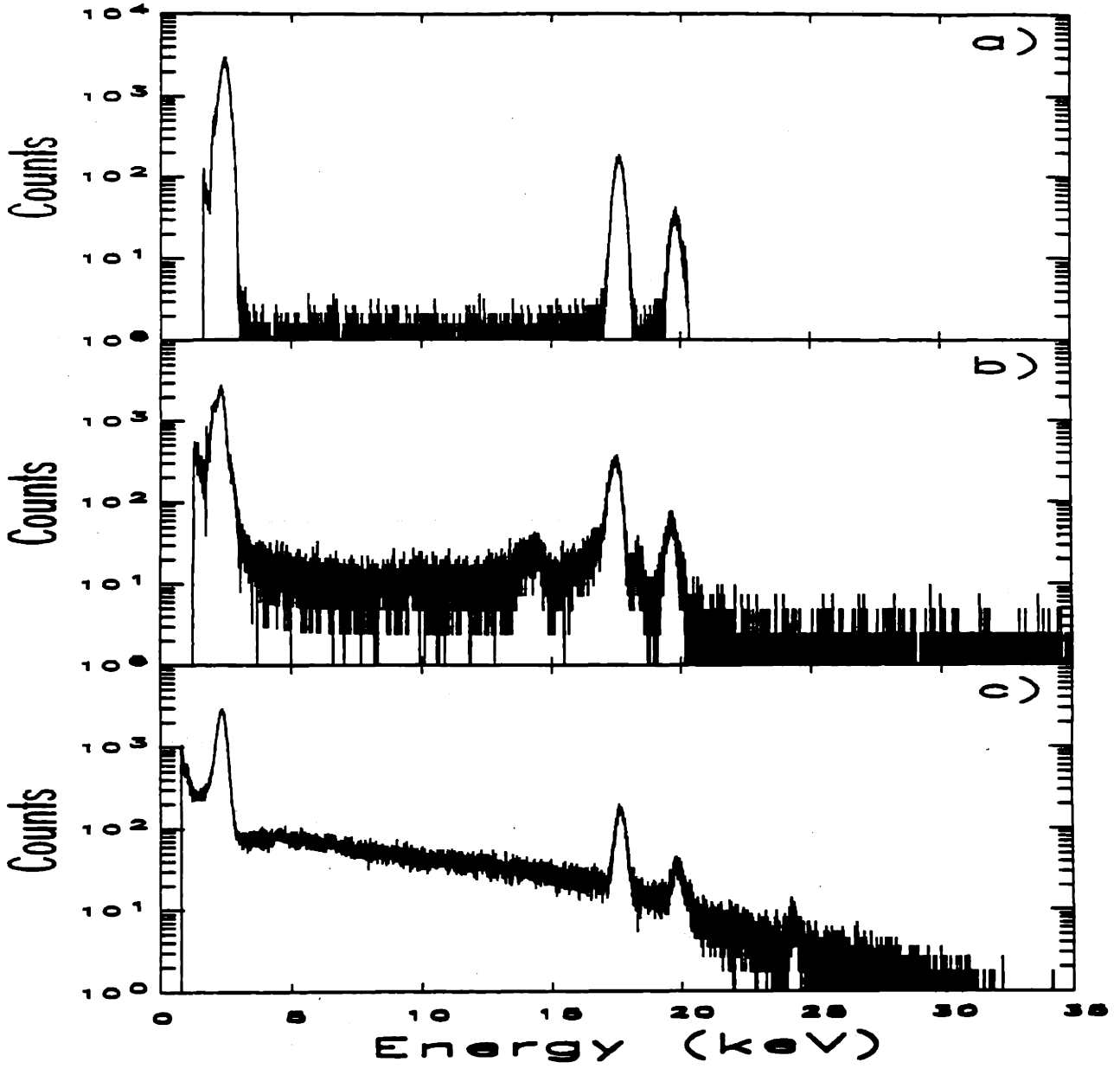

Figure 10-3: Spectra of molybdenum x rays, (a) from PIXE, (b) from X-Ray KIT, and (c) from an electron beam x-ray generator. A Kevex Si(Li) detector has been used for these measurements.

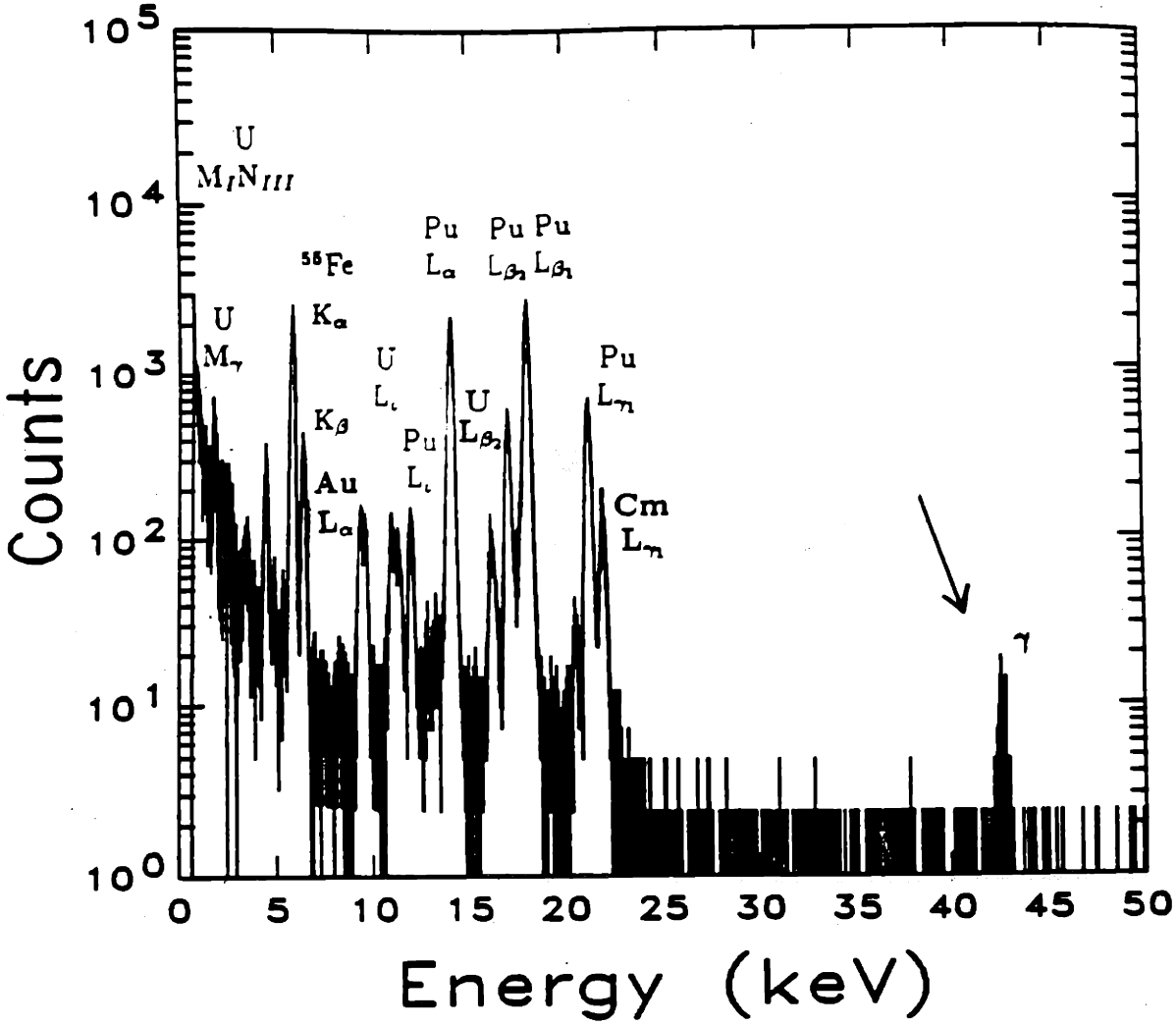

Figure 10-4: The x-ray and γ-ray spectrum of ^{244}Cm α recorded by placing the source directly in front of the Ortec Si(Li) detector. In order to avoid the 5.9 MeV α's directly hitting the detector, 1 mil plastic filter has been used. An ^{55}Fe (5.9 keV Mn K line) source is used as a reference. The x rays are resulted from L and M lines of ^{240}Pu and ^{236}U, the products of the first and second α-decays, and of ^{244}Cm fluoresced by α particles. The 9.71 keV x rays are x-ray fluoresced Au L_α lines from the Au electrodes of the Si(Li) detector. The 42.82 keV γ rays (see arrow) come from the tiny branch of α decay from ^{244}Cm to ^{240}Pu. All these, as shown before, contribute to the background continuum of the x-ray spectrum of the α fluoresced target.

10.4 Discussion

The PIXE x-ray spectra show the crucial feature of intense line radiation with negligible background continuum. For the applications of absolutely calibrating x-ray detectors and optics, and measuring x-ray filter transmission, this feature offers a unique advantage in that one doesn't need any technique to eliminate the continuum and not to shield out visible light. Practically, however, the application of this particular PIXE source is limited to providing characteristic x rays below a few keV (i.e. in ultra-soft x-ray regions) because of the low PIXE production cross section at the proton beam energy available to us ($\lesssim$ 165 keV). However, the maximum cross section for PIXE x-ray production occurs when the proton beam energy is of order MeV. In contrast to the PIXE source, the electron-beam x-ray source emits significant thick-target bremsstrahlung because of the $1/m_e$ dependence in the differential radiative cross section. Similarly, although it is fluoresced by α particles, X-Ray KIT also emits severe background continuum. And even worse, considerably wide background continuum region in the high energy regime [see Fig.(10-5), the high energy regime beyound the aluminum K line] is very difficult to be eliminated using conventional filter technique without sacrificing the desired line radiation.

Another issue for absolute calibration of x-ray detector is current-mode operation, which demands a significantly high signal to noise ratio. Because for SBDs the noise level is of order 1-100 pA (thermal noise, dark current, electronic noise, and other factors of the detectors,) in a practical experiment, the signal level needs to be of order nA - μA. Consequently, a large x-ray flux is required. Considering the factors such as the efficiency for generating line radiation ($10^{-4} - 10^{-3}$), the emission current (10 - 200 mA), the solid angle and the attenuations (due to bremsstrahlung and visible light rejections) etc., our electron-beam source is able to achieve a desirable x-ray flux for x-ray energy $\gtrsim$ 1 keV, but not for the

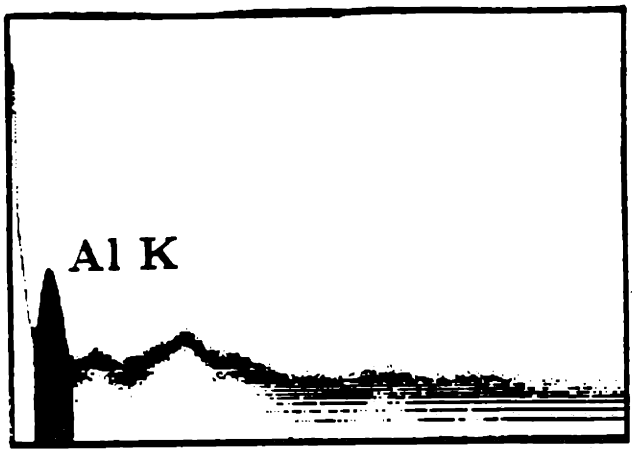

Figure 10-5: Spectra of Aluminum x rays from X-Ray KIT.

ultra-soft x rays ($\lesssim$ 1 keV). For our ^{244}Cm source, the α flux from the ^{244}Cm is too small [1 mCi activity ideally can only deliver $\sim$ 10^7 α's per second to the target (about 1 cm^2 in area)]. After taking into account factors like the efficiency of α fluorescence, solid angle and the source holder blockage, etc., one can only achieve a useful x-ray flux of $\lesssim 10^3$/sec-cm^2 at a distance of about 1 cm away. This small flux eliminates our X-Ray KIT from being a source for calibrating detectors operated in current mode. Also, the configuration of the ^{244}Cm prevents one from simultaneously monitoring the x-ray flux, so that this too makes it extremely difficult to make an absolute measurement. Consequently, if the x-ray flux is sufficient, PIXE offers unique advantages over either electron-beam or α fluorescence x-ray sources, specifically it can provide 10^{15} proton per second to the target (300 μA proton emission current); no filter is needed to obtain pure line radiation (this is a crucial point for ultra-soft x rays); the configuration (symmetric about two diagnostic arms) allows for easily making absolute calibration.

10.5 Summary

We comparatively investigated three different x-ray sources from the point of view of calibrating x-ray detectors and optics, and measuring x-ray filter transmission. A proton induced x-ray emission (PIXE) source has been demonstrated to be able to generate intense line radiation with extra low background continuum. This unique feature makes it possible for the PIXE source to be developed into an important tool for calibrating x-ray instruments, especially in the ultra-soft x-ray region. An electron-beam x-ray source is good for generating x rays having energy $\gtrsim$ 1 keV, but is very difficult to be developed to provide spectrally clean ultra-soft x rays. Our radioactive ^{244}Cm α fluorescence x-ray source is also found to be emitting a severe background continuum. In addition, it cannot be used for characterizing x-ray detectors operated in current mode.

Chapter 11

Summary and Recommendation for Future Work

11.1 Summary

In this thesis, two studies have been presented: first, the conceptual study of the moderately coupled plasmas; and second, the experimental comparison of laboratory x-ray techniques.

11.1.1 Conceptual Study of Moderately Coupled Plasmas

The fundamental concepts of moderately coupled plasmas, for which $ln\Lambda_b \simeq$ 2-10, were presented in Chapter 2. This classification is based not only on the plasma coupling parameter and the Coulomb logarithm, but also on the understanding and validity of the associated kinetic theories. This new regime is desirable because neither the conventional Fokker-Planck approximation (for weakly coupled plasmas) nor the approach of dielectric response with correlation function (for strongly coupled plasmas) satisfactorily addressing issues in moderately coupled

regime. A new collision operator, which is a compromise between the Fokker-Planck equation and the Boltzmann-like collision operator, was found to have advantages for treating moderately coupled plasmas. In addition, we have given a variety of examples for moderately coupled plasmas.

In Chapter 3, the standard Fokker-Planck operator for Coulomb collisions was modified by including terms that are directly associated with large-angle scattering. This procedure allows us to effectively treat plasmas for which $ln\Lambda_b \gtrsim 2$, i.e. moderately coupled plasmas. In particular, a Rosenbluth-like vector potential was introduced into the modified Fokker-Planck equation. Its properties and relations to other potentials have been discussed. Correspondingly, the Landau form and other forms of this modified equations have also been presented. By using this modified Fokker-Planck operator, moderately coupled plasmas can be effectively treated with a proper justification. In particular, precise calculations of some relaxation rates, and approximate calculations of electron transport coefficients, have been made (Chapter 4). In most cases, the results differ from Braginskii's and Trubnikov's results by terms of order $1/ln\Lambda_b$. However, in the limit of large $ln\Lambda_b$ ($\gtrsim 10$), these results reduce to the standard (Braginskii) form as expected. Some other interesting physical problems, such as the 90° electron scattering mean-free path in short-pulse laser plasmas and the collision frequency in the solar core, have also been discussed. In addition, we have calculated a reduced electron-ion collision operator that, for the first time, manifests the $1/ln\Lambda_b$ corrections.

As one of major applications of the modified Fokker-Planck equation, we have calculated the stopping powers and ρR of charged fusion products (α, ^{3}H, ^{3}He, . .) and hot electrons interacting with plasmas relevant to inertial confinement fusion pellet. As discussed in Chapter 5, the effects of scattering, which limited

previous calculations to upper limits, have been now properly treated. In this comprehensive calculation, the important effects of ion stopping, electron quantum properties, and collective plasma oscillations have also been included in a unified framework. We have demonstrated that the quantum effects are very important for the earlier dynamics of pellet evolution, especially in the shifting of the effective degenerate electron velocity which greatly enhances the charged particle stopping powers and shortens the range. Ion stopping is found to be important for all charged fusion products. For hot electrons interacting with cold dense plasmas, the contributions of scattering and collective oscillations are significant. An example of heavy ion stopping in ICF hohlraum plasmas was discussed in Chapter 6. It is found that the approach of classical binary interaction, supplemented by collective effects is adequate. The conventional restriction that requires the Coulomb logarithm $\gtrsim 10$ is unduly restrictive for this specific case. However, the stopping power in hohlraum plasmas must be dynamically treated because of the evolution of the plasma density. This finite temperature effect is significant for heavy ion stopping in a practical hohlraum plasma even for very high energy ions. In addition, we have compared the binary and dielectric response approaches for treating heavy ion interacting with hohlraum plasmas, and found that they are essentially the same in this regime. However the former approach is much simpler and physically transparent.

11.1.2 Experimental Comparison Laboratory X-Ray Sources

In Chapter 7, the fundamental theories of x-ray generation, both the discrete line radiation and background bremsstrahlung continuum, have been briefly reviewed. Three models for inner-shell ionization cross section (the plane-wave Born approximation, impulse approximation, and ECPSSR) have been discussed. In addition, we also reviewed issues of charged particle stopping in solid materials. Finally

two fundamental x-ray detection methodes, - - the pulse mode and current mode - - were briefly described. X-ray detectors that have been widely used in the laboratory such as the Si(Li) spectrometer and flow gas proportional counter (both for pulse mode), surface barrier diode and X-UV diode (for current mode), were discussed.

Of greatest importance in the x-ray generation, we used a Cockcroft-Walton linear accelerator, a charged particle induced x-ray emission (PIXE) source has been developed for the purpose of characterizing x-ray detectors and optics, and measuring x-ray filter transmission. Intense line x radiation (including $K-$, $L-$, $M-$, and N-lines) from 0.5 Å to 111 Å have been successfully produced. The background continuum is orders of magnitude lower than that from a conventional electron-beam x-ray source. We have also measured the PIXE x-ray yields for many elements. The yields roughly agree with the results from our theoretical estimate and with that from other researchers. This PIXE source has been demonstrated to be very useful as a tool for characterizing x-ray instrumentation, which have been described in detail in Chapter 8. In Chapter 9, we presented the development of a new high intensity electron-beam x-ray generator, including its detailed design, construction, characterization and application. Because the detector and monitor systems are all installed and operated inside the vacuum chamber, it is found that this new generator is very useful for calibrating x-ray detectors in the soft x-ray region. In particular, we have used this generator successfully to calibrate the new X-UV semiconductor diodes in both DC and AC modes. Finally in chapter 10, we have made an experimental comparison of these two newly developed x-ray sources with a commercially available α fluorescence x-ray source. In addition to characteristics of the target, ^{244}Cm α fluorescence x-ray source is found to emitting a non-negligible background continuum.

11.2 Recommendation for Future Work

11.2.1 Stopping Power (dE/dx) and Fuel-Areal Radius (ρR)

For future work, three experiments related to the measurements of stopping power and fuel-areal radius in ICF are of immediate interests.

A. Development of a Charged Particle Spectrometer for ρR Measurement

The energetic particles of primary interest are:

- 3 MeV D-D protons;
- 14.7 MeV protons from ^{3}He-D (the 0.8 MeV ^{3}He derives from D-D);
- 1 MeV tritons from D-D;
- $\lesssim$ 12.5 MeV deuterons from 14.1 MeV neutron knock-ons (D-T capsules);
- $\lesssim$ 10.6 MeV tritons from 14.1 MeV neutron knock-ons;
- 3.5 MeV α's from D-T.

The four possible phases involved in this program are to: (1) investigate possible candidates for the spectrometer (e.g. magnetic spectrometers, surface barrier detectors, etc.), and consider the signal-to-noise issues and the experimental feasibility; (2) design of hardware, utilizing the Cockcroft-Walton charged particle generator to test and validate design concepts; (3) construction, calibration, and fielding a detector; (4) and data collection and analysis.

B. A γ-ray Diagnostic for ρR Measurement

The measurement of γ rays from an ICF pellet offers a unique ρR diagnostic because the kinematic broadening of the γ-ray energy is very small. The γ ray of primary interest is from α capture,

$$\alpha + T \rightarrow {}^{7}Li + \gamma \,, \tag{11.1}$$

where the energy of the capture γ ray depends on α energy. In order to develop this diagnostic in our laboratory, the first step is to investigate the candidates for the γ-ray detector. This should be followed by the actual construction of the selected detector and, finally, its characterization. We believe that our experience on γ detection[147, 148] and our facilities, especially the Cockcroft-Walton accelerator, provide a unique opportunity for carrying out this project.

C. Measurement of Charged Particle Stopping in a Plasma

The measurement of charged particle stopping power in a plasma is of great importance to fusion plasma research. Many important theoretical predictions need to be verified experimentally in a plasma, such as the model of the effective equilibrium charge states of the projectile ions, the enhancement of the stopping power and shortening of the range of charged particle, etc. However, only a few experiments have been carried out so far. Our group possesses many fundamental attributes for performing this kind of experiment:

- the charged particle sources (Cockcroft-Walton accelerator and radioactive α sources);
- the plasma targets (self-built RF plasma and VTF tokamak plasma);

- the diagnostics for various measurements (plasma parameters, energy spectrometer, mass spectrometer, time-of-flight energy analysis, etc.).

D. Experiment for Non-Neutral Plasma Physics

Using our facilities, it will be interesting to investigate other non-neutral plasma physics related issues, such as pure electron plasma equipartition rates and confinement, space charge effects, etc.

11.2.2 Laboratory X-Ray Techniques

In order to advance plasma x-ray imaging technology through the testing of various detectors and the development of superior x-ray calibration techniques, several complementary programs can be start.

- Diamond photoconductors detectors have $\gtrsim 10^3$ greater resistance to neutron damage than the conventional (silicon) diodes presently used in x-ray arrays. Through the use of our x-ray calibration sources (PIXE, electron-beam, and radioactive) and our neutron generator, we can undertake studies of the temporal and spectral characteristics of these detectors before and after neutron irradiation.

- The pulsed x-ray source needs to be upgraded such that μsec time scales can be conveniently investigated. It is important to establish the frequency response of our x-ray array detectors if we are to later use them for studying rapid instabilities in plasma. In addition, we should also further modify the existing DC electron beam x-ray generator into a pulsed device.

- Work is needed to increase the x-ray emission levels of the PIXE source so that it can be used to calibrate detectors in the current mode, with high accuracy. The present PIXE x-ray emission levels, while adequate for filter and window calibration, are a factor 10 lower than needed for detector calibration in the current mode. By increasing our proton beam current as well as by redesigning our PIXE target chamber, a factor of 10 increase in incident intensity (on the detector) can be achieved. With this accomplishment, spectrally pure x-ray calibrations in the current mode would then be possible.

Appendix A

Calculations of the Modified Change of Moments.

A.1 Coordinates

The coordinate system is artificially chosen such that the relative velocity, **u**, is along the z axis as shown in Fig. (A-1). A test particle collides elastically with a fixed collision center (the field particle). After the collision the test particle velocity **u**′ changes direction but its magnitude remains unchanged.

From this configuration and the kinematics of the collisions, the only non-zero component of relative velocity is u_z. Thus the components of the change of the velocity are given by

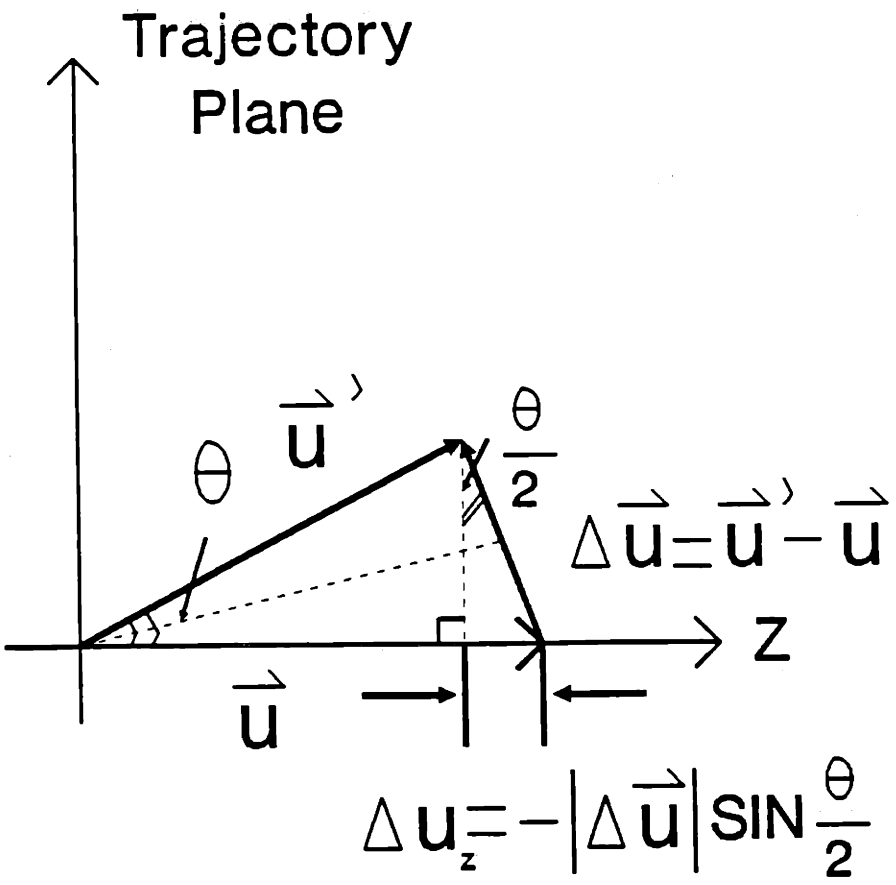

Figure A-1: The coordinate system used for calculation of the change of moments in velocity space.

$$\begin{cases} \Delta u_x = u\ sin\theta cos\phi \\ \Delta u_y = u\ sin\theta sin\phi \\ \Delta u_z = -u(1-cos\theta) \end{cases} \tag{A.1}$$

Since the scattering is due to the Coulomb interaction, one has $tan(\theta/2) = p_\perp/p$, and from which it follows

$$\begin{cases} \Delta u_x &= 2u\frac{pp_\perp}{p^2+p_\perp^2}cos\phi \\ \Delta u_y &= 2u\frac{pp_\perp}{p^2+p_\perp^2}sin\phi \\ \Delta u_z &= -2u\frac{p_\perp^2}{p^2+p_\perp^2} \end{cases} \tag{A.2}$$

A.2 Corrections to the Second-Order Change of Moment

In the course of the conventional evaluation of the second-order moment, the assumption that the Coulomb logarithm is greater than 10 has been made and all terms of the order of $1/ln\Lambda_b$ in the second-order moment have been neglected[3, 4, 6] (i.e. the parallel parts of the second-order moment, which contribute largely to the large-angle scattering.). But these terms need to be retained when we deal with plasmas in the transition regime (i.e. the moderately coupled plasmas for which $ln\Lambda_b \simeq$ 2-10). The rate of the change of the second-order moment is determined as follows,

$$< \Delta v_i \Delta v_j >^{t/f} = \int \mathbf{W}_{ij} f_f(\mathbf{v}') d\mathbf{v}' . \tag{A.3}$$

We hereafter follow the convention of Rosenbluth[3] and Trubnikov[4] as the start point, the second-rank tensor is defined as

$$\mathbf{W}_{ij} = (\frac{m_{tf}}{m_t})^2 \int\int \Delta u_i \Delta u_j u p dp d\phi \tag{A.4}$$

where f_f is the distribution function of the field particles in velocity space and m_{tf} is the reduced mass of the test and field mass system. In this coordinate system the second-rank tensor is a diagonal matrix, i.e.

$$\mathbf{W}_{ij} = \begin{pmatrix} \mathbf{W}_{xx} & 0 & 0 \\ 0 & \mathbf{W}_{yy} & 0 \\ 0 & 0 & \mathbf{W}_{zz} \end{pmatrix} \tag{A.5}$$

which can be determined by substituting Eq.(A.2) into Eq.(A.4) and performing the integrations. Thus

$$\mathbf{W}_{ij} = \frac{1}{4\pi u}(\frac{4\pi e_t e_f}{m_t})^2(ln\Lambda_b - \frac{1}{2})\delta_{ij} - \frac{1}{4\pi u}(\frac{4\pi e_t e_f}{m_t})^2(-ln\Lambda_b + \frac{3}{2})\frac{u_i u_j}{u^2} \; . \tag{A.6}$$

With the relations,

$$\frac{\partial}{\partial v_i}\frac{1}{|\mathbf{u}|} = -\frac{u_i}{u^3} \; , \tag{A.7}$$

and

$$\frac{\partial^2}{\partial v_i \partial v_j}|\mathbf{u}| = \frac{\delta_{ij}}{u} - \frac{u_i u_j}{u^3} \; , \tag{A.8}$$

and the Rosenbluth potentials:

$$H(\mathbf{v}) = -\frac{1}{4\pi}\int \frac{f_f(\mathbf{v}')}{|\mathbf{u}|} d\mathbf{v}' \; , \tag{A.9}$$

$$G(\mathbf{v}) = -\frac{1}{8\pi}\int |\mathbf{u}| f_f(\mathbf{v}')d\mathbf{v}' , \tag{A.10}$$

the rate of change of the moment is readily expressed as follows

$$\begin{aligned} < \Delta v_i \Delta v_j >^{t/f} &= \int \mathbf{W}_{ij} f_f(\mathbf{v}')d\mathbf{v}' \\ &= -2(\frac{4\pi e_t e_f}{m_t})^2 ln\Lambda_b \frac{\partial^2}{\partial v_i \partial v_j} G(\mathbf{v}) + (\frac{4\pi e_t e_f}{m_t})^2 [3\frac{\partial^2}{\partial v_i \partial v_j} G(\mathbf{v}) - \delta_{ij} H(\mathbf{v})] \end{aligned} \tag{A.11}$$

where δ_{ij} is a component of the unit tensor. Note that the second and third terms in this equation are usually dropped in the conventional Fokker-Planck equation.

A.3 The Third-Order Change of Moment

The third-order moment, which is also the order of Coulomb logarithm smaller than the first two standard moments, has not been previously determined in an explicit expression. The rate of change of the third-order moment is given by

$$< \Delta v_i \Delta v_j \Delta v_k >^{t/f} = \int \mathbf{W}_{ijk} f_f(\mathbf{v}')d\mathbf{v}' , \tag{A.12}$$

and the third-rank tensor can be calculated by

$$\mathbf{W}_{ijk} = (\frac{m_{tf}}{m_t})^3 \int\int \Delta u_i \Delta u_j \Delta u_k u p dp d\phi . \tag{A.13}$$

With this definition, the third-rank tensor is an axisymmetric matrix with some of its elements being zero. After substituting Eq.(A.2) into Eq.(A.13) and performing some algebraic manipulations, the third-rank tensor becomes

$$\mathbf{W}_{ijk} = -\frac{1}{8\pi}\frac{m_{tf}}{m_t}\left(\frac{4\pi e_t e_f}{m_t}\right)^2\left(\frac{u_i}{u}\delta_{jk}+\frac{u_j}{u}\delta_{ki}+\frac{u_k}{u}\delta_{ij}-\frac{u_i u_j u_k}{u^3}\right). \quad (A.14)$$

Since

$$\frac{\partial^2}{\partial v_i \partial v_j}\mathbf{u}|\mathbf{u}| = \frac{u_i}{u}\delta_{jk}+\frac{u_j}{u}\delta_{ki}+\frac{u_k}{u}\delta_{ij}-\frac{u_i u_j u_k}{u^3}, \quad (A.15)$$

we obtain the rate of change of the third-order moment as

$$<\Delta v_i \Delta v_j \Delta v_k>^{t/f} = -\frac{1}{8\pi}\frac{m_{tf}}{m_t}\left(\frac{4\pi e_t e_f}{m_t}\right)^2\frac{\partial^2}{\partial v_i \partial v_j}\int \mathbf{u}|\mathbf{u}| f_f(\mathbf{v}')d\mathbf{v}' . \quad (A.16)$$

Analogous to the Rosenbluth potentials[3, 4], we define a vector potential:

$$\mathbf{\Phi}(\mathbf{v}) = -\frac{1}{32\pi}\int \mathbf{u}|\mathbf{u}| f_f(\mathbf{v}')d\mathbf{v}', \quad (A.17)$$

with the reduced mass $m_{tf} = m_t m_f/(m_t + m_f)$. the third order change of moment is then expressed as utilizing this potential, the calculation of the third-order moment of the Fokker-Planck equation for some applications is substantially simplified:

$$<\Delta v_i \Delta v_j \Delta v_k>^{t/f} = 4\left(\frac{m_f}{m_t+m_f}\right)\left(\frac{4\pi e_t e_f}{m_t}\right)^2\frac{\partial^2}{\partial v_i \partial v_j}\mathbf{\Phi}(\mathbf{v}) . \quad (A.18)$$

Appendix B

Derivations of Relations for the First Three Moments of the Fokker-Planck Equation.

In this appendix, the relations of the first three moments in the modified Fokker-Planck equation are derived. As shown in Chapter 3, the first three moments are given

$$\begin{cases} < \Delta v_i >^{t/f} & = & -L^{t/f}(\frac{m_t+m_f}{m_f})\frac{\partial}{\partial v_i}H(\mathbf{v}) \\ < \Delta v_i \Delta v_j >^{t/f} & = & -2L^{t/f}\frac{\partial^2}{\partial v_i \partial v_j}G(\mathbf{v}) + \frac{L^{t/f}}{ln\Lambda_b}[3\frac{\partial^2}{\partial v_i \partial v_j}G(\mathbf{v}) - \delta_{ij}H(\mathbf{v})] \\ < \Delta v_i \Delta v_j \Delta v_k >^{t/f} & = & 4L^{t/f}\frac{1}{ln\Lambda_b}(\frac{m_f}{m_t+m_f})\frac{\partial^2}{\partial v_i \partial v_j}\Phi(\mathbf{v}) \end{cases} \tag{B.1}$$

The relations between the Rosenbluth potentials (H and G) and the new vector potential (Φ) are also given as,

$$\nabla_{\mathbf{v}}^2 \nabla_{\mathbf{v}} \cdot \mathbf{\Phi}(\mathbf{v}) = \nabla_{\mathbf{v}}^2 G(\mathbf{v})$$

$$= H(\mathbf{v}) \,. \tag{B.2}$$

B.1 Relation Between the First and Second Moments

By partial differentiating the second moment with $\frac{\partial}{\partial v_j}$, one has

$$\frac{\partial}{\partial v_j} < \Delta v_i \Delta v_j >^{t/f} = -2L^{t/f} \frac{\partial^3}{\partial v_i \partial v_j \partial v_j} G(\mathbf{v})$$

$$+ \frac{L^{t/f}}{ln\Lambda_b} [3 \frac{\partial^3}{\partial v_i \partial v_j \partial v_j} G(\mathbf{v}) - \delta_{ij} \frac{\partial}{\partial v_j} H(\mathbf{v})] \,. \tag{B.3}$$

Since

$$\frac{\partial^2}{\partial v_j \partial v_j} G(\mathbf{v}) = \nabla_{\mathbf{v}}^2 G(\mathbf{v}) = H(\mathbf{v}) \,, \tag{B.4}$$

and

$$\delta_{ij} \frac{\partial}{\partial v_j} = \frac{\partial}{\partial v_i} \,, \tag{B.5}$$

and substituting the first moment, thus

$$\frac{\partial}{\partial v_j} < \Delta v_i \Delta v_j >^{t/f} = (-2L^{t/f} + \frac{3L^{t/f}}{ln\Lambda_b} - \frac{L^{t/f}}{ln\Lambda_b}) \frac{\partial}{\partial v_i} H(\mathbf{v})$$

$$= \frac{2ln\Lambda_b - 2}{ln\Lambda_b} (\frac{m_f}{m_t + m_f}) < \Delta v_i >^{t/f} . \qquad \text{(B.6)}$$

Therefore, one obtains

$$< \Delta v_i >^{t/f} = \frac{ln\Lambda_b}{2ln\Lambda_b - 2} (\frac{m_t + m_f}{m_f}) \frac{\partial}{\partial v_j} < \Delta v_i \Delta v_j >^{t/f} . \qquad \text{(B.7)}$$

B.2 Relation Between the First and Third Moments

Similarly, by partial differentiating the third moment with $\frac{\partial^2}{\partial v_j \partial v_k}$, one has

$$\frac{\partial^2}{\partial v_j \partial v_k} < \Delta v_i \Delta v_j \Delta v_k >^{t/f} = \frac{4L^{t/f}}{ln\Lambda_b} (\frac{m_f}{m_t + m_f}) \frac{\partial}{\partial v_i} \frac{\partial^2}{\partial v_j \partial v_j} \frac{\partial}{\partial v_k} \mathbf{\Phi}(\mathbf{v}) . \qquad \text{(B.8)}$$

Since

$$\frac{\partial^2}{\partial v_j \partial v_j} \frac{\partial}{\partial v_k} \mathbf{\Phi}(\mathbf{v}) = \nabla_{\mathbf{v}}^2 \nabla_{\mathbf{v}} \cdot \mathbf{\Phi}(\mathbf{v}) = H(\mathbf{v}) , \qquad \text{(B.9)}$$

and substituting the first moment, thus

$$\frac{\partial^2}{\partial v_j \partial v_k} < \Delta v_i \Delta v_j \Delta v_k >^{t/f} = \frac{4L^{t/f}}{ln\Lambda_b} (\frac{m_f}{m_t + m_f}) \frac{\partial}{\partial v_i} H(\mathbf{v})$$

$$= -\frac{4}{ln\Lambda_b}(\frac{m_f}{m_t+m_f})^2 < \Delta v_i >^{t/f} \quad . \quad \text{(B.10)}$$

Therefore, one obtains

$$< \Delta v_i >^{t/f} = -\frac{ln\Lambda_b}{4}(\frac{m_t+m_f}{m_f})^2 \frac{\partial^2}{\partial v_j \partial v_k} < \Delta v_i \Delta v_j \Delta v_k >^{t/f} \quad . \quad \text{(B.11)}$$

Appendix C

Derivation of $ln\Lambda_C$ for Collective Plasma Oscillations.

In the dielectric response function approach, the stopping power due to field plasma oscillations is given by[68, 69, 70],

$$\frac{dE^{t/f}}{dx} = -\frac{2}{\pi}(\frac{Z_t e}{v_t})^2 Re \int_0^\infty \frac{i\omega}{\epsilon(\omega)}(\frac{\omega\lambda_D}{v_t})K_0(\frac{\omega\lambda_D}{v_t})K_1(\frac{\omega\lambda_D}{v_t})d\omega \ , \qquad (C.1)$$

where $K_0(\omega\lambda_D/v_t)$ and $K_1(\omega\lambda_D/v_t)$ are the modified Bessel functions, and the dielectric constant with damping constant σ is $\epsilon(\omega) = 1 - \omega_{pf}^2/(\omega^2 + i\omega\sigma)$. Because

$$Re[\frac{i\omega}{\epsilon(\omega)}] = \omega_{pf}^2 \frac{\omega^2\sigma}{(\omega^2 - \omega_{pf}^2)^2 + \omega^2\sigma^2}|_{\omega\simeq\omega_{pf}} \ , \qquad (C.2)$$

and since the significant frequencies in the integral turn out to be $\omega \sim \omega_{pf}$, one has

$$\frac{dE^{t/f}}{dx}|_{\omega\simeq\omega_{pf}} = -\frac{2}{\pi}(\frac{Z_t e}{v_t})^2(\frac{\omega_{pf}\lambda_D}{v_t})K_0(\frac{\omega_{pf}\lambda_D}{v_t})K_1(\frac{\omega_{pf}\lambda_D}{v_t})\int_0^\infty \omega_{pf}^2 \frac{\omega^2/\sigma^3}{(\frac{\omega_{pf}^2}{\sigma^2}-\frac{\omega^2}{\sigma^2})^2-\frac{\omega^2}{\sigma^2}}d\omega \ . \tag{C.3}$$

To perform this integral, let $\omega/\sigma = y$ therefore

$$\frac{dE^{t/f}}{dx}|_{\omega\simeq\omega_{pf}} = -\frac{2}{\pi}(\frac{Z_t e}{v_t})^2(\frac{\omega_{pf}\lambda_D}{v_t})K_0(\frac{\omega_{pf}\lambda_D}{v_t})K_1(\frac{\omega_{pf}\lambda_D}{v_t})\omega_{pf}^2\int_0^\infty \frac{y^2}{(\frac{\omega_{pf}^2}{\sigma^2}-y^2)^2-y^2}dy \ , \tag{C.4}$$

where the integral is evaluated through the identity

$$\int_0^\infty \frac{y^2}{(\frac{\omega_{pf}^2}{\sigma^2}-y^2)^2-y^2}dy = \frac{\pi}{2} \ . \tag{C.5}$$

Thus, the stopping power formula is given by

$$\frac{dE^{t/f}}{dx}|_{\omega\simeq\omega_{pf}} = -(\frac{Z_t e}{v_t})^2\omega_{pf}^2(\frac{\omega_{pf}\lambda_D}{v_t})K_0(\frac{\omega_{pf}\lambda_D}{v_t})K_1(\frac{\omega_{pf}\lambda_D}{v_t}) \ . \tag{C.6}$$

With the relation that

$$(\frac{\omega_{pf}\lambda_D}{v_t}) = \frac{v_f}{v_t} = \frac{1}{\sqrt{x^{t/f}}} \ , \tag{C.7}$$

and the definition of the Coulomb logarithm for such collective effects as

$$ln\Lambda_c = (\frac{\omega_{pf}\lambda_D}{v_t})K_0(\frac{\omega_{pf}\lambda_D}{v_t})K_1(\frac{\omega_{pf}\lambda_D}{v_t})$$

$$= \frac{K_0(1/\sqrt{x^{t/f}})K_1(1/\sqrt{x^{t/f}})}{\sqrt{x^{t/f}}} , \qquad (C.8)$$

the stopping power due to the collective plasma oscillations has the simple form of

$$\frac{dE^{t/f}}{dx} \simeq -\frac{(Z_t e)^2}{v_t^2}\,\omega_{pf}^2\,ln\Lambda_c . \qquad (C.9)$$

The Coulomb logarithm can further be reduced for extreme cases due to the asymptotic properties of the modified Bessel functions.

(1) For $\sqrt{x^{t/f}} \ll 1$,

$$K_0(\frac{1}{\sqrt{x^{t/f}}}) \simeq \sqrt{\frac{\pi\sqrt{x^{t/f}}}{2}}e^{\frac{-1}{\sqrt{x^{t/f}}}} , \qquad (C.10)$$

and

$$K_1(\frac{1}{\sqrt{x^{t/f}}}) \simeq \sqrt{\frac{\pi\sqrt{x^{t/f}}}{2}}e^{\frac{-1}{\sqrt{x^{t/f}}}}[1+\frac{3\sqrt{x^{t/f}}}{8}+\cdot\ \cdot\ \cdot\ \cdot\ ] . \qquad (C.11)$$

Therefore, the Coulomb logarithm is given by

$$ln\Lambda_c = \frac{K_0(\frac{1}{\sqrt{x^{t/f}}})K_1(\frac{1}{\sqrt{x^{t/f}}})}{\sqrt{x^{t/f}}}$$

$$\simeq \frac{\pi}{2}e^{\frac{-2}{\sqrt{x^{t/f}}}}[1+\frac{3\sqrt{x^{t/f}}}{8}] . \qquad (C.12)$$

(2) For $\sqrt{x^{t/f}} \gg 1$,

$$K_0(\frac{1}{\sqrt{x^{t/f}}}) \simeq -[ln(\frac{1}{2\sqrt{x^{t/f}}}) + 0.5772 + \cdot \quad \cdot \quad \cdot \quad \cdot \quad] . \qquad (C.13)$$

and

$$K_1(\frac{1}{\sqrt{x^{t/f}}}) \simeq \frac{\Gamma(1)}{2}(2\sqrt{x^{t/f}}) , \qquad (C.14)$$

Therefore the Coulomb logarithm is given by

$$ln\Lambda_c = \frac{K_0(1/\sqrt{x^{t/f}})K_1(1/\sqrt{x^{t/f}})}{\sqrt{x^{t/f}}}$$

$$\simeq ln(1.123\sqrt{x^{t/f}}) . \qquad (C.15)$$

In summary, the Coulomb logarithm for collective plasma oscillations is given

$$ln\Lambda_c \simeq \begin{cases} ln(1.123\sqrt{x^{t/f}}) & \sqrt{x^{t/f}} \gg 1 \\ \frac{K_1(1/\sqrt{x^{t/f}})K_0(1/\sqrt{x^{t/f}})}{\sqrt{x^{t/f}}} & \sqrt{x^{t/f}} \sim 1 \\ \frac{\pi}{2}e^{-\frac{2}{\sqrt{x^{t/f}}}} & \sqrt{x^{t/f}} \ll 1 \end{cases} \quad \text{(C.16)}$$

Bibliography

[1] L. D. Landau, *J. Phys. (U.S.S.R.)*, **10**, 154 (1936).

[2] L. Spitzer, *Monthly Notices Royal Astron. Soc.*, **100**, 396 (1940), L. Spitzer, *Physics of Fully Ionized Gases*, Interscience Publication, INC., (1956), L. Spitzer and R. Härm, *Phys. Rev.*, **89**(5), 977 (1953).

[3] M. N. Rosenbluth, W. M. MacDonald, and D. L. Judd, *Phys. Rev.*, **107**(1), 1 (1957).

[4] B. Trubnikov, *Review of Plasma Physics 1*, Consultants Bureau, New York, 1965.

[5] S. I. Braginskii, *Review of Plasma Physics 1*, Consultants Bureau, New York, 1965.

[6] D. C. Montgomery and D. A. Tidman, *Plasma Kinetic Theory*, McGeaw-Hill, Inc. New York, 1964.

[7] I. P. Shkarosky, T. W. Johnston, and M. P. Backynski, *The Particle Kinetics of Plasmas*, Addison-Wesley, Mass., 1966.

[8] W. L. Allis, *Handbuch der Physik*, Berlin: Springer, 1956, Vol 21, pp.383-444.

[9] I. B. Bernstein and S. K. Trehan, *Nuclear Fusion*, **1**, 3-41 (1960).

[10] R. D. Petrasso, *Nature*, (London) **343** (4), 21 (1990).

[11] S. Ichimaru, *Plasma physics*, Consultants Bureau, New York, 1965.

[12] S. Ichimaru, *et al. Physical Review A*, **32**(3), 1768-1798 (1985).

[13] X. Z. Yan, S. Tanaka, S. Mitake and S. Ichimaru, *Physical Review A*, **32**(3), 1785 (1985).

[14] "Strongly Coupled Plasma Physics," *Proceedings of Yamada Conference,* edited S. Ichimaru, (North-Holland, Amsterdam, 1990).

[15] C. K. Li and R. D. Petrasso, *Phys. Rev. Lett.*, **70**(20), 3063 (1993).

[16] C. K. Li and R. D. Petrasso, *Proceedings of Short Wavelength V: Physics with Intense Laser Pulse*, San Diego, CA, 29-31 March 1993.

[17] A. F. Alexandrov, L.S. Bogdankevich, and A. A. Rukhadze, *Principles of Plasma Electrodynamics*, Springer-Verlag, New York, 1984

[18] I. H. Hutchinson, *Course Note of Fusion Energy (1)*, Massachusetts Institute of Technology, (1987).

[19] J. P. Freidberg, *Course Note of Fusion Energy (1) and (2)*, Massachusetts Institute of Technology, (1988).

[20] M. E. Glinsky, T. M. O'Neil, M. N Rosenbluth, K. Tsuruta, and S. Ichimaru, *Phys. Fluids B*, **4**(5), 1156 (1992).

[21] T. M. O'Neil and P. G. Hjorth, *Phys. Fluids*, **28**(11), 3241 (1985).

[22] E. G. Gibson, *The Quiet Sun*, NASA, Washington, 1973.

[23] J. Hubbard, *Proc. Roy. Soc. Ser. A.*, **260**, 114 (1961), J. Hubbard, *Proc. Roy. Soc. Ser. A.*, **261**, 371 (1961).

[24] G. Ecker, *Theory of Fully Ion Plasmas*, Academic Press, New York, 1972.

[25] A. D. Fokker, Ann Phys. **43**, 812 (1914).

[26] M. Planck, *Sitzungsber. Preuss. Akad. Wiss. Phys. Math. Kl*, 324 (1916).

[27] S. Chandrasekhar, *Principle of Stellar Dynamics*, Dover Publications, INC. New York, 1943, S. Chandrasekhar, *Rev. Mod. Phys.*, **15**(1), 1 (1943).

[28] R. S. Cohen, L. Spitzer, and P. Mc. Routly, *Phys. Rev.*, **80**(2), 230 (1950).

[29] D. L. Book, *NRL Plasma Formulary*, (1990).

[30] "Strongly Coupled Plasma Physics," *Proceedings of Santa Cruz Conference,* edited F. J. Rogers and H. E. Dewitt, Plenum Press, New York, 1987.

[31] R. C. Davidson, *Physics of Nonneutral Plasmas*, (Addison-Wesley, Palo Alto, 1990).

[32] J. J. Bollinger and D. J. Wineland, *Scientific American*, **262**(1), 124 (1990); S. L. Gilbert, J. J. Bollinger and D. J. Wineland, *Phys. Rev. Lett.*, **60**(20), 2022 (1988).

[33] E. Y. Andrei, S. Yücel, L. Menna, *Phys. Rev. Lett.*, **67**(26), 3704 (1991).

[34] F. J. Rogers, H. E. Dewitt and D. B. Boercker, *Phys. Lett.*, **82 A**(7), 331 (1981).

[35] H. M. Milchberg, R. R. Freeman, S. C Davey, and R. M. More, *Phys. Rev. Lett.*, **61**(20), 2364 (1988).

[36] D. Riley, L. A. Gizzi, F. Y. Khattak, A. J. Mackinnon, S. M. Viana, and O. Willi, *Phys. Rev. Lett.*, **69**, 3739 (1992).

[37] J. Denavit, *Phys. Rev. Lett.*, **69**, 3052 (1992).

[38] A. Ng, D. Parfeniuk, P. Celliers, L. DaSilva, R. M. More, and Y. T. Lee, *Phys. Rev. Lett.*, **57**, 1595 (1986).

[39] W. L. Kruer, *The Physics of Laser Plasma Interactions*, Addison-Wesley publication company, 1988. W. L. Kruer, *Comments Plasma Phys. Controlled Fusion* **5**, 69 (1979).

[40] E. M. Epperlein, and R. W. Short, *Phys. Fluids B*, **3**(11), 3092 (1991); E. M. Epperlein, G. J. Rickard, and A. R. Bell, *Phys. Rev. Lett.*, **61**(21), 2453 (1988); E. M. Epperlein, G. J. Rickard, and A. R. Bell, *Comput. Phys. Commun.*, **52**, 7 (1988).

[41] G. J. Rickard, A. R. Bell, E. M. Epperlein, *Phys. Rev. Lett.*, **62**(23), 2687 (1989);

[42] A. R. Bell, R. G. Evans, and D. J. Nicholas, *Phys. Rev. Lett.*, **46**(24), 243 (1981).

[43] D. Shvarts, J. Dellettrez, R. L. McCrory, and C. P. Verdon, *Phys. Rev. Lett.*, **47**(4), 247 (1981).

[44] D. L. Matthews, P. L. Hagelstein, M. D. Rosen, M. J. Eckart, N. M. Ceglio, A. U. Hazi, H. Medecki, B. J. MacGowan, J. E. Trebes, B. L. Whitten, E. M. Campbell, C. W. Hatcher, A. M. Hawryluk, R. L. Kauffman, L. D. Pleasance, G. Rambach, J. H. Scofield, G. Stone, and T. A. Weaver, *Phys. Rev. Lett.*, **54**(2), 110 (1985); references therein. Private communication, 1993.

[45] M. D. Rosen, P. L. Hagelstein, D. L. Matthews, E. M. Campbell, A. U. Hazi, B. L. Whitten, B. MacGowan, R. E. Turner, R. W. Lee, G. Charatis, Gar. E. Busch, C. L. Shepard, and P. D. Rockett, *Phys. Rev. Lett.*, **54**(2), 106 (1985).

[46] J. N. Bahcall, *Neutrino Astrophysics*, Cambridge Univ. Press, New York, 1989; references therein.

[47] C. Shoub, *The Astrophys. J.*, **389**, 558 (1992).

[48] K. Molvig, *Course Note of Kinetic Theory,* Massachusetts Institute of Technology, (1990).

[49] C. K. Li and R. D. Petrasso, *Phys. Rev. Lett.*, **70**(20), 3059 (1993).

[50] L. Spitzer and R. Härm, *Phys. Rev.*, **89**(5), 977 (1953).

[51] J. R. Albritton, *Phys. Rev. Lett.*, **50**(26), 2078 (1983).

[52] J. P. Matte, T. W. Johnston, J. Delettrez, and R. L. McCrory, *Phys. Rev. Lett.*, **53**(15), 1461 (1984); D. Shavarts, J. Delettrez, R. L. McCrory, and C. P. Verdon, *Phys. Rev. Lett.*, **47**(4), 247 (1981).

[53] J. J. Duderstadt and G. A. Moses, *Inertial Confinement Fusion*, John Wiley & Sons, New York, 1982.

[54] D. J. Sigmar and G. Joyce, *Nucl. Fusion*, **11**, 447 (1971).

[55] D. J. Rose, *Nuclear Fusion*, **9**, 183 (1969).

[56] J. D. Lindl, R. L. McCrory, and E. M. Campbell, *Phys. Today*, **45**(9), 32 (1992).

[57] T. A. Mehlhorn, *J. Appl. Phys.*, **52**(11), 6522 (1981).

[58] N. Bohr, *Philos. Mag*, **25**, 10 (1913).

[59] S. Skupsky *Phys. Rev. A*, **16**(2), 727 (1977).

[60] N. R. Arista and W. Brandt, *Phys. Rev. A*, **23**(4), 1898 (1981).

[61] E. Nardi, E. Peleg, and Z. Zinaman, *Phys. Fluids*, **21**, 574 (1978).

[62] G. Maynard and C. Deutsch, *Phys. Rev. A*, **26**(1), 665 (1982).

[63] C. Deutsch, *Proc. of a NATO Advanced Res. Workshop on Strong Coupled Plasma Phys.*, Plenum Press, New York, 1987, C. Deutsch, P. Fromy, X. Garbet and G. Maynard, *Fusion Technology*, **13**, 362 (1988).

[64] M. D. Cable and S. P. Hatchett, *J. Appl. Phys.*, **62**(6), 2233 (1987); private communication, 1993.

[65] G. B. Zimmerman, Report No. UCRL-JC-105616, 1990 (unpublished).

[66] G. S. Fraley, E. J. Linnebur, R. J. Mason, and R. L. Morse, *The Physics of Fluids*, **17**(2), 474 (1974).

[67] *I. E. Tamm: Selected Papers*, p128, B. M. Bolotovskii and V. Ya. Frenkel (Editors), Springer-Verlag, New York, 1991.

[68] E. Fermi, *Phys. Rev.*, **16**(2), 727 (1943).

[69] D. Pines and D. Bohm, *Phys. Rev.*, **85**(2), 3 (1952).

[70] J. D. Jackson, *Classical Electrodynamics*, John Wiley & Sons, New York, 1975.

[71] D. J. Sigmar, *Course Notes of Plasma Transport Phenomenon*, Massachusetts Institute of Technology, 1989.

[72] R. Kubo, *Statistical Mechanics*, North-Holland Publication Company, Amsterdam, 1981.

[73] Y. T. Lee and R. M. More, *Phys. Fluids*, **27**(5), 1273 (1984).

[74] H. Azechi, N. Miyanaga, R. O. Stapt, K. Itoga, H. Nakaishi, M. Yamanaka, H. Shiraga, R. Tsuji, S. Ido, K. Nishhara, Y. Izawa, T. Yamanaka, and C. Yamanaka, *J. Appl. Phys.*, **49**(10), 555 (1986).

[75] R. S. Craxton, R. L. McCrory, and J. M. Soures *Scientific American*, **255**, 68 (1986).

[76] W.J. Hogan, R. Bangerter, and G. L. Kulcinski *Physics Today*, **45**(9), Sept. (1992).

[77] J. Meyer-ter-Vehn, *Plasma Phys. and Controlled Fusion*, **31**(10), 1613 (1989).

[78] S. Atzeni, *Europhys. Lett.*, **11**, 639 (1990).

[79] R. D. Evans, *The Atomic Nucleus*, McGraw-Hill, Inc. New York, 1955.

[80] J. Linhard, M. Scharff, and H. E. Schiott, Klg. Danske Videnslab. Selskab, *Mat. Fys. Medd.*, **33**(14), (1963).

[81] J. F Ziegler, *The Stopping and Ranges of Ions in Matter*, Pergamon Press, New York, 1985.

[82] L. C. Northcliffe and R. F. Schilling, *Nucl. Data Sect.*, **A 7**, 233 (1970).

[83] K. A. Brueckner, L. Senbetu, and N. Metzler *Phys. Rev. B*, **25**, 4377 (1982).

[84] S. Karashima, and T. Watanabe, *Laser and Particle beams*, **5**(3), 525 (1987)

[85] A. Dar, J. Grunzweig-Genossar, A. Peres, M. Revzen, and A. Ron, *Phys. Rev. Lett.*, **32**(23), 1299 (1974).

[86] J. N. Olsen *et al.*, *J. Appl. Phys.*, **58**(11), 2958 (1985).

[87] F. C Young, D. Mosher, S. J. Stephanakis, Shyke A. Goldstein, and T. A. Mehlhorn, *Phys. Rev. Lett.*, **49**, 549 (1982).

[88] D. H. H. Hoffmann, K. Weyrich, H. Wahl, D. Gardes, R. Bimbot and C. Fleurier, *Phys. Rev. A*, **42**(4), 1251 (1990).

[89] K. G. Dietrich, K. Mahrt-Olt, J. Jacoby, E. Boggasch, M. Winkler, B. Heimrich, and D. H. H. Hoffmann, *Laser and Particle beams*, **8**(4), 583 (1990)

[90] H. D. Betz, *Rev. Mod. Phys.*, **44**, 465 (1972).

[91] J. S. Forster, D. Ward, H. R. Andrews, G. C. Ball, G. J. Costa, W. G. Davis, and I. V. Mitchell, *Nucl. Instrum. Mehodes*, **136**, 349 (1976).

[92] B. S. Yarlasadda, J. E. Robinson, and W. Brandt, *Phys. Rev. B*, **17**(9), 3473 (1978).

[93] E. Nardi and Z. Zinaman, *Phys. Rev. Lett.*, **49**, 1251 (1982).

[94] Th. Peter, *Laser and Particle beams*, **8**(4), 643 (1990)

[95] M. Brown and C. D. Moak, *Phys. Rev. B*, **6**, 90 (1972).

[96] V. S. Nikolaev and I. S. Dmitriev, *Phys. Lett.*, **28**, 277 (1978).

[97] J. Lindhard, *Dan. Mat. Fys. Medd.***28**, No. 8 (1954)

[98] I. H. Hutchinson, *Principles of Plasma Diagnostics*, Cambridge University Press, 1987.

[99] R. D. Petrasso, M. Gerassimenko, F. H. Seguin, et al., *Rev. Sci. Instrum.*, **51** 585 (1980)

[100] K. W. Wenzel and R. D. Petrasso, *Rev. Sci. Instrum.*, **59** 1380 (1988)

[101] K. W. Wenzel, *Ph. D. Thesis*, Massachusetts Institute of Technology, 1990.

[102] W. A. Blanpied, *Modern Physics*, Holt, Rinehart and Winston, INC. 1971.

[103] V. Valcovic, *Trace Element Analysis*, Taylor and Francis, UK (1987).

[104] American Society for Testing and Materials Special Publication, edited by J. C. Russ, 485 (1971).

[105] T. A. Carlson, *Photoelectron and Auger Electron Spectroscopy*, Plenum Press, New York 1976.

[106] M. O. Krause, *J. Phys. Chem. Ref. Data*, **8**, 307 (1979).

[107] W. Bambynek, B. Crasemann, R. W. Fink, H. U. Freund, H. Mark, C. D. Swift, R. E. Price and P. Venugopalo Rao, *Revs. Mod. Phys.*, **44**, 716 (1972).

[108] N. Troulfanidis, *Measurement and Detection of Radiation*, Hemisphere Pub. Corporation, New York (1972).

[109] E. Merzbacher and H. W. Lewis, *Encyclopedia of Physics*, edited by S. Flugge (Springer-Verlag, Berlin, 1958), **34**, 166.

[110] J. D. Garcia, *Physical Review A*, 1(2), 280 (1970).

[111] J. D. Garcia, R. J. Fortner, T. M. Kavanagh, *Reviews of Modern Physics*, **45**(2), 111 (1973).

[112] W. Brandt and G. Lapicki, *Physical Review A*, **23**, 1717 (1981).

[113] H. Paul, *Nucl. Instrum. and Meth. Phys. Res.*, **B4**, 211 (1984).

[114] D. D. Cohen, *Nucl. Instrum. and Meth. Phys. Res.*, **B22**, 55 (1987).

[115] G. F. Knoll, *Radiation Detection and Measurement*, Wiely, New York (1979).

[116] EG&G ORTEC, *Solid-State Photon Detector Operators Manual*, (1991).

[117] F. G. Goulding, *LBL-5368* (1976), Lawrence Berkeley Laboratory, Univ. of California.

[118] D. D. Cohen, *Nucl. Instrum. and Meth. Phys. Res.*, **193**, 15 (1982).

[119] LND, *Nuclear Detector Manual*, (1991).

[120] R. Korde and L. R. Canfield, *Proc. Symp. on X-Ray Instrum, in Medicine, Biology and Plasma Physics*, SPIE **1140**, 126 (1989).

[121] R. Korde, K. W. Wenzel, C. K. Li, and D. A. Pappas, *Proc. IEEE Symp.*, Nov. 1993.

[122] C. K. Li, K. W. Wenzel, R. D. Petrasso, D. H. Lo, J. W. Coleman, J. R. Lierzer, Wei, E. Hsieh, and T. Bernat, *Rev. Sci. Instrum.*, **63**(10). 4843 (1992).

[123] J. Chardwick, *Phil. Mag.*, **24**, 594 (1912).

[124] Sven A. E. Johansson and T. B. Johansson, *Nucl. Instr. and Meth.*, **137**, 473-516 (1976).

[125] Sven A. E. Johansson and J. L. Campbell, *PIXE: A Novel Technique for Elemental Analysis*, John Wiley and Sons, 1988.

[126] K. W. Wenzel, D. H. Lo, R. D. Petrasso, J. W. Coleman, C. K. Li, J. R. Lierzer, C. Borrás, T. Wei, E. Hsieh, and T. Bernat, *Rev. Sci. Instrum.*, **63**(10), 4837 (1992).

[127] F. Folkmann, G. Gaarde, T. Huus et al., *Nucl. Instr. and Meth.*, **116**, 487 (1974).

[128] K. Ishii and S. Morita, *Nucl. Instrum. and Meth. Phys. Res.*, **B22**, 68 (1987).

[129] D. D. Cohen and E. Clayton, *Nucl. Instrum. and Meth. Phys. Res.*, **B22**, 59 (1987).

[130] P. B. Needham and B. D. Sartwell, *Advances in X-Ray Analysis*, **14** 184, Plenum Press, (1970).

[131] N. A. Guardala, private communication, 1991.

[132] S. Humphries, Jr., *Charged Particle Beams*, John Wiley & Sons, Inc., 1990.

[133] K. W. Wenzel, J. W. Coleman, R. D. Petrasso, C. K. Li, and D. H. Lo, *Bull. Am. Phys. Soc.*, **35**, 2043 (1990).

[134] C. K. Li, K. W. Wenzel, R. D. Petrasso, J. W. Coleman, and D. H. Lo, *Bull. Am. Phys. Soc.*, **35**, 2043 (1990).

[135] C. Kurz, *Topics in Current Physics*,

[136] M. Green, *Proc. Phys. Soc.*, **83**, 435 (1964).

[137] M. Green, *X-Ray Optics and X-Ray Micro-analysis*, 185 (1962).

[138] M. Green and V. E. Cosslett, *Prit. J. Phys.*, **1** (2), 425 (1968).

[139] G. L. Johnson, *X-Ray Optics and X-Ray Micro-analysis*, 229 (1962).

[140] E. F. Priestley, *X-Ray Optics and X-Ray Micro-analysis*, 193 (1962).

[141] K. W. Wenzel, C. K. Li, R. D. Petrasso, D. H. Lo, M. Boutan, G. Ricker, and E. Hsieh, *Rev. Sci. Instrum.*, **64** 1380 (1993)

[142] K. W. Wenzel, C. K. Li, D. A. Pappas, and R. Korde, to be submitted for publication in *Appl. Phys. Lett.*, (1993).

[143] L. R. Canfield, J. Kerner, and R. Korde, *Appl. Opt.*, **28**, 3940 (1989).

[144] L. R. Canfield, J. Kerner, and R. Korde, *SPIE*, **1344**, 372 (1990).

[145] C. K. Li, R. D. Petrasso, K. W. Wenzel et al., to be published.

[146] Isotope Products Laboratory, *Radiation Sources for Research Industry Environmental Applications*, (1986).

[147] R. D. Petrasso, C. L. Fiore, and C. K. Li, *Rev. Sci. Instrum.*, **59**(8), 1721 (1988).

[148] K. W. Wenzel, R. D. Petrasso, D. H. Lo, C. K. Li, J. W. Coleman, J. R. Lierzer, Hsieh, and T. Bernat, *Rev. Sci. Instrum.*, **63**(10), 4840 (1992).